Annals of Anatomy 205 (2016) 22–36

Contents lists available at ScienceDirect

Annals of Anatomy

journal homepage: www.elsevier.com/locate/aanat

Research article

Vasavasoruminthetunicamediaandtunicaadventitia oftheporcineaorta

Zbynek˘ Tonar[a,*], Petr Tomásek˘ [a], Petr Loskot[b], Jirí˘ Janácek˘ [c], Milena Králícková˘ [a], Kirsti Witter[d]

[a] DepartmentofHistologyandEmbryologyandBiomedicalCenter,FacultyofMedicineinPilsen,CharlesUniversityinPrague,Karlovarska48, 30166Pilsen,CzechRepublic [b] DepartmentofAnatomy,FacultyofMedicineinPilsen,CharlesUniversityinPrague,Karlovarska48,30166Pilsen,CzechRepublic [c] DepartmentofBiomathematics,InstituteofPhysiologyAcademyofSciencesoftheCzechRepublic,Videnska1083,14220Prague,CzechRepublic [d] InstituteofAnatomy, HistologyandEmbryology,DepartmentforPathobiology,UniversityofVeterinaryMedicineVienna,Veterinärplatz1, A-1210Vienna,Austria

article info

Articlehistory:
Received1October2015
Receivedinrevisedform
14November2015 Accepted5
January2016

Keywords:
Artery
Microvessels
Pig
Stereology Vascularwall
vonWillebrandfactor.

abstract

Vasa vasorum supply both the tunica adventitia and the tunica media of major arteries with nutrients and oxygen. We estimated the density of von Willebrand factor-positive profiles of vasa vasorum visible in transversal histological sections of 123 tissue samples collected from five anatomical positions in the porcine aorta of growing pigs (n=25). The animals ranged in age from 0 to 230 days. The tunica media of the thoracic aorta had a greater vasa vasorum density, with microvessels penetrating deeper towards the lumen than in the abdominal aorta. The density of vasa vasorum gradually decreased with age in both the media and the adventitia. The relative depth into which the vasa vasorum penetrated and where they branched remained constant during the ageing and growth of the media. The ratio of the tunica media and tunica adventitia thicknesses did not change in the single aortic segments during ageing. The media of older animals received fewer but equally distributed vasa vasorum. A greater density of vasa vasorum in the media was correlated with greater media thickness and a greater elastin fraction (data on elastin taken from another study on the same samples). Immunohistochemical quantification revealed deeper penetration of vasa vasorum towards the adluminal layers of the tunica media that were hitherto reported to be avascular. The complete primary morphometric data, in the form of continuous variables, have been made available as a supplement. Mapping of the vasa vasorum profile density and position has promising illustrative potential for studies on atherosclerotic and inflammatory neovascularization, aortic aneurysms, and drug distribution from arterial stents in experimental porcine models.

1.Introduction

Vasa vasorum deliver oxygen and nutrients into and drain metabolites from the wall of larger blood vessels, thus providing essential physiological support for growth, repair, and homeostasis of the vascular wall. Two anatomically distinct distribution patterns of vasa vasorum have been distinguished: (i) the first order vasa run more or less longitudinally to the host vessel, and (ii) their second-order branches are arranged preferentially spirally or circumferentially (Moreno et al., 2006). Although vasa vasorum occur predominantly in the adventitia, their branches also penetrate into the media of the larger vessels. Conventional studies on aortic vasa vasorum in human and other mammals (Wolinsky and Glagov, 1967, 1969) have shown that in healthy elastic arteries, an inner (adluminal) zone contains no vasa vasorum, as it is supposedly supplied by diffusion from the vascular lumen. This avascular zone has been described to be approximately 0.5-mm thick on average in adults, which corresponds to 29 lamellar units, each of them consisting of vascular smooth muscle cells sandwiched between collagen and elastin fibres and ground substance (thickness of one lamellar unit: approximately 15–16 m; Shadwick, 1999). These findings have been repeatedly confirmed, thus demonstrating that ontogenesis, the anatomical position of the vessel, local oxygen tension and wall thickness are important determinants of the presence or absence of vasa vasorum (Okuyama et al., 1988). The avascular or less vascularized regions

* Corresponding author. Tel.: +420377593320. E-mail address: tonar@lfp.cuni.cz (Z. Tonar).

http://dx.doi.org/10.1016/j.aanat.2016.01.008 0940-9602/

of major arteries, and especially the aorta, have proved to be prone to atherosclerosis (Ritman and Lerman, 2007). In contrast, vasa vasorum proliferation within the intima and media is a part of the inflammatory response during atherosclerotic plaque development. This arterial neovascularization heavily contributes to leukocyte recruitment, intimal hyperplasia (Newby and Zaltsman, 2000), and the instability of atherosclerotic plaques (Moulton et al., 2003; Moreno et al., 2006; Baikoussis et al., 2011), thus increasing the rupture risk (Fleiner et al., 2004). Moreover, vasa vasorum play a significant role in the pathogenesis of a number of surgical aortic diseases, such as aortic aneurysm (Eberlova et al., 2013), acute or chronic aortic dissection, intramural haematoma, and restenosis after transluminal angioplasty (Baikoussis et al., 2011).

1.1. Visualization of vasa vasorum

In histological sections, larger vasa vasorum are easily identified within the tunica adventitia using overall staining (Okuyama et al., 1988), but for quantitative visualization of all vasa vasorum in the tunica media, staining for specific endothelial markers, such as von Willebrand factor (Witter et al., 2010; Tonar et al., 2012; Houdek et al., 2013; Xu et al., 2015) or CD markers such as CD31 (Eberlova et al., 2013) or CD34, if available for the respective mammalian species (for review, see, e.g., Ordónez, 2012), is necessary. To overcome the limitations of two-dimensional histological studies, three-dimensional in vivo micro-CT imaging (X-ray microtomography) has been used for detailed mapping and spatial reconstruction of the branching pattern of vasa vasorum (Galili et al., 2004; Moreno et al., 2006). These studies have revealed an immense heterogeneity of adventitial vasa vasorum among different vascular beds. Three-dimensional methods also offer a number of quantitative parameters for assessment of the vasa vasorum network, e.g., the volume fraction of vasa vasorum within the wall, the ratio between the second-order and the first-order vasa vasorum, the in vivo diameter, or the numerical density of branching points (Galili et al., 2004). Several of these findings were suggested to be helpful for explaining the variable propensity for vascular disease among different vascular beds. An even higher resolution than in in vivo can be achieved by micro-CT of microvascular corrosion casts using injections of capillary-passable polymers (Ritman and Lerman, 2007). To assess the vasa vasorum in superficially positioned arteries, contrast-enhanced ultrasound techniques were tested in animal models (Granada and Feinstein, 2008). However, histological studies on vasa vasorum are still valuable because they may be applied to archive material. Additionally, the vasa vasorum can be assessed together with angiogenic or hypoxia markers, and the labelling of vasa vasorum in histological and histopathological sections is very reliable and reproducible and still shows the highest resolution of all available methods.

1.2. Aortic vasa vasorum in experimental porcine models

Due to its size and thickness, anatomical proportions, wall structure, and physiological similarities, the porcine aorta is the most suitable animal model of the human aorta and is currently being used in cardiovascular surgical (Dziodzio et al., 2011; Funder et al., 2012; Saari et al., 2012; Sarda-Mantel et al., 2012; Johnson et al., 2013) and biomechanical (Kim and Baek, 2011; Lillie et al., 2012) studies. Vasa vasorum quantification has been used as a marker of inflammatory neovascularization following reaction of the porcine aortic wall to tissue glues tested for the treatment of aortic dissection (Witter et al., 2010). Similarly, vasa vasorum have been used as a histopathological marker of pharmacologically mitigated progression of experimental aneurysm in the porcine abdominal aorta (Houdek et al., 2013). Nedorost et al. (2013) assessed vasa vasorum not in the aorta, but rather in the pulmonary artery, when examining the histopathological reaction to pulmonary artery banding in a growing porcine model. The porcine aorta was successfully used for testing anti-angiogenic drugs on adventitial neovascularization in experiments regarding early atherosclerotic lesions (Xu et al., 2015). Aguirre-Sanceledonio et al. (2003) investigated vasa vasorum hypertrophy in a porcine model of experimental coarctation of the thoracic aorta, demonstrating anastomoses between vasa vasorum and collateral aorto-aortic anatomical shunts. Angouras et al. (2000) found that after interrupting the vasa vasorum in the thoracic porcine aorta, decreased vasa vasorum blood flow resulted in necrosis, accompanied by elastin and collagen abnormalities in the outer media. The resulting interlaminar shear stresses and increased aortic stiffness were believed to contribute to the development of aortic dissection (Angouras et al., 2000). Mapping of porcine aortic vasa vasorum also has promising potential for explaining the diffusion of macromolecules through the wall of large elastic arteries (Hwang and Edelman, 2002), including the drug distribution from arterial stents with fine control of locally directed drug release (Kusanagi et al., 2007). Moreover, vasa vasorum are important for physiologically relevant porcine aortic models evaluating manufactured endovascular stent-grafts (Desai et al., 2011).

Summarizing the studies cited above, the distribution and quantity of porcine aortic vasa vasorum rely on a number of factors that affect the microenvironment of the media and adventitia. A number of microscopic differences must therefore be assumed to exist along the whole aorta (cf. Sokolis, 2007; Sokolis et al., 2008). However, a detailed study comparing any potential regional and age-related differences in vasa vasorum of the porcine aorta is still missing. None of the studies cited above provided quantitative information on vasa vasorum in the media and adventitia of various aortic segments at the same time. The first rationale for our study was to quantify the immunohistochemically detectable vasa vasorum in various aortic segments and in different age groups of pigs that are frequently used in experiments using statistically comparable variables. As we recently published a quantitative study on segmental and age differences in the elastin network, collagen, and the smooth muscle phenotype in the tunica media of the porcine aorta (Tonar et al., 2015b), we decided to analyse vasa vasorum in parallel sections of the same tissue blocks. Providing quantitative information on vasa vasorum within the context of the aortic wall composition became the second rationale for the present study.

1.3. Study aims

The aim of our study has been to assess the density and distribution of vasa vasorum by immunohistochemical detection in transversal histological sections of the porcine aorta and to compare the data between single aortic segments and between age groups. Moreover, possible correlations between vasa vasorum morphometry and the histological composition of the same aortic samples as published in a previous study (Tonar et al., 2015b) were tested. The following null hypotheses were formulated and tested:

H_0(A): The two-dimensional density of vasa vasorum profiles per section area unit is the same in all proximodistal aortic segments of the same individual when comparing the aortae of growing domestic pigs (age 0–230 days). This was tested separately for the media, adventitia, and whole wall. Due to considerable variations in the thickness of the tunica media observed in our unpublished preliminary studies, the density of vasa vasorum in the media was studied in five artificially defined virtual sublayers in particular, with each of these sublayers comprising one-fifth of the media thickness.
H_0(B): The mean relative position of vasa vasorum profiles within the media and adventitia is the same for suckling piglets, weaners, and fattening pigs when comparing corresponding aortic segments. This was tested separately for the media and adventitia. H_0(C): The two-dimensional density of vasa vasorum profiles per section area unit is the same in the adventitia as in all virtual sublayers of the media. This was tested separately for all three age groups and all five aortic segments under study.
H_0(D): The density and the distribution of the vasa vasorum do not correlate with the thickness of the aortic layers or with the histological composition of the porcine aorta, as published previously (Tonar et al., 2015b).

2. Materials and methods

2.1. Animals, specimen preparation, aortic segments, and age groups

We used the aortic samples previously collected for studies on vascular smooth muscle orientation (Tonar et al., 2015a) and the histological composition of the aorta (Tonar et al., 2015b). Whole aortae of domestic pigs were collected. The animals

(commercial fattening hybrids, n = 25; 12 males, 11 females, 1 castrated male, 1 without documented sex; age 0–230 days; weight 0.7–95 kg) were euthanized at the end of other experiments related to immunology and parasitology (Worliczek et al., 2010; Gabner et al., 2012; Ondrovics et al., 2013). All of the animals were raised conventionally and treated in compliance with the European Convention on Animal Care.

The aortae were without any macroscopic signs of pathological changes. After routine fixation using buffered formalin according to Lillie (Romeis, 1989), the aortae were divided into five aortic segments, each of them representing one of the following regions: the ascending aorta (aorta ascendens), aortic arch (arcus aortae), thoracic descending aorta (aorta thoracica), suprarenal abdominal aorta (aorta abdominalis, pars suprarenalis), and infrarenal abdominal aorta (aorta abdominalis, pars infrarenalis; Fig. 1A). After fixation, the samples were rinsed in 70% ethanol. From each aortic segment, one tissue block was embedded in paraffin for transversal sectioning. To compare the aortic samples according to age, the animals were divided into the following three groups: suckling piglets (age 0–28 days, n = 64 vascular segments collected from 13 animals), weaners (age 29–75 days, n = 35 vascular segments collected from 7 animals), and fattening pigs (age 180–230 days, n = 24 vascular segments from 5 animals). In total, 123 tissue samples were collected (two infrarenal segments were missing because they were damaged during dissection).

2.2. Preparation of histological sections

Two histological sections per sample (section thickness 4 m) were cut perpendicularly to the longitudinal axis of the vessel. The sections were deparaffinized and rehydrated. In one section, the layers of the aortic wall were identified using a combination of Verhoeff's haematoxylin and green trichrome staining according to Kocova (1970). In the other section, vasa vasorum were detected immunohistochemically using an anti von Willebrand factor antibody. After blocking the endogenous peroxidase activity in the rehydrated sections with 0.6% H_2O_2 in methanol and following antigen retrieval by protease digestion (1 mg protease from Streptomyces griseus (Sigma-Aldrich, Vienna, Austria)/1-ml phosphate-buffered saline (PBS; pH 7.4)) for 20 min at room temperature, unspecific binding activity was blocked with 1.5% normal goat serum (DakoCytomation, Glostrup, Denmark) in PBS for 30 min. Afterwards, the sections were incubated overnight at 4 °C with primary polyclonal rabbit anti-human von Willebrand factor antibody (DakoCytomation). The immunoreaction was detected using the BrightVision PolyHRP-Anti-rabbit kit (ImmunoLogic, Duiven, The Netherlands) according to the manufacturer's instructions. The reaction was visualized with diaminobenzidine (Sigma-Aldrich, Vienna, Austria) in 0.03% H_2O_2 in PBS. After immunohistochemistry, the sections were counterstained with Mayer's haematoxylin, dehydrated and mounted with a medium soluble in xylene.

2.3. Micrographs

For each section with immunohistochemically visualized vasa vasorum, two micrographs were taken from the opposite sides of the aortic ring using a 4× objective mounted on an Olympus BX51 microscope (Olympus, Tokyo, Japan). The magnification was low enough to capture the whole thickness of the aortic wall, but, at the same time, the micrographs provided a resolution of 1 pixel = 2.2 m, guaranteeing reliable identification of all immunopositive vasa vasorum. With a total sampled area of 19 mm^2 per section, the whole or a significant part of the aortic

section profile was captured by the two micrographs, depending on the anatomical size and wall thickness. The sampling micrographs were randomly positioned on the section, without preferential sampling of the dorsal, ventral, or lateral sides, as the information on anatomical directions was not labelled on the slides. In total, 246 micrographs were captured and analysed from the 123 tissue samples. The sampling of the micrographs from the sections is explained in Fig. 1B.

2.4. Morphometry of vascular layers and of vasa vasorum within the tunica media and adventitia

In each micrograph, three morphologically clearly visible linear border profiles were highlighted (Fig. 1C) using the Multiline tool of Ellipse software (ViDiTo, Kosice, Slovak Republic): (i) the section profile of the adluminal surface of the intima (labelled as line 1), (ii) the section profile of the border between the media and the adventitia (labelled as line 2), and (iii) the section profile of the outer (abluminal) border between the adventitia and the periaortic loose connective tissue (labelled as line 3). The media adventitia border was defined as the most abluminal regularly repeating lamellar unit of the tunica media. The outer adventitial border was defined as the transition between the adventitial dense collagenous connective tissue (counted as the adventitia) and the highly variable surrounding loose periaortic connective tissue (not included in the adventitia). These morphological borders were clearly visible, even in immunohistochemically stained sections. If necessary, the adjacent sections stained with elastic and trichrome stain were consulted to identify the border lines (not shown). Examples of microvessel identification in the tunica media and tunica adventitia are shown in Fig. 1D and E, respectively.

The thickness of the vascular layers was estimated using the LocalizeInWall2 module of the Ellipse software, as follows: the intima + media thickness was defined as the mean distance between line 1 and line 2 in both sections. This was performed by averaging the shortest connections between the points of both lines. As the intima was very thin and practically indistinguishable from the media, they were counted as part of the same reference area. The adventitial thickness was the mean distance between line 2 and line 3 in both sections. The measurement of wall thickness used in the present study differed from the technique applied in the adjacent sections in the previous study (Tonar et al., 2015a,b). The present technique relied on a much larger sampling area and was immediately linked to the assessment of the vasa vasorum density and distribution in all sections (see below). The profile areas of all of the layers (A(layer)) were calculated.

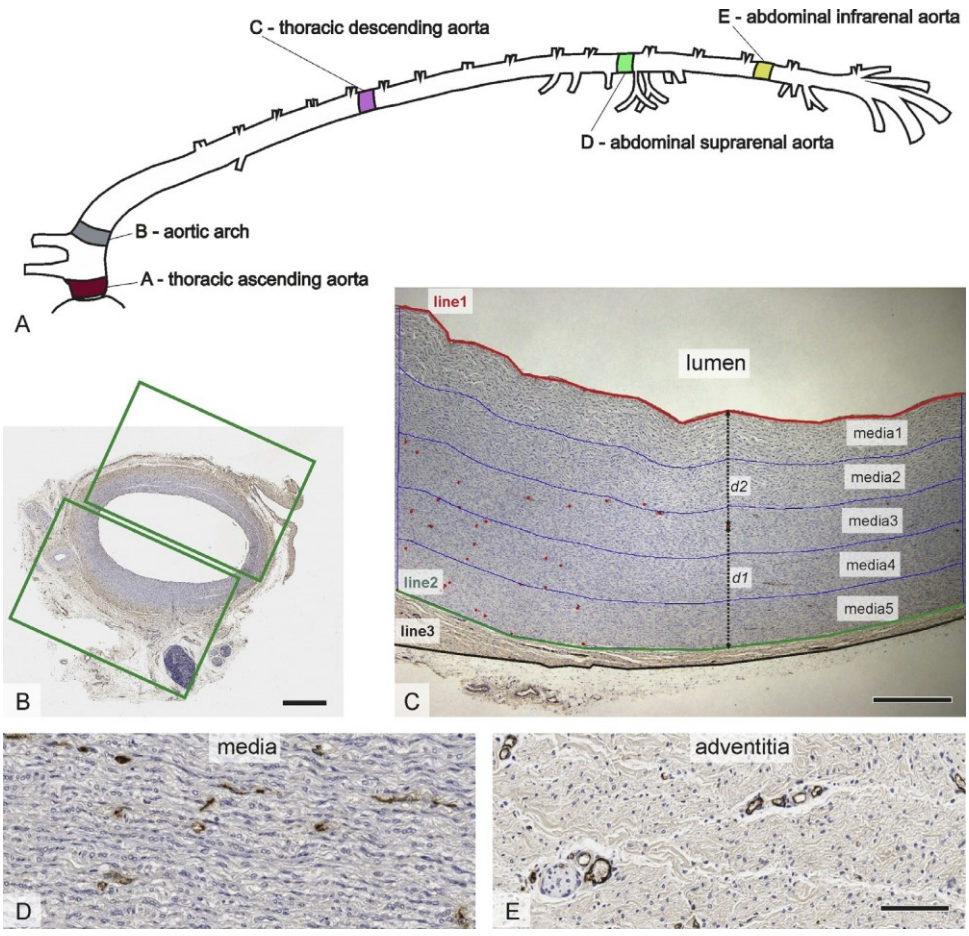

Fig. 1. Position and sampling of the porcine aortic wall and quantitative assessment of the vasa vasorum. (A) Anatomical position of the aortic segments (A–E) collected in the present study. The positions were redrawn according to the anatomical dissection of the porcine aortae (KW) and according to Nickel et al. (1996). Reproduced from Tonar et al. (2015b) with the permission of Elsevier. (B) Two micrographs (demonstrated with proportionally sized rectangles) were taken from the opposite sides of the aorta, recording all of the aortic layers. The pair of the micrographs had no preferential position in relation to the original anatomical directions. (C) The outlines of the aortic wall layers were drawn manually onto the micrographs, with line 1 (red) marking the adluminal surface of the intima, line 2 (green) marking the border between the media and the adventitia, and line 3 (black) outlining the border between the adventitia and the periaortic loose connective tissue. The intima + media thickness was measured as the mean distance between line 1 and line 2. Five virtual sublayers of media (media 1 to media 5, each comprising 20% of the local thickness) were projected onto the micrograph. The adventitia thickness was the mean distance between line 2 and line 3. The number and position of the vasa vasorum profiles were recorded (marked with red points in the left part of the image, otherwise stained dark brown). The relative position of the profiles within the media was expressed as the ratio between the d1 and the d1 + d2 distances (see the Section 2 for further details and an assessment of the vessel position in the adventitia). (D) Examples of vasa vasorum in the media. (E) Examples of vasa vasorum in the adventitia. Immunohistochemical detection of the endothelial von Willebrand factor, visualization with horseradish peroxidase/diaminobenzidine (brown), and counterstaining with haematoxylin. Scale bars: 1 mm (B), 500 m (C) and 100 m (D,E) (B–E taken from animals of various ages to illustrate the size differences) (For interpretation of the references to color in this figure legend, the reader is referred to the web version of this article).

The position and number of all vasa vasorum profiles within the defined layers were marked and counted using the Point tool of the Ellipse software. Using the LocalizeInWall2 module of the same software, the quantity of vasa vasorum was assessed as the number of von Willebrand factor-positive microvessel profiles per section area Q_A of the vascular wall (Witter et al., 2010; Tonar et al., 2012; Eberlova et al., 2013; Houdek et al., 2013): $Q_A(\text{microvessels, layer}) = Q/A(\text{layer})$ (mm^{-2}),

where, Q was the number of microvessel profiles counted and A(layer) was the estimated reference area of the section through the aortic wall layers. This was performed separately (i) for the tunica media and intima reference areas and (ii) for the tunica adventitia reference area. Afterwards, the number of microvessel profiles per area unit of the individual layers was summed and related to the total cross-sectional area of the whole aortic section to calculate the mean vasa vasorum density of the whole sample. To assess the depth of vasa vasorum penetration into the media in more detail, five virtual sublayers were arbitrarily defined within the intima+media. Each of these sublayers had an equal thickness comprising exactly 20% of the local intima + media thickness. As the intima contained no microvessels at all, these sublayers of media were numbered media 1 to media 5, starting from the innermost adluminal sublayer (Fig. 1C).

The relative position of the vasa vasorum profiles within their relevant layers (i.e., their penetration depth) was assessed using an arbitrarily defined function f describing the relative distance of the profiles in the radial direction across the wall: f = d1/(d1+d2), where, d1 was the distance of the vessel profile from the abluminal border of each layer and d2 was the distance of the vessel profile from the more adluminal border of the same layer. The value of f equalled 0 at the abluminal border and equalled 1 at the adluminal border of each layer (Fig. 1C).

All quantitative parameters assessed in this study are defined and explained in Table 1. To eliminate the possible edge effect (Gundersen, 1977) and repeated counting of the same vessel profiles crossing the borders between media/adventitia and adventitia/periaortic loose connective tissue, the left adluminal part of the vessel profile was arbitrarily determined to include or exclude

Table 1
Quantitative parameters used in this study for morphometry of vasa vasorum within the porcine aortic wall.

Quantitative parameter abbreviation	Definition, reference area, interpretation and units
Q_A(media)	Number (or two-dimensional density) of vasa vasorum profiles found within the intima and media per area unit of the intima and media in a transverse section of the aorta (mm^{-2}).

f(media)	Meanrelativedistanceofvasavasorum profiles foundwithintheintimaandmedia fromtheborder betweenthemediaand theadventitia.A dimensionlessparameter rangingbetween0and1, where0refersto vasavasorumdirectlyatthe media-adventitiaborderand1refersto vasavasorumonthe intraluminalborder
Int+mediathickness (IMT)	oftheintima(−). Thecombinedthicknessoftheintimaand media, measuredasthemeandistance betweentheintimal surfaceprofile (Fig.1C,line1)andthemedia-adventitia borderprofile(Fig.1C,line2)(m).
Q_A(adventitia)	Densityofvasavasorumprofileswithin the adventitia(mm^{-2}).
f(adv)	Meanrelativedistanceofvasavasorum profilesinthe tunicaadventitiafromthe
Adventitiathickness (AT)	outeradventitialborder(−). Thicknessoftheadventitia,measuredas themean distancebetweenthe media-adventitiaborder(Fig. 1C,line2) andtheouteradventitialborder(Fig.1C, line3)(m).
Q_A(wall)	Densityofallvasavasorumprofilesper areaunitof thewholesectionprofileofthe aortic wall (mm^{-2}).
Wallthickness(WT)	IMTsummedwiththeAT(m).
A_A (elastin, collagen, actin, desmin, and vimentin)	Theareafractionsoftheelastin,collagen, actin, desmin,andvimentinwithinthe tunicaintimaand mediareferenceareas(−).

See also Section 2 and Fig. 1C for further explanation. The values of the area fractions of the aortic wall constituents (elastin, collagen, actin, desmin, and vimentin) were taken from previously published resultsanalysingthesametissuesamples(Tonaretal.,2015b).

the microvessel profile from the counting. In case of occasional preparation and sectioning artefacts, such as microcracks and folds, the section under study was replacedbyadjacentserialsectionto preventanybiastothequantificationofdensity and position of the vasa vasorum profiles. Only technically well-prepared sections were eligible for the quantification. In total, 15,070 vasa vasorum profiles were counted (7799 within the intima + media and 7271 within the adventitia reference area).

2.5.Statistics

Shapiro–Wilk's W-test was used for normality testing of the data and demonstratedthatthedistributionofthevaluesdifferedfromthenormaldistributionin certainaorticsegments. Therefore,nonparametricstatisticswereappliedforfurther analysis. The Friedman ANOVA test for dependent variables and the Wilcoxon matched-pairstestwereusedtoassessthedifferences betweenaorticsegments(A–E) from the same animals under study and between the aortic layers of the same individuals. The Kruskal–Wallis ANOVA test and the Mann–Whitney U-test were used to assess the differences between the age groups. The correlation between the density and distribution of vasa vasorum profiles, the thickness of the aortic wall layers, and the composition of the tunica media were evaluated using the Spearman correlation coefficient. These tests were used as available in the Statistica Base 11 package (StatSoft, Inc., Tulsa, OK, USA). Significant results are reported as * ($p < 0.05$), ** ($p < 0.01$), and *** ($p < 0.001$).

3. Results

3.1.Segmentaldifferencesinthevasavasorumdensityand distribution

In the tunica media, differences in both the vasa vasorum profile density and their distribution were found when comparing the values for all aortic proximodistalsegments(i.e.,fromtheherttothe terminalbranchingoftheaorta) ofthesameanimal.Thedensityof thevasavasorumprofiles(Fig.2A)decreasedin the proximodistal direction, and highly significant differences were found between nearly all aortic segments under study, except the suprarenal and infrarenalaortae.Themeanrelativedistanceofthevasavasorum profilesfromthe media-adventitia border was greater in thoracic aortic segments A–C than in abdominalsegmentsD–Eanddiffered betweenallsegments,exceptbetweenthe aorta ascendens and the arcus aortae and between the aorta ascendens and the thoracic descendingaorta(Fig.2B).

In the tunica adventitia, no significant differences were found in either the densityorthedistributionofthevasavasorumprofiles (Fig.2CandD).

When considering the mean density of the vasa vasorum profiles calculated perwholewall,thethoracicaorticsegments differedfromtheabdominalsegments (Fig.2E),withthevalues beinggreaterintheabdominalsegments.Theratioofthe intimamedia thickness to the wall thickness gradually decreased in the proximodistaldirection(Fig.2F).

As expected, no vasa vasorum were found in the most adluminal fifth of the media (media1). When comparing the five virtual sublayers of the media, the proximal segments of the aorta (segments A–C) had greater densities of vasa vasorum profiles in the media2 to media4 sublayers than the abdominal aortic segments(D–E)did (Fig.3A).

To summarize the segmental differences, the H_0(A) hypothesis was rejected forthetunicamedia,formostofthevirtualsublayers ofthemedia,andforthewhole aorticsectionalprofile,butitwas retainedforthetunicaadventitia.

3.2.Comparisonofthevasavasorumdensityanddistribution betweentheage groups

Quantitativedifferencesbetweentheagegroupsaredisplayed inFig.4.Inthe media,thedensityofthevasavasorumprofileswas lowerinfatteningpigsthanin sucklingsorweaners(Fig.4A)but retainedthesamedistribution(Fig.4B).Inthe adventitia,thedensityofthevasavasorumprofileswaslowerinfatteningpigsthan in suckling pigs (Fig. 4C), and the distance of the vasa vasorum profiles from the outerborderoftheadventitia(thepenetrationdepth) decreasedwithage(Fig.4D). When considering the mean density of the vasa vasorum profiles calculated per wholewall,itgradually decreasedwithage(Fig.4E).Theratiooftheintima-media thicknesstothewallthicknessremainedconstantduringageing(Fig.4F).

Whencomparingthefivevirtualsublayersofthemedia,the densityofthevasa vasorum within the outermost media5 sublayer showed a significant decrease withage(Fig.3B).

To summarize the age differences, the H_0(B) hypothesis was rejected for both the density and the distribution of vasa vasorum in the tunica media, in the most abluminal sublayer of the media (media5), in the adventitia, and also in the whole sectional profile of the wall.

3.3.Comparisonofthevasavasorumdensitybetweenthe vascularlayers

In all aortic segments (Fig. 5A–E), the adventitia had the greatest density of vasa vasorumprofiles,followedbythemostabluminal

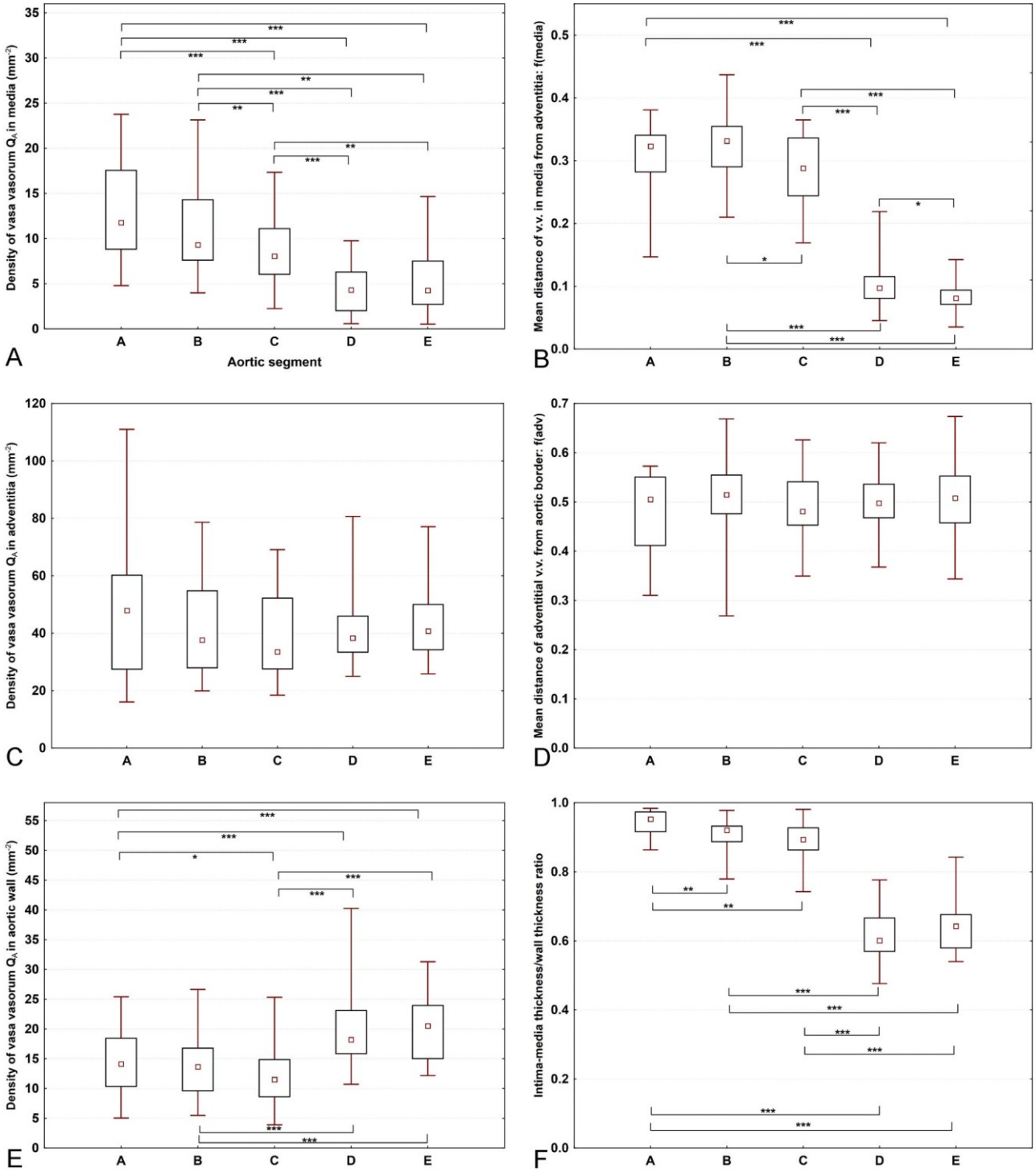

Fig. 2. Density of vasa vasorum (v.v.) profiles (Q_A) in the tunica media (A), the adventitia (C) and the aortic wall (E) of 0–230-day-old pigs, together with the relative position of vasa vasorum profiles within the media (B) and adventitia (D) and the ratio of the intima-media thickness to the whole-wall thickness (F). The relative positions of vasa vasorum profiles were determined as the distance from the outer wall layer divided by the wall layer thickness. Segments A, B, C, D, and E on the x-axis denote the aorta ascendens, arcus aortae, thoracic descending aorta, suprarenal abdominal aorta, and infrarenal abdominal aorta, respectively. The age groups were pooled for this comparison. Only the corresponding paired values from the same individuals were tested. The differences between the segments were first tested using the Friedman ANOVA test, which showed significant differences ($p<0.001$) in the parameters shown under A, B, E, and F. For the parameters shown in A, B, E, and F, the Wilcoxon matched-pairs test was performed to compare the aortic segments (significant p-values are presented within the diagrams: $^{*}p<0.05$, $^{**}p<0.01$, $^{***}p<0.001$). The data are displayed as the median values, with boxes spanning the upper limits of the first and third quartiles and with whiskers spanning the minimum and maximum values for each group.

sublayer of the media (media5). The density of vasa vasorum gradually decreased towards the adluminal sublayers of the media until it reached zero in the innermost layer (media1). In contrast, the thoracic aorta (Fig. 5A–C) contained vasa vasorum profiles even within the middle sublayers of the media (media3, i.e., 40–60% of the media thickness measured from the intima), and these layers were avascular in the abdominal aortic segments (Fig. 5D–E).

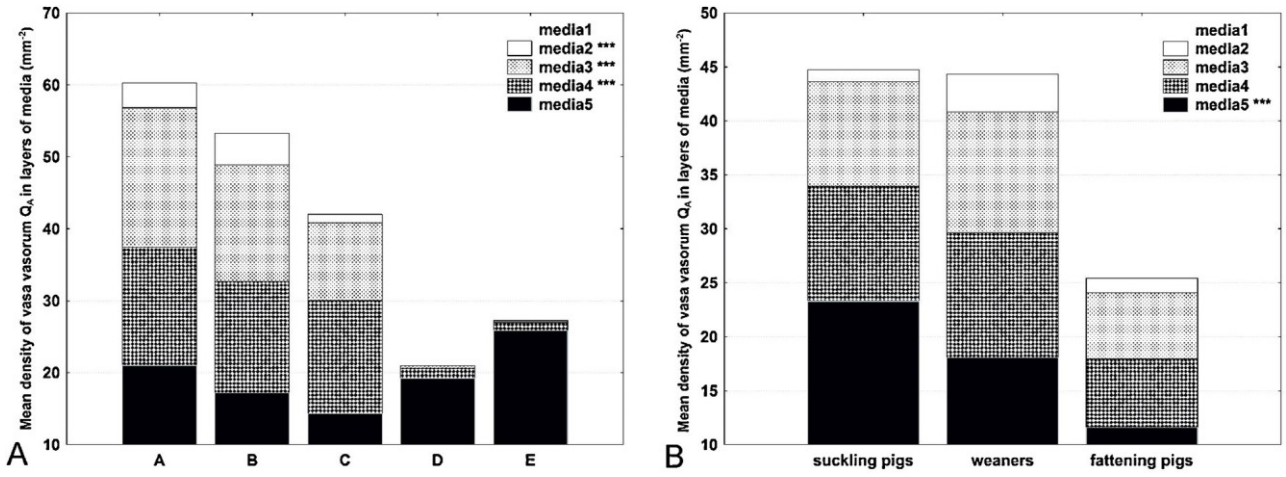

Fig.3.Meandensitiesofvasavasorumprofileswithinfivearbitrarylayersofthetunicamediaandcomparisonbetweentheporcineaorticsegments(A)andbetweentheagegroups(B).SegmentsA,B,C,D,andEonthe x-axisin(A)denotetheaortaascendens,arcusaortae,thoracicdescendingaorta,suprarenalabdominalaorta,andinfrarenal abdominalaorta,respectively.Thedataarepresentedasstackedplotsdemonstratingthe proportionsamongtheindividuallayers.Eachofthemediasublayersrepresented one-fifthofthemediathickness.Thesublayerswerelabelledstartingfromtheintimalsurface,withmedia1andmedia5representing theinnermostandoutermostmedia layers,respectively.Sublayermedia1didnotcontainvasavasorum.(A)Theproximalaorticsegments(segmentsA–C)hadgreaterdensitiesofvasavasorumprofilesinthe media2 to media4 sublayers than the abdominal aortic segments did (D–E) (*** denotes highly significant differences at p <0.001 in the Friedman ANOVA test). (B) When

comparing the age groups, the densities within the outermost media5 sublayer showed a significant decrease in the vasa vasorum density with age (*** denotes p <0.001 in

theKruskal–WallisANOVAtest).

In all age groups (Fig. 6A–C), the adventitia had the greatest density of vasa vasorumprofiles,followedbythemostabluminalsublayerofthemedia(media5).The densityofvasavasorum graduallydecreasedtowardstheadluminalsublayersofthe media until it reached zero in the innermost layer (media1) in all age groups. No differences were found between the media3 and the media4 sublayers in all groups; i.e.,thedensityofprofileswas thesamewithinthemiddleregionofthemedia(40–80% of themediathicknessmeasuredfromtheintima),independent ofage.

To summarize the differences between the layers, the H_0(C) hypothesis was rejected.

3.4.Correlationofthevasavasorumdensityanddistribution withthethickness oftheaorticwallandwiththetunicamedia histologicalcomposition

TheSpearmanrank-ordercorrelationsbetweenquantitative parametersthatwere found to be significant ($p<0.05$) are listed in Table 2. H_0(D) was rejected, as both the density and the distribution of vasa vasorum in both the media and the adventitia correlated with the thickness of the aortic wall layers as well as with the aortic wall composition.

3.5.Complementaryqualitativemorphologicalfindings

No direct communication of vasa vasorum with the aortic lumen (vasa vasorum interna)wasobserved.Examplesofsegmentaland age-relateddifferencesinthevasa vasorumprofiledensityanddistributionareshowninFig.5.Differencesintherelative thicknesses of the media and adventitia between the proximodistal aortic segments were clearly visible, even without quantification, but the density estimates were reliably detectable only by quantitative assessment and statistics. However, the deeper penetration of the vasa vasorum profiles into the vessel wall of the thoracic aorta when compared with the abdominal aorta was clearly visible, even by microscopicexamination(Fig.7).

Thecompletedataset withallthemorphometricresultsforall ofthesamplesofall aorticsegmentsisprovidedinAppendixA.

4. Discussion

4.1.Thetunicamediaofthethoracicaortahadagreatervasa vasorumdensity, andthesevesselspenetrateddeeperintothe aorticwalltowardsthelumenthanin theabdominalaorta

The vasa vasorum density within the media decreased in the proximodistal direction (Fig. 2A), but the overall vasa vasorum density calculated per whole vesselwallshowedgreatervaluesinthe abdominalaortathaninthethoracicaorta (Fig. 2E). This finding appears to be a contradiction, but it is most probably the numerical result of a much thinner aortic media and whole wall in the abdominal segments(Fig.2FinTonaretal.,2015b).Thereference areaofthewholevascular wallsectionincreaseswiththesecond powerofthewallthickness,andtherefore, thesectionareaused asthedenominatoroftheQA parameterisrelativelygreaterin the thicker thoracic segments but relatively smaller in the thinner abdominal segments. Nevertheless, the greatest vasa vasorum density in the media found in the thoracic aorta suggests that the highly elastic thoracic segments require an especiallyrichmicrovessel networkandthatthethickerthoracicsegmentsreceive lessdirect diffusionalsupport(Werberetal.,1987)fromthelumenthanthe thinner distal segments do. The greater vasa vasorum density in the media3 sublayer than in the deeper (more abluminal) media4 to media5 sublayers in the thoracic aorta (Fig. 3A) suggests that another branching is generated in approximately the middlethicknessofthemediaofthethoracicaorta.

Moreover, lower vasa vasorum densities within the media of the abdominal aorta might partially explain the vulnerability of the abdominal aorta to atherosclerosis or aneurysm formation (Heistad and Marcus, 1979). The precise role of the vasa vasorum in the mechanobiological stability (Humphrey and Holzapfel, 2012; Cyron and Humphrey, 2014a) and the propensity of the abdominalaortatoaneurysmformation(Cyronetal.,2014b)remains unclear.Itis notknown,whetherthevasavasorummorphologyandpenetrationdepthislinked toaorticremodellingand aneurysmsformationduetotheimbalancebetweenthe matrix metalloproteinasesandtheirinhibitors(SokolisandIliopoulos, 2014).

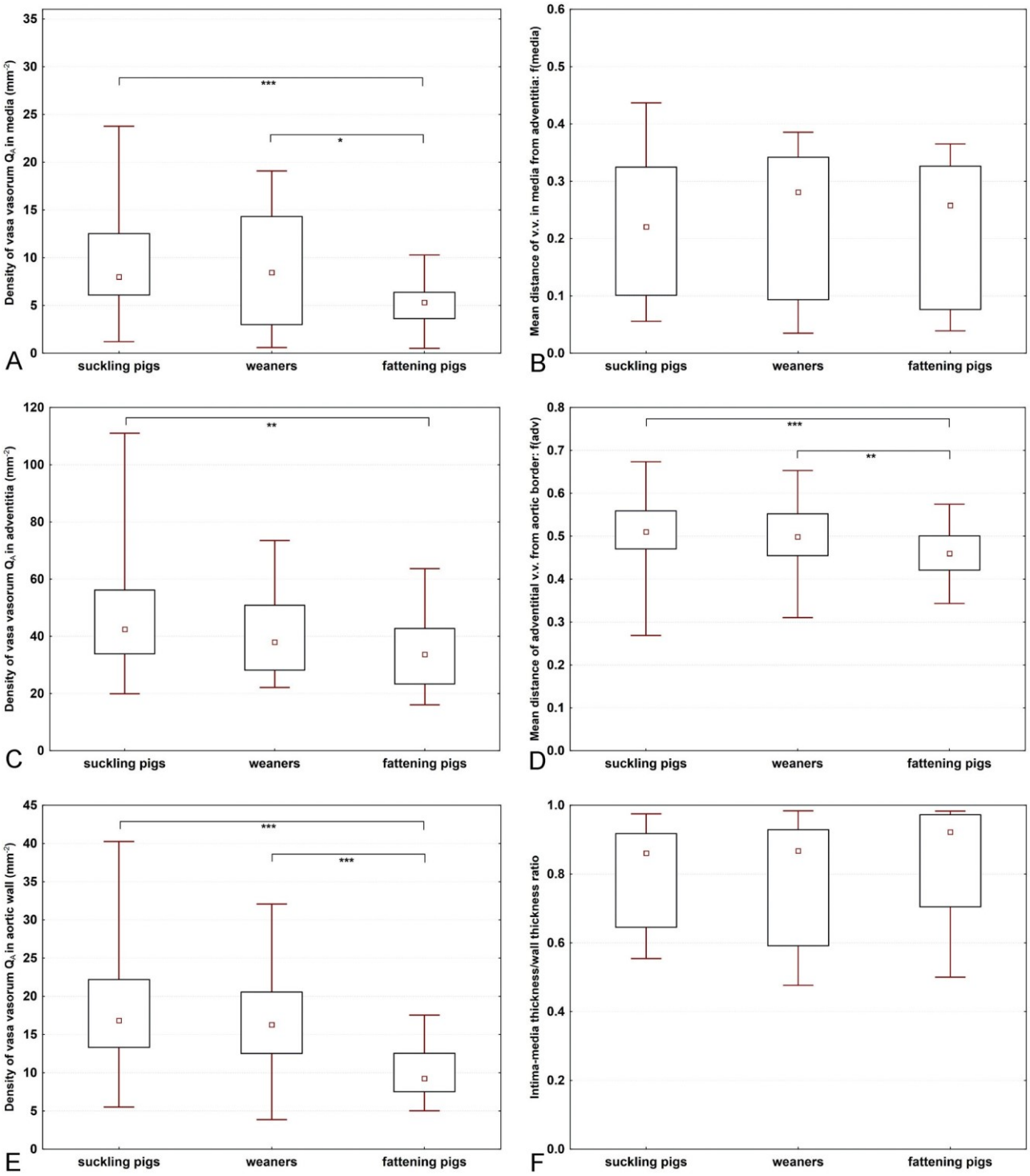

Fig. 4. Density of vasa vasorum (v.v.) profiles (Q_A) in the tunica media (A), the adventitia (C), and the aortic wall (E), together with the relative position of vasa vasorum profiles within the media (B) and adventitia (D) and the ratio of the intima-media thickness to the whole-wall thickness (F) in the three age groups of pigs. Aortic segments were pooled for this comparison. The differences between the age groups were first tested using the Kruskal–Wallis ANOVA test, which showed significant differences in the parameters shown under A ($p = 0.001$), C ($p = 0.02$), D ($p = 0.003$), and E ($p < 0.001$). For these parameters, the age groups were compared using the Mann–Whitney test (significant p-values are presented within the diagrams: $^{*}p < 0.05$, $^{**}p < 0.01$, $^{***}p < 0.001$). The data are displayed as the median values, with boxes spanning the upper limits of the first and third quartiles and with whiskers spanning the minimum and maximum values for each group.

Morphologically, the tunica adventitia proved to be a highly variable layer with respect to the aortic segments. In the proximodistal direction, the tunica adventitia is surrounded by a variety of tissues and microanatomical structures; i.e., a serous pericardial cavity, the loose connective tissue of the mediastinum and retroperitoneal fat, accompanied by a variable number of lymph nodes, aortic branches, and other structures. Surprisingly, this high level of anatomical variability did not affect the vasa vasorum density and distribution within the adventitia.

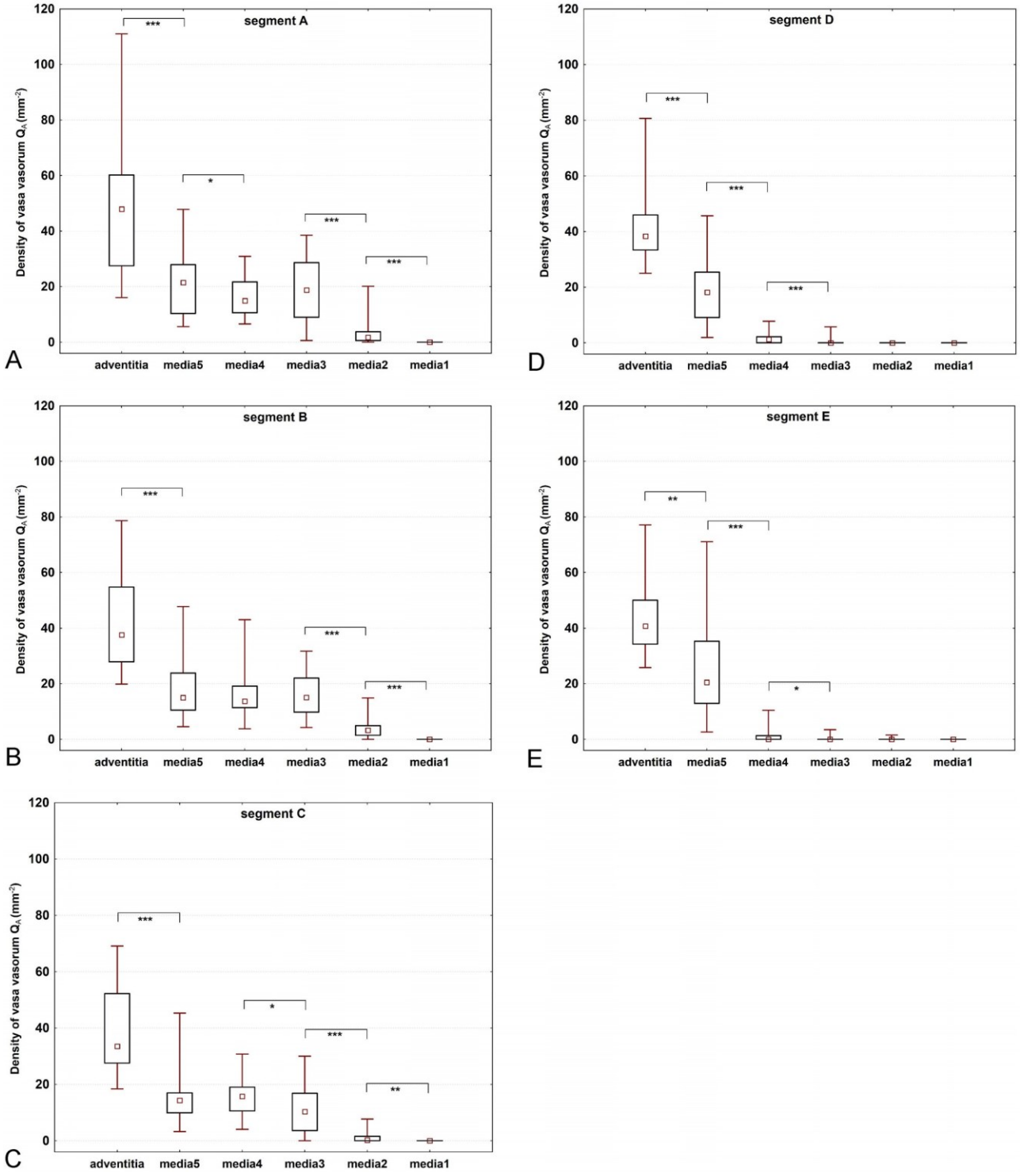

Fig. 5. Density of vasa vasorum profiles (Q_A) in the tunica adventitia and in the five virtual tunica media sublayers in the five proximodistal segments of the porcine thoracic (segments A–C in images A–C) and abdominal aorta (segments D–E in images D–E). For this comparison, the age groups were pooled, and the data from the corresponding images, sections and animals were exactly matched. The differences between layers were first tested using the Friedman ANOVA test, which showed significant differences in all segments ($p < 0.001$). Further comparisons between anatomically adjacent layers were performed using the Wilcoxon matched-pairs test (significant results are presented within the diagrams: $^{*}p < 0.05$, $^{**}p < 0.01$, $^{***}p < 0.001$). In all segments, the adventitia had the greatest density of vasa vasorum profiles, followed by the most abluminal

sublayer of the media (media5). The density of vasa vasorum gradually decreased towards the adluminal sublayers of the media until it reached zero in the innermost layer (media1) in the thoracic segments (A–C) or in the two innermost layers (media2 to media1) in the abdominal segments. Whereas the thoracic aorta (A–C) contained vasa vasorum profiles even within the middle medial sublayers (media3, i.e., 40–60% of the media thickness measured from the intima), these layers were avascular in the abdominal aortic segments (D–E). The data are displayed as the median values, with boxes spanning the upper limits of the first and third quartiles and with whiskers spanning the minimum and maximum values for each group.

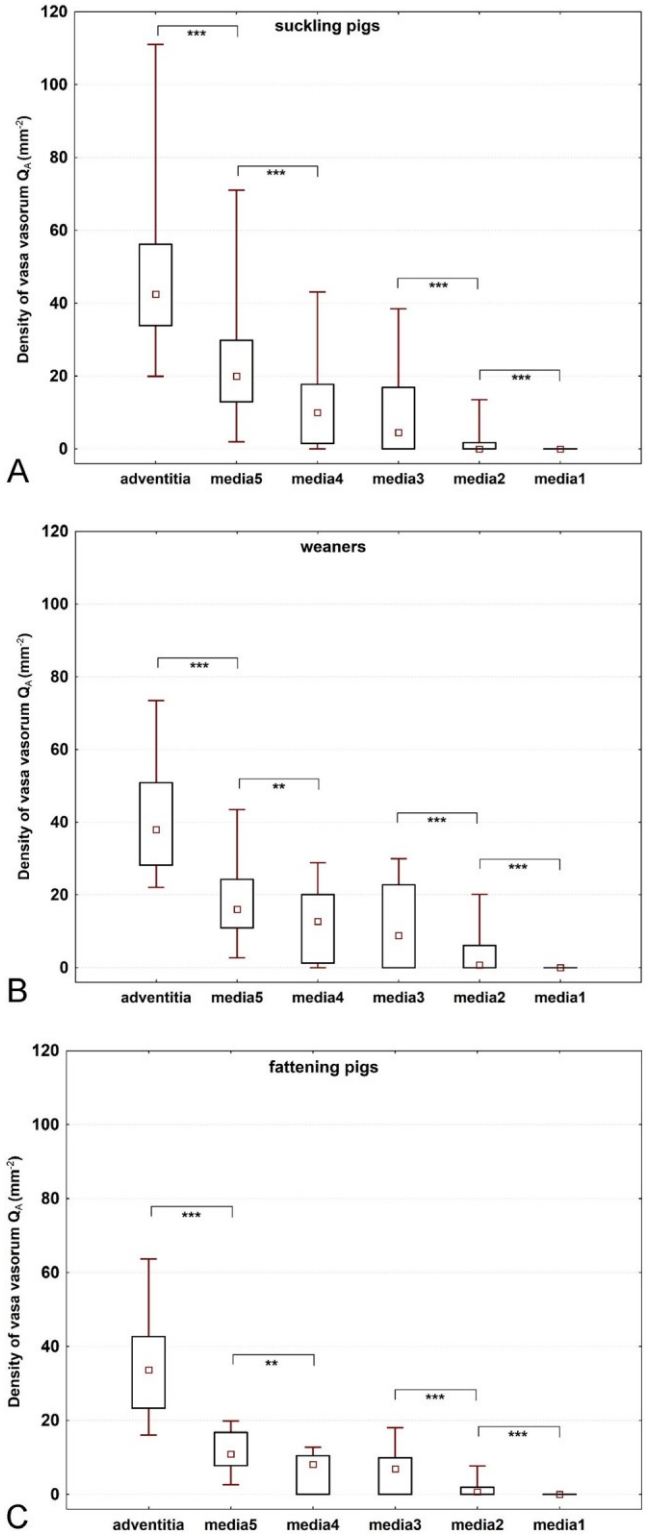

Fig. 6. Density of vasa vasorum profiles (Q_A) in the tunica adventitia and in the five tunica media sublayers in the three age groups of pigs: (A) suckling pigs, (B) weaners, and (C) fattening pigs. For this comparison, the aortic segments were pooled, and the data from the corresponding images, sections and animals were exactly matched. The differences between the layers were first tested using the Friedman ANOVA test, which showed significant differences in all age groups ($p<0.001$). Further comparisons between anatomically adjacent layers were performed using the Wilcoxon matched-pairs test (significant results are presented within the diagrams: $^{*}p<0.05$, $^{**}p<0.01$, $^{***}p<0.001$). In all age groups, the adventitia had the greatest density of vasa vasorum profiles, followed by the most abluminal sublayer of the media (media5). No differences were found between the media3 and the media4 sublayers in any group, i.e., the density of profiles was the same within the middle region of the media (40–80% of the media thickness measured from the intima). The data are displayed as the median values, with boxes spanning the upper limits of the first and third quartiles and with whiskers spanning the minimum and maximum values for each group.

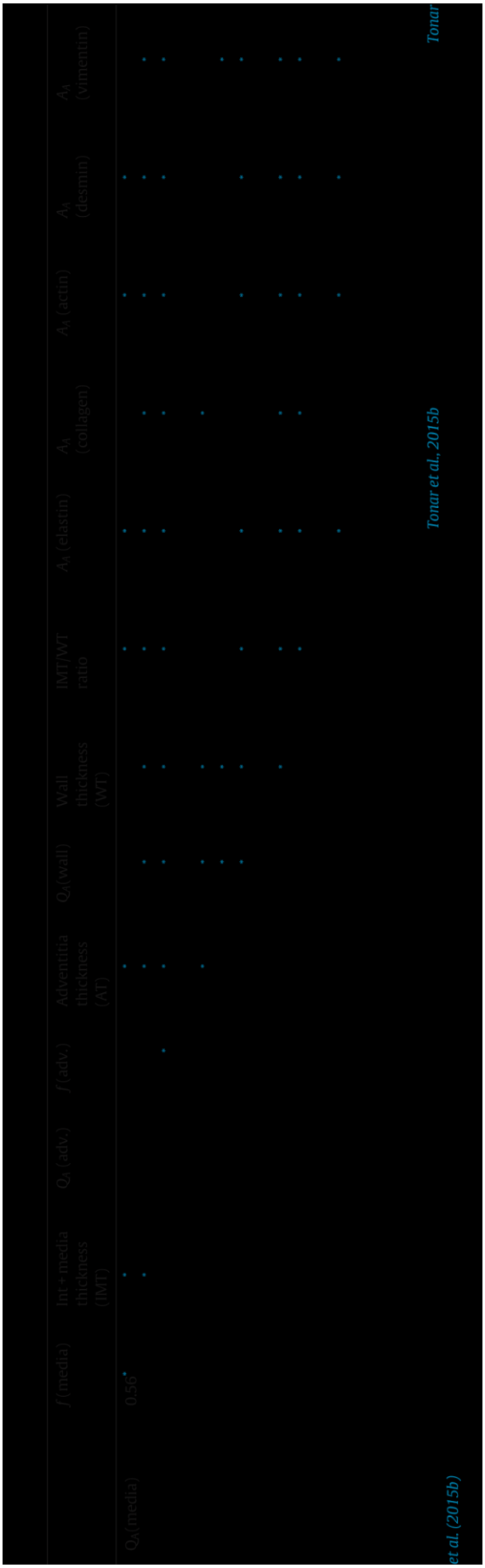

4.2. The density of vasa vasorum gradually decreased with age in both the media and the adventitia

Vasa vasorum seemed to grow and branch less than necessary to maintain the same density of the microvascular bed within the aortic wall during growth and ageing (Fig. 4A and C). Interestingly, the relative position of vasa vasorum remained constant during ageing in most of the media (Fig. 4B), except the most abluminal fifth (Fig. 3B), but it was shifted outwards in the adventitia (Fig. 4D). This finding suggests that the depth into which vasa vasorum penetrate and where they branch remain proportional during the growth of the media. This phenomenon corresponds well with the relative proportions between the media and the adventitia, which remained constant during ageing as well (Fig. 4F). The aortic segments tend to retain their relative proportions of media thickness during growth, and the media of older animals receives less but equally distributed vasa vasorum. Although the absolute values of the media thickness increase significantly with age (Fig. 3F in Tonar et al., 2015b), the density of vasa vasorum does not differ between sucklings and weaners. This result can be regarded as indirect proof of vasa vasorum proliferation up to the weaners' age (29–75 days).

4.3. The adventitia contained more microvessels than the outer media did in all segments and age groups

Interpreting the greater density of vasa vasorum profiles in the adventitia when compared with the media (Figs. 5 and 6) is not entirely straightforward due to different histological compositions and presumably also to the differing metabolism of these layers. The adventitia of older animals had more vasa vasorum close to the adluminal border of the adventitia (Fig. 7). We believe that from these "near-media" adventitial vessels, branches enter the media, as suggested in a vasa vasorum analysis of the monkey aorta (Werber et al., 1987) and canine aorta (Stefanadis et al., 1995).

The completely avascular adluminal regions of the media in various proximodistal segments and age groups were mostly thinner than the approximate 0.5 mm value reported by Wolinsky and Glagov (1967, 1969) and Okuyama et al. (1988). This finding can be explained by the fact that appropriate immunohistochemical staining methods were not yet available in previous studies. Interestingly, the middle regions of the media comprising the 40–60% depth of the media thickness (measured from the intima) still contained non-negligible amounts of vasa vasorum profiles.

4.4. A thicker tunica media with higher elastin content correlated with greater density and deeper adluminal penetration of vasa vasorum

The number of significant correlations that we found (Table 2) demonstrates general mutual relations between the aortic wall microcirculation, the thickness, and aortic layer proportions. These relations are preserved beyond any biological inter individual variability or variability between the proximodistal segments and between age groups within the range of 0–230 days.

A greater density of the microvascular network in the media was significantly linked to deeper adluminal penetration. The vasa vasorum density within the media increased in aortic samples with relatively thicker media and thinner adventitia. This phenomenon was probably caused by extensive branching of the vasa vasorum within the media in proximal segments (see Section 4.3), where the adventitia was particularly thin and the media was comparatively thick. When the branching of the vasa vasorum was shifted into deeper layers, i.e., into the media and more close to the lumen, it appeared as an increased number of microvessel profiles with a greater probability of being sectioned and counted, and therefore, a greater microvessel density was observed.

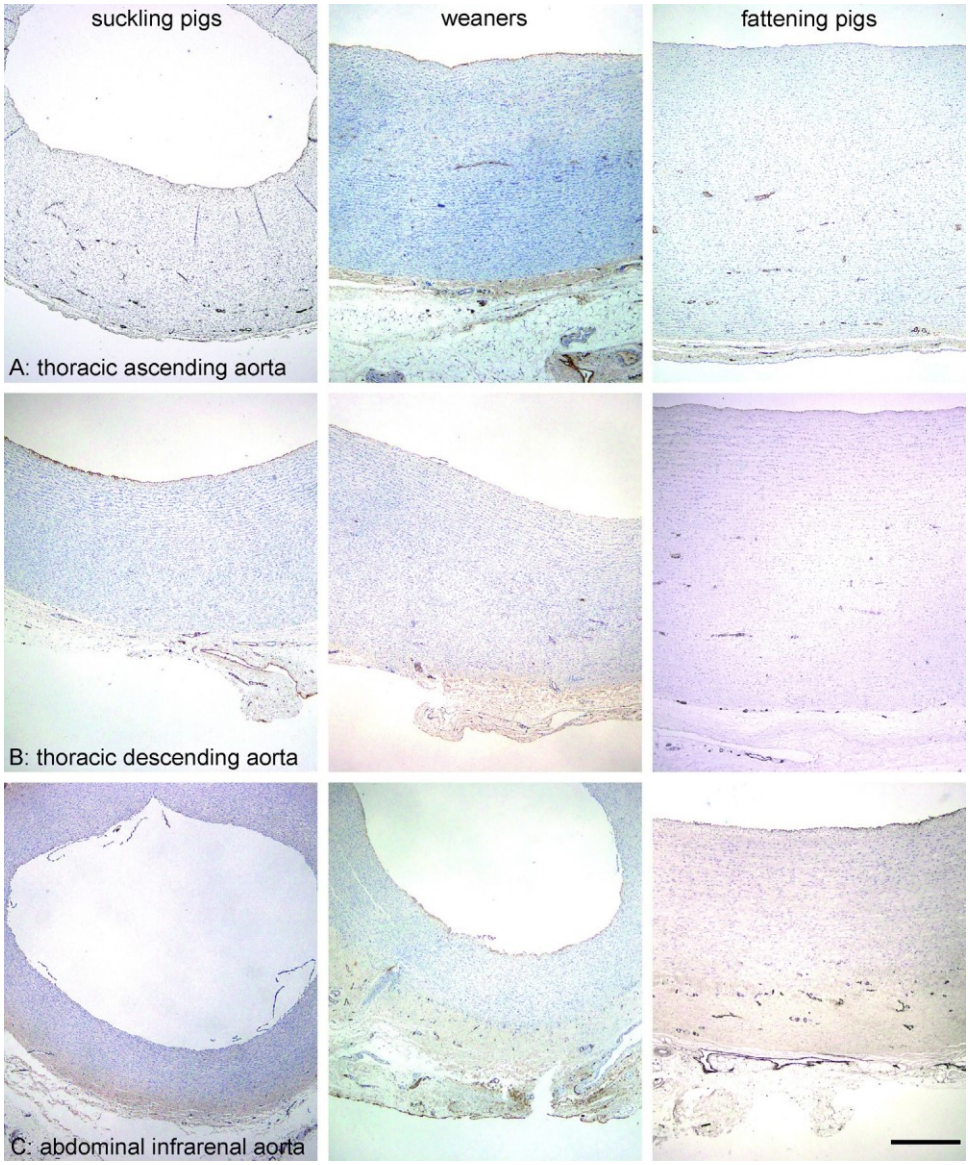

Fig. 7. Vasa vasorum within the thoracic ascending aorta (A), thoracic descending aorta (B), and infrarenal abdominal aorta (C) of sucklingpiglets (left), weaners (middle), and fatteningpigs (right). The vasa vasorum density was highest in sucklingpigs in both the media and the adventitia, and it gradually decreased with age. The relative position of the vasa vasorum within the media did not change with age, but older animals had more adventitial vasa vasorum close to the adluminal border of the adventitia. The relative media and adventitia thicknesses were retained during ageing in the corresponding aortic segments, although the overall thickness of the aortic wall increased. The density of the vasa vasorum in the media, but not in the adventitia, decreased in the proximodistal direction. In the thoracic aortic segments (A–B), the vasa vasorum penetrated deeper into the tunica media than in the abdominal aorta (C). In the thoracic aorta (A–B), the adventitia was thinner than in the abdominal aorta (C). Immunohistochemical detection of endothelial von Willebrand factor, visualization with horseradish peroxidase/diaminobenzidine (brown), counterstaining with haematoxylin. Scale bar: 500 m (For interpretation of the references to color in this figure legend, the reader is referred to the web version of this article).

Segments with a greater elastin fraction within the media also had a greater density of vasa vasorum in the media. This result might be partially explained by the fact that an elastin network with transversally oriented elastic lamellae facilitates diffusion along the lamellae but restrains the diffusion of large molecules (such as albumin) across the media due to binding to these molecules (Hwang and Edelman, 2002; Goriely et al., 2007). Thus, segments with a rich elastin network can be expected to require an especially rich vascular network in the media, even though these segments have a smaller fraction of vascular smooth muscle cells at the same time. Conversely, the segments that contained relatively more vascular smooth muscle cells than elastin (mainly the abdominal segments, cf. Tona et al., 2015b) had relatively lower vasa vasorum densities in the media and the microvessels did not penetrate too deeply (Table 2). Okuyama et al. (1988) suggested that the relatively greater vasa vasorum density in sucklingpiglets may be explained as the persistence of a prenatal rich vascular bed, which was interpreted as an adaptation to intrauterine hypoxia. However, this hypothesis was never confirmed.

4.5. Study implications

The adventitia thickness observed in the various segments under study was extremely variable, depending on both the proximodistal positions of the segments and anatomical directions; i.e., the adventitial structure and thickness lacked rotational symmetry. Moreover, it seems that two different layers of connective tissue outside the tunica media could be found: (i) a more adluminal layer of dense connective tissue that was unambiguously apart of the vessel wall and (ii) a more abluminal layer of loose connective tissue often containing large numbers of fat cells. The latter was not considered as a part of the adventitia for the purposes of our study because it often contained preparation and dissection artefacts (namely microcracks), variable amounts of lymphatic tissue, and therefore, the vasa vasorum density would have been biased. However, this layer deserves a comparative anatomical study involving more animal species to clarify the general definition of the aortic adventitia.

Detailed mapping of vasa vasorum, including the segmental and age-related biological variability of the porcine aorta, is useful for understanding the drug distribution from arterial stents with fine control of locally directed drug release

(Hwang and Edelman, 2002; Kusanagi et al., 2007), aortic implantation of mesenchymal stem cells in porcine models of aneurysm (Turnbull et al., 2011), or in hypercholesteroleamic pigs used as models in atherosclerosis research (Porras et al., 2015; Xu et al., 2015). Additionally, other experiments using a growing porcine model might benefit from the method and the data provided by the present study when evaluating aortic reconstruction and aortic arch replacement (Ioannou et al., 2003; Chen et al., 2012) or postoperative aortic compliance (Ioannou et al., 2013). For this purpose, the growth of the aortic wall may be described using the growth curves according to Gielecki et al. (2006) or Szpinda (2007). Analysis of vasa vasorum penetration would be useful also in tissue-engineered neovessels using polymeric scaffold matrices for developing biocompatible vascular grafts (Udelsman et al., 2014; Miller et al., 2015). In our opinion, future studies on vasa vasorum would highly benefit from using stereological morphometric parameters related to the vasculature, as recently summarized by Mühlfeld (2014).

The data provided in Appendix A can be directly used in modelling the spatial distribution of vasa vasorum using the stochastic geometry of point processes. This statistical technique already has many applications in quantitative description of geometrical structures in biology, medicine, and other research areas (for review, see Stoyan et al., 1995). For this purpose, the cross-sectional profiles of the originally three-dimensional microvessels appear as points, as usual in histological sections. Public-domain software is available (Baddeley and Turner, 2005; Baddeley et al., 2015) for modelling and analysing point patterns in two-, three-, or multidimensional space-time, which would be helpful when modelling the growth of vasa vasorum during ageing.

4.6. Study limitations and remarks on methods

Vasa vasorum represent a three-dimensional branching network, but the present study was based on their two-dimensional projections into a standardized transverse sectional plane. Analysis of prevailing directions (anisotropy) would require a threedimensional approach (see Kochová et al. (2011) for current methods on the anisotropy of microvessels in histology), or at least a comparison of vasa vasorum profiles in multiple sectional planes (Tonar et al., 2012). By comparing longitudinal vs. transversal aortic sections, branching patterns of aortic vasa vasorum could be revealed in further studies, because more longitudinal firstorder vasa have more probability to be sectioned by the transversal plane, whereas more circumferential second-order branches would appear more frequently on longitudinal sections. Another advance in quantifying vasa vasorum density would be using the orientator technique (Mattfeldt et al., 1990) to produce isotropic uniform random (IUR) sections, in which an unbiased length density L_V can be calculated from the two-dimensional density of vasa vasorum profiles Q_A using the simple formula $L_V = 2Q_A$. However, we did not select this IUR design, because analysis of media sublayers (hypotheses $H_0(A)$ and $H_0(C)$) relied on transversal sections; therefore, three-dimensional density of microvessels may not be calculated from our present results (Mühlfeld and Ochs, 2014).

Our vasa vasorum quantification did not differentiate the calibre of the vessels or whether they belonged to the arterial or venous part of the aortic microvascular bed. However, a reliable estimation of microvessel luminа in histological sections is difficult because the volume of, e.g., vasa vasorum is often collapsed in routinely processed histological samples. Volume collapse may be avoided by using perfusion fixation, which was not available during the collection of our samples. However, non-standard perfusion might introduce other artefacts into the preparations, such as overdistension or irregular distension of the vessels due to different wall properties.

Other study limitations are the same as in the previous paper on the same aortic segments (Tonar et al., 2015b), namely (i) the wall thickness measurements were affected by dissection of the aortae and by the post mortem contraction of the vascular segments, and no correction for the tissue shrinkage was performed; (ii) the study did not differentiate samples from the dorsal, lateral, and ventral sides of the abdominal aorta; (iii) the estimates were always based on one section per staining and anatomical position; and (iv) due to the number of animals, we did not perform simultaneous statistical analyses with grouping of the samples according to the aortic segments and age. Moreover, this morphological study does not offer information on the real perfusion rates of the aortic segments, as it is known that vasa vasorum are highly reactive and that their tone is physiologically regulated by a number of endogenous factors (Scotland et al., 2000).

4.7. Comparing porcine vs. human aortic vasa vasorum

Despite a thorough literature search, the information on human aortic vasa vasorum and their development are extremely rare. In our opinion, the results of the present study may not be extrapolated to the human aorta. Histological studies on age-dependent changes of human aortic vasa vasorum are lacking. Arteriolar and venous vasa vasorum of the ascending aorta, aortic arch, and descending aorta were examined in human between birth and 15 years of age using X-ray microscopy (Clarke, 1965), but the resolution limit of this radiological study was approximately 40 m in diameter and most of the precapillary, capillary, and postcapillary vasa vasorum were missing in the study. Similarly to our study, Clarke (1965) proved that in human, the ascending aorta and aortic arch had a greater vasa vasorum density in neonates than at the end of the first year. Interestingly, the reverse was true for the descending thoracic and abdominal aorta. In human, Clarke (1965) reported a greater density of vasa vasorum arterioles and venules in the human abdominal than in the thoracic aorta, but the study did not detect the capillaries, which represent the most numerous population of the vasa vasorum in our immunohistochemical study. Moreover, statistical connections to the local wall thickness and histological composition of aortic wall (collagen, elastin, and smooth muscle fractions) in human ontogenesis are lacking. Increased knowledge on human aortic vasa vasorum would also be beneficial to transplantation medicine, because the external vascular supply of aortic branches originates from aortic vasa vasorum. This is important, e.g., for anastomosis of renal arteries during kidney transplantations (Kurzidim et al., 1999).

Studies mapping any age-related differences between these two species are missing. Despite many similarities between the porcine and human histology, such as diameter, thickness, and numbers of lamellar units (Wolinsky and Glagov, 1967), the results of the present study should be used in porcine models only and may not be easily extrapolated to the human aorta for several reasons. Major arteries (and also veins) contributed to the reorganization of the orthodynamics as a part of adaptations to the human upright gait (bipedism). Development of bipedal posture caused changes in pressure gradients, which required further changes in aortic compliance when compared to quadrupeds. While the blood flow within the proximal part of the human aortic arch is under contraposition of gravity, the blood flow in the descending aorta goes along with the gravitational force vector. These differences may be measured when comparing the human vs. quadrupeds pulse wave velocity between carotid and femoral arteries (Neto, 2006). Moreover, hemodynamic responses to the orthostatic stress in human are modulated by the systolic volume ejection fraction, baroreflex sensitivity, activation of the renin–angiotensin–aldosterone system, renal sodium and water retention, systolic volume, and other cardiovascular adaptations, in which differences are found between quadrupeds and human (Neto, 2006). In addition, differences in aortic gross anatomy and histology are to be taken into account, such as variations in branching aortic patterns (especially in the aortic arch), and various amounts of periaortic connective tissue and anatomical relations between descending aorta to the vertebral bodies.

5. Conclusion

We estimated the density of von Willebrand factor-positive profiles of vasa vasorum per profile area of the aortic wall using transversal histological sections in five proximodistal segments sampled from the porcine aortae of growing pigs of age ranging from 0 to 230 days. The tunica media of the thoracic aorta had a greater vasa vasorum density, with microvessels penetrating deeper towards the lumen than in the abdominal aorta. The density of vasa vasorum gradually decreased with age in both the media and the adventitia. The depth into which vasa vasorum penetrated and where they branched remained proportional during the ageing and growth of the media. The aortic segments retained their relative proportions

between the media thickness and the adventitia thickness during growth, and the media of older animals received less but equally distributed vasa vasorum. A greater density of vasa vasorum in the media was significantly linked to greater media thickness and a greater elastin fraction (data on elastin taken from another study on the same samples). The immunohistochemical quantification revealed deeper penetration of vasa vasorum into the tunica media, reaching adluminal layers of the vessel wall that were hitherto reported to be avascular. The complete primary morphometric data in the form of continuous variables have been made available as a supplement to this paper. Mapping of the vasa vasorum profiles density and position has promising illustrative potential for studies on the aorta in experimental porcine models, such as models of atherosclerotic and inflammatory neovascularization, aortic aneurysms and drug distribution from arterial stents.

Acknowledgements

This study was supported by the National Sustainability Program I (NPU I) Nr. LO1503 provided by the Ministry of Education, Youth and Sports of the Czech Republic and by the Prvouk P36 Project of the Charles University in Prague. This study was also partially supported by Ministry of Health of the Czech Republic, Project Nr. AZV 15-32727A. Skilful technical support from Ms. Magdalena Helmreich, Ms. Anne Flemming, Ms. Claudia Höchsmann and Ms. Brigitte Machacis gratefully acknowledged.

Appendix A. Supplementary data

Supplementary data associated with this article can be found, in the online version, at http://dx.doi.org/10.1016/j.aanat.2016.01. 008.

References

Aguirre-Sanceledonio, M., Fossum, T.W., Miller, M.W., Humphrey, J.D., Berridge, B.R., Herráez, P., 2003. Collateral circulation in experimental coarctation of the aorta in minipigs: a possible association with hypertrophied vasa vasorum. J. Comp. Pathol. 128, 165–171.

Angouras, D., Sokolis, D.P., Dosios, T., Kostomitsopoulos, N., Boudoulas, H., Skalkeas, G., Karayannacos, P.E., 2000. Effect of impaired vasa vasorum flow on the structure and mechanics of the thoracic aorta: implications for the pathogenesis of aortic dissection. Eur. J. Cardiothorac. Surg. 17, 468–473.

Baddeley, A., Turner, R., 2005. Spatstat: an R package for analyzing spatial point patterns. J. Stat. Softw. 12, 1–42.

Baddeley, A., Rubak, E., Turner, R., 2015. Spatial Point Patterns: Methodology and Applications with R. Chapman and Hall/CRC Press, London.

Baikoussis, N.G., Apostolakis, E.E., Papakonstantinou, N.A., Siminelakis, S.N., Arnaoutoglou, H., Papadopoulos, G., Goudevenos, J., Dougenis, D., 2011. The implication of vasa vasorum in surgical diseases of the aorta. Eur. J. Cardiothorac. Surg. 40, 412–417.

Chen, C.C., Tseng, Y.C., Lin, C.C., Li, C.F., Yeh, M.L., 2012. A modular branched stent graft system for suturelessanastomoses in extensive aortic arch replacement—a porcine study. Ann. Vasc. Surg. 26, 527–536.

Clarke, J.A., 1965. An x-ray microscopic study of the postnatal development of the vasa vasorum in the human aorta. J. Anat. 99, 877–889.

Cyron, C.J., Humphrey, J.D., 2014a. Vascular homeostasis and the concept of mechanobiological stability. Int. J. Eng. Sci. 85, 203–223.

Cyron, C.J., Wilson, J.S., Humphrey, J.D., 2014b. Mechanobiological stability: a new paradigm to understand the enlargement of aneurysms? J. R. Soc. Interface 11, 20140680.

Desai, M., Ahmed, M., Darbyshire, A., You, Z., Hamilton, G., Seifalian, A.M., 2011. An aortic model for the physiological assessment of endovascular stent-grafts. Ann. Vasc. Surg. 25, 530–537.

Dziodzio, T., Juraszek, A., Reineke, D., Jenni, H., Zermatten, E., Zimpfer, D., Stoiber, M., Scheikl, V., Schima, H., Grimm, M., Czerny, M., 2011. Experimental acute type B aortic dissection: different sites of primary entry tears cause different ways of propagation. Ann. Thorac. Surg. 91, 724–727.

Eberlova, L., Tonar, Z., Witter, K., Krizkova, V., Nedorost, L., Korabecna, M., Tolinger, P., Kocova, J., Boudova, L., Treska, V., Houdek, K., Molacek, J., Vrzalova, J., Pesta, M., Topolcan, O., Valenta, J., 2013. Asymptomatic abdominal aortic aneurysms show histological signs of progression: a quantitative histochemical analysis. Pathobiology 80, 11–23.

Fleiner, M., Kummer, M., Mirlacher, M., Sauter, G., Cathomas, G., Krapf, R., Biedermann, B.C., 2004. Arterial neovascularization and inflammation in vulnerable patients: early and late signs of symptomatic atherosclerosis. Circulation 110, 2843–2850.

Funder, J.A., Frost, M.W., Klaaborg, K.E., Wierup, P., Hjortdal, V., Nygaard, H., Hasenkam, J.M., 2012. Aortic root distensibility after subcoronary stentless valve implantation. J. Heart Valve Dis. 21, 181–188.

Gabner, S., Tonar, Z., Tichy, A., Saalmüller, A., Worliczek, H.L., Joachim, A., Witter, K., 2012. Immunohistochemical detection and quantification of T cells in the small intestine of Isospora suis-infected piglets—influence of fixation technique and intestinal segment. Microsc. Res. Tech. 75, 408–415.

Galili, O., Herrmann, J., Woodrum, J., Sattler, K.J., Lerman, L.O., Lerman, A., 2004. Adventitial vasa vasorum heterogeneity among different vascular beds. J. Vasc. Surg. 40, 529–535.

Gielecki, J.S., Syc, B., Wilk, R., Musiał-Kopiejka, M., Piwowarczyk-Nowak, A., 2006. Quantitative evaluation of aortic arch development using digital-image analysis. Ann. Anat. 188, 19–23.

Goriely, A.R., Baldwin, A.L., Secomb, T.W., 2007. Transient diffusion of albumin in aortic walls, effects of binding to medial elastin layers. Am. J. Physiol. Heart Circ. Physiol. 292, H2195–H2201.

Granada, J.F., Feinstein, S.B., 2008. Imaging of the vasa vasorum. Nat. Clin. Pract. Cardiovasc. Med. Suppl 2, S18–S25.

Gundersen, H.J., 1977. Notes on the estimation of the numerical density of arbitrary profiles: the edge effect. J. Microsc. 111, 219–223.

Heistad, D.D., Marcus, M.L., 1979. Role of vaso vasorum in nourishment of the aorta. Blood Vessel. 16 (5), 225–238.

Houdek, K., Molácek, ˇ J., Treˇ ska, ˇ V., Kríˇ zková, ˇ V., Eberlová, L., Boudová, L., Nedorost, L., Tolinger, P., Kocová, ˇ J., Kobr, J., Baxa, J., Liska, ˇ V., Witter, K., Tonar, Z., 2013. Focal histopathological progression of porcine experimental abdominal aortic aneurysm is mitigated by atorvastatin. Int. Angiol. 32, 291–306.

Humphrey, J.D., Holzapfel, G.A., 2012. Mechanics, mechanobiology, and modeling of human abdominal aorta and aneurysms. J. Biomech. 45, 805–814.

Hwang, C.W., Edelman, E.R., 2002. Arterial ultrastructure influences transport of locally delivered drugs. Circ. Res. 90, 826–832.

Ioannou, C.V., Stergiopulos, N., Katsamouris, A.N., Startchik, I., Kalangos, A., Licker, M.J., Westerhof, N., Morel, D.R., 2003. Hemodynamics induced after acute reduction of proximal thoracic aorta compliance. Eur. J. Vasc. Endovasc. Surg. 26, 195–204.

Ioannou, C.V., Stergiopulos, N., Georgakarakos, E., Chatzimichali, E., Katsamouris, A.N., Morel, D.R., 2013. Effects of isoflurane anesthesia on aortic compliance and systemic hemodynamics in compliant and noncompliant aortas. J. Cardiothorac. Vasc. Anesth. 27, 1282–1288.

Johnson, J.J., Jacocks, M.A., Gauthier, S.C., Irwin, D.A., Wolf, R.F., Garwe, T., Lerner, M.R., Lees, J.S., 2013. Establishing a swine model to compare vascular prostheses in a contaminated field. J. Surg. Res. 181, 355–358.

Kim, J., Baek, S., 2011. Circumferential variations of mechanical behavior of the porcine thoracic aorta during the inflation test. J. Biomech. 44, 1941–1947.

Kochová, P., Cimrman, R., Janácek, ˇ J., Witter, K., Tonar, Z., 2011. How to asses, visualize and compare the anisotropy of linear structures reconstructed from optical sections—a study based on histopathological quantification of human brain microvessels. J. Theor. Biol. 286, 67–78.

Kocova, J., 1970. Overall staining of connective tissue and the muscular layer of vessels. Folia Morphol. 18, 293–295.

Kurzidim, M.H., Oeschger, M., Sasse, D., 1999. Studies on the vasa vasorum of the human renal artery. Ann. Anat. 181, 223–227.

Kusanagi, M., Matsui, O., Sanada, J., Ogi, T., Takamatsu, S., Zhong, H., Kimura, Y., Tabata, Y., 2007. Hydrogel-mediated release of basic fibroblast growth factor from a stent-graft accelerates biological fixation with the aortic wall in a porcine model. J. Endovasc. Ther. 14, 785–793.

Lillie, M.A., Armstrong, T.E., Gérard, S.G., Shadwick, R.E., Gosline, J.M., 2012. Contribution of elastin and collagen to the inflation response of the pig thoracic aorta: assessing elastin's role in mechanical homeostasis. J. Biomech. 45, 2133–2141.

Mattfeldt, T., Mall, G., Gharehbaghi, H., Moller, P., 1990. Estimation of surface area and length with the orientator. J. Microsc. 159, 301–317.

Miller, K.S., Khosravi, R., Breuer, C.K., Humphrey, J.D., 2015. A hypothesis-driven parametric study of effects of polymeric scaffold properties on tissue engineered neovessel formation. Acta Biomater. 11, 283–294.

Moreno, P.R., Purushothaman, K.R., Zias, E., Sanz, J., Fuster, V., 2006. Neovascularization in human atherosclerosis. Curr. Mol. Med. 6, 457–477.

Moulton, K.S., Vakili, K., Zurakowski, D., Soliman, M., Butterfield, C., Sylvin, E., Lo, K.M., Gillies, S., Javaherian, K., Folkman, J., 2003. Inhibition of plaque neovascularization reduces macrophage accumulation and progression of advanced atherosclerosis. Proc. Natl. Acad. Sci. USA 100, 4736–4741.

Mühlfeld, C., 2014. Quantitative morphology of the vascularisation of organs: a stereological approach illustrated using the cardiac circulation. Ann. Anat. 196, 12–19.

Mühlfeld, C., Ochs, M., 2014. Measuring structure—what's the point in counting? Ann. Anat. 196, 1–2.

Nedorost, L., Uemura, H., Furck, A., Saeed, I., Slavik, Z., Kobr, J., Tonar, Z., 2013. Vascular histopathologic reaction to pulmonary artery banding in an in vivo growing porcine model. Pediatr. Cardiol. 34, 1652–1660.

Neto, E., 2006. Great arteries contribution in orthostasis cardiovascular adaptation. Arq. Bras. Cardiol. 87, 209–222.

Newby, A.C., Zaltsman, A.B., 2000. Molecular mechanisms in intimal hyperplasia. J. Pathol. 190, 300–309.

Nickel, R., Schummer, A., Seiferle, E., 1996. Lehrbuch der Anatomie der Haustiere. Band III Kreislaufsystem, Haut und Hautorgane, third ed. Parey Buchverlag, Berlin.

Okuyama, K., Yaginuma, G., Takahashi, T., Sasaki, H., Mori, S., 1988. The development of vasa vasorum of the human aorta in various conditions. A morphometric study. Arch. Pathol. Lab. Med. 112, 721–725.

Ondrovics, M., Silbermayr, K., Mitreva, M., Young, N.D., Razzazi-Fazeli, E., Gasser, R.B., Joachim, A., 2013. Proteomic analysis of Oesophagostomum dentatum (Nematoda) during larval transition, and the effects of hydrolase inhibitors on development. PLoS ONE 8, e63955.

Ordónez, ˜ N.G., 2012. Immunohistochemical endothelial markers: a review. Adv. Anat. Pathol. 19, 281–295.

Porras, A.M., Shanmuganayagam, D., Meudt, J.J., Krueger, C.G., Hacker, T.A., Rahko, P.S., Reed, J.D., Masters, K.S., 2015. Development of aortic valve disease in familial hypercholesterolemic swine: implications for elucidating disease etiology. J. Am. Heart Assoc. 4, e002254.

Ritman, E.L., Lerman, A., 2007. The dynamic vasa vasorum. Cardiovasc. Res. 75, 649–658.

Romeis, B., 1989. Mikroskopische Technik. Urban & Schwarzenberg, München.

Saari, P., Lähteenvuo, M., Honkonen, K., Manninen, H., 2012. Antegrade in situ fenestration of aortic stent graft: in-vivo experiments using a pig model. Acta Radiol. 53, 754–758.

Sarda-Mantel, L., Alsac, J.M., Boisgard, R., Hervatin, F., Montravers, F., Tavitian, B., Michel, J.B., LeGuludec, D., 2012. Comparison of 18F-fluoro-deoxy-glucose, 18F-fluoro-methyl-choline, and 18F-DPA714 for positron-emission tomography imaging of leukocyte accumulation in the aortic wall of experimental abdominal aneurysms. J. Vasc. Surg. 56, 765–773.

Scotland, R.S., Vallance, P.J., Ahluwalia, A., 2000. Endogenous factors involved in regulation of tone of arterial vasa vasorum: implications for conduit vessel physiology. Cardiovasc. Res. 46, 403–411.

Shadwick, R.E., 1999. Mechanical design in arteries. J. Exp. Biol. 202, 3305–3313.

Sokolis, D.P., 2007. Passive mechanical properties and structure of the aorta: segmental analysis. Acta Physiol. (Oxf.) 190, 277–289.

Sokolis, D.P., Boudoulas, H., Karayannacos, P.E., 2008. Segmental differences of aortic function and composition: clinical implications. Hellenic J. Cardiol. 49, 145–154.

Sokolis, D.P., Iliopoulos, D.C., 2014. Impaired mechanics and matrix metalloproteinases/inhibitors expression in female ascending thoracic aortic aneurysms. J. Mech. Behav. Biomed. Mater. 34, 154–164.

Szpinda, M., 2007. Morphometric study of the ascending aorta in human fetuses. Ann. Anat. 189, 465–472.

Stefanadis, C., Vlachopoulos, C., Karayannacos, P., Boudoulas, H., Stratos, C., Filippides, T., Agapitos, M., Toutouzas, P., 1995. Effect of vasa vasorum flow on structure and function of the aorta in experimental animals. Circulation 91, 2669–2678.

Stoyan, D., Kendall, W.S., Mecke, J., 1995. Stochastic Geometry and its Applications, second ed. John Wiley & Sons, Chichester.

Tonar, Z., Kural Jr., T., Kochova, P., Nedorost, L., Witter, K., 2012. Vasa vasorum quantification in human varicose great and small saphenous veins. Ann. Anat. 194, 473–481.

Tonar, Z., Kochova, P., Cimrman, R., Perktold, J., Witter, K., 2015a. Segmental differences in the orientation of smooth muscle cells in the tunica media of porcine aortae. Biomech. Model. Mechanobiol. 14, 315–332.

Tonar, Z., Kubíková, T., Prior, C., Demjén, E., Liska,ˇ V., Králícková,ˇ M., Witter, K., 2015b. Segmental and age differences in the elastin network, collagen, and smooth muscle phenotype in the tunica media of the porcine aorta. Ann. Anat. 201, 79–90.

Turnbull, I.C., Hadri, L., Rapti, K., Sadek, M., Liang, L., Shin, H.J., Costa, K.D., Marin, M.L., Hajjar, R.J., Faries, P.L., 2011. Aortic implantation of mesenchymal stem cells after aneurysm injury in a porcine model. J. Surg. Res. 170, e179–e188.

Udelsman, B.V., Khosravi, R., Miller, K.S., Dean, E.W., Bersi, M.R., Rocco, K., Yi, T., Humphrey, J.D., Breuer, C.K., 2014. Characterization of evolving biomechanical properties of tissue engineered vascular grafts in the arterial circulation. J. Biomech. 47, 2070–2079.

Werber, A.H., Armstrong, M.L., Heistad, D.D., 1987. Diffusional support of the thoracic aorta in atherosclerotic monkeys. Atherosclerosis 68, 123–130.

Witter, K., Tonar, Z., Matejka, V.M., Martinca, T., Jonak, M., Rokosny, S., Pirk, J., 2010. Tissue reaction to three different types of tissue glues in an experimental aorta dissection model: a quantitative approach. Histochem. Cell Biol. 133, 241–259.

Wolinsky, H., Glagov, S., 1967. Nature of species differences in the medial distribution of aortic vasa vasorum in mammals. Circ. Res. 20, 409–421.

Wolinsky, H., Glagov, S., 1969. Comparison of abdominal and thoracic aortic medial structure in mammals. Deviation of man from the usual pattern. Circ. Res. 25, 677–686.

Worliczek, H.L., Buggelsheim, M., Alexandrowicz, R., Witter, K., Schmidt, P., Gerner, W., Saalmüller, A., Joachim, A., 2010. Changes in lymphocyte populations in suckling piglets during primary infections with Isosporasuis. Parasite Immunol. 32, 232–244.

Xu, X., Mao, W., Chai, Y., Dai, J., Chen, Q., Wang, L., Zhuang, Q., Pan, Y., Chen, M., Ni, G., Huang, Z., 2015. Angiogenesis inhibitor, endostar, prevents vasa vasorum neovascularization in a swine atherosclerosis model. J. Atheroscler. Thromb. 22, 1100–1112.

Journal of Chemical Neuroanatomy 88 (2018) 22–32

Contents lists available at ScienceDirect

Journal of Chemical Neuroanatomy

journal homepage: www.elsevier.com/locate/jchemneu

Numerical and length densities of microvessels in the human brain: Correlation with preferential orientation of microvessels in the cerebral cortex, subcortical grey matter and white matter, pons and cerebellum

Tereza Kubíková[a], Petra Kochová[a], Petr Tomášek[a,b,c], Kirsti Witter[d], Zbyněk Tonar[a,*]

[a] NTIS, European Centre of Excellence, Faculty of Applied Sciences, University of West Bohemia, Univerzitni 8, 306 14 Pilsen, Czech Republic [b] Department of Histology and Embryology, Faculty of Medicine in Pilsen, Charles University, Karlovarska 48, 301 66 Pilsen, Czech Republic [c] Department of Forensic Medicine, Second Faculty of Medicine, Charles University, Budinova 2, 180 81 Prague 8, Prague, Czech Republic

[d] Institute of Anatomy, Histology and Embryology, Department of Pathobiology, University of Veterinary Medicine Vienna, Veterinärplatz 1, A-1210 Vienna, Austria

ARTICLEINFO

Keywords:
Blood vessels
Capillaries
Disector
Histology
Laminin
Microvessel density
Stereology

ABSTRACT

To provide basic data on the local differences in density of microvessels between various parts of the human brain, including representative grey and white matter structures of the cerebral hemispheres, the brain stem and the cerebellum, we quantified the numerical density N_V and the length density L_V of microvessels in two human brains. We aimed to correlate the density of microvessels with previously published data on their preferential orientation (anisotropy).

Microvessels were identified using immunohistochemistry for laminin in 32 samples harvested from the following brain regions of two adult individuals: the cortex of the telencephalon supplied by the anterior, middle, and posterior cerebral artery; the basal ganglia (putamen and globus pallidus); the thalamus; the subcortical white matter of the telencephalon; the internal capsule; the pons; the cerebellar cortex; and the cerebellar white matter. N_V was calculated from the number of vascular branching points and their valence, which were assessed using the optical disector in 20-µm-thick sections. L_V was estimated using counting frames applied to routine sections with randomized cutting planes.

After correction for shrinkage, N_V in the cerebral cortex was 1311 ± 326 mm^{-3} (mean ± SD) and L_V was 255 ± 119 mm^{-2}. Similarly, in subcortical grey matter (which included the basal ganglia and thalamus), N_V was 1350 ± 445 mm^{-3} and L_V was 328 ± 117 mm^{-2}. The vascular networks of cortical and subcortical grey matter were comparable. Their densities were greater than in the white matter, with N_V = 222 ± 147 mm^{-3} and L_V = 160 ± 96 mm^{-2}. N_V was moderately correlated with L_V. In parts of brain with greater N_V, blood vessels lacked a preferential orientation.

Our data were in agreement with other studies on microvessel density focused on specific brain regions, but showed a greater variability, thus mapping the basic differences among various parts of brain. To facilitate the planning of other studies on brain vascularity and to support the development of computational models of human brain circulation based on real microvascular morphology; stereological data in form of continuous variables are made available as supplements.

1. Introduction

Human brain microcirculation is fundamental to brain development, aging, metabolism, and function. It is therefore intensively studied using perfusion imaging methods such as dynamic and contrastenhanced magnetic resonance imaging (Bladowska et al., 2013a; Peng et al., 2014), or enhanced computed tomography (Cuenod and Balvay, 2013). Although the brain perfusion may be indirectly assessed using these methods, the morphology of the microvascular network still remains beyond their resolution limits and histological evaluation is necessary for this purpose.

1.1. Organ-specific guidelines for quantitative microanatomy

To the best of our knowledge, a sampling scheme suitable for stereological evaluation of the grey and white matter of the human brain has not yet been described in the literature. However, Burke et al. (2009) published highly informative guidelines for unbiased stereology in the non-human primate brain, which could be combined with the practical recommendations on sampling of brain banks by Perl et al. (2000). Similarly, for a number of organs, well-documented and practical guidelines for dissection, sampling of tissue blocks, histological embedding, sectioning, and quantification have been published. General recommendations on planning, sampling, and avoiding risks were recently summarized by sources including Tschanz et al. (2014) and Mühlfeld and Ochs (2014). Organ-specific approaches are known, e.g., for the kidneys (Nyengaard, 1999), heart (Mühlfeld et al., 2010), stomach and intestine (Nyengaard and Alwasel, 2014), placenta (Mayhew, 2014), lungs (Nyengaard and Gundersen, 2006; Ochs, 2014, and liver (Marcos et al., 2012). For analysis of blood vessels, including microvessels, stereological techniques have reviewed by sources including Dockery and Fraher (2007) and, more recently, Mühlfeld (2014).

1.2. Current knowledge on the density of brain microvessels

Despite the number of design-based stereological techniques successfully established for quantitative description of microvessels in different organs, surprisingly few papers quantitatively compare various parts of the human brain in the same individuals. Most of the data published so far refer to animal models, such as mice (Lee et al., 2005; Steinman, 2013; Kolinko et al., 2015, 2016) and rats (McMillan et al., 1994; Cavaglia et al., 2001; Tsai et al., 2009; Shao et al., 2010; Kubínová et al., 2013). More closely related to the human brain is the detailed study on microvessel density in the visual cortex of the macaque (Weber et al., 2008). In the human brain, Lokkegaard et al. (2001) analyzed the number and length of capillaries in the hippocampus. Lauwers et al. (2008) analyzed the density and orientation of microvessels in the parahippocampal and fusiform gyri. Similarly, Burke et al. (2014) assessed the length density of blood vessels in the hippocampi of patients with vascular dementia. Müller-Starck et al. (2014) mapped the length density of microvessels in the infant cerebellum. Kreczmanski et al. (2005, 2009) analyzed the length density of microvessels in the frontal cortex and subcortical regions of schizophrenics. Richard et al. (2010) compared capillary length density between the temporal and occipital cortex. Data for most of the remaining parts of the brain are lacking. However, quantitative descriptions of the differences in microvessel density between various parts of the human brain would be very valuable. Such information could be beneficial for explaining the metabolism and blood flow of the brain (Karbowski, 2011); the pharmacokinetics of drugs and diagnostic contrast agents in various parts of the brain (Phan et al., 2014); the varying sensitivity or resistance of different parts of the brain to ischemia (including necrotic infarction, the penumbra, or brain recovery and reperfusion injury, Zechariah et al., 2013); aging (Schmitz and Hof, 2007), dementia (Burke et al., 2014) and neurodegenerative diseases (Bladowska et al., 2013b; Menke et al., 2014); the grading and therapy of brain tumors (Bonekamp et al., 2017); some cases of epilepsy (Gerstner et al., 2006); schizophrenia (Chiapponi et al., 2013); cognitive disorders; and other phenomena in many branches of medicine.

There might be several reasons for the lack of data on human brain microcirculation. The human brain is an organ of extreme anatomical complexity, with several ontogenetic levels of folding. It is a large organ that cannot be sampled as a whole but instead has a number of potential regions of interest, defined either from the point of view of blood supply or from the point of view of neuroanatomy. The results of any histological analysis depend on appropriate sampling. A suitable sampling strategy in an organ with such a complicated structure would benefit from a pilot study revealing the variability in microvascular density between various parts of the human brain.

*Corresponding author.
E-mail address: tonar@ntis.zcu.cz (Z. Tonar).

http://dx.doi.org/10.1016/j.jchemneu.2017.11.005
Received 6 October 2017; Received in revised form 3 November 2017; Accepted 3 November 2017 Available online 04 November 2017

1.3. Aims of the study

To provide basic data on the local differences in microvessel density between various parts of the human brain, including representative grey and white matter structures of the cerebral hemispheres, the brain stem and the cerebellum, we first aimed to quantify the numerical and length densities of microvessels in two human brains, i.e. to provide preliminary data without assessing the interindividual variability in a real human population. The vessels of interest included microscopic arterioles, precapillaries, capillaries, postcapillaries, and small venules. Our main aim was to use this data to determine whether the density of human brain microvessels is statistically linked to their preferential orientation (anisotropy).

2. Material and methods

2.1. Specimen preparation

The analysis of the numerical density of brain microvessels was based on tissue blocks and sections used in a previous study on the orientation of human brain microvessels (Kochova et al., 2011). Briefly, samples of brain tissue were taken from two individuals who died in the Department of Neurology, University Hospital, Pilsen. Routine pathological autopsy was performed to confirm the clinical diagnoses and to evaluate the effects of the treatment according to Acts No. 20/1996 and 19/1988, valid under the Law of the Czech Republic. Brain #1 belonged to a healthy 53-year-old woman, and there were no visible pathological findings within the brain. Brain #2 belonged to a 70-year-old man with presumed microvascular atrophy. In both patients, the pathological autopsy revealed that the cause of death was not related to any obvious deterioration of brain tissue. As the Health Act and the Burial Act cited above explicitly permit tissue samples to be taken from pathological autopsies for the purpose of medical research, the pathological anatomist saved the slabs of the brains for the purpose of our study. In each individual, sixteen tissue samples (approx. 1 × 1 × 1 cm) were taken from the left hemisphere of each brain, representing the following parts: the cortex of telencephalon supplied by the anterior, middle, and posterior cerebral artery; the basal ganglia (putamen and globus pallidus) and thalamus as representatives of subcortical grey matter; the subcortical white matter of the telencephalon supplied by the anterior, middle, and posterior cerebral arteries and the interterritorial regions between these arteries; the white matter of the anterior and posterior limbs of the internal capsule; the white matter of the pons; the cerebellar cortex; and the cerebellar white matter (see Supplement 1 for detailed positions, labelling, and vascular supply of the sampled regions). Each of the 32 tissue samples was divided into three smaller blocks with cutting planes oriented in the frontal, sagittal and transversal directions. All tissue blocks (n = 96) were handled separately, and their orientation was maintained carefully during processing. The tissue samples were fixed in Lillie's buffered formalin (Romeis, 1989) at room temperature for one week. Afterwards, the samples were rinsed in 70% ethanol, dehydrated in increasing ethanol concentrations and routinely embedded in paraffin.

2.2. Thick histological sections with arbitrary cutting planes

Thick sections were produced for counting the branching nodes of the microvessels using optical sections. As previously described (Kochova et al., 2011), the tissue blocks were oriented according to the anatomical planes, which was not necessary for the present study, but it was done nonetheless because of the previous study on the orientation and isotropy of brain microvessels based on arbitrarily oriented sections. Series of four consecutive 20-μm-thick histological sections were cut from each block, mounted on Super Frost slides (Sigma-Aldrich, Vienna, Austria), deparaffinized, rehydrated and permeabilized with chilled acetone (−20 °C) for 10 min. Immunohistochemical staining for laminin was performed as described below.

Apart from the numerical density of microvessels (see below), four measures of the orientation and anisotropy of the microvessels were taken from Kochova et al. (2011), who already used these thick

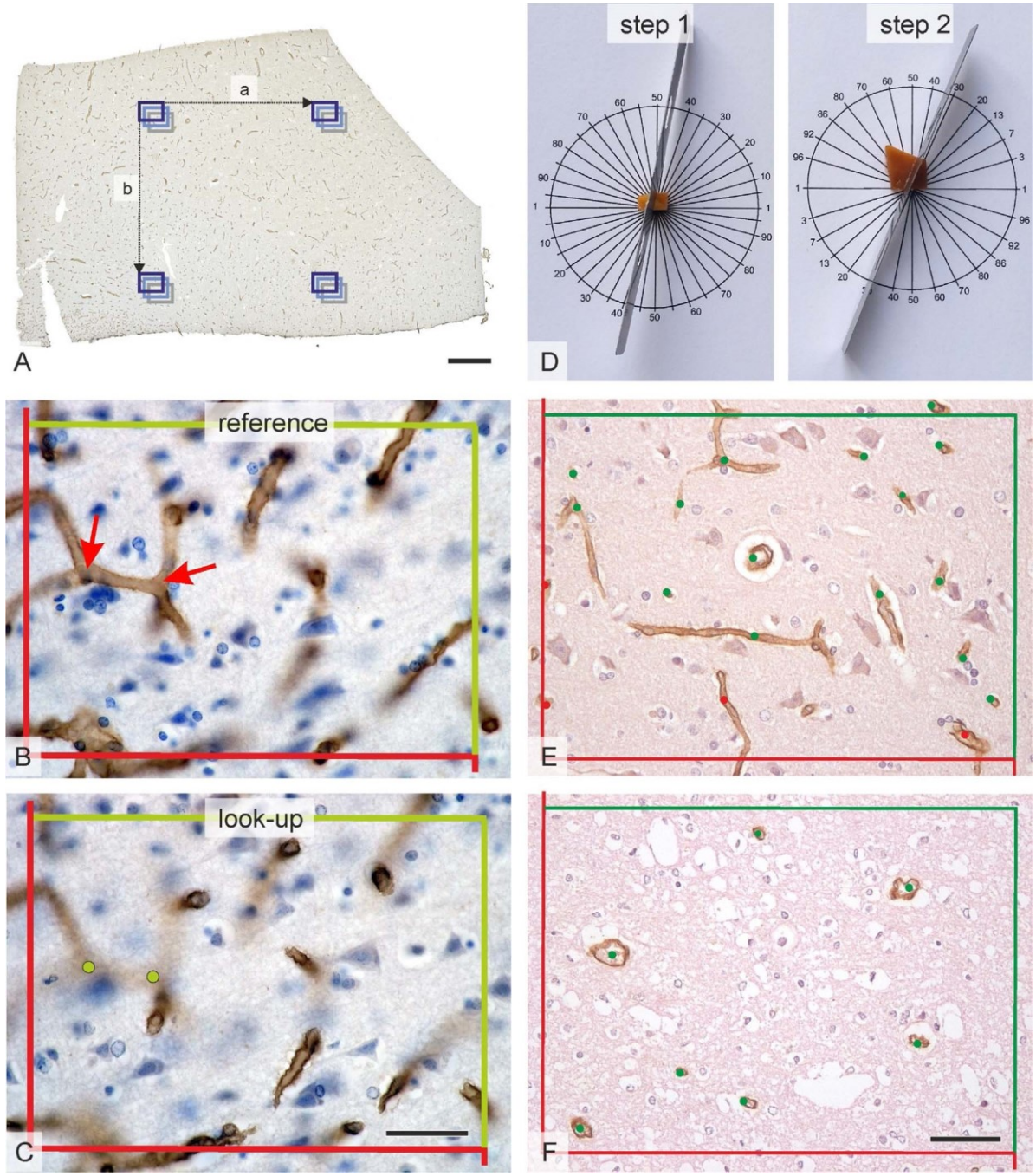

Fig. 1. Microscopic sampling and quantification of numerical density (A–C) and length density (D–F) of brain microvessels. A – In each of the arbitrarily oriented 20-µm-thick sections, four equidistant fields of view (FOVs) were sampled. The distances between the micrographs (a, b) were uniform within each individual section and covered the entire section. The size of the uniform sampling step (a, b) was modified in proportional to the size of the section. In each FOV (real size 230 × 172.5 µm), a series of three optical sections (dark blue, light blue and gray rectangles, depicted here at 2.5 times actual size for clarity) was captured and used for the optical disector. B – In the first (reference) optical plane and in the second optical plane (not shown), branching points were identified (red arrows) and their valence was noted (valence = 3 in both nodes shown). C – In the look-up plane, the branching points from the previous two optical sections were counted in, provided they were already out of focus or had completely disappeared as shown here by the green dots. D – Before the same tissue blocks were re-embedded, the cutting plane was randomized using the orientator technique according to Nyengaard and Gundersen (2006). In step 1, the block was placed on an equiangular circle and cut at a randomly generated angle. In step 2, the block was placed on a cosine-weighted angular circle with the plane produced during step 1 and with the edge of the previous resting face parallel to the 1-1 direction. The new isotropic cutting plane was produced by cutting at another random angle. E, F – Using an unbiased counting frame, the microvessel profiles inside the frame or touching its green allowance borders were counted in (green dots). Objects outside the frame or touching the red forbidden borders were not counted in (red dots). Examples for grey matter (E) and white matter (F). Immunohistochemical detection of laminin, visualized with immunoperoxidase, counterstained with hematoxylin. Scale bars

1 mm (A), 40 µm (B–C), 50 µm (C–D). (For interpretation of the references to colour in this figure legend, the reader is referred to the web version of this article.)

sections: (i) P (χ^2) is a chi-squared method for evaluating anisotropy based on comparing the real distribution of orientations with a discrete uniform distribution using Pearson′s χ^2 test. (ii) n_max (f = 0.5) is the number of preferential directions covering 50% of the microvessel orientations, i.e., brain parts with a more isotropic arrangement of microvessels have greater values of n_max (f = 0.5). (iii) Fractional anisotropy (Dryden et al., 2009) ranges between 0 (isotropy) and 1 (total anisotropy). (iv)

Ellipsoidal anisotropy, as the ratio of the length of the longest axis of an ellipsoid circumscribing the vectors of vessel orientation (based on covariation matrices of all the orientations found in the sample, see Dryden et al., 2009 for details) to the average of the lengths of the other two axes of the ellipsoid, ranges between 1 (isotropy) and infinity (total anisotropy, only one direction present).

2.3. Routine histological sections with isotropic cutting planes

After the thick sections were cut, the tissue blocks with the original arbitrary frontal cutting plane orientation were melted, and the sectional plane was randomized using the orientator principle (Mattfeldt et al., 1990), as shown in Fig. 1D (Nyengaard and Gundersen, 2006; Mühlfeld et al., 2010). Afterwards, the tissue blocks were re-embedded in paraffin with isotropically orientated sectional planes. This is a prerequisite for estimating the length density of microvessels (Mattfeldt et al., 1990). Four 5-µm-thick histological sections were cut from each block, and laminin staining was performed.

2.4. Immunohistochemical detection of blood microvessels

The sections were deparaffinized, rehydrated and transferred to phosphate-buffered saline (PBS, pH 7.4). Endogenous peroxidase activity was blocked using 0.6% (v/v) H_2O_2 in distilled water, and nonspecific binding activity was blocked with normal goat serum (DakoCytomation, Glostrup, Denmark; 150 µl/10 ml PBS) at room temperature. For antigen retrieval, the sections were digested with 1 mg of protease from Streptomyces griseus (Sigma, Vienna, Austria) for 20 min at room temperature. All sections were incubated overnight with a polyclonal rabbit anti-rat laminin antibody (DakoCytomation, 1:500) at 4 °C. The immune reaction was detected using the anti-rabbit PowerVision Kit (Immunovision Technologies, Daly City, CA, USA) according to the manufacturer′s instructions. The reaction was visualized with diaminobenzidine (Sigma-Aldrich) in 0.03% (v/v) H_2O_2 in Tris-buffered saline (pH 7.4). All sections were counterstained with Mayer′s hematoxylin, dehydrated and mounted with a xylene-soluble medium.

2.5. Microscopic sampling and quantification

2.5.1. Numerical density of microvessels

From each of the four 20-µm-thick sections, four stacks, each comprising three 6-µm-thick optical sections, were taken in a systematic, uniform, random manner using a calibrated microscope stage (Fig. 1A). In this way, 48 micrographs each in the frontal, sagittal, and transversal directions of the cutting plane, and therefore 144 micrographs per brain tissue sample, were recorded and analyzed. The optical sections were taken using an oil immersion objective (60×, numerical aperture 1.35). The top and bottom borders of the thick sections were avoided to prevent the lost caps phenomenon (Hedreen, 1998) and the real height of each stack of three optical sections used for the study was 18 µm, as verified using a calibrated Z-stage and oil immersion objective mounted on an Olympus BX51 (Olympus, Tokio, Japan) research microscope. The disector probe (Sterio, 1984), as available in the Disector module of the Ellipse stereological software (ViDiTo, Kosice, Slovak Republic), was used for counting the branching nodes of brain microvessels according to Lokkegaard et al. (2001). A microvessel was defined as a loop between two nodes of the vascular network. Calculation of the numerical density of microvessels was based on the equation by Nyengaard and Marcussen (1993), as used in neurostereological context by Lokkegaard et al. (2001), and modified by Kolinko et al. (2015, 2016) as follows:

$$N_V = \frac{N\,mv}{\sum h \cdot a\,fra \cdot (\quad)} \quad \frac{\quad}{(1)} \quad \frac{\quad}{} = + 1 = + 1,\ V\,ref(\ ) \sum v\,dis($$

where N_V is the number of microvessels N(mv) per reference volume V (ref), P_n is the number of nodes of valence n (number of vessel segments joined at the node), v(dis) is the volume of the disectors, h is the height of the disector and a(fra) is the area of the counting frame. This equation assumed that the sampling scheme was designed so that a sufficient number of counting events (approx. 100 branching nodes) would be observed. An example of the optical disector counting rules is shown in Fig. 1B–C.

2.5.2. Length density of microvessels

Using a series of four routine 5-µm-thick isotropic sections representing each block, we estimated the two-dimensional density of microvessel profiles Q_A (profiles/mm^2) using a stereological counting frame:

$$Q_A = \frac{\sum Q}{\sum A}, \qquad (2)$$

where Q is the number of microvessel profiles counted per area A of the counting frames. An example of the counting frame used in routine sections is shown in Fig. 1E–F. In each sample, 8 micrographs were taken from four sections using a 40 × objective, i.e., 256 micrographs were used in total. In each micrograph, two counting frames (Gundersen, 1977; module CountingFrame, software Ellipse) were applied, resulting in a total reference area of 1.54 mm^2 per sample. On average, 210 vascular profiles were counted per sample. The length density of microvessels (L_V), i.e., the total length of blood vessels per reference volume, was calculated (Baddeley and Jensen, 2005) from the average density of microvessel profiles as follows:

$$L_V = 2 \cdot Q_A. \qquad (3)$$

As L_V refers to the length (mm) divided by volume (mm^3), it has the same dimension as Q_A, i.e., mm^{-2}. The technique is compliant with another state-of the art assessment of length density, namely three-dimensional spherical probes (Calhoun and Mouton, 2001; Mouton et al., 2002). The sampling scheme for both numerical and length density is summarized in Table 1.

2.5.3. Correction for brain shrinkage

Standard histological processing causes shrinking of tissues. When fixed and embedded in paraffin, reference areas and volumes in the histological sections thus appear smaller than they would in unprocessed tissue (Dorph-Petersen et al., 2001). To make the results more comparable with other histological studies or with methods not biased by tissue shrinkage, e.g., micro-CT of corrosion casts (Eberlova et al., 2017) or cryosections (Burggraf et al., 2005), we performed a simple shrinkage analysis and correction using 30

Table 1
Sampling scheme used for quantitative assessment. Two approaches were used for quantification of numerical and length density of brain microvessels.

Parameter estimated	Brains	Tissue probes per brain	Histological blocks per probe; orientation of cutting plane	Sections per histological block	Fields of view per section	Micrographs per field of view
Numerical density of microvessels N_V (mm-3)	n = 2 (53-year-old female, 70-year-old male)	n = 16 (approx. 1 cm^3 each)	n = 3; three arbitrary anatomical planes: frontal, sagittal, and transversal	n = 4 (20-µm-thick each)	n = 4	n = 3 optical sections (60 × immersion oil objective)
Length density of microvessels L_V (mm-2)			n = 1; randomized cutting plane	n = 4 (5-µm-thick each)	n = 8	n = 1 (40 × objective)

separate tissue blocks. We used another 10 blocks from cortical grey matter, 10 blocks
from white matter and 10 blocks from subcortical grey matter (basal ganglia) taken during pathological autopsies from two fresh brains (within 28 h after death), matching the previous brains in age and medical history. Each block was a precisely shaped cuboid bounded with six quadrilateral faces. The X-, Y-, and Z- dimensions of each tissue block were precisely measured using a caliper with a reading error of 0.5 mm, and the volume of each block was calculated. In all samples, the X-, Y-, and Z-directions were preserved consistently to allow for evaluation of the isotropy of the shrinkage as follows: the X-direction was anterior-posterior; the Y-direction was medial-lateral; the Z-direction was perpendicular to the brain surface, thus running from the brain surface into the deeper parts of the brain. The X-, Y-, and Z- dimensions of each tissue block were precisely measured after routine fixation, water rinsing, and 4 h of immersion in 70% alcohol. After dehydration and embedding, the whole tissue blocks were cut. One section from each tissue block was stained with hematoxylin and eosin. The X- and Y- dimensions of each processed block were measured using the histological sections, and the Z-dimension was measured during cutting on a Leica RM2135 Rotary Microtome (Leica Biosystems Nussloch Gmbh, Nussloch, Germany). The volume of the block was calculated from those three measurements. As shown in Fig. 2A, histological processing caused a significant decrease in the volume of the fresh samples. Formalin fixation, paraffin processing and sectioning were responsible for the reduction of the tissue volume. The differences between the shrinkage of the cerebral cortex, white matter and basal ganglia were not significant. As expected (von Bartheld, 2012; Janáček et al., 2012), the shrinkage was anisotropic, affecting mostly the Z-direction during fixation, embedding and cutting (Fig. 2B–D) Adding up the total shrinkage showed no overall differences between dimensions in the Xand Y-axes, but the XY cutting plane of the sections was less shrunken than the perpendicular Z-direction. The areas of the counting frames were scaled down by the factor X*Y, which was, on average, 0.875*0.899 = 0.787 (Supplement 2). Hence, we corrected the area dimensions by multiplying the areas of the counting frames by 1/ 0.787 = 1.270 (Supplement 1). Similarly, the disector volume probes were corrected using a factor X*Y*Z = 0.875*0.899*0.594 = 0.467, i.e., the reference volume was multiplied by 1/0.467 = 2.141 (Supplement 1). We did not observe any signs of differential shrinkage in the XY plane, such as microcracks or separation of anatomical layers visible in the sectional plane.

2.6. Statistics

The whole study was based on quantification of 4608 micrographs for the numerical density of microvessels and 256 micrographs for the length density of microvessels. The software Statistica Base 11 package (StatSoft, Inc., Tulsa, OK, USA) was used for statistical analysis. ANOVA and post hoc Scheffé tests were used to compare the tissue shrinkage during processing. The Shapiro–Wilk W-test for normality showed that some of the data on the numerical and length densities did not comply

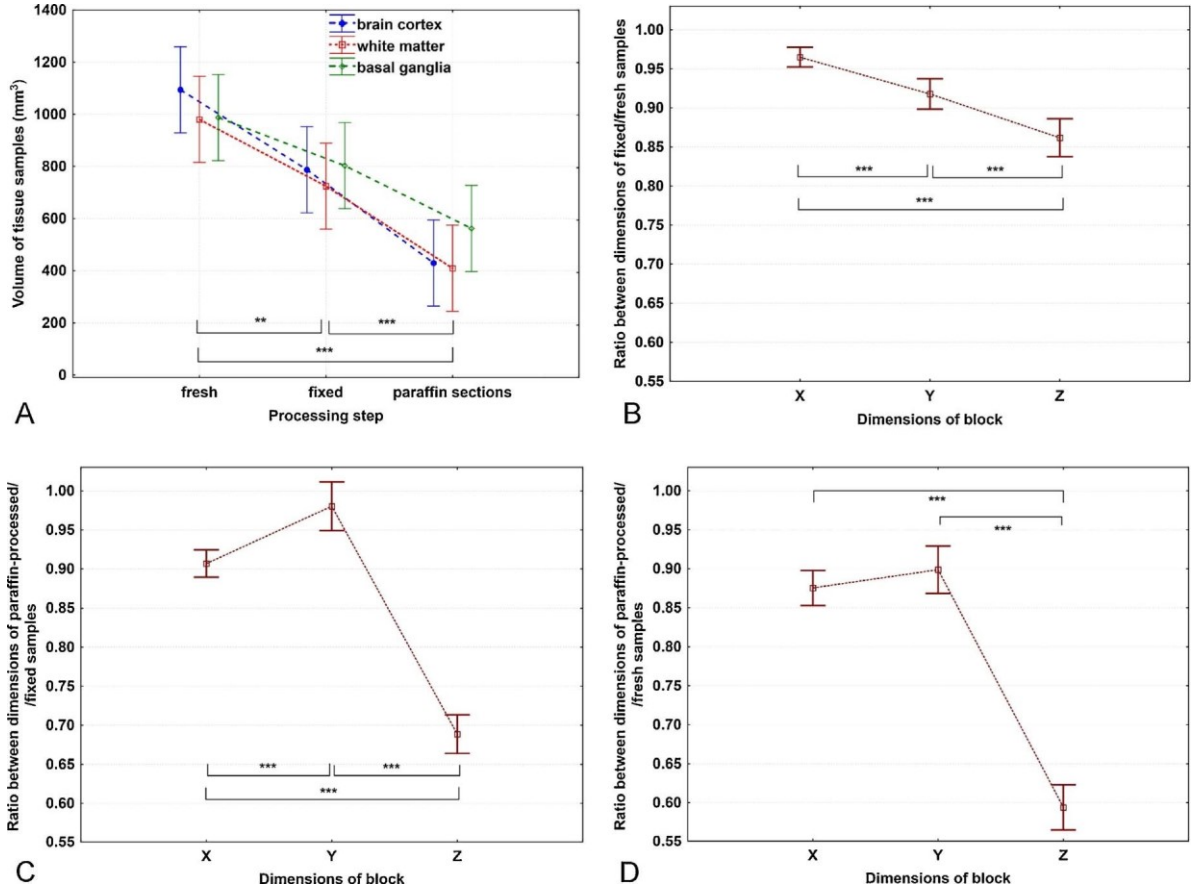

Fig. 2. Analysis of shrinkage during histological processing of brain samples. Volumes and three (X, Y, Z) dimensions of fresh brain tissue samples, formalin-fixed blocks, and exhaustively cut paraffin-embedded serial sections are shown. A – Histological processing caused a significant decrease in the volume of the samples (ANOVA $p < 0.001$). Formalin fixation ($p = 0.002$), as well as paraffin processing and sectioning ($p < 0.001$), reduced the tissue volume. There were no significant differences between the shrinkage of cerebral cortex, white matter and basal ganglia. B – During formalin fixation, anisotropic shrinkage was observed. The samples shrunk in the Z-axis (perpendicular to the brain surface) more than in the Y-axis (medio-lateral) or the X-axis (antero-posterior). C – During sectioning and paraffin processing, the shrinkage was, once again, greatest in the Z-axis. D – Adding up the total shrinkage showed no overall differences between dimensions in the X- or Y-axis, but the XY cutting plane of the sections was less shrunken than the perpendicular Z-direction. Significant differences (*$p < 0.05$, **$p < 0.01$, ***$p < 0.001$) identified using the post hoc Scheffé test (A) and Wilcoxon matched pairs test (B–D) are presented. The point markers show mean values, and the vertical bars denote 0.95 confidence intervals. See Supplement 2 for source data.

Table 2

Estimated numerical density (Nv) and length density (Lv) of brain microvessels. Data from both brains are pooled and presented as the means, medians, minimum (min) and maximum (max) values; the variability is illustrated as standard deviation (SD) and interquartile range (IQR; the value of the 75th percentile minus the value of the 25th percentile, including 50% of the cases). See Supplement 1 for the complete data set.

	Cortical grey matter		Subcortical grey matter		White matter	
	N_V(mm^{-3})	L_V(mm^{-2})	N_V (mm^{-3})	L_V(mm^{-2})	N_V(mm^{-3})	L_V(mm^{-2})
Mean	1311.6	255.7	1350.2	328.3	222.0	159.8
Median	1301.0	264.7	1392.4	340.0	197.8	116.5
Min	675.6	96.1	802.1	194.2	57.5	71.5
Max	1757.8	455.9	1982.7	518.2	605.3	370.0
SD	326.1	119.2	444.7	116.5	146.8	96.1
IQR	337.3	150.8	730.8	144.1	168.7	130.8

with the normal distribution; therefore, we used nonparametric tests for further analyses. The Wilcoxon matched pairs test was used to compare the corresponding anatomical parts of the two brains. For the assessment of differences between the cortical grey matter, subcortical grey matter, and white matter, Kruskal–Wallis ANOVA and the Mann–Whitney U test were used. The correlations were evaluated using Spearman's rank order correlation coefficient. We calculated the sample size needed to detect the expected relative decrease in the numerical and length density of microvessels in various brain compartments using the method described by Chow et al. (2008).

3. Results

N_V in the cerebral cortex was 1311 ± 326 mm^{-3} (mean ± SD), and L_V was 255 ± 119 mm^{-2}. Similarly, in subcortical grey matter (basal ganglia and thalamus), N_V was 1350 ± 445 mm^{-3} and L_V was 328 ± 117 mm^{-2}. The vascular networks of cortical and subcortical grey matter were comparable. Their vascular densities were greater than that of the white matter, in which N_V = 222 ± 147 mm^{-3} and L_V = 160 ± 96 mm^{-2}. The main descriptive statistics are summarized in Table 2.

No differences in the numerical density or length density of microvessels were found between the two brains when anatomically corresponding regions were compared (Fig. 3A–B). Both the cortical (cerebral and cerebellar cortex) and the subcortical grey matter (basal ganglia and thalamus) had greater numerical and length densities than the white matter (Fig. 3C–D).

The low number of brain samples did not allow the data to be grouped for a detailed comparison of anatomical parts of the brain. As shown in Fig. 4, the pontine white matter showed a low numerical density but a high length density of microvessels.

Typical histological findings illustrating the microvessels in various parts of grey and white matter are shown in Fig. 5. The greatest density of microvessels was found typically in the basal ganglia (specifically, the globus pallidus) (Fig. 5B), followed by the cerebellar cortex (Fig. 5C) and cerebral cortex (Fig. 5A). In white matter, specifically that of the pons and cerebellum, the microvessels often showed preferential orientation (see Kochova et al. (2011) for quantification of the preferential orientation of human brain microvessels).

The numerical density of microvessels was moderately correlated with the length density (Table 3) of microvessels within the same anatomical parts of the brain. While the length density of microvessels was not correlated with the local degree of isotropic orientation of microvessels, the numerical density of microvessels had a moderate to strong negative correlation with two of the four measures of anisotropy, namely, with ellipsoidal and fractional anisotropy (Table 3). This means that in parts of brain with more individual microvessels, these microvessels were lacking preferential orientations.

4. Discussion

4.1. Microvessel density of the human brain – comparison with prior data

The ranges of N_V and L_V assessed in our study partially match those found by other authors in individual parts of human brain. Due to the variability of methods used in the literature for estimating microvascular densities, our data will be compared only with the results of studies using well-documented design-based stereological methods. Our data suggest that the numerical density of microvessels in the human cerebral cortex of the hemispheres is greater (mean 1311 mm^{-3}) than the numerical density reported in the hippocampus (mean values from its five subdivisions, 805 mm^{-3}) in the classic and excellently documented paper by Lokkegaard et al. (2001). It must be acknowledged that the data of Lokkegaard et al. (2001) had far lower variability, probably due to very detailed and careful sampling of the comparatively small hippocampus and its subdivisions. In contrast, our sampling scheme included the complete brain and accordingly took fewer samples from each individual part. These differences in the variability of N_V impressively demonstrate the heterogeneity of the microvascular supply in different anatomical parts of the human brain. In addition, the values of N_V presented by Lokkegaard et al. (2001) were not corrected for shrinkage because, in the glycolmethacrylate-embedded material used in their study, shrinkage was reported to be insignificant (West and Gundersen, 1990). However, they used formalin-fixed brains, and as our Fig. 2 shows, the shrinkage caused by formalin fixation is significant.

The data published by Kreczmanski et al. (2009) on the length density of microvessels in human subcortical grey matter (caudate nucleus, putamen, thalamic nuclei, mean values ranging between 400 and 450 mm^{-2} according to the graphs) report slightly larger values than our averaged results from the putamen, globus pallidus, and thalamus (mean 328 mm^{-2}), but again, Kreczmanski et al. (2009) achieved lower variability in their data through detailed sampling of a circumscribed region of interest. The same applies for the comparison of the length densities found by the same authors (Kreczmanski et al., 2005) in frontal cortex (mean approx. 400 mm^{-2}) with our results, which report an average cortical length density of 255 mm^{-2}.

Our data on the length density of the cerebellar cortex in two adult individuals (mean 296 mm^{-2}, see Supplement 1) are much lower than the length densities estimated by Müller-Starck et al. (2014) in cerebellum samples of infants aged 2–10 months (mean 2003 mm^{-2}). This suggests that the length densities are much greater during the ontogenetic period of fast postnatal brain growth than in adults. However, these figures might also be biased due to shrinkage, as the authors used cerebella that had been fixed for 10–12 years in 10% formalin but did not report any correction for shrinkage. The brain tissue of infants, with its greater fraction of tissue fluid, might be especially prone to shrinkage, after which the densities would appear greater (also known as the reference trap; Howard and Reed, 2004; Mouton, 2011).

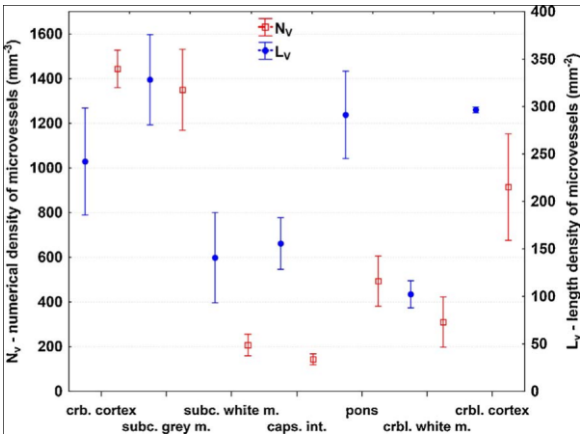

segments between the branching nodes). Moreover, preferential orientations of microvessels appeared usually in the brain parts with smaller N_V, i.e., in regions with less branched microvessel networks. Conversely, the branching of microvessels resulting in greater N_V, occurred in regions with a more homogeneous and more uniform distribution of spatial orientations of these vascular segments. The absence of preferential directions (i.e., the isotropy) of brain microvessels depends on their local branching (greater N_V) rather than on their local length (L_V).

4.3. Implications of the study

All original data assessed in our study are available to contribute to the computational models of human brain perfusion, combining data from advanced imaging methods with real microvascular morphology (Korfiatis and Erickson, 2014; Utsuki, 2015; Bhandari et al., 2017).

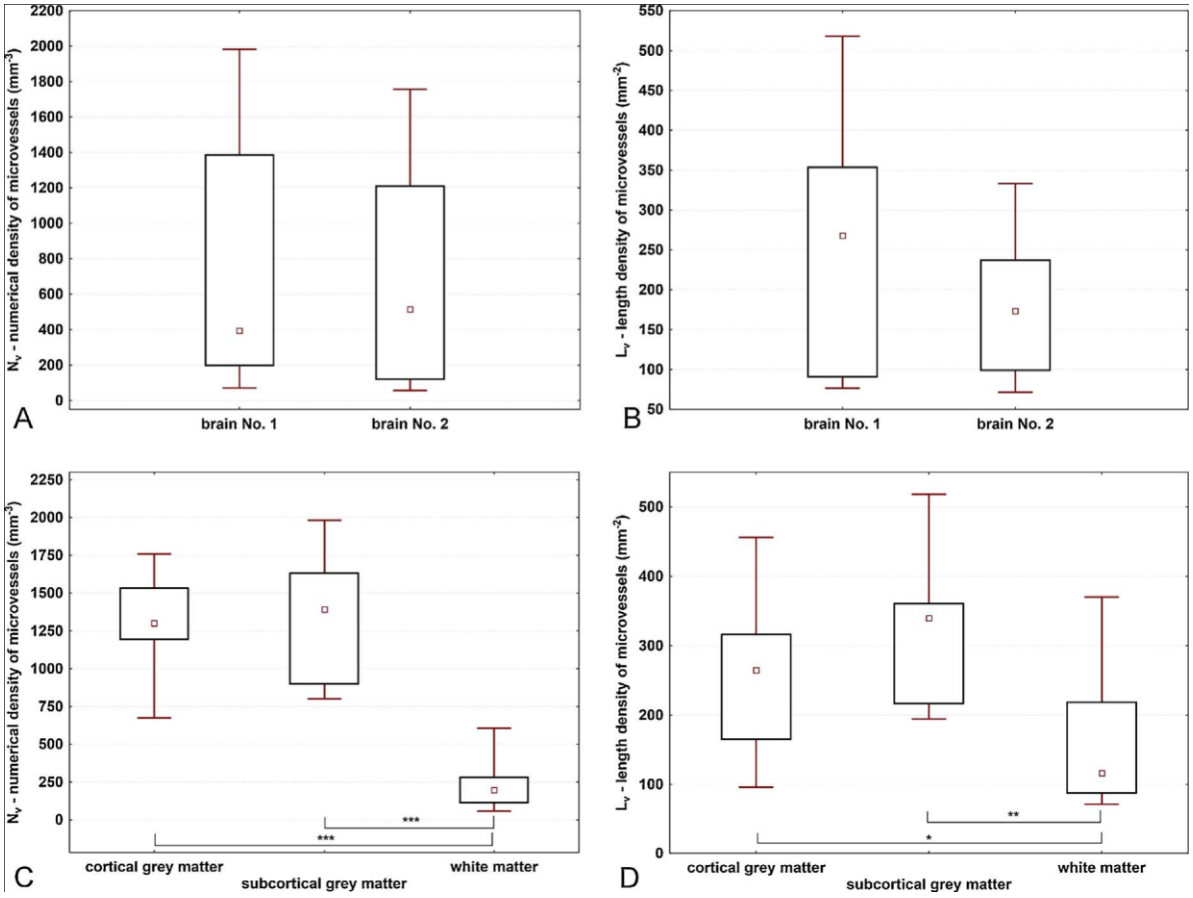

Fig. 3. Comparison of the numerical and length density of microvessels between the two brains under study (A-B) and between the types of brain matter (C–D). A, B – No differences were found when comparing paired samples from corresponding parts of the brains. C, D – The cortical grey matter and the subcortical grey matter (basal ganglia and thalamus) had greater numerical and length densities of microvessels than the white matter (data from both brains were pooled for this comparison). Data are displayed as median values with boxes that span the limits of the first and third quartiles and whiskers that span the minimum and maximum values for each group. Significant differences (*$p < 0.05$, **$p < 0.01$, ***$p < 0.001$) identified using the Mann–Whitney U test are presented. For the data source, see Supplement 1.

Fig. 4. Numerical and length density of microvessels in different anatomical parts of the human brain. In the grey matter (m.), such as the cerebral (crb.) cortex, thalamus and basal ganglia (subc., i.e., subcortical grey matter), and cerebellar (crbl.) cortex, both numerical and length densities were higher than those in white matter regions (subc., i.e., subcortical white matter, internal capsule, and cerebellar white matter). The only exception was the pontine white matter, whose length density was comparable to that of grey matter. Data from both brains were pooled for this comparison and are presented as the means ± standard errors. The number of samples does not allow statistical comparison of the brain parts.

4.2. Greater density of microvessels is linked with lacking preferential orientation

A correlation analysis (Table 3) showed that parts of brain that contain denser microvessel networks (greater L_V) also contain more microvessels from a topological point of view (greater N_V, i.e., greater numbers of microvascular

Although this study investigated 32 samples harvested from various parts of the brains of two individuals, the data grouped in Table 2 may be used for an approximate power analysis, i.e., for calculating the minimum number of samples per study group in planned studies. For example, when the mean numerical microvessel density of the cortical grey matter is expected to be reduced by 20% (i.e., from 1312 to 1049 mm^{-3}) in samples taken from similar regions as in our study, the minimum number of samples per group would be 25, using the typical test power $1-\beta = 0.8$ (where β is the type II error) and $\alpha = 0.05$ (where α is the type I error) (Chow et al., 2008). When a 30% reduction (from 1312 to 918 mm^{-3}) is expected, only 11 samples per group are required. Due to the greater variability found in white matter, the numbers of necessary white matter samples would be greater, i.e., detecting a 30% reduction in length density (from 160 to 112 mm^{-2}) would require up to 63 samples. However, a further reduction in the amount of material and the number of samples can probably be achieved using systematic random sampling strategies at all levels of brain processing, or with smooth fractionator sampling (Gundersen, 2002; Tschanz et al., 2014). It needs to be emphasized that the present data do not allow for assessing interindividual variability of human brain microcirculation in real populations.

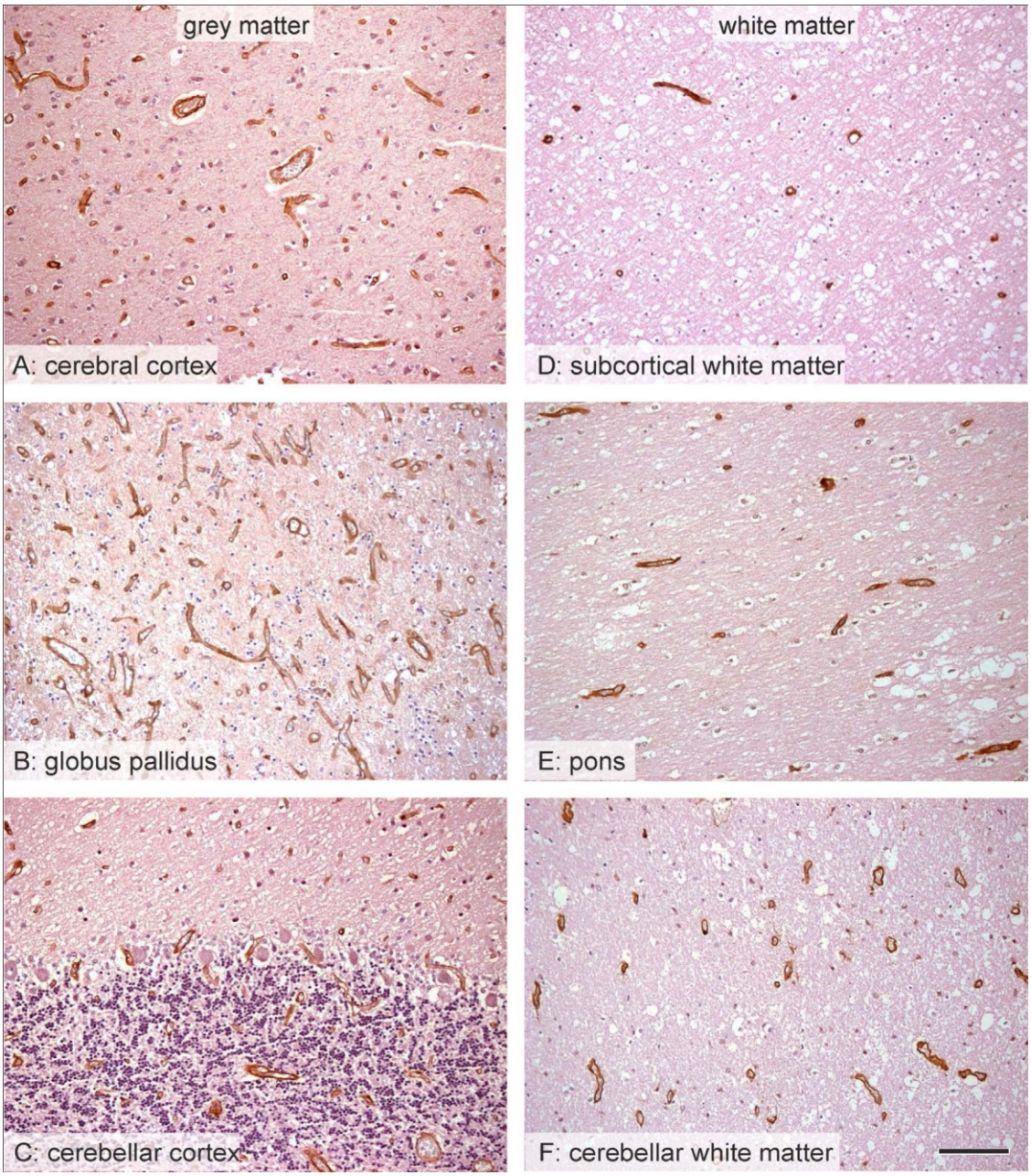

Fig. 5. Typical histological findings illustrating the microvessels in various parts of grey and white matter of the human brain. Even without quantification, it is obvious that the microvessel profiles and their branching are found more frequently in grey matter (A–C) than in white matter (D–E). The greatest density of microvessels was typically found in the basal ganglia (globus pallidus, B), followed by the cerebellar cortex (C) and cerebral cortex (A). In the white matter, the microvessels often showed preferential orientation, especially in the pons and cerebellum. Immunohistochemical detection of laminin, visualized with immunoperoxidase, counterstained with hematoxylin. Scale bar 50 µm.

As an alternative to the approach inspired by Lokkegaard et al. (2001) and used in our study, the numerical density of brain microvessels might also be calculated using the Euler-Poincaré characteristic (Mühlfeld, 2014). Moreover, advanced studies on the topology of brain microvasculature seem to provide enhanced insight into the hemodynamics of the brain, such as the plasma flow and distribution of hematocrit (Hirsch et al., 2012).

Weber et al. (2008) found in macaque brains that the length density of brain microvessels may vary up to fourfold between neocortex layers at different depths from the brain surface. This should definitely be considered during future

studies on the cerebral cortex, as the sampling method must guarantee fair representation of all the cortical layers to prevent bias.

Table 3
Spearman rank-order correlations among the quantitative parameters describing the density and preferential orientation (degree of anisotropy) of human brain microvessels.

	L_V(mm^{-2})	P (χ^2)	n_max (f = 0.5)	Ellipsoidal anisotropy	Fractional anisotropy
N_V(mm^{-3})	0.50	n.s.	n.s.	-0.70	−0.65
L_V(mm^{-2})	–	n.s.	n.s.	n.s.	n.s.

Note: The data were pooled across all parts of both brains under study. N_V− numerical density of microvessels; L_V − length density of microvessels; P (χ^2) − chi-squared method for evaluating anisotropy; n_max (f = 0.5) − number of preferential directions covering 50% of the microvessel orientations. Only correlations significant at $p < 0.05$ are presented. The remaining correlations have no statistical significance (n.s.). Autocorrelations are replaced by the−sign. The data on P (χ^2), n_max (f = 0.5), ellipsoidal anisotropy, and fractional anisotropy from the same brain tissue blocks were taken from Kochova et al. (2011).

4.4. Practical recommendations for further work

Shrinkage correction must be taken into account in planning a quantitative histological study (Dorph-Petersen et al., 2005; Janáček et al., 2012; Tschanz et al., 2014). In our study, the samples shrunk in the Z-axis (perpendicular to the brain surface) more than in the Y-axis (medio-lateral) or the X-axis (antero-posterior). However, we did not distinguish between the shrinkage caused by the histological sectioning procedure itself and, for example the possible effects of the anatomical arrangement of the neocortex layers. Additionally, the total shrinkage during processing was measured in the 5-μm-thick sections only and applied to both the 5-μm-thick and 20-μm-thick sections, but the approach using the 20-μm-thick sections would probably require a different shrinkage correction due to the differential Z-axis collapse (von Bartheld, 2012). The effect of non-uniform shrinkage that differs between routine and thick sections (Hosseini-Sharifabad and Nyengaard, 2007) was not examined in the present study, which is one of its limitations. Moreover, this issue is known to be even more important when much thicker sections are used, such as 100-μm-thick vibratome sections (Andersen and Gundersen, 1999). The total number of microvessels per human brain (or its parts), which is a parameter independent of shrinkage, remains to be counted, preferably using the optical fractionator method (Gundersen et al., 1988). Another possible solution to minimize the effect of shrinkage on microvessel density assessment might be the use of capillary-passable microvascular corrosion casts (Weber et al., 2008; Eberlova et al., 2017) evaluated by microcomputed tomography coupled with stereological evaluation (Jirik et al., 2016).

Another limitation of the present study is that some important brain structures were not included (such as the hippocampal region, a comparison of motor vs. somatosensory cortex, or visual cortex). However, due to the complicated anatomy and especially the size of the human brain, the sampling of the whole cerebral cortex or different regions of the white matter still represents a challenge, as it is much more difficult than comparable tasks in mouse or rat brains, where the organ can be processed as a whole (West et al., 1991; McMillan et al., 1994; Cavaglia et al., 2001; Tsai et al., 2009; Shao et al., 2010; Steinman, 2013). One possible way is to proceed step by step by focusing on specific parts of the human brain, as has been done when analyzing microvessels in the hippocampal region (Lokkegaard et al., 2001), frontal cortex (Kreczmanski et al., 2005), caudate nucleus, putamen, and thalamic nuclei (Kreczmanski et al., 2009). Thick frozen or plastic-embedded sections (Heinsen et al., 2000; Lokkegaard et al., 2001) provide threedimensional data in a more efficient way than routine histological sections.

The reference volumes V_{ref} of each macroscopic subregion were not estimated in the present study. However, this could be done in future studies using stereological point grid cast over approx. 6−10 macroscopic sections through each subregion and calculation of their anatomical volumes using the Cavalieri method ($V_{ref} = \Sigma A \cdot T$, where A is the area of the subsection profile on each section and T is the section thickness). Known V_{ref} may be used to scale the local estimated densities N_V and L_V to total number (Total N) and total lenght (Total L) of microvessels for each subregion, e.g., Total N]$N_V \cdot \cdot V_{ref}$. Data on total number and length of microvessels per subregion may be helpful, e.g., when interpreting the findings of imaging methods visualizing blood flow and distribution of oxygen and nutrients between various brain compartments (Hoge and Pike, 2001).

It should be noted that compared to the orientator method used for obtaining isotropic sections for L_V estimates, a less labor-intensive and a more efficient approach is available for further studies. To avoid orientation bias when estimating lengths of microvessels, either the section or the probe should be isotropic. Rather than making the sections isotropic, virtual software-generated isotropic spheres (Calhoun and Mouton, 2001) can be placed across the quantified region to obtain more precise results in a small fraction of the time and effort as generating isotropic sections using the orientator. The virtual spheres and other benefits of automated stereology (Mouton et al., 2017) are promising tools for improved efficiency in neurostereology. The source images of microvessels for automated counting could be based either on using conventional biological microscopes with immersion objectives with high numerical aperture, such as in the present study, or on confocal microscopes (Janáček et al., 2011).

5. Conclusions

Stereological quantification of the numerical (N_V) and length (L_V) densities of brain microvessels demonstrated that the vascular networks of cortical and subcortical grey matter are comparable but revealed considerable variability within these cerebral compartments: In parts of cerebral cortex with different blood supply, N_V was 1311 ± 326 mm^{-3} and L_V was 255 ± 119 mm^{-2}. Similarly, in subcortical grey matter (which included the basal ganglia and thalamus), N_V was 1350 ± 445 mm^{-3} and L_V was 328 ± 117 mm^{-2}. As expected, both densities were much greater in grey than in white matter (N_V = 222 ± 147 mm^{-3} and L_V = 160 ± 96 mm^{-2}). The corresponding anatomical regions sampled from two individuals (16 samples per individual) had similar N_V and L_V. The numerical and length densities were mutually correlated, but only the numerical density was also correlated with the local loss of preferential orientation of microvessels. Despite the relatively low number of samples, the present data can be utilized for planning and power analyses of detailed studies mapping the differences among various parts of the brain. Our data might also contribute to the computational models of human brain perfusion based on real microvascular morphology. To facilitate this, we have provided all stereological data in the form of continuous variables as supplements.

Acknowledgements

This publication was supported by project LO1506 of the Czech Ministry of Education, Youth and Sports. P.T. was also supported by the Charles University Research Fund (Progres Q39). We thank Dr. Sarka Hadravska for her kind help during dissection. Skillful technical support from Ms. Magdalena Helmreich is also gratefully acknowledged.

Appendix A. Supplementary data

Supplementary data associated with this article can be found, in the online version, at https://doi.org/10.1016/j.jchemneu.2017.11.005.

References

Andersen, B.B., Gundersen, H.J., 1999. Pronounced loss of cell nuclei and anisotropic deformation of thick sections. J. Microsc. 196, 69−73.
Baddeley, A., Jensen, E.B.V., 2005. Stereology for Statisticians. CRC Press, Boca Raton.

Bhandari, A., Bansal, A., Singh, A., Sinha, N., 2017. Perfusion kinetics in human brain tumor with DCE-MRI derived model and CFD analysis. J. Biomech. 59, 80–89. Bladowska, J., Zimny, A., Knysz, B., Małyszczak, K., Kołtowska, A., Szewczyk, P., Gąsiorowski, J., Furdal, M., Sąsiadek, M.J., 2013a. Evaluation of early cerebral metabolic, perfusion and microstructural changes in HCV-positive patients: a pilot study. J. Hepatol. 59, 651–657.

Bladowska, J., Zimny, A., Kołtowska, A., Szewczyk, P., Knysz, B., Gąsiorowski, J., Furdal, M., Sąsiadek, M.J., 2013b. Evaluation of metabolic changes within the normal appearing gray and white matters in neurologically asymptomatic HIV-1-positive and HCV-positive patients: magnetic resonance spectroscopy and immunologic correlation. Eur. J. Radiol. 82, 686–692.

Bonekamp, D., Mouridsen, K., Radbruch, A., Kurz, F.T., Eidel, O., Wick, A., Schlemmer, H.P., Wick, W., Bendszus, M., Ostergaard, L., Kickingereder, P., 2017. Assessment of tumor oxygenation and its impact on treatment response in bevacizumab-treated recurrent glioblastoma. J. Cereb. Blood Flow Metab. 37, 485–494.

Burggraf, D., Martens, H.K., Liebetrau, M., Vosko, M.R., Dichgans, M., Hamann, G.F., 2005. A new approach to reduce the number of animals used in experimental focal cerebral ischemia models. Neurosci. Lett. 386, 88–93.

Burke, M., Zangenehpour, S., Mouton, P.R., Ptito, M., 2009. Knowing what counts: unbiased stereology in the non-human primate brain. J. Vis. Exp. 27, 1262.

Burke, M.J., Nelson, L., Slade, J.Y., Oakley, A.E., Khundakar, A.A., Kalaria, R.N., 2014. Morphometry of the hippocampal microvasculature in post-stroke and age-related dementias. Neuropathol. Appl. Neurobiol. 40, 284–295.

Calhoun, M.E., Mouton, P.R., 2001. Length measurement: new developments in neurostereology and 3D imagery. J. Chem. Neuroanat. 21, 257–265.

Cavaglia, M., Dombrowski, S.M., Drazba, J., Vasanji, A., Bokesch, P.M., Janigro, D., 2001. Regional variation in brain capillary density and vascular response to ischemia. Brain Res. 910, 81–93.

Chiapponi, C., Piras, F., Piras, F., Fagioli, S., Caltagirone, C., Spalletta, G., 2013. Cortical grey matter and subcortical white matter brain microstructural changes in schizophrenia are localised and age independent: a case-control diffusion tensor imaging study. PLoS One 8, e75115.

Chow, S.C., Wang, H., Shao, J., 2008. Sample Size Calculations in Clinical Research, second edition. Chapman & Hall/CRC Biostatistics Series, Boca Raton.

Cuenod, C.A., Balvay, D., 2013. Perfusion and vascular permeability: basic concepts and measurement in DCE-CT and DCE-MRI. Diagn. Interv. Imaging 94, 1187–1204.

Dockery, P., Fraher, J., 2007. The quantification of vascular beds: a stereological approach. Exp. Mol. Pathol. 82, 110–120.

Dorph-Petersen, K.A., Nyengaard, J.R., Gundersen, H.J., 2005. Tissue shrinkage and unbiased stereological estimation of particle number and size. J. Microsc. 204, 232–246.

Dryden, L.L., Koloydenko, A., Zhou, D., 2009. Non-Euclidean statistics for covariance matrices, with applications to different tensor imaging. Ann. Appl. Stat. 3, 1102–1123.

Eberlova, L., Liska, V., Mirka, H., Tonar, Z., Haviar, S., Svoboda, M., Benes, J., Palek, R., Emingr, M., Rosendorf, J., Mik, P., Leupen, S., Lametschwandtner, A., 2017. The use of porcine corrosion casts for teaching human anatomy. Ann. Anat. 213, 69–77.

Gerstner, T., Woelfing, C., Witsch, M., Longin, E., Bell, N., König, S., 2006. Capillary microscopy and hemorheology in children during antiepileptic monotherapy with carbamazepine and valproate. Seizure 15, 606–609.

Gundersen, H.J.G., Bagger, P., Bendtsen, T.F., Evans, S.M., Korbo, L., Marcussen, N., Moller, A., Nielsen, K., Nyengaard, J.R., Pakkenberg, B., et al., 1988. The new stereological tools: disector, fractionator, nucleator and point sampled intercepts and their use in pathological research and diagnosis. APMIS 96, 857–881.

Gundersen, H.J.G., 1977. Notes on the estimation of the numerical density of arbitrary profiles: the edge effect. J. Microsc. 111, 219–223.

Gundersen, H.J., 2002. The smooth fractionator. J. Microsc. 207, 191–210.

Hedreen, J.C., 1998. Lost caps in histological counting methods. Anat. Rec. 250, 366–372.

Heinsen, H., Arzberger, T., Schmitz, C., 2000. Celloidin mounting (embedding without infiltration) – a new, simple and reliable method for producing serial sections of high thickness through complete human brains and its application to stereological and immunohistochemical investigations. J. Chem. Neuroanat. 20, 49–59.

Hirsch, S., Reichold, J., Schneider, M., Székely, G., Weber, B., 2012. Topology and hemodynamics of the cortical cerebrovascular system. J. Cereb. Blood Flow Metab. 32, 952–967.

Hoge, R.D., Pike, G.B., 2001. Oxidative metabolism and the detection of neuronal activation via imaging. J. Chem. Neuroanat. 22, 43–52.

Hosseini-Sharifabad, M., Nyengaard, J.R., 2007. Design-based estimation of neuronal number and individual neuronal volume in the rat hippocampus. J. Neurosci. Methods. 162, 206–214.

Howard, C.V., Reed, M.G., 2004. Unbiased Stereology. Three-dimensional Measurement in Microscopy. Garland Science, New York.

Janáček, J., Cvetko, E., Kubínová, L., Travnik, L., Eržen, I., 2011. A novel method for evaluation of capillarity in human skeletal muscles from confocal 3D images. Microvasc. Res. 81, 231–238.

Janáček, J., Kreft, M., Cebašek, V., Eržen, I., 2012. Correcting the axial shrinkage of skeletal muscle thick sections visualized by confocal microscopy. J. Microsc. 246, 107–112.

Jirik, M., Tonar, Z., Kralickova, A., Eberlova, L., Mirka, H., Kochova, P., Gregor, T., Hosek, P., Svobodova, M., Rohan, E., Kralickova, M., Liska, V., 2016. Stereological quantification of microvessels using semiautomated evaluation of X-ray microtomography of hepatic vascular corrosion casts. Int. J. Comput. Assist. Radiol. Surg. 11, 1803–1819.

Karbowski, J., 2011. Scaling of brain metabolism and blood flow in relation to capillary and neural scaling. PLoS One 6, e26709.

Kochova, P., Cimrman, R., Janacek, J., Witter, K., Tonar, Z., 2011. How to asses, visualize and compare the anisotropy of linear structures reconstructed from optical sections – a study based on histopathological quantification of human brain microvessels. J. Theor. Biol. 286, 67–78.

Kolinko, Y., Krakorova, K., Cendelin, J., Tonar, Z., Kralickova, M., 2015. Microcirculation of the brain: morphological assessment in degenerative diseases and restoration processes. Rev. Neurosci. 26, 75–93.

Kolinko, Y., Cendelin, J., Kralickova, M., Tonar, Z., 2016. Smaller absolute quantities but greater relative densities of microvessels are associated with cerebellar degeneration in lurcher mice. Front. Neuroanat. 10, 35.

Korfiatis, P., Erickson, B., 2014. The basics of diffusion and perfusion imaging in brain tumors. Appl. Radiol. 43, 22–29.

Kreczmanski, P., Schmidt-Kastner, R., Heinsen, H., Steinbusch, H.W., Hof, P.R., Schmitz, C., 2005. Stereological studies of capillary length density in the frontal cortex of schizophrenics. Acta Neuropathol. 109, 510–518.

Kreczmanski, P., Heinsen, H., Mantua, V., Woltersdorf, F., Masson, T., Ulfig, N., SchmidtKastner, R., Korr, H., Steinbusch, H.W., Hof, P.R., Schmitz, C., 2009. Microvessel length density, total length, and length per neuron in five subcortical regions in schizophrenia. Acta Neuropathol. 117, 409–421.

Kubínová, L., Mao, X.W., Janáček, J., 2013. Blood capillary length estimation from threedimensional microscopic data by image analysis and stereology. Microsc. Microanal. 19, 898–906.

Lauwers, F., Cassot, F., Lauwers-Cances, V., Puwanarajah, P., Duvernoy, H., 2008. Morphometry of the human cerebral cortex microcirculation: general characteristics and space-related profiles. Neuroimage 39, 936–948.

Lee, G.D., Aruna, J.H., Barrett, P.M., Lei, D.L., Ingram, D.K., Mouton, P.R., 2005. Stereological analysis of microvascular parameters in a double transgenic model of Alzheimer's disease. Brain Res. Bull. 65, 317–322.

Lokkegaard, A., Nyengaard, J.R., West, M.J., 2001. Stereological estimates of number and length of capillaries in subdivisions of the human hippocampal region. Hippocampus 11, 726–740.

Mühlfeld, C., Ochs, M., 2014. Measuring structure – What's the point in counting? Ann. Anat. 196, 1–2.

Mühlfeld, C., Nyengaard, J.R., Mayhew, T.M., 2010. A review of state-of-the-art stereology for better quantitative 3D morphology in cardiac research. Cardiovasc. Pathol. 19, 65–82.

Mühlfeld, C., 2014. Quantitative morphology of the vascularisation of organs: a stereological approach illustrated using the cardiac circulation. Ann. Anat. 196, 12–19.

Müller-Starck, J., Büttner, A., Kiessling, M.C., Angstma, N.B., Császár, N.B., Haeussner, E., Hochstrasser, T., Sternecker, K., Hof, P.R., Milz, S., Frank, H.G., Schmitz, C., 2014. No changes in cerebellar microvessel length density in sudden infant death syndrome: implications for pathogenetic mechanisms. J. Neuropathol. Exp. Neurol. 73, 312–323.

Marcos, R., Monteiro, R.A.F., Rocha, E., 2012. The use of design-based stereology to evaluate volumes and numbers in the liver: a review with practical guidelines. J. Anat. 220, 303–317.

Mattfeldt, T., Mall, G., Gharehbaghi, H., Möller, P., 1990. Estimation of surface area and length with the orientator. J. Microsc. 159, 301–317.

Mayhew, T.M., 2014. Estimating oxygen diffusive conductances of gas-exchange systems: a stereological approach illustrated with the human placenta. Ann. Anat. 196, 34–40. McMillan, P.J., Archambeau, J.O., Gokhale, A., Archambeau, M.H., Oey, M., 1994. Morphometric and stereological analysis of cerebral cortical microvessels using optical sections and thin slices. Acta Stereol. 13, 33–38.

Menke, R.A., Szewczyk-Krolikowski, K., Jbabdi, S., Jenkinson, M., Talbot, K., Mackay, C.E., Hu, M., 2014. Comprehensive morphometry of subcortical grey matter structures in early-stage Parkinson's disease. Hum. Brain Mapp. 35, 1681–1690.

Mouton, P.R., Gokhale, A.M., Ward, N.L., West, M.J., 2002. Stereological length estimation using spherical probes. J. Microsc. 206, 54–64.

Mouton, P.R., Phoulady, H.A., Goldgof, D., Hall, L.O., Gordon, M., Morgan, D., 2017. Unbiased estimation of cell number using the automatic optical fractionator. J. Chem. Neuroanat. 80, A1–A8.

Mouton, R., 2011. Unbiased Stereology. A Concise Guide. The Johns Hopkins University Press, Baltimore.

Nyengaard, J.R., Alwasel, S.H., 2014. Practical stereology of the stomach and intestine. Ann. Anat. 196, 41–47.

Nyengaard, J.R., Gundersen, H.J.G., 2006. Sampling for stereology in lungs. Eur. Respir. Rev. 15, 107–114.

Nyengaard, J., Marcussen, N., 1993. The number of glomerular capillaries estimated by an unbiased and efficient stereological method. J. Microsc. 171, 27–37.

Nyengaard, J.R., 1999. Stereologic methods and their application in kidney research. J. Am. Soc. Nephrol. 10, 1100–1123.

Ochs, M., 2014. Estimating structural alterations in animal models of lung emphysema. Is there a gold standard? Ann. Anat. 196, 26–33.

Peng, S.J., Harnod, T., Tsai, J.Z., Ker, M.D., Chiou, J.C., Chiueh, H., Wu, C.Y., Hsin, Y.L., 2014. Evaluation of subcortical grey matter abnormalities in patients with MRI-negative cortical epilepsy determined through structural and tensor magnetic resonance imaging. BMC Neurol. 14, 104.

Perl, D.P., Good, P.F., Bussiere, T., Morrison, J.H., Erwin, J.M., Hof, P.R., 2000. Practical approaches to stereology in the setting of aging- and disease-related brain banks. J. Chem. Neuroanat. 20, 7–19.

Phan, T.G., Hilton, J., Beare, R., Srikanth, V., Sinnott, M., 2014. Computer modeling of anterior circulation stroke: proof of concept in cerebrovascular occlusion. Front. Neurol. 5, 176.

Richard, E., van Gool, W.A., Hoozemans, J.J., van Haastert, E.S., Eikelenboom, P., Rozemuller, A.J., van de Berg, W.D., 2010. Morphometric changes in the cortical microvascular network in Alzheimer's disease. J. Alzheimers Dis. 22, 811–818.

Romeis, B., 1989. Mikroskopische Technik. Urban & Schwarzenberg, München.

Schmitz, C., Hof, P.R., 2007. Design-Based stereology in brain aging research. In: Riddle, D.R. (Ed.), Brain Aging: Models, Methods, and Mechanisms. CRC Press/ Taylor & Francis, Boca Raton (Chapter 4).

Shao, W.H., Li, C., Chen, L., Qiu, X., Zhang, W., Huang, C.X., Xia, L., Kong, J.M., Tang, Y., 2010. Stereological investigation of age-related changes of the capillaries in white matter. Anat. Rec. (Hoboken) 293, 1400–1407.

Steinman, J., 2013. Development of a Novel Imaging Methodology for Quantitative Analysis of the Mouse Cortical Vasculature. Master Thesis. Available at http://hdl.handle.net/1807/42945. University of Toronto.

Sterio, D.C., 1984. The unbiased estimation of number and sizes of arbitrary particles using the disector. J. Microsc. 134, 127–136.

Tsai, P.S., Kaufhold, J.P., Blinder, P., Friedman, B., Drew, P.J., Karten, H.J., Lyden, P.D., Kleinfeld, D., 2009. Correlations of neuronal and microvascular densities in murine cortex revealed by direct counting and colocalization of nuclei and vessels. J. Neurosci. 29, 14553–14570.

Tschanz, S., Schneider, J.P., Knudsen, L., 2014. Design-based stereology Planning, volumetry and sampling are crucial steps for a successful study. Ann. Anat. 196, 3–11.

Utsuki, T., 2015. Development of a cerebral circulation model for the automatic control of brain physiology. Conf. Proc. IEEE Eng. Med. Biol. Soc. 2015, 1890–1893.

Weber, B., Keller, A.L., Reichold, J., Logothetis, N.K., 2008. The microvascular system of the striate and extrastriate visual cortex of the macaque. Cereb. Cortex. 18, 2318–2330.

West, M.J., Gundersen, H.J., 1990. Unbiased stereological estimation of the number of neurons in the human hippocampus. J. Comp. Neurol. 296, 1–22.

West, M.J., Slomianka, L., Gundersen, H.J.G., 1991. Unbiased stereological estimation of the total number of neurons in the subdivisions of the rat hippocampus using the optical fractionator. Anat. Rec. 231, 482–497.

Zechariah, A., ElAli, A., Doeppner, T.R., Jin, F., Hasan, M.R., Helfrich, I., Mies, G., Hermann, D.M., 2013. Vascular endothelial growth factor promotes pericyte coverage of brain capillaries, improves cerebral blood flow during subsequent focal cerebral ischemia, and preserves the metabolic penumbra. Stroke 44, 1690–1697.

von Bartheld, C.S., 2012. Distribution of particles in the Z-axis of tissue sections: relevance for counting methods. Neuroquantology 10, 66–75.

Biomedical Materials

PAPER

Electrospun vascular grafts fabricated from poly(Llactide-co-ε-caprolactone) used as a bypass for the rabbit carotid artery

IOP Publishing Biomed.Mater.13 (2018) 065009

https://doi.org/10.1088/1748-605X/aade9d

Biomedical Materials

PAPER

Electrospun vascular grafts fabricated from poly(L-lactide-co-ε-caprolactone) used as a bypass for the rabbit carotid artery

RECEIVED
4August2018
REVISED
3September2018
ACCEPTED FOR PUBLICATION
4September2018
PUBLISHED
20September2018

JanaHorakova[1,8],PetrMikes[1],DavidLukas[1],AlesSaman[1],VeraJencova[1],AndreaKlapstova[1],TerezaSvarcova[1],MichalAckermann[2],VitNovotny[3],MartinKalab[4],VladimirLonsky[4],MartinBartos[5],MichalaRampichova[6],AndrejLitvinec[6],TerezaKubikova[7],PetrTomasek[7] andZbynekTonar[7]

[1] DepartmentofNonwovensandNanofibrousMaterials,Facultyof TextileEngineering, TechnicalUniversity ofLiberec,Studentska 1402/2,46001Liberec,Czechia
[2] DepartmentofIndustrialTechnology,InstituteofNanomaterials,AdvancedTechnologiesandInnovation,TechnicalUniversity of Liberec,Studentska1402/2,46001Liberec,Czechia
[3] DepartmentofNanomaterialsinNaturalSciences,InstituteofNanomaterials,Advanced TechnologiesandInnovation,Technical University ofLiberec,Studentska1402/2,46001Liberec,Czechia
[4] DepartmentofCardiosurgery, FacultyofMedicineandDentistry,PalackyUniversity Olomouc,Hnevotinska3,77515Olomouc,Czechia
[5] InstituteofDentalMedicine,InstituteofPathologicalPhysiology,InstituteofAnatomy,FirstFacultyofMedicine,CharlesUniversityand GeneralUniversity HospitalinPrague,Katerinska32,12108Prague2,Czechia
[6] InstituteofExperimental MedicineofASCR,v.v.i.,Videnska1083,14220Prague4,Czechia
[7] DepartmentofHistology andEmbryologyandBiomedicalCenter,FacultyofMedicineinPilsen,CharlesUniversityinPrague, Karlovarska48,30166Pilsen,Czechia
[8] Authortowhomanycorrespondence shouldbeaddressed.

E-mail:jana.horakova@tul.cz

Keywords:vasculargraft,electrospinning,copolymerpoly-L-lactide-co-ε-caprolactone,rabbitanimalmodel

Abstract

Thestudyinvolvedtheelectrospinningofthecopolymerpoly(L-lactide-co-ε-caprolactone)(PLCL)into tubulargrafts.Thesubsequentmaterialcharacterization,includingmicro-computedtomographyanalysis, revealedalevelofporosityofaround70%,withporesizesof9.34±0.19μmandfiberdiametersof 5.58±0.10μm.UnlikefibrouspolycaprolactoneelectrospunPLCLcopolymerpromotedfibroblast andendothelialcelladhesionandproliferationinvitro.Moreover,theregenerationofthevesselwallwas detectedfollowingimplantationand,aftersixmonths,theendothelializationofthelumenandthe infiltrationofarrangedsmoothmusclecellsproducingcollagenwasobserved.However,thedegradation ratewasfoundtobeacceleratedintherabbitanimalmodel.Thestudywasconductedunderconditions thatreflectedtheclinicalrequirements—theprostheseswereresuturedintheend-to-sidefashionandthe long-termendpointofprosthesishealingwasassessed.Theregenerationofthevesselwallintermsof endothelialization,smoothcellinfiltrationandthepresenceofcollagenfiberswasobservedaftersix monthsinvivo.Apartofthegraftsfailedduetotherapiddegradationrateofthe PLCLcopolymer.

Introduction

Extensive research has been conducted worldwide on the materials and methods to be employed for the fabrication of ideal vascular grafts, a process that is particularly challenging due to the large number of requirements such as the appropriate mechanical properties, surface properties with respect to the endothelialization of the graft lumen, together with non-thrombogenicity, hemocompatibility, nonimmunogenicity etc. Electrospun materials resembling the natural extracellular matrix have been found to fulfill the majority of these requirements; thus, the further investigation of such materials would seem to present a promising way forward in terms of the developmentofvasculargrafts.

The last few years have witnessed huge progress concerning the application of biodegradable materials that enhance the healing process. Polyesters such as polycaprolactone (PCL), polylactide (PLA) and their respective copolymers (PLCL) have found uses in a broad range of tissue engineering applications. While PCL and PLA differ in terms of their surface properties and degradation rate, it is possible to tailor the properties of the copolymers of these two polymers via the composition of the final copolymer. The long-term evaluation of PCL-based electrospun vascular grafts revealed calcification on the regenerated vessel wall; therefore, it is necessary to examine the potential of other polymers for use in this application [1]. The PLCL copolymer is an elastomeric material developed fortheconstructionofvasculargrafts[2–4].

Mechanical properties make up one of the most important requirements with concern to the effective replacement of blood vessels. Studies devoted to the mechanical assessment of electrospun biodegradable vascular grafts in general have previously been conducted by Enis et al, Johnson et al, Limbert et al, Xie et al [5–8] while the mechanical properties of the material used in our study have been investigated by Johnson et al including the comparison of biodegradable polyesters such as PCL, PLA, polyglycolide and the copolymers thereof inthe form ofelectrospun tubular structures and commercially-available grafts and human vessels. The polymers were dissolved in hexafluoroisopropanol and electrospun on a rotating mandrel to a final wall thickness of 650±65 μm, and it was determined that the PLCL electrospun copolymer exhibited the highest level of compliance of all the tested grafts, attaining an average value of 8.2% mm Hg, which is higher than that of the human carotid artery with a compliance value of 5.4% mm Hg. Moreover, theburst pressureofaprosthesismade fromPLCLwas determined at 2.5 MPa, which is substantially higher thanthatofthecoronaryartery(around0.4MPa)[6].

With concern to vascular grafts, the optimal fiber diameter (and thus the resulting porosity and pore size) is crucial for cell infiltration following implantation. The morphological analysis of vascular grafts is usually performed by means of scanning electron microscopy (SEM) and image analysis tools; however, these techniques do not truly reflect the 3D structure of tubular grafts. New techniques such as micro-computed tomography (micro-CT) provide for the evaluation of 2D and 3D structural parameters including the basic parameters (e.g. volume, surface, number of objects),advancedparameters (e.g.structurethickness and separation based on the 3D sphere-fitting algorithm [9, 10], porosity) and stereology parameters [11–13]. The results obtained are based on the unique non-destructive 3D analysis of a selected specimen which allows the direct measurement of selected parameters.

The assessment of vascular grafts in vivo has been addressedbyanumber ofresearchgroups(seetable1); however, the results published to date suffer from certain limitations such as the animal models used, the mode of implantation and the length of the period of study. Most of the research was conducted on rats following implantation in the form of a bypass of the aorta with high blood flow. The suturing technique has been found to exert a huge impact on the healing of vascular grafts and end-to-side anastomosis appears to be more suitable in terms of further clinical use despite the turbulent flow in such anastomosis potentially creating problems with respect to vascular graft closure. In short, the detailed assessment of these materials requires the conducting of long-term studies. De Valence et al [1] and Li et al [14] investigated the performance of PCL grafts after 18 months in rats makingthem,tothebestofourknowledge, thelongest studies of their kind conducted to date. Other studies, especially those conducted employing larger animal models such as rabbits, pigs, dogs or sheep, have been limitedtojustweeksorafewmonthsatmost.

However, none of the studies presented above dealt with challenging end-to-side implantation over the long term. Therefore, our study focused on the development, characterization and biological assessment of a biodegradable graft implanted end-to-side inrabbitsoveraperiodofsixmonths.

Methods

Materialsandelectrospinningsolutionpreparation

The electrospinning solution was prepared from a GMPgradecopolymerofL-lactideandε-caprolactone in a 70/30 molar ratio suitable for medical device applications (PLCL, Corbion n.v., Netherlands). Polymeric granules were dissolved in a solvent system composed of chloroform/ethanol/acetic acid in the ratio 8/1/1v/v/v (Penta s.r.o., CzechRepublic) with a finalpolymerconcentrationof10 wt%.

The cell interactions of the newly-developed PLCL electrospun material were compared with electrospun pure polycaprolactone (PCL, average M_n

45.000, Merck KGaA, Germany) which was dissolved in the same solvent system at a final concentration of 18 wt% and electrospun on a Nanospider™ 1WS500U (Elmarco s.r.o., Czech Republic). The PLCL copolymer was also electrospun by means of this technique. Planar samples of electrospun PCL and PLCL were employedforinvitroassessmentpurposes.

Preparationofthevasculargrafts

The electrospinning solution was stirred overnight and immediately electrospun on a custom-made device as schematically depicted in figure 1. The resulting fibers were collected on a rotating mandrel with an inner diameter of 2 mm. The distance between the needle tip and the collector was set at 20 cm. The polymer dosage applied during the preparation of the sample was maintained at 1.5 ml h^{-1}, the needle was charged at 15 kV and the collector was grounded. The movingneedleenabledtheproductionofsampleswith a length of up to 15 cm. The ambient conditions consisted of a temperature of 25 °C and humidity between 50% and 55%. Electrospinning was applied until the resulting tubular samples achieved a thickness of 100 μm, whereupon they were pushed manuallyfromthemandrel.

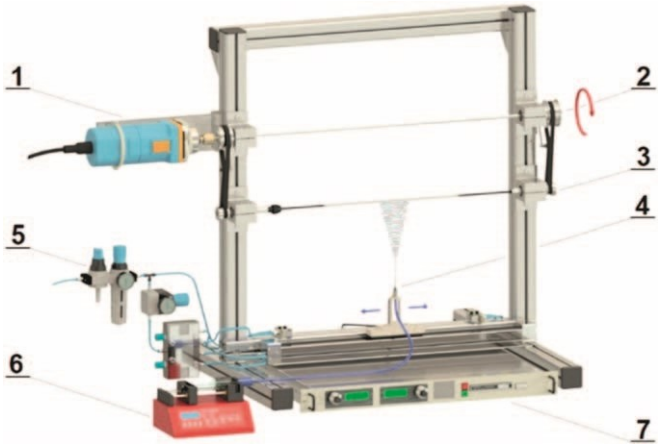

Figure1. Schematicpresentation ofthecustom-madeelectrospinning deviceusedforthefabricationoftubulargraftsandcomposed ofahighspeedengine (1),atorqueconverter (2),agroundedcollectorintheform ofarotating mandrel (3),apositivelycharged electrospinning needle (4),apneumaticcontrolunit (5),apolymericsolutionpump (6) andahighvoltagesource (7).

Table1.Overviewofinvivo-testedvasculargraftsfabricatedfromelectrospunpolycaprolactone,polylactideandtheirrespectivecopolymers. PDS=polydioxanone,VEGF=vascularendotheliagrowthfactor,HGFI=classIhydrophobin,RGD=arginylglycylasparticacid.

Animalmodel,implantationarea	Typeof implantation	Grafttype	Investigatedtime points	References
Mouseaorta	End-to-end	ElectrospunPLAcoatedwithPLCL	4,8,12months	Tara2014[3]
Rataorta	End-to-end	ElectrospunPCL	1.5,3,6,12,18 months	De Valence2012[1]
Rataorta	End-to-end	ElectrospunPCL-plasmatreated	3weeks	De Valence2013[15]
Rataorta	End-to-end	WetspunPCL+electrospunPCL	3,18months	Li2018[14]
Rataorta	End-to-end	ElectrospunPCL	7,14,28,100days	Wang2014[16]
Rataorta	End-to-end	ElectrospunPCL,PCL+PDS,PDS	4,12weeks	Pan2017[17]
Rataorta	End-to-end	ElectrospunPCL	3,6,12,18,24weeks	Pektok2008[18]
Rataorta	End-to-end	ElectrospunPCL	3,12months	Yang 2016[19]
Rataorta	End-to-end	ElectrospunPCL-VEGF,HGFI modified	1month	Wang2017[20]
Rabbitcarotidartery	End-to-end	ElectrospunPCL-RGD functionalized	2,4weeks	Zheng 2012[21]
Rabbitcarotidartery	End-to-end	ElectrospunPCL	4,12weeks	Wang2016[22]
Rabbitaortoiliacbypass	End-to-side	ElectrospunPCL-collagen	4weeks	Tillman 2009[23]
Beagledogsfemoral artery	End-to-end	ElectrospunPLC-collagen-chitosan	12weeks	Wu2015[4]
Pigscarotidartery	End-to-end	ElectrospunPCL	4weeks	Mrówczyński 2014[24]

Characterizationofthefibroussamples

The morphology of the fibrous scaffold was analyzed by means of SEM and micro-CT. The fibrous samples were cut into pieces, placed in a SEM holder and covered with a 7 nm layer of gold. Subsequently, a cross-section of the tubular graft was captured by a TESCAN Vega 3SB Easy probe (TESCAN s.r.o, Czech Republic). The planar samples employed for cell seeding purposes were analyzed in the same way and the fiber diameter was characterized using NIS Elements software (LIM s.r.o., Czech Republic). The fiber diameter was assessed from a total of 200 measurements per material taken from three to five independent SEM pictures; the data was then presented in the formofthemean±standarddeviation.

Micro-CT scans of the tubular graft were acquired using a micro-CT SkyScan 1272 (Bruker, Kontich, Belgium). For micro-CT scanning purposes, grafts with a wall thickness of 400 μm were obtained over an extended electrospinning time under the same conditions as those described previously. The

analyzed sample was scanned in air applying the following scanning parameters: 0.5 μm pixel size, camera binning 1×1, rotation step 0.1°, source voltage 50 kV, source current 200 μA, no filter, frame averaging (10) and 180° rotation. The scanning time was approximately 6 h for each specimen (n = 10). The flat-field correction was updatedpriortoeachacquisition.

Cross-sectional images were reconstructed from projection images by means of NRecon software (Bruker, Kontich, Belgium) employing a modified Feldkamp algorithm. Computed tomography artifacts were reduced via the requisite setting of the correction parameters (misalignment, ring artifact and beam hardening). Visualizations were acquired by means of DataViewer (2D cross-sectional images) and CTVox (3Dimages;Bruker,Kontich,Belgium).

The 3D analysis of the specimen structure was conducted by means of CTAn (Bruker, Kontich, Belgium). The volume of interest (VOI) was set in the form of a cube (side = 250 μm) in the middle of the specimen so as to exclude the effect of potential superficial alterations resulting from the handling of the specimen. A total of ten specimens were analyzed for morphological parameters. Image data analysis was optimized employing TeIGen software [25]. Binarization was achieved employing global thresholding which was determined to provide a suitable method in this case. Image noise reduction was ensured using despeckleoperationsin3D.

Invitroassessment

Prior to the performance of the animal experiments, the interaction of the materials was assessed using 3T3 mouse fibroblast cell lines (ATCC, USA) and human umbilical vein endothelial cells (HUVEC, Lonza Biotec s.r.o., Czech Republic). The in vitro tests were performed on planar samples prepared by means of the needle-less electrospinning of PCL and the PLCL copolymer. The samples were cut into circles with a diameter of 6 mm. Prior to cell seeding, the materials were soaked in 70% ethanol for 30 min followed by double rinsing in phosphate-buffered saline(PBS,pH7.4).

The mouse 3T3 fibroblasts were cultivated in Dulbecco's Modified Eagle Medium (Lonza Biotec s.r.o., Czech Republic) supplemented with 10% fetal bovine serum(LonzaBiotec s.r.o.,CzechRepublic),1% glutamine (Biosera, Czech Republic) and 1% penicillin/ streptomycin/amfotericin B (Lonza Biotec s.r.o., Czech Republic). The fibroblasts (passage 19) were seeded on scaffolds placed in 96 well plate at a density of 5×10^3 perwell.

The human umbilical vein endothelial cells were cultivated in Endothelial Basal Medium (EBM-2, Lonza Biotech s.r.o., Czech Republic) supplemented with EGM-2 Single Quots (Lonza Biotec s.r.o., Czech Republic). The endothelial cells (passage 6) were seeded on scaffolds placed in 96 well plate at a density of 7.5×10^3 perwell.

The interactions of the cells with the electrospun PCL and PLCL were evaluated after 1, 3, 7 and 14 days of culturing by means of the metabolic MTT test. The MTT [3-(4,5-dimethylthiazol-2-yl)-2,5-diphenyl-2Htetrazolium bromide] was reduced to purple formazan by means of mitochondrial dehydrogenase in cells that indicated normal metabolisms. MTT solution (50 μl) was added to 150 μl of the complete medium and the samples were incubated at 37 °C for 4 h. The resulting formazan violet crystals were solubilized using acidic isopropanol and the optical density of the suspension was measured (λ_{sample} 570 nm, $\lambda_{reference}$ 690 nm). Four samples of each material were incubated with MTT solution on each of the testing days and the average absorbance was calculated as the difference between absorbance measured at 570 nm and the referencewavelengthof690 nm.

In order to allow for the evaluation of cell morphology and spreading 1 day following cell seeding, the samples were rinsed twice in PBS and fixed in 2.5% glutaraldehyde for 30 min at 4 °C and, subsequently, 0.1% Triton X-100 in 0.1% bovine serum albumin solution in PBS was used as a blocking buffer for 10 min. The samples were stained using phalloidinFITC (Merck KGaA, Germany, dilution 1:1000) which binds to the actin filaments of the cells and stains them green. DAPI (Merck KGaA, Germany, dilution 1:1000) was used for the counterstaining of the cell nuclei to blue. The stained cells were then observed by means of a Nikon Eclipse-Ti-E inverted fluorescence microscope(NikonImaging,CzechRepublic).

The viability testing and cell quantification data obtained was processed using two-way analysis of variance (ANOVA) with the Bonferonni multiple comparisontest.

Invivotesting

The materials intended for in vivo implantation were sterilized using ethylene oxide and aerated for one week at room temperature. The animals were treated according to the Czech National Convention for the Protection of Vertebrate Animals used for Experimental and other Specific Purposes Act, Collection of Legislation No. 246/1992 and its amendments concerning the Protection of Animals

from Cruelty, the Public Notice of the Ministry of Agriculture of the CzechRepublicandCollection ofLegislationNo.419/ 2012 (the Keeping and Exploitation of Experimental Animals). Vascular grafts were implanted into New Zealandwhite rabbits(n = 10) intheform ofacarotid artery bypass. The rabbits were six months old and weighed between 3.6 and 5.0 kg. The animals were anesthetized with Narcotan (Halotan)+O_2 prior to implantation and Diazepam (Apaurin), Ketamin (Narketan) and Xylazin (Xylapan) were administered to the rabbits prior to surgery. The skin on the left side of the necks of the rabbits was shaved and disinfected using iodopovidon. The incision of the neck and the preparation of the subcutaneous and muscle tissue were performed followed by the isolation of the arteria carotis communis. Heparin was administered intravenously (300 mU kg^{-1}) and the proximal part of the carotid artery was clamped. The vascular prosthesis was then sutured using Prolene 7-0 (Ethicon, Johnson & Johnson, Czech Republic) in the proximal section. The same procedure was applied to the distal section ofanastomosis. The length ofthe implanted prosthesis was1.5 cm. Thevasculargraftwassutured bymeansof the end-to-side technique and the bypassed section of the carotid artery was ligated. Following surgery, the animals received Meloxikam (Meloxydil 5) and Marbofloxacin (Marbocyl) medication for five days. During the time of observation, acetylsalicic acid (Kardegic 0.5 g) was administered daily (10 mg/rabbit peros).

The ten rabbits subjected to investigation were divided into two groups for the assessment of different graft healing time-points. The first group was analyzed aftertenweeksofimplantation(n = 5rabbits)andthe second group was monitored for long-term healing aftersixmonths(n = 5rabbits).

Histologicalevaluation

For histological processing purposes, the grafts were explanted together with the proximal and distal parts of the carotid artery after ten weeks and after six months of survival. The explanted grafts with the surrounding tissue were then processed employing standard histological techniques. For the purpose of comparison, a native carotid artery without a replacement was assessed in the same way at both the ten weeksandsixmonthstime-points.

Following formalin fixation, the tissue blocks were cut into 4 μm thick histological sections with a section plane perpendicular to the long axis of the artery. The sections were stained using a variety of general (table 2) and specialized histological stains with respect to their immunohistochemical reactions (table 3). The staining methods were selected in order to be able to characterize the cellular populations of the grafts employing a similar approach to that of other research papers on the topic [1, 16, 21, 23, 24]. The visualization of the immunohistochemical reaction was based on diaminobenzidine (DAB+, Liquid; DakoCytomation, Glostrup, Denmark). The immunohistochemical sections were counterstained with Gill's hematoxylin and all the sections were

Table2.Histological stainingmethodsusedinthestudy.

Staining	Purpose
hematoxylin-eosin[26]	Overallmorphologyofthegraft,foreign-bodygiantcells
Verhoeff'shematoxylinandgreentrichrome [27]	Overallmorphology,differentiating connectivetissue,elastin andvascularsmoothmuscle
Orcein(Tanzer'sorcein,BowleyBiochemicalInc.,Danvers,MA,USA)	Elastinfibers
Picrosiriusred(DirectRed80,SigmaAldrich,Munich,Germany)[28–30]	TypeIandtypeIIIcollagenwhenobserved undercircularly polarizedlight

Table3.Primaryantibodiesusedfortheimmunohistochemistry.

Antibody(andstainingpurpose)	Manufacturer	Dilution	Pretreatment
MonoclonalMouseAnti-HumanSmoothMuscleActin, Clone1A4(smooth muscleandmyofibroblastmarker)	DakoCytomation(Glostrup, Denmark)	1:100	20 min96 °CDakoTarget RetrievalSolution,pH9
MonoclonalAnti-CD31 antibodyCloneJ70A(endothelialmarker)	DakoCytomation	1:40	20 min96 °CDakoTarget RetrievalSolution,pH9
MonoclonalMouseAnti-HumanNeurofilamentProtein,Clone2F11(nervefibermarker)	DakoCytomation	1:75	20 min96 °CDakoTarget RetrievalSolution,pH9
MonoclonalMouseAnti-HumanCD68,CloneKP1 (macrophage marker)	DakoCytomation	1:100	20 min96 °CDakoTarget RetrievalSolution,pH9

dehydrated in graded ethanol solutions and mounted with a xylene-soluble medium. The sections were then observed by means of bright field microscopy and polarized light microscopy. However, when processed using standard histological techniques, it was found that most of the grafts lost their integrity which prevented the reliable quantification of the results. Due to the variability of the histological findings, all the significantfeaturesaredescribedseparately.

The explanted native rabbit carotid arteries were characterized according to their wall thicknesses and inner diameter measurements. The average thickness of the tunica intima and the media was calculated from 4 native vessel positions. A line perpendicular to the lumen and connecting the luminal surface of the intima with the most abluminal elastic lamellar unit was drawn in each position using an Ellipse software linear measurement tool. Similarly, the average thickness of the whole of the wall was calculated from the length of the lines connecting the luminal surface of the intima with the outermost layer of the dense collagenous connective tissue of the adventitia according to Witter et al [31]. The average diameter of the native carotid arteries was calculated from the measurement of the area profile of the lumen visible in the histological sections according to Kochova et al [32]. Similar measurements could not be applied to the grafts since they usually failed to retain their round shape;

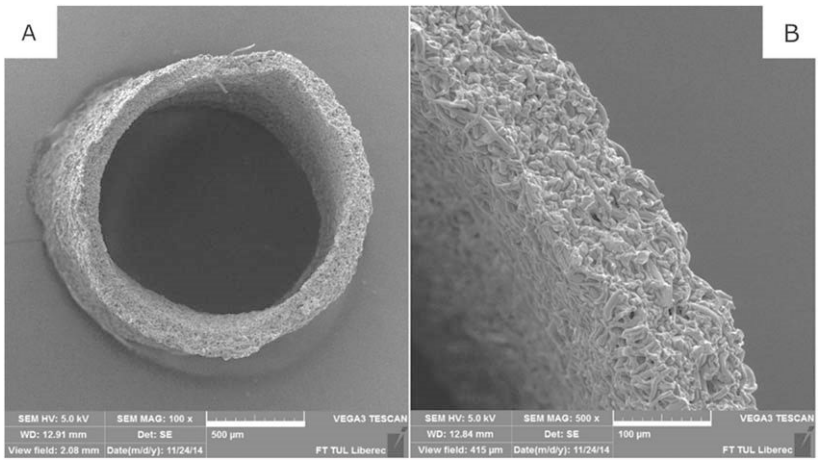

Figure2. SEMphotographofacross-sectionofanelectrospunPLCLvasculargraft;scalebars1mm (A),100 µm (B).

moreover, cross-sections through thegrafts wereoften deformedinthehistologicalsections.

Determinationofgraftdegradationinvivo Following the histological evaluation, the explanted graftsembedded inparaffinwere analyzedby means of gel permeation chromatography (GPC) in order to detect changes in the molecular weight upon implantation. The paraffin was removed via the serial rinsing and vortexing of the grafts with the surrounding tissue in hexane. The samples were then allowed to dry. Finally, the grafts were dissolved in tetrahydrofuran (THF) and the solution was left to evaporate under nitrogen so as to obtain a volume of 0.2 ml for use in the GPC analysis phase. A granulate of the PLCL copolymer and an electrospun graft were also assessed for comparison purposes. The control samples were diluted in THF so as to attain a concentration of approximately1 g l^{-1}.

The analysis included the use of the Dionex Ultimate 3000 HPLC system with a diode array and a Varian LC-385 ELSD detector along with a polymeric PhenomenexPhenogel1E4GPCcolumnwithalength of 30 cm with an i.d. of 4.6 mm and a particle size of 5 µm. The temperature of the column compartment was set at 30 °C and THF of HPLC grade purity at a flow rate of 1 ml min^{-1} was applied. The chromatograms were recorded at wavelengths of 200, 210, 220 and 250 nm employing an ELSD detector for 23 min. The nebulizer temperature of the ELSD detector and the evaporator temperature were set at 80 °C; the nitrogen flow rate applied was 1.3 l min^{-1} with an injectionvolumeof30 µl.

The elution of the polymeric substances was observed between 5 and 9 min; consequently, the corresponding graph was compiled so as to illustrate this specific retention time interval. The grafts with the highest peak intensity were selected for the demonstrationoftheshiftsinthemolecularweight.

Results

Vasculargraftmorphology

The electrospinning of the PLCL copolymer was performed using a custom-designed device with a rotating mandrel collector. The production process was very sensitive to ambient conditions especially relative humidity that was required to be maintained at between 50% and 55%. A cross-section of the resulting tubular structure is shown in figure 2. The collector in the form of a rotating mandrel had a diameter of 2 mm. However, following removal, the grafts shrank to an inner diameter of approximately 1.4 mm. The average fiber diameter of the tubular samples measured from the SEM images was determinedat5.40±2.09 µm.

The tubular samples were characterized by means of micro-CT. A visualization of the VOI (the cube inside the tubular graft wall) is depicted in figure 3 in the form of 2D (A), (B) and 3D images (C), (D). The grayscale images show plane fibers at selected sections and the pores between them; the spatial resolution and partial volume effect may have resulted in blurred fiber edges. Thus, the binarization (figure 3(B)) required prior to the image analysis may possibly influence the outcomes. The structure thickness (in 3D) can be clearly presented as a color-coded image (figure 3(D)). However, whole specimen visualization in various 2D sections or in the form of 3D volume imaging presents a unique opportunity for the evaluationofthespecimens.

The morphological features revealed by the microCT analysis can be seen in table 4. The PLCL copolymer occupied approximately 30% of the graft structure with a porosity of around 70%. The thickness of the structure corresponds to a fiber diameter of 5.58±0.10 µm. The pores within the

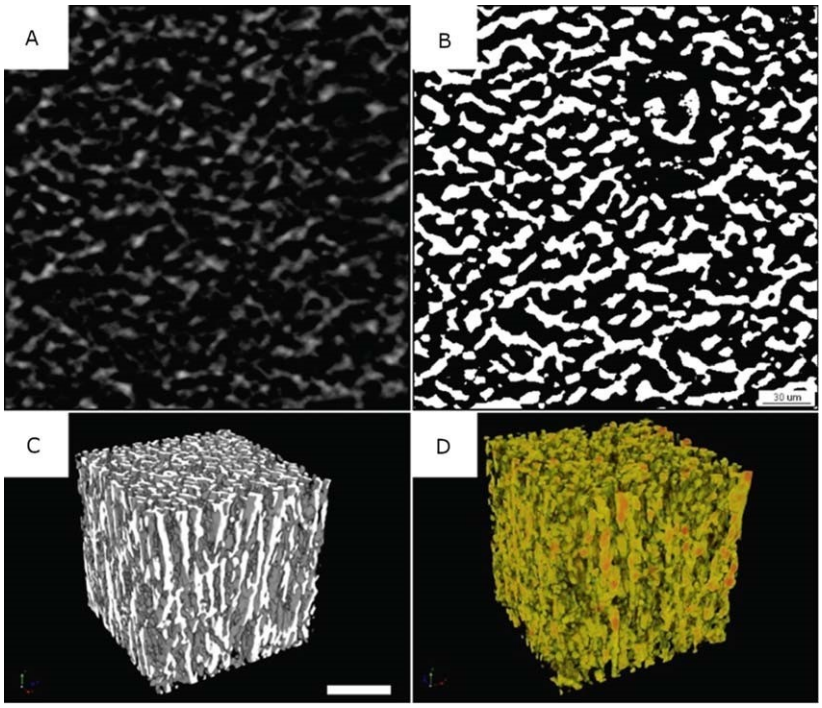

Figure3. Grayscaleimageofamicro-CTtransversalsection (perpendiculartothe fibrouslongaxis) (A) andfollowingimage binarization (B),scalebar30 μm.3Dvisualizationofabinarizedspecimen (C),3Dvisualizationincolor-coded modeshowing differences instructurethickness:gradienttransitionfromgreentoviolet:green =2 μm,yellow =4 μm,red =8 μm, violet=12 μm (D),scalebar100 μm.

structure evince a mean of 9.34±0.19 μm (represented as structure separation in the table). More than 99.99% of the porosity constituted open porosity, i.e. approximatelyequaltothepresentedtotalporosityvalue.

Table4.Resultsofthemicro-CT3Danalysisofselected parameters(mean,median, standarddeviation).

	MEAN	MED	SD
Percentobjectvolume(mm^3)	30.37	30.22	0.76
Structurethickness(μm)	5.58	5.58	0.10
Structureseparation(μm)	9.34	9.31	0.19
Totalporosity(%)	69.63	69.78	0.76

MEAN=mean value, MED=median, SD=standard deviation.

Morphologyoftheplanarsamples

The electrospun morphology of PCL and PLCL is depicted in figure 4. The PLCL copolymer created homogeneous fibers with a diameter of 1.35± 0.57 μm in the form of electrospun planar sheets. The electrospinning of the PCL produced fibers with a diameter of 0.49±0.95 μm. The high standard deviation in the PCL fibrous layer indicated the presence of tiny fibers (minimum fiber diameter of 0.3 μm) as well as thick fibers within the structure (3.54 μm maximummeasured fiberdiameter).

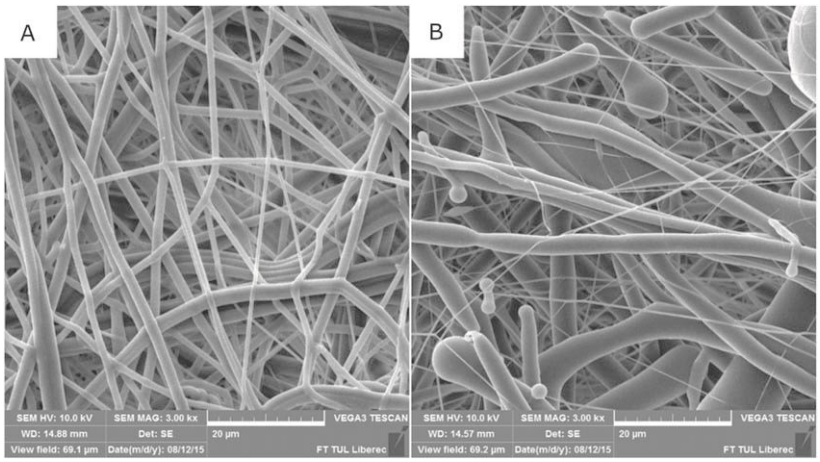

Figure4. SEMphotosoftheelectrospunplanarsamplesfabricatedfrom PLCL (A) and PCL (B); scalebar 20 µm.

Interactionswiththecelllines

The electrospun samples were prepared for in vitro assessment purposes by means of the needle-less electrospinning technique which resulted in planar samples suitable for the assessment of cell material interaction. Fibrous samples fabricated fromthe PLCL copolymer under study as well as PCL were seeded with two types of cell lines, i.e. 3T3 mouse fibroblasts and endothelial cells. Polycaprolactone was chosen for comparisonpurposes sincethispolymeriswidelyused for vascular graft purposes in its electrospun form. Viability testing revealed that the PLCL copolymer supported the proliferation of both cell types over 14 days of experimentation (figures 5(A), (B)). The higher cell viability of cells cultured on the PLCL copolymer was recorded following the culturing of both cell types over 14 days; moreover, the difference in the proliferation rate was more remarkable with respect to the fibroblasts, concerning which higher cell viability was recorded as soon as on the seventh day following cell seedingonthePLCLcopolymer.

The adhesion of cells on the surface of the fibrous materials was assessed by means of fluorescence microscopy. The staining of the actin filaments indicatescellularspreading.Thecounterstainingofthec ell nuclei with blue DAPI allowed for the comparison of cell quantity on the tested materials. Figures 6(A)–(D) depicts cells captured on electrospun PLCL and PCL one day following seeding. More cells adhered to the PLCL copolymer than to the electrospun PCL, which alsoexhibitedalowerdegreeofcellularspreading.

Implantationofvasculargrafts

The prepared vascular grafts exhibited excellent surgical handling and suture retention following implantation as a bypass of the carotid artery. No significant blood leakage was observed subsequent to the restoration of blood flow and pressure. Blood flow was monitored at the end of the study by means of palpitation.Allthetestedanimalsevincedpulsation.

Histologicalevaluationoftheexplantedgrafts Two vascular graft healing time-points were assessed, i.e. the prostheses and the control carotid arteries without replacements were explanted after ten weeks and six months (n = 5 + 5). The intima and media thickness of the native rabbit carotid artery ranged from 120 to 155 µm after ten weeks and from 145 to 180 µm after six months. The total thickness of the carotid artery, including the adventitia, ranged from 205 to 230 µm after ten weeks and from 260 to 288 µm after six months. The histological sections of the native rabbit carotid arteries are shown in figure 7. The vessel wall was composed of layers of elastin and a collagen extracellular matrix infiltrated by smooth muscle cells. The inner diameter of the histological sections of the normal rabbit carotid artery ranged from 1140 to 1360 µm after ten weeks and from 1270 to1510aftersixmonths.

Macroscopic images of prostheses prior to explanting are depicted in figures 8(A), (B). After ten weeks, four of the five tested grafts were found to be patent (an 80% patency rate after ten weeks); a cross-section of such a prosthesis is depicted in figures 8(C), (E). At the later time-point of six months, two of the tested prostheses (40%) were observed to contain invaginated and partially fibrotized islands of connective tissue surrounded by the graft lumen. The initial strength of the mechanical properties of the grafts were lost during the long-term healing process; four of the grafts were broken in the middle or near an anastomosis when explanted (80% of the implanted grafts). Full vascular graft patency was observed with respect to one graft with a freely passable lumen (a 20% patency rate after six months),

as depicted in figures 8(D), (F); the whole width of the wall had been penetrated by cells. After six months, the thickness of the vessel wall decreased to 68 μm suggesting that the degradation of the prosthesis was more rapid than tissue regeneration. No apparent inflammatory infiltrates or foreign-body giant cells were discovered except for small areas associated with the stitches betweenthewallandthegrafts(datanotshown).

Inadditiontotheconsiderationoftheoverallhealing process, the characterization of the cells and resultant extracellular matrices was conducted by means of specific staining as depicted in figure 9. The endothelial cells were stained via the visualization of CD 31. Despite partial damage to the graft surfaces during the histological processing phase, following ten weeks of healing, remnants of endothelial-like cells were found to be partially preserved; however, they were negative with respect to CD 31 immunohistochemistry (see figure 9(A)). The longer period of six months resulted in the positivity of the endothelial cells with respect to the staining method employed (figure 9(B)). Smooth muscle cells were presented as early as after ten weeks, at which time they were observed to have integrated within the graft wall assuming a spindle shape as can be seen in figure 9(C). The smooth muscle cells were arranged in layers resembling the natural composition of arteries during the healing process (see figure 9(D)). The extracellular matrix was composed of collagen, which was present in the regenerated vessel walls at both time-points as can be observed from the green trichrome staining depicted in figures 8(D)–(F) and the picrosirius red staining shown in figures 9(G), (H). The staining of elastin was also performed and the results are visible in figures 9(E), (F). Despite the presence of smooth muscle cells, no elastic fibers were observed. The heavy false positivity of the orcein staining was discovered at the later time-point of six months (figure 9(F)). Nervi vasorum and vasa vasorum werenotpresentatanytimewithinthegrafts.

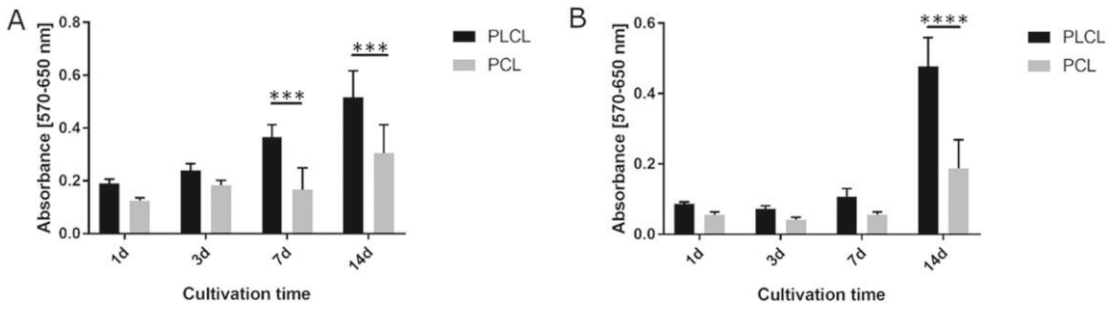

Figure5. ResultsoftheMTTviabilitvassayofseeded 3T3 fibroblasts (A) andendothelialcells (B) onelectrospunPLCLandPCL, **** denotes $p < 0.0002$, **** refersto $p < 0.0001$ (2 wayANOVA,Bonferonni).

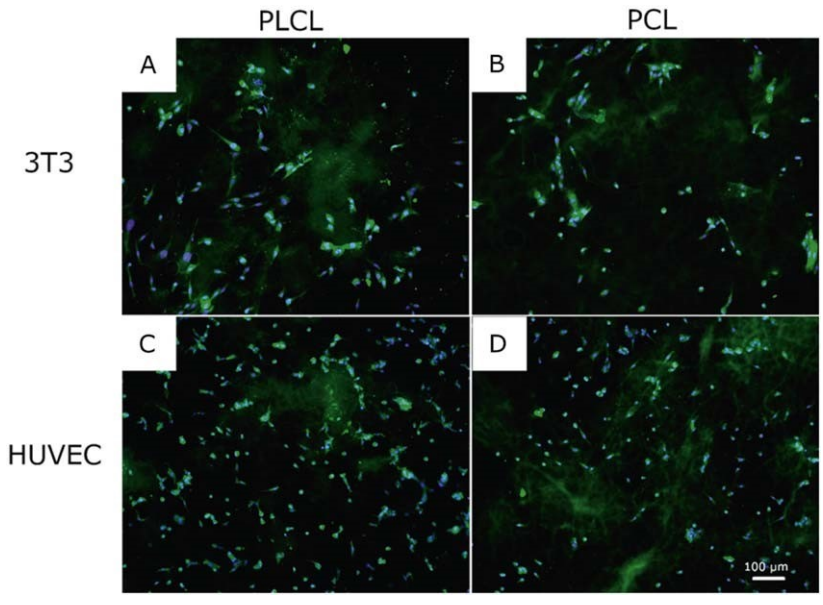

Figure6. Theadhesionof fibroblaststothesurfaceoftheelectrospunPLCLcopolymer (A) andPCL (B),theadhesionofendothelial cellsto fibrousPLCL (C) andPCL (D);scalebar100 µm.

Following ten weeks of healing, one of the five implants was destroyed by a thrombus (as shown in figures 10(A), (C)) that was organized with connective tissue. The thrombus was recanalized by CD31-positive micro-vessels. Long-term healing over six months resulted in the prolapse of two prostheses containing invaginated and partially fibrotized islands of connective tissue surrounded by the graft lumen (see figures10(B),(D)).

Assessmentofthemolecularweightshiftfollowing implantation

The molecular weight of granules of the PLCL copolymer, an electrospun vascular graft fabricated from the same polymer and the grafts following implantation in rabbits after ten weeks and six months were assessed by means of GPC. The retention time (t_R) of the peaks corresponds to the molecular weight, i.e. a shift thereof towards longer retention times indicates a decrease in molecular weight. The results are expressed in the form of relative values which compare the input materials with their stages followingimplantation(seefigure11).

The molecular weight clearly shifted towards lower values as a result of the electrospinning process (from a retention time of 5.8 to 6.2 min), and a further massive weight loss was observed following implantation, i.e. the retention times of the explanted grafts shifted to average values of 7.8 min after ten weeks and 8.0 min after six months. While the peaks of highest intensity are depicted in figure 11, it is important to note that the retention times of the analyzed samples varied from 6.8 to 8.2 min with respect to both of the assessedtime-points.

Discussion

The effectiveness of vascular grafts based on

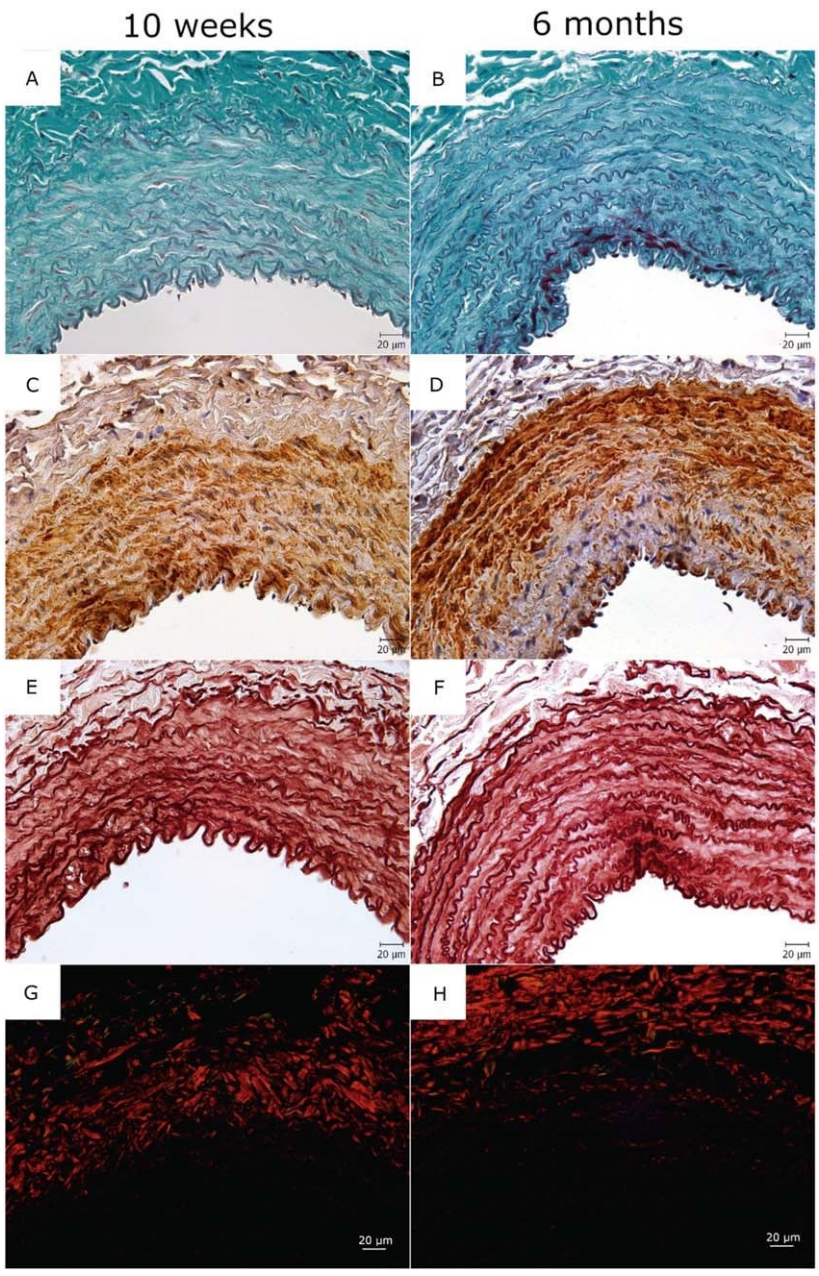

Figure7. Morphologyofthewallofthenative carotidarterytenweeks (1stcolumn) andsixmonths (2ndcolumn) following the procedure. Thetunicamediaconsisted principallyofrepeatingelasticunitsasdemonstrated byVerhoeff 'shematoxylinandgreen trichrome (A), (B),orceinstainshowingtheelasticmembranes (C), (D) andvascularsmoothmusclecellspositiveforalphaSM-actin (E), (F).MostofthetypeIcollagenwasfoundintheadventitiaasdemonstrated bypicrosiriusredphotographedunderpolarized light (G), (H);scalebars20 µm.

electrospun biodegradable polyester were investigated due to theneedforsuch'off-the-shelf'materials inthefieldof cardio surgery. Our previous studies concentrated primarily on the development and characterization of polycaprolactone-based vascular prostheses [33, 34]. Due to the excellent elastic properties of the PLCL copolymer as reported by Johnson et al [6] and Horakova et al [35], this material is proving to be of particular interest with respect to the fabrication of vascular grafts. Moreover, cell culture experiments suggest that PLCL is preferred to PCL by fibroblasts and the endothelial cell line (see figures 5, 6). It is possible to explain this outcome by the increased surface wettability of the PLCL copolymer compared to that of the PCL. Polycaprolactone is a hydrophobic polymer with a water contact angle of around 130° [15] while polylactide is more hydrophilic due to its shorter side chain. The water contact angle of electrospun polylactide has been reported at around 100° [36]. It is supposed that the PLCL copolymer containing 70% of polylactide units is more hydrophilic than pure polycaprolactone, thus rendering it more beneficial in terms of cell adhesion. It is known that slightly hydrophilic surfaces are preferred by most cell types. Even though both materials are, nevertheless, considered hydrophobic, it is proposed that the decreased hydrophobicity of the PLCL copolymer may well enhance cell material interactions. Vascular grafts werefabricatedbymeansoftheneedleelectrospinning of the PLCL copolymer for implantation in rabbits in the form of a carotid artery bypass. Prior to implantation, the materials were sterilized using ethylene oxide, the effects of which on electrospun PLCL has been reported in our previous study [35]. While other studies have also considered the PLCL copolymer, a comparison with these studies was deemed inappropriate since differing ratios of L-lactide and ε-caprolactone were applied. Whereas, for example, Tara et al [3] and Wu et al [4] applied a ratio of 50/50 and Laurent et al [37] employed a ratio of 85/15, our study was based on the utilization of the medical grade GMP copolymer with a ratio of 70/30. The composition and organization of monomer units exert a huge impact on the overall behavior of the polymer. A recent study by Pisani et al considered a polymer with the same composition, i.e. 70/30, the aim being to develop a material for use in the healing of esophageal defects. Different solvents were employed for electrospinning (methylene chloride and N,N-dimethylformamide) to those used in our study and higher concentrations of the polymer were added to the electrospinning solution (15%–25%) [38]; both of these parameters are capable of influencing the behaviorofthefinalmaterial.

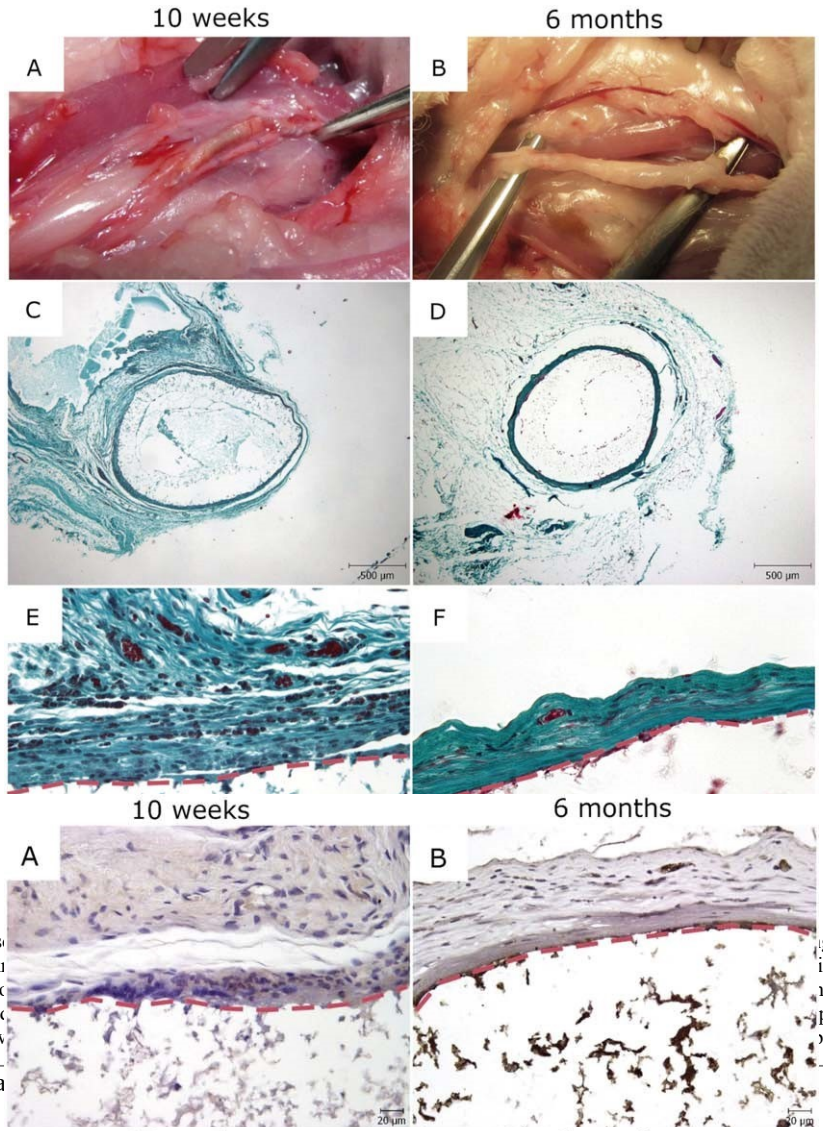

Figure8. Macros g ten weeks (A) andsix inedwith Verhoeff'shemat elumenand theadluminalbor partially remodeled bynew onents.

It is essentia

characterization be conducted. The gold standard consists of the evaluation of the fiber diameter and pore size solely by means of SEM, which does not in fact fully correspond with reality since the consideration of the 3D structure is not included when applying this method of analysis (compare figures 2 and 3). Modern techniques such as micro-CT enable 2D and 3D visualization accompanied by the structure analysis with the advantages of non-destructivity, whole specimen evaluation, direct 3D analysis, increased time efficacy, the reduction of subjectivity and the potential for combination and comparison with standard destructive (section-based) analysis methods [11, 39–41]. However, micro-CT also presents a number of significant drawbacks, i.e. the spatial resolution is lower than that of SEM, thin structures are influenced by the partial volume effect which decreases the x-ray density thereof in reconstructed images, and micro-CT images are negatively influenced by computed tomography artifacts and image noise [42]. While the binarization process in such structures most likely influences the results, the extent of such bias is not yet known. Hence, our group developed software for virtual 3D object generation [43] aimed at enhancing the calibration of micro-CT analysis. 3D analysis is based on the sphere-fitting algorithm [9, 10], which provides a powerful tool with respect to structure characterization. In the case of more complex structures (e.g. a combination of fibers below and above micro-CT spatial resolution), it is important that we consider the above drawbacks, which may lead to the determination of significant differences between micro-CT and SEM values due to some parts of the structure not being detected via micro-CT analysis. A recent study by Bartos et al analyzed the limitations of micro-CT compared to SEM with respect to the pore size analysis of collagen-based composite scaffolds. Their results revealed significant differences regarding pore size evaluation between these two approaches, with micro-CT being considered the most beneficial overall approach [44]. Nevertheless, while this drawback applies to the planar specimens used in this study due to their smaller fiber diameters and the wide distribution of the fiber diameters (1.35±0.57 μm in the case of electrospun PLCL and 0.49±0.95 μm in that of electrospun PCL), it does not apply to the tubular specimens, concerning which conformity between the SEM image analysis and micro-CT analysis was determined (a fiber diameter of 5.40±2.09 μm as measured by SEM compared to 5.58±0.10 μm as measuredbymicro-CT).

The data obtained by means of micro-CT revealed that the grafts exhibited a porosity of around 70% with pore sizes of around 9.3 μm and a fiber diameter of 5.6 μm. These parameters are of prime importance in terms of the further cell infiltration of the prosthesis following implantation. A number of studies have been devoted to determining the optimal pore size for the regeneration of the vessel wall. Wang et al used electrospun PCL in their study in order to create small-pore tubular grafts with a pore size of 4.66±1.63 μm (porosity of 66%) and a fiber diameter of 0.69±0.54 μm, and large pore grafts with a pore size of 40.88±13.67 μm (porosity of 83%) and a fiber diameter of 5.59±0.67 μm. They concluded that large pores supported the regeneration of the tissue towards M2 macrophages responsible for cellular infiltration and vascularization [16]. De Valence et al also described the need for appropriate pore sizes within vascular grafts. Their study involved the covering of a high porosity graft prepared via the electrospinning of PCL from either the luminal or adventitial side with a low porosity layer of the same polymer. The high porosity layer had a fiber diameter of 2.21±1.40 μm and a pore

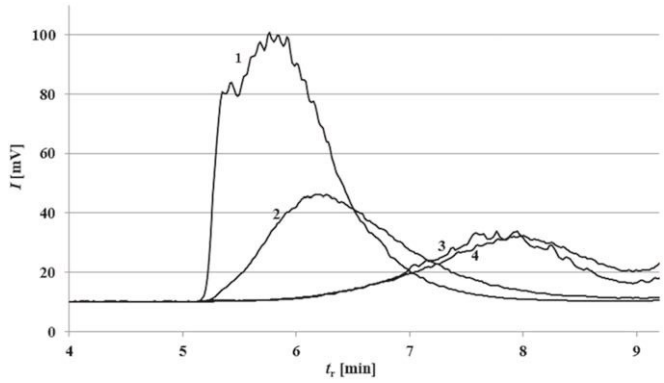

Figure11. GPCchromatogramsofthePLCLcopolymer: polymericgranulate (1),electrospunvasculargraft (2),vasculargraftafter tenweeks invivo (3) andaftersixmonths invivo (4).

size of 9.1±2.2 µm (porosityof81%) whereasthelow porositylayerhadafiber diameter of 0.83±0.56 µm and a pore size of 3.3±1.7 µm (porosity of around 63%). The aim of the study was to create a structure that would allow for cell infiltration through large pores and the prevention of blood leakage that may occur through highly porous materials. They concluded that an inner layer composed of low porosity fibers reduced blood leakage and did not impede cell infiltration from the adventitialsideofthegraft[45].

The histological part of the explanted graft analysis was characterized by severe limitations which prevented us from quantifying the histological findings. The routine processing and staining of the paraffinprocessed sections produced a large number of sectioning and staining artifacts, a loss in integrity due to the presence of partially dissolved graft components and unspecific and biased staining results. Thus, an alternative approach is recommended using frozen sections which avoids the use of paraffin embedding and alcohol solvents when processing samples which include a significant proportion of PLCL fibers. However, it was possible to assess the tissue reaction of the grafts according to our previous studies of the vascular wall [31, 46, 47]. A further limitation consists of the factthatthe measurementofthewallthicknessandthe diameter of the native carotid artery were affected by tissue shrinkage which occurred during the histological processing of the paraffin-embedded sections. According to data published by Matsumoto et al, the diameter of the carotid artery in vivo should be approximately 1.35 times greater [48], i.e. the native carotid arteries investigated in this study exhibited an inner diameter of 1140–1360 µm after ten weeks compared to 1540–1840 µm in reality and 1270–1510 µm after six months compared to 1720–2040 µm. Thus, the inner diameters of the implanted electrospun grafts (1400 µm) were even smaller than that of the native carotid arteries. The properties required of the final prosthesis were discussed with cardio surgeons and, based on their suggestions, grafts were produced with an inner diameter of 2 mm (1.4 mm following the shrinkage of the material) and wall thickness of 100 µm. With respect to our study, the walls of the implanted grafts were not thick enough to comply with the regeneration rate. Ideally, the thickness should match native carotid artery values, i.e. between 200 and 300 µm. With respect to biodegradable materials, since the degradationratemustbeconsidered,itisreasonabletoassume that an even greater wall thickness is necessary so as to ensure the regeneration of the vessel wall over the long term. That said, even though the materials were significantly thinner (wall thickness of 100 µm), the material remained mechanically stable up to ten weeks in vivo. With concern to the later time-point of six months, therefore, it can be assumed that a thicker structure would ensure the maintaining of the appropriate mechanical properties, thus leading to the requiredfunctioningofthematerial.

The grafts considered in our study had become fully penetrated by cells ten weeks and six months following implantation, which suggests that the pore size and porosity were appropriate (as depicted in figures 8, 9). After six months, endothelial cells were found to cover the luminal side of the graft and smooth muscle cells had assembled into layers as in normal vessels (see figures 9(B), (D)). The infiltrated cells had created their own extracellular matrix composed of collagen without the presence of elastin, an outcome that could be explained by the mechanical properties of the graft. The PLCL copolymer exhibits high degrees of elongation at break (around 500% of its initial length as measured for an inner diameter of 4 mm and a wall thickness of 200 µm as reported in

[35]), compliance (8%/mm Hg) and burst pressure (2.5 MPa measured in an electrospun graft with a 6 mm inner diameter and a vessel wall thickness of 650 μm [6]). However, the elastic properties are usually converse to the mechanical strength of the material; thus, the production and deposition of collagenwaspreferred tothatofelastin.

With respect to our study, complications were observed in terms of thrombogenicity and rapid degradation accompanied by the loss of the mechanical properties. After ten weeks in vivo, four of the five implanted grafts were found to be patent and in one case an organized thrombus was observed (figures 10(A), (C)). The interaction with blood was assessedinourpreviousstudy,which revealedthe high thrombogenicity of electrospun biodegradable polymers to an extent comparable to collagen materials [49]. The further anti-thrombogenic modification of the electrospun grafts will therefore be necessary, especiallywithconcerntosmalldiameterprostheses.

After six months in vivo, two of the five examined prostheses exhibited prolapsed vascular walls (figures 10(B), (D)), which is associated with weakened mechanicalproperties. Over the long-term healingperiod of six months, the vascular grafts lost their mechanical strength due to the rapid degradation process in vivo as measured via GPC (figure 11). A decrease in molecular weight was observed as soon as after ten weeksdespitetherebeingnovisiblesignsthereofduring either explantation or the histological examination. However, evidence of weak mechanical properties was apparent after the longer six month period at which time four of the five grafts were found to have broken. This development may have been caused either by the explantationtechniqueordirectlyinvivoduetoalossof mechanicalsupport.Suchdegradationhasbeenstudied previously by, for example, Horakova et al with respect to a simulated enzyme environment [35]. A study by Pisani et al addressed the degradation of electrospun PLCL in PBS (pH 7.4) and under conditions simulating inflammation with a lower pH of 6.0. They discovered that after 28 days the material had lost 0.5%–2% of its initial weight in PBS and 0.9%–4% in the pH 6.0

environment [38]. However, all these experiments consisted of the simulation of real conditions and their value lay inthe comparisonofdifferent materialswith a view to the prediction of the degradation rate; a real assessment,however,canonlybeprovided byan invivo study. Degradation is dependent on the material properties. It is known that polyesters undergo hydrolysis that may be facilitated by certain enzymes. As a statistical copolymer, PLCL makes up one of the amorphous polymer group that degrades more rapidly than semicrystalline polymers. Water penetrates more quickly into amorphous regions accompanied by surface erosionthatalterstheмorphologyofthefibers[35].More over, other structural properties such as fiber diameter and the mass of the material present influence degradation. In addition, the biological variability of animal specimens, particularly the availability of enzymes presented within the implanted scaffold, exert a huge impact on the degradation rate. Our study demonstrated that the degradation of the PLCL statistical amorphous copolymer led to a decrease in the molecular weight in the first ten weeks following implantationthatremaineduptothesixmonthtime-point.

Conclusion

Vascular grafts were successfully fabricated via the needle electrospinning of the PLCL copolymer resulting in tubular structures with adequate morphological properties which facilitated the regeneration of the vessel wall in vivo. From the histological point of view, the grafts appeared to be well tolerated and no adverse tissue reaction was determined. After six months in vivo, the lumen of the vascular graft had been endothelialized and the vascular wall comprised arranged smooth muscle cells that produced collagen fibers. However, complications in the form of thrombosis and a rapid degradation rate were observed and discussed in the study with a view to the further developmentofsmalldiameterbypassgrafts.

Acknowledgments

The study was supported by the 'Nanofiber Materials for Tissue Engineering' project, reg. no. CZ.1.05/3.1.00/14.0308 co-financed by the European Social Fund and the state budget of the Czech Republic. The authors are particularly grateful to Dr Ondrej Novak and Josef Vosahlo for the construction of the spinning device.

TK and ZT were supported by the National Sustainability Program I (NPU I) no. LO1503 of the Ministry of Education, Youth and Sports of the Czech Republic and the Progress Q39 project of the Charles University.

MB was supported by the Ministry of Education, Youth and Sports (Progress Q29/LF1), the Charles University (First Faculty GAUK 5070/2018), the Ministry of Health of the Czech Republic (NV 1525813A) and the 'Technological development of postdoc programs' project (reg. no. CZ.1.05/41.00/16.0346) supported by the Research and Development for Innovations Operational Program (RDIOP), cofinanced by European regional development funds andthestatebudgetoftheCzechRepublic.

ORCIDiDs

JanaHorakova https://orcid.org/0000-0003-2926-0570
PetrMikes https://orcid.org/0000-0003-2470-6430
ZbynekTonar https://orcid.org/0000-0002-7200-9894

References

[1] deValenceS,TilleJC,MugnaiD,MrowczynskiW,GurnyR, MöllerMandWalpothBH2012Longtermperformanceof polycaprolactonevasculargraftsinaratabdominalaorta replacementmodelBiomaterials3338–47

[2] ShinYM,LeeYB,KimSJ,KangJK,ParkJC,JangWand ShinH2012Mussel-inspired immobilizationofvascular endothelialgrowthfactor(VEGF)forenhanced endothelializationofvasculargraftsBiomacromolecules.13 2020–8

[3] TaraS, KurobeH,RoccoKA,MaxfieldMW,BestCA,YiT, BreuerCKandShinokaT2014Well-organizedneointimaof large-porepoly(L-lactic acid)vasculargraftcoatedwithpoly (L-lactic-co-ε-caprolactone)preventscalcificdeposition comparedtosmall-pore electrospunpoly(L-lactic acid)graftin amouseaorticimplantationmodelAtherosclerosis 237 684–91

[4] WuT,JiangB,WangY,YinA,HuangC,WangSandMoX 2015Electrospunpoly(L-lactide-co-ε-caprolactone)-collagenchitosanvasculargraftinacaninefemoralarterymodel J.Mater.Chem.B285760–8

[5] EnisYI,SezginHandGok SadikogluT2018Fullfactorial experimentaldesignformechanicalpropertiesofelectrospun vasculargraftsJ.Ind.Textiles471378–91

[6] JohnsonJ,OhstD,GroehlT,Hetterscheidt SandJonesM2015 Developmentofnovel,bioresorbable, small-diameter electrospunvasculargraftsJ.TissueSci.Eng.6151

[7] LimbertG,OmarR,KrynauwH,BezuidenhutDandFranzT 2016Theanisotropicmechanicalbehaviourofelectro-spun

biodegradablepolymerscaffolds:experimental characterisationandconstitutive formulationJ.Mech.Behav. Biomed.Mater.5321–39

[8] XieY,GuanY,KimSHandKingMW2016Themechanical performanceofweft-knitted/electrospunbilayersmall diametervascularprosthesesJ.Mech.Behav.Biomed.Mater. 61 410–8

[9] HildebrandTandRuegsegger P1997Anewmethodforthe modelindependentassessmentofthicknessinthree dimensionalimagesJ.Microsc.18567–75

[10] RemyEandThielE2002Medialaxisforchamferdistances: computinglook-up tablesandneighbourhoodsin2Dor3D PatternRecognit.Lett.23649–61

[11] StockS2008MicroComputedTomography:Methodologyand Applications(BocaRaton,FL:CRCPress)

[12] SchladitzK2011Quantitativemicro-CTJ.Microsc.243111–7

[13] BrukermicroCT1–49Brukermicro-CT, Morphometric parametersmeasuredbySkyscan CT-analysersoftwarehttp://bruker-microct.com/next/CTAn03.pdf

[14] LiWetal2018Long-termevaluationofvasculargraftswith circumferentiallyalignedmicrofibersinaratabdominalaorta replacementmodelJ.Appl.Biomed. Mater.Res.B (https://doi. generelatedpeptide concentrationinratswitharterial org/10.1002/jbm.b.34076) hypertensionActaVet.Brno78595–602

[15] deValenceS,TilleJC,ChaabaneC,GurnyR, [33] YalcinI,HorakovaJ,MikesP,Gok SadikogluT,DominRand Bochaton-PiallatML,WalpothBHandMollerM2013 LukasD2016Designofpolycaprolactone vasculargraftsJ.Ind. Plasmatreatmentforimproving cellbiocompatibilityofa Textiles45813–33 biodegradablepolymerscaffoldforvasculargraft applications [34] EnisYI,HorakovaJ,GokSadikogluT,NovakOandLukasD2017 Eur.J.Pharm.Biopharm. 8578–86 Mechanicalinvestigationofbilayervasculargraftselectrospun

[16] WangZetal2014Theeffectofthickfibersandlargeporesof fromaliphaticpolyestersPolym.Adv.Technol.8201–13 electrospunpoly(ε-caprolactone)vasculargraftson [35] HorakovaJ,MikesP,SamanA,JencovaV,KlapstovaA, macrophagepolarizationandarterialregeneration SvarcovaT,AckermannM,NovotnyV,SuchyTandLukasD Biomaterials355700–10 2018Theeffectofethylene oxidesterilizationonelectrospun

[17] PanYetal2017Small-diameterhybridvasculargrafts vasculargraftsmadefrombiodegradablepolyesters Mater.Sci. composedofpolycaprolactone andpolydioxanonefibersSci. Eng.C92132–42 Rep.73615 [36] LiuY,LiangX,ZangR,LanWandQinW2017Fabrication of

[18] PektokE,NoteletB,TilleJC,GurnyR,KalangosA, electrospunpolylacticacid/cinnamaldehyde/β-cyclodextrin MoellerMandWalpothBH2008Degradation andhealing fibersasanantimicrobialwounddressingPolymers9464 characteristicsofsmall-diameterpoly(epsilon-caprolactone) [37] LaurentCP,VaquetteC,LiuX,SchmittJFandRahouadjR vasculargraftsintheratsystemicarterialcirculation 2018SuitabilityofaPLCLfibrousscaffoldforsofttissue Circulation. 1182563–70 engineeringapplications:acombinedbiologicaland

[19] YangX,WeiJ,LeiD,LiuYandWuW2016Appropriate mechanicalcharacterization J.Biomater.Appl.321276–88 densityofPCLnano-fibersheathpromotedmuscular [38] PisaniS,DoratiR,ContiB,ModenaT,BruniGandGentaI remodelingofPGS/PCLgraftsinarterialcirculation 2018Designofcopolymer PLA-PCLelectrospunmatrixfor Biomaterials8834–47 biomedicalapplicationsReactive Funct.Polym.12477–89

[20] WangKetal2017Functionalmodification ofelectrospunpoly [39] LandisENandKeaneDT2010X-raymicrotomography (ε-caprolactone)vasculargraftswiththefusionproteinVEGF Mater.Charact.611305–16 −HGFIenhanced vascularregeneration ACSAppl.Mater. [40] BartosM,SuchyT,TonarZ,FoltánRandHubalekKalbacovaM Interfaces911415–27 2018Micro-CTintissueengineeringscaffoldsdesignedforbone

[21] ZhengWetal2012Endothelializationandpatency ofRGD- regeneration:principlesandapplicationCERAM.,Silik.62 functionalizedvasculargraftsinarabbitcarotidarterymodel 194–9 Biomaterials332880–91 [41] SuchyT,SupovaM,BartosM,SedlacekR,PiolaM,SonciniM,

[22] WangKetal2016Three-layeredPCLgraftspromotedvascular FioreGB,SauerovaPandHubalekKalbacovaM2018Dry regenerationinaRabbitCarotidArterymodelMacromol. versushydrated collagenscaffolds:aredrystatesrepresentative Biosci.16608–18 ofhydratedstates?J.Mater.Sci.,Mater.Med.291–14

[23] TillmanBW,Yazdani SK,LeeSJ,GearyRL,AtalaAand [42] BoasFEandFleischmannD2012CTartifacts:causesand YooJJ2009Theinvivostabilityofelectrospun reductiontechniquesImagingMed.4v229–40 polycaprolactone-collagen scaffoldsinvascularreconstruction [43] JirikMetal2018Generating standardizedimagedatafor Biomaterials30583–8 testingandcalibratingquantificationofvolumes,surfaces,

[24] MrówczyńskiW,MugnaiD,deValenceS,TilleJC,KhabiriE, lengths,andobjectcountsinfibrousandporousmaterials CikirikciogluM,MöllerMandWalpothBH2014Porcine usingx-raymicrotomography Microsc.Res.Tech.81551–68 carotidarteryreplacementwithbiodegradableelectrospun [44] BartosM,SuchyTandFoltanR2018Noteoftheuseof poly-e-caprolactone vascularprosthesisJ.Vascular Surg.59 differentapproachestodetermine thepore sizesoftissue 210–9 engineeringscaffolds:whatdowemeasure?Biomed.Eng.

[25] JirikM2017Teigen—TEstImageGENeratorsoftware Online17110 https://mjirik.github.io/teigen/ [45] deValenceS,TilleJC,GilibertoJP,MrowczynskiW,GurnyR, [26] BancroftJDandStevensA1996TheoryandPracticeof WalpothBHandMollerM2012Advantagesofbilayered HistologicalTechniques (NewYork:ChurchillLivingstone) vasculargraftsforsurgicalapplicabilityandtissueregeneration

[27] JunqueiraLC,BignolasGandBrentaniRR1979Picrosirius ActaBiomater.83914–20 stainingpluspolarizationmicroscopy,aspecificmethodfor [46] TonarZ,TomasekP,LoskotP,JanacekJ,KralickovaMand collagendetectionintissuesectionsHistochem.J.11447–55 WitterK2016Vasavasoruminthetunicamediaandtunica

[28] JunqueiraLC,MontesGSandSanchezEM1982The adventitiaoftheporcineaortaAnn.Anat.20522–36 influenceoftissuesectionthicknessonthestudy ofcollagenby [47] TonarZ,KubikovaT,PriorC,DemjenE,LiskaV, thePicrosirius-polarizationmethodHistochemistry. 74153–6 KralickovaMandWitterK2015Segmantalandagedifferences

[29] KocovaJ1970Overallstainingofconnectivetissueandthe intheelastinnetwork, collagen,andsmoothmusclephenotype muscularlayerofvesselsFoliaMorphologica18293–5 inthetunicamediaoftheporcineaortaAnn.Anat. 20179–90

[30] RichLandWhittakerP2005Collagenandpicrosiriusred [48] MatsumotoT,OkumuraE,MiuraYandSatoM1999 staining:apolarized lightassessmentoffibrillarhueandspatial Mechanicalanddimensionaladaptationofrabbitcarotid distributionBraz.J.Morphol.Sci.2297–104 arteryculturedinvitroMed.Biol.Eng.Comput.37252–6

[31] WitterK,TonarZandSchopperH2017Howmanylayershas [49] HorakovaJ,MikesP,SamanA,SvarcovaT,JencovaV, theadventitia?Structure oftheartterialtunicaexternarevisited SuchyT,HeczkovaB,JakubkovaS,JirousovaJand Anat.Histol.Embryol. 46110–20 ProchazkovaR2018Comprehensiveassessmentof

[32] KochovaP,TonarZ,MatejkaVM,Svigelova J,StenglMand electrospunscaffoldshemocompatibility Mater.Sci.Eng.C82 KuncovaJ2009Aortaremodelilingassociatedwithcalcitaonin 330–5

Received: 15 November 2017 | Revised: 22 January 2018 | Accepted: 12 February 2018

DOI: 10.1002/jemt.23011

RESEARCH ARTICLE

WILEY MICROSCOPY RESEARCH & TECHNIQUE

Generating standardized image data for testing and calibrating quantification of volumes, surfaces, lengths, and object counts in fibrous and porous materials using X-ray microtomography

Miroslav Jiřík[1]* | Martin Bartos[2]* | Petr Tomasek[3] | Anna Malečkova[1,3] | Tomas Kural[3] | Jana Horakova[4] | David Lukas[4] | Tomas Suchy[5] | Petra Kochova[6] | Marie Hubalek Kalbačova[1,7] | Milena Králíčkova[1,3] | Zbynek Tonar [1,3]

[1]Biomedical Center, Faculty of Medicine in Pilsen, Charles University, Pilsen, 323 00, Czech Republic

[2]Institute of Dental Medicine, First Faculty of Medicine, Charles University and General University Hospital in Prague, Prague 2, 128 01, Czech Republic

[3]Department of Histology and Embryology, Faculty of Medicine in Pilsen, Charles University in Prague, Pilsen, 301 66, Czech Republic

[4]Faculty of Textile Engineering, Technical University of Liberec, Liberec 1, 461 17, Czech Republic

[5]Department of Composites and Carbon Materials, Institute of Rock Structure and Mechanics, Academy of Sciences of the Czech Republic, Prague 8, Czech Republic

[6]European Centre of Excellence NTIS, Faculty of Applied Sciences, University of West Bohemia, Univerzitní 22, Pilsen, 306 14, Czech Republic

[7]Institute of Pathological Physiology, First Faculty of Medicine, Charles University, U nemocnice 5, 128 53 Prague, Czech Republic

Correspondence
Zbynek Tonar, Department of Histology and Embryology, Faculty of Medicine in Pilsen, Charles University, Karlovarska 48, 301 66 Pilsen, Czech Republic.
Email: zbynek.tonar@lfp.cuni.cz

Funding information
National Sustainability Program I (NPU I) Nr. LO1503 provided by the Ministry of Education, Youth and Sports of the Czech Republic, by the Progres Q39 and Progres Q29/LF1 (MB) projects of the Charles University, Grant/Award Numbers: SVV 260390/2017 and SVV 260392/2017 and UNCE/MED/006 projects of the Charles University. PK was supported by project LO1506 of the Czech Ministry of Education, Youth and Sports under program NPU I. ZT was also supported by the Ministry of Education, Youth and Sports under the project, Grant/Award Number: CZ.02.1.01/0.0/0.0/16_019/0000787. Technological development of post doc programs, Grant/ Award Number: CZ.1.05/41.00/16.0346, Research and Development for Innovations Operational Programme (RDIOP)

Review Editor: Prof. George Perry

*The first two authors contributed equally to the manuscript.

Abstract

Quantification of the structure and composition of biomaterials using micro-CT requires image segmentation due to the low contrast and overlapping radioopacity of biological materials. The amount of bias introduced by segmentation procedures is generally unknown. We aim to develop software that generates three-dimensional models of fibrous and porous structures with known volumes, surfaces, lengths, and object counts in fibrous materials and to provide a software tool that calibrates quantitative micro-CT assessments. Virtual image stacks were generated using the newly developed software TeIGen, enabling the simulation of micro-CT scans of unconnected tubes, connected tubes, and porosities. A realistic noise generator was incorporated. Forty image stacks were evaluated using micro-CT, and the error between the true known and estimated data was quantified. Starting with geometric primitives, the error of the numerical estimation of surfaces and volumes was eliminated, thereby enabling the quantification of volumes and surfaces of colliding objects. Analysis of the sensitivity of the thresholding upon parameters of generated testing image sets revealed the effects of decreasing resolution and increasing noise on the accuracy of the micro-CT quantification. The size of the error increased with decreasing resolution when the voxel size exceeded 1/10 of the typical object size, which simulated the effect of the smallest details that could still be reliably quantified. Open-source software for calibrating quantitative micro-CT assessments by producing and saving virtually generated image data sets with known morphometric data was made freely available to researchers involved in morphometry of three-dimensional fibrillar and porous structures in micro-CT scans.

Microsc Res Tech. 2018;81:551–568. wileyonlinelibrary.com/journal/jemt

KEYWORDS
fibers, Python, pores, scaffolds, spatial statistics, stereology, textile

1 | INTRODUCTION

1.1 | Assessment of the three-dimensional structure of fibrous and porous biomaterials using micro-CT: Present state and methodological problems

High-resolution quantitative X-ray microtomography (micro-CT) has become a method of choice for three-dimensional and quantitative (Schladitz, 2011) characterization of tissue-engineered scaffolds (Ho & Hutmacher, 2006) used, e.g., to support the healing of organs.

Newly manufactured biomaterials, such as electrospun nanofibrous scaffolds (Szentivanyi, Chakradeo, Zernetsch, & Glasmacher, 2011; Zhong, Zhang, & Lim, 2012) or fiber-polymer composite foams (Shen, Nutt, & Hull, 2004) undergo morphometric assessments before being used in vitro or in vivo. A good correlation between micro-CT and histology was found in bone research (Particelli et al., 2012). Software supplied by manufacturers of micro-CT facilities supports a plethora of morphometric parameters characterizing volume fractions, outer and inner surfaces (Pyka, Kerckhofs, Schrooten, & Wevers, 2014), porosities in bone and dental research (De Souza et al., 2013; Draenert et al., 2012; Karageorgiou & Kaplan, 2005; Tonar, Khadang, Fiala, Nedorost, & Kochova, 2011), pore size and distribution in bone scaffolds (Montufar, Vojtova, Celko, & Ginebra, 2017) and synthetic bone model foams (Gomez, Vlad, L opez, Navarro, & Fern andez, 2013) and the topology of multiple phases of tissue scaffolds in user-defined regions of interest (ROIs). The three-dimensional and quantitative nature of the micro-CT makes it a tool of choice for estimating shrinkage of materials (Burey et al., 2018) and propagation of material fractures and cavitation (Neves, Coutinho, Alves, & de Assis, 2015). Some of the estimates are based on or fully compatible with stereological principles and spatial statistics (Baddeley & Jensen, 2004; Mouton, 2002; Stoyan, Kendall, & Mecke, 1995) and may be assessed automatically, provided the image data have a sufficient contrast (Jirík et al., 2016; Mouton et al., 2017). However, surfaces are especially potentially sensitive to the settings of the micro-CT scanning and further image postprocessing, such as resolution, noise, preferential spatial arrangement (anisotropy), filtration, and thresholding during binarization of grayscale images. The amount of potential bias introduced by these variables is generally unknown. The sensitivity of

micro-CT to steps performed during thresholding might become an issue, especially in biomaterials combining multiple phases with similar or overlapping radiological opacity, such as partially mineralized collagen scaffolds combined with other substances, such as glycosaminoglycans. To the best of our knowledge, there are currently no published guidelines or fixed routines for thresholding biological samples, which is understandable due to the growing number of newly manufactured biomaterials and rapidly developing methodology of micro-CT. However, the entire measurement is as weak as its weakest link. Moreover, a precise knowledge of the morphometry of tissueengineered materials would be necessary to test the consistency of their production and biodegradation once implanted. The motivation of the work presented in this article is the absence of a freely accessible and reliable source of calibration tools for use as realistic phantoms that simulate the micro-CT image stacks. As far as we know, the manufacturers of micro-CT facilities do not provide users with such software, which could be used by micro-CT operators to (i) calculate the bias and error during the processing of micro-CT scanned stacks using phantom image series with known volumes, surfaces, lengths, and numbers of objects and (ii) demonstrate the impact of changes to the thresholding routines on the results of quantitative micro-CT.

1.2 | Preprocessing and segmentation of micro-CT images of biomaterials

Before quantification of the structure and composition of biomaterials, the micro-CT images undergo segmentation. This is not a straightforward and routinely standardized procedure due to the low contrast and overlapping radiooopacity of biological materials. Although sophisticated approaches are now available for noise suppression or removal (Maia et al., 2015; Rau, Wurfel, Lenarz, & Majdani, 2013), in micro-CT, the€ noise might overlap with the smallest nanofibers and microfibers of the tissue scaffolds. Currently used micro-CT devices (in our study, Bruker micro-CT, Belgium) are usually provided with a software package that is applicable for acquisition of projection images, their reconstruction into cross-section images, visualization of datasets (both in 2D and 3D), resizing, and production of a region or volume of interest (ROI, VOI), and finally, imageameters are commonly available (e.g., Bruker). Currently, employment of operations for image processing is usually very convenient and user-friendly since the typical micro-CT user is neither an information-technology scientist nor a biomathematician. This has to be considered along with subjectivity in the assessment of many procedural parameters in image processing and binarization because exact evaluation of these processes and their calibration is not achievable to date. Manuals and detailed descriptions of both two-dimensional parameters (evaluation of each separate cross-section image in a dataset) and three-dimensional analysis (evaluation of the entire dataset) require image binarization (i.e., conversion of a grayscale image into a black and white image, where white pixels represent objects and black pixels represent the background), e.g., (Burghardt et al., 2007; Zhang, Yan, Chui, & Ong, 2010). This step is crucial, with substantial effect on image analysis results; its sensitivity is dependent on object properties (e.g., size, shape, density, and connections) that we would like to examine in our study. Two basic approaches can be differentiated: subjective threshold values assessment (especially in life sciences) and automatic threshold assessment leading to higher reproducibility (in material or technical sciences) (Stock, 2009).

Influences of threshold variations were assessed in several studies mostly focused on bone micro-CT 3D morphometry (Hara, Tanck, Homminga, & Huiskes, 2002; Jones et al., 2007; Parkinson, Badiei, & Fazzalari, 2008; Yan, Qi, Qiu, Teo, & Lei, 2012). We should consider progressive development of micro-CT devices (Landis & Keane, 2010), resulting in better spatial resolution and lower noise level, thus reducing (not eliminating) the dependency of result variations on threshold values. Possibilities of image binarization in CTAn software (Bruker Corporation, 2017) are as follows: global-threshold, adaptive threshold (mean, median, mean of minimal and maximal values), and Otsu threshold (automatic and automatic multi-level) (Otsu, 1979).

Usually, the signal to noise ratio has to be enhanced. This can be performed by, e.g., using filtering procedures—sharpening or smoothing in 2D or 3D (e.g., Gaussian blur, median, uniform, Kuwahara, unsharp mask). These are usually applied in grayscale images, but binary images can be filtered as well. After binarization, despeckle operations in 2D or 3D are used to remove white "noise" pixels (e.g., remove white/black speckles less than X pixels/voxels, remove pores, sweep—remove all object except the largest one). Many other procedures are offered by CTAn, e.g., morphological operations (dilatation, erosion, opening, and closing procedures), bitwise and arithmetical operations and geometrical transformations. Demonstration of image processing prior to microCT analysis is available in, e.g., (Buie, Campbell, Klinck, MacNeil, & Boyd, 2007). Eventually, we decided to perform image processing and binarization in the simplest manner (filtering, automatic thresholding, and despeckle) to minimize the number of variable processes influencing the results and enhance the time efficacy.

To summarize the main problem of quantitative imaging of biomaterials, the combination of various steps using mathematical morphology can affect the morphometric results in an significant but unpredictable manner. A good visual representation of the thresholded structures in micro CT scans does not always guarantee accuracy and precision in a quantitative sense. A solution to this problem would be generating virtual (phantom) data mimicking the real micro-CT examination and comparing the results of the thresholding routines to the a priori known results.

1.3 | Options in calibrating quantitative micro-CT

Micro-CT analysis results in 2D and 3D structural parameters values. However, verification of these values is generally not possible or hardly achievable in complex structures. Micro-CT results are very often presented as precise values even though they may be inaccurate or biased. Phantom models available for common micro-CT users with known parameters would allow calibration of micro-CT analysis procedure and assessment of

its accuracy. To date such phantoms are lacking, since it is not possible to produce these phantoms (especially in case of complex interconnected structures and material porosity) at micrometerscale with adequate level of confidence in its structural parameters. Calibration phantoms exist for material X-ray density assessment (Bone Mineral Density based on X-ray attenuation coefficient calibration) applicable e.g., in bone biology.

Using test images for calibration is a commonly used practice in imaging techniques. One of the most known test image is the Shepp-Logan phantom (Shepp & Logan, 1974). The discrete version of this image can also be generated using the SheppLogan plugin of the public domain ImageJ software (Schneider, Rasband, & Eliceiri, 2012). Several other ImageJ plugins are available for generating test images, such as Random Ovals, Fractal Generator, and RandomJ plugins. However, these algorithms generate two-dimensional images only and do not allow for modeling different object shapes. This prevents these plugins from being suitable for calibration of threedimensional micro-CT. Spatial test objects can be generated using the freely available Gensei software (Cimrman, 2010; Tonar, Kochova, Cimrman, Witter, Janacek & Rohan, 2011). However, Gensei is limited to ellipsoids only.

1.4 | Aims of the study

The commercially available software packages supplied with most of the micro-CT facilities are notably efficient in thresholding the structures of interest, creating visual reconstructions, and quantitatively describing their geometry and composition. These software packages do provide the operator with sufficient feedback on how the final quantitative data might be affected by numerous combinations of procedures involving filtration, operations of mathematical morphology, and thresholding. Therefore, the aims of our study are as follows: To develop open-source software that generates three-dimensional models of fibrous and porous structures with known volumes, surfaces, lengths, and object counts in fibrous materials and to provide a software tool for calibrating quantitative micro-CT assessments. To identify combinations of object and image stack properties, which may easily lead to biased results using thresholding procedures of fibrous biomaterials in microCT.

To provide practical recommendations on how to avoid potential pitfalls during segmentation in quantitative X-ray microtomography of fibrous and porous biomaterials.

To help users of micro-CT understand where errors can occur, ensuring that micro-CT segmentation procedures can be proved to be valid and correct.

2 | MATERIALS AND METHODS

TABLE 1 Stereological parameters used for spatial statistics of artificially generated objects simulating biomaterials for in-vivo implantation

Parameter	Abbreviation	Unit	Definition	Possible biological interpretation in biomaterials
Volume density (fraction)	V_V	(2)	Volume of objects per Reference volume	measure of the in-vivo degradation of the total mass of a biomaterial
Surface density	S_V	(mm^{21})	Surface of objects per Reference volume	relative surface area available for the release of substances; thrombogenicity
Length density	L_V	(mm^{22})	Length of objects per Reference volume	fragmentation of fibers into shorter fragments as a measure of in-vivo material degradation
Numerical density	N_V	(mm^{23})	Number of objects per Reference volume	showing the degree of branching and connectivity of the biomaterial or its remnants after some period of in-vivo degradation

2.1 | Parameters used for spatial statistics of generated objects

The choice of the basic parameters to be quantified by our software generator was based on studies with real micro-CT (Jirík et al., 2016). This includes volume, surface, length, and number of objects, which are often expressed as relative densities calculated per ROI. The definitions, abbreviations, and possible biological interpretations in the context of biomaterials are summarized in Table 1. The simulation of biomaterials was inspired by real tissue scaffolds, namely: (i) electrospun polyesters (polycaprolactone) or polypropylene meshes used for manufacturing artificial vascular prostheses or reinforcement of scars (Horakova et al., 2018; Plencner et al., 2014) and consisting of fibers with diameters of 1–6 mm, occupying 25–70% of the volume fraction; and (ii) composite porous scaffolds (Gomez, Vlad, L opez, & Fernandez, 2016; Prosecka et al., 2015; Suchy et al., 2015) manufac- tured for healing of bone defects and consisting of collagen, polyDLlactide sub-micron fibers, and sodium hyaluronate, containing typically 70%–80% porosities.

2.2 | Generating virtual objects and image stacks: Algorithm and software development

The program was written in the Python programming language. The software runs under Linux, Windows or Mac OS operating systems. The TeIGen application is designed to generate structures ranging in shape from very elongated fibers to spheres. The output is an image stack that mimics

the data obtained using micro-CT and metadata describing the parameters of the generated 3D structure. The application can be used through a graphical user interface, noninteractively from the command line, or directly from the Python environment.

The graphical user interface is created using the pyqt module, the numpy, scipy and scikit modules are used for the calculations, 3D modeling is performed using the VTK package, and the pandas and seaborn packages are used for data processing. Loading and storing data is mediated by our io3d package, which uses SimpleITK and pydicom. 3D noise was generated by the ndnoise package created for this purpose.

The basic concept of the algorithm (Table 2) includes the definition of objects to generate, the generation of the framework of the fiber structure, the surface representation, the quantitative description, the volume representation, and finally the file storage.

The basic element used in this task is a tube. It is a cylindrical body that ends with hemispheres. The user can set parameters for object length, object radius, and parameters that affect the direction and isotropy of objects. The concept and implementation of quantitative measured isotropy was done according to Kochova, Cimrman, Janaček, Witter, and Tonar (2011). The fibrous structure is created by repeatedly inserting these objects into the sample area and can be affected by allowing the overlay of the objects. The collision detection algorithm is based on minimum distance computation, and it is preprocessed by a bounding box collision detection algorithm (Jimenez, Thomas, & Torras, 2001; Moore & Wilhelms, 1988). This process ends when the object number, volume density, or maximum number of iterations defined by the user is reached.

To determine the geometrical properties of the generated objects, a triangulated model of the surface of each tube is created using the VTK package (Schroeder, Avila, & Hoffman, 2000; Schroeder, Martin, & Lorensen, 1998). The measurement_resolution parameter affects the number of triangulation points and hence the accuracy of the measurement and the computation time. By using the vtkBooleanOperation PolyDataFilter function, a connection of two objects is made in the case of a contact. The vtkMassProperties functions are used to determine the numeric volume and numeric body surface.

The intensities of the volume representation are controlled by the background_intensity parameters and the intensity_profile function, which defines the intensity depending on the relative distance from the center of the tube to its edge. The volume representation process begins by creating a 3D array with a homogeneous intensity corresponding to the selected background intensity. Tube-shaped objects are placed in this array in the first iteration. The radius and intensity of an object correspond to the intensity profile (Supporting Information S4A) with the highest relative radius. The second iteration places the same objects with different radius and intensity that correspond to the second largest relative radius of the intensity profile. The entire process is repeated until all the intensity profile values are used. Then, intensity filtering by a Gaussian filter with user-defined parameters is performed.

The next step is to add noise. For this purpose, the ndnoise module was created. The noise parameters are the minimum and maximum noise wavelengths in millimeters and the exponent that controls the ratio of the individual components to the wavelength.

Volumetric data are stored using the imtools package. Data can be stored in a single DICOM or RAW file or as a file series in JPG, PNG, TIFF, DICOM, etc. format. Together with volumetric data, the surface model in VTK and metadata are stored. Metadata contain information about the configuration and quantitative data for all object segments. They are exported in the open and human-readable YAML format or as CSV files. These are either readable by spreadsheet applications or processed by data scripts.

TABLE 2 Outline of the steps of the algorithm of the TeIGen software

Input: Parameters defined by the user
1. Type of the generator: Objects or Porosities (Figure 2 and Supporting Information S4)
2. Definition of the objects to be generated 2.1. Properties of objects 2.1.1 Separate objects or Intersecting objects 2.1.2 Number of objects and volume fraction 2.1.3 Distribution of radii and lengths of cylinders and spheres 2.1.4 Isotropy of the objects 2.1.5 Intensity profiles of the objects on virtual micro-CT sections 2.2. Properties of generated virtual micro-CT stacks 2.2.1 Resolution and size in three dimensions (X3 Y3Z) 2.2.2 Gaussian blur of the objects (optional) 2.2.3 Generating noise (parametric settings, optiona) 2.2.4 Number of iterations for calculation of the numerical estimates of spatial statistics 2.2.5 Setting connected component seed (optional) 2.3 Saving all the parameters listed in steps 1.1-1.2 to a configuration file (YAML)
3. Generating the skeleton and envelopes of the objects (repeat step 2 until the desired values are reached) 3.1. Defining the empty sample area 3.2 Inserting a tube into the sample area according to the defined parameters 3.3. Quantitative analysis of the objects 3.3.1. Calculating analytical lengths, radii, volumes, surfaces 3.3.2. Numeric lengths, radii, volumes and surfaces calculation 3.3.3 Preview of the values for the user
4. Generating and saving virtual micro-CT stacks (volumetric data) (repeat step 2 until all intensity profile values are used) 4.1. Creating the initial volumetric array with the defined background intensity 4.2. Inserting tubes with intensity and radius according to the intensity profile from a high relative radius to a zero radius 4.3 Gaussian filtering 4.4. Inserting the noise 4.5. Image saving to a defined file format
Output: Three-dimensional volumetric data with a known voxel size and known values of quantitative parameters (volume fractions, surface densities, length densities, numerical densities). Export of the 3D model into VTK format. Export of the image stacks (DICOM, JPEG). Export of the morphometric results (CSV file).

The computation time depends mainly on the dimensions of the requested volumetric representation and the measurement_resolution. To process a stack from our dataset consisting of 500 3 500 3 500 voxels with a measurement_resolution of 35 and element_number using a computer with an 8x Intel(R) Core(TM) i5–2520M CPU at 2.50 GHz, 8 GB RAM, and an NVIDIA GF119M NVS 4200M graphical adapter, the computation time is approximately 4 min. The minimum and maximum time on this dataset is 1 and 34 min, respectively.

2.3 | Evaluating numerical estimates of volume and surface vs. values calculated using analytic geometry

The parameters evaluated in the objects of our measurements are the surface, volume, length of cylindrical part l and radius of the spherical surfaces and cylindrical part r. From the specified length and radius, the analytical expression of surface $S_{analytic}$ and volume $V_{analytic}$ is given by the following equations.

$$S_{analytic} = 2\pi rl + 4\pi r^2 \quad (1)$$

$$V_{analytic} = \pi r^2 l + \frac{4}{3}\pi r^3 \quad (2)$$

One of our goals is also the modeling of connected objects. Analytical expressions of surfaces and volumes of such bodies are generally difficult and often do not have a definitive solution. For this reason, we use a numerical solution to this problem, which is based on the triangulation of the tube object. The base of the cylindrical part consists of a regular polygon. The number of its sides is given by the measure_resolution parameter. The hemispheres are replaced by triangles with triangulation points located at the intersections of imaginary meridians and parallels. The triangulated tube is inscribed in the original object. Its surface and volume asymptotically approximate the analytically measured values with increasing measurement_resolution. This method of triangulation is further referred to as "inscribed."

To increase the accuracy, we perform some compensation. The radius of the regular inscribed polygon that is the base of the cylindrical model is chosen so that the body on it has the same surface (volume, respectively) as the model cylinder. The compensated surface and volume radii are not the same. The hemisphere parts are unchanged. This method of

triangulation with the compensation of the cylindrical part is referred to as "surface" and "volume." The calculation is given by the following equation, where r is the radius of the model tube, n is the measurement_resolution, r_{eqsurf} is the radius of the surface compensated polygon, and r_{eqvol} is the radius of the polygon for volume compensation:

$$r_{eqSurf} = \frac{pr}{n \sin \frac{p}{n}} \quad (3)$$

$$r_{eqVol} = \sqrt{\frac{2pr^2}{s}} \sin \frac{p}{2n} \quad (4)$$

Compensation of the spherical part is performed by experimental measurement using the equation for calculating the radius of the spherical part with knowledge of the surface or volume. r_c is the compensated factor, and r_0 is the model radius. These compensation methods are further referred to as "surface1 sphere error" and "volume1 - sphere error."

$$r_0 r_c = \frac{1}{\frac{S}{2p}} \quad (5)$$

$$r_0 r_c = \sqrt[3]{\frac{3V}{4p}} \quad (6)$$

Similarly, experimental measurements were made to estimate the compensation factor for the error compensation from the connection of the cylindrical and spherical parts. This is referred to as "volume 1 sphere error 1 joint error" and "volume 1 sphere error 1 joint error." However, these corrections did not increase the precision of either volume or surface estimates and therefore were not included.

2.4 | Evaluating morphometric values using image processing on a micro-CT console

CTAn software (Skyscan CT analyzer (21)) was applied for image processing and subsequent 3D analysis using a "custom processing" mode. A universal procedure (a "standard" procedure) of image processing leading to acceptable and reproducible outcomes was found for datasets with the following variable parameters: count, isotropy, noise, and resolution. However, noise and resolution datasets required modification of the procedure based on the value of the variable parameter.

Standard procedure was based on filtering using Gaussian blur in 3D (with a radius of 2 voxels). Binarization was performed by an automatic Otsu threshold method to eliminate subjectivity in assessment of the threshold value. Noise reduction was achieved by a despeckle function (remove white speckles less than 12 voxels in 3D). Resolution variable datasets were filtered using Gaussian blur in 3D with reduction of the value of the radius (from 2 voxels to one voxel; for a pixel size of 80 mm and higher, this operation was not performed). Binarization was achieved by an automatic Otsu threshold method in 3D. Despeckle was performed with decreasing value of the defined volume limit for object elimination (12 voxels and less; for a pixel size of 80 mm and higher, this operation was not performed).

Image processing in datasets with a noise variable was based on Gaussian blur in 3D with a gradual increase in the radius value (from 2 to 5 voxels). The generated noise intensity was set to zero, but the standard deviation of the noise intensity gradually increased. Binarization was performed by a global threshold with an increase in the lower gray threshold value from 87 to 135 as noise was intensified. A despeckle operation was performed with an increase of the defined volume (remove white speckles less than: from 12 to 250 mm. According to preliminary results, noise reduction was preferred over object volume preservation, resulting in noise being binarized as an object.

Procedures in noise and resolution variables were modified regarding object count and subjective assessment (more in 4.1). 3D analysis of the entire dataset and 3D analysis of all individual objects in the dataset were performed in each dataset after the described image processing. The following parameters were evaluated based on analysis: object count, mean and total object length, mean and total object volume, mean and total object surface, surface density (total object surface/dataset volume), and mean object diameter. Objects and volumes are calculated via the marching cubes method (Lorensen & Harvey, 1987). Object length was defined as the furthest distance between two points within the analyzed object volume. Mean diameter was calculated as structure thickness, which is based on object medial axis computation and a subsequent sphere-fitting algorithm. Because these spheres finally have known diameters, it can be used for structure thickness evaluation (Bruker Corporation, 2017; Hildebrand & Ruegsegger, 2003; Remy & Thiel, 2002). Typical time costs for performing the despeckle operation using a computer recommended for micro-CT SkyScan1272 (Bruker) application (Intel(R) Xeon (R) CPU E5–2687W 3.1GHz (2 processors), 128 GB RAM, NVIDIA Quadro1 Tesla graphical adapter) were approximately 1–2 min (depending on number of selected parameters in analysis results).

3 | RESULTS

3.1 | Open-source software for generation of three-dimensional objects and virtual micro-CT image stacks

The source code of our software named TeIGen, which was written in the Python programming language, all of the files necessary for its launch, the calculation of the results, and the production of all graph types have been made openly available to the scientific community (Jirík, 2017). The source data and configurations for generation of the following results and all the data sets described in this article can be downloaded as Supporting Information S1–S3. The documentation can be downloaded as well (Jirík &

Tonar, 2018). The basic concept of the algorithm (Figure 1, Table 2) is to gather the required parameters of the phantom data from the user; generate, visualize and measure the data; receive approval from the user; and then save image stacks with all configuration files and quantitative results to disc. The software allows for the generation of noncolliding tubes, colliding tubes (for simulating of branching fibers and a greater volume fraction of the material), and isolated or connected (overlapping) porosities (Figure 2). Most of the application functions can be performed noninteractively using command line parameters.

3.2 | Comparing the numerical estimates of volume and surface with known true values calculated using analytic geometry

After implementing the corrections described above, there was very good agreement between the surfaces and volumes of tubes precisely calculated using analytic geometry and the measurement done by the TeIGen software (Figure 3 with source data provided as Supporting Information S1).

3.3 | Analysis of the sensitivity of surface error and volume error on the numbers of generated objects and measurement resolution

Based on these results and the computational time, the accuracy of surface and volume measurement was strongly dependent on the measurement resolution parameter and the radius compensation method. Compared to uncompensated methods (inscribed), methods using radius compensation provide improvement, especially for low values of measure_resolution. The lowest relative surface errors, expressed as 1003(true value-numerical estimate), were achieved by implementing the cylinder surface 1 sphere error corrections. When combined with increasing resolution, the surface error was gradually reduced to values below 0.1 (Figure 4a–d). The volume error was successfully minimized by using the cylinder volume compensation or cylinder volume 1 sphere error compensation (Figure 4e–h), converging to an error below 0.1 even at lower resolutions than the surface (Figure 4h vs. Figure 4d). Based on these experiments and the time costs of the computations, we recommend using the "cylinder surface" method for surface measurement. For volume measurement, we recommend the "cylinder volume 1 sphere error" method.

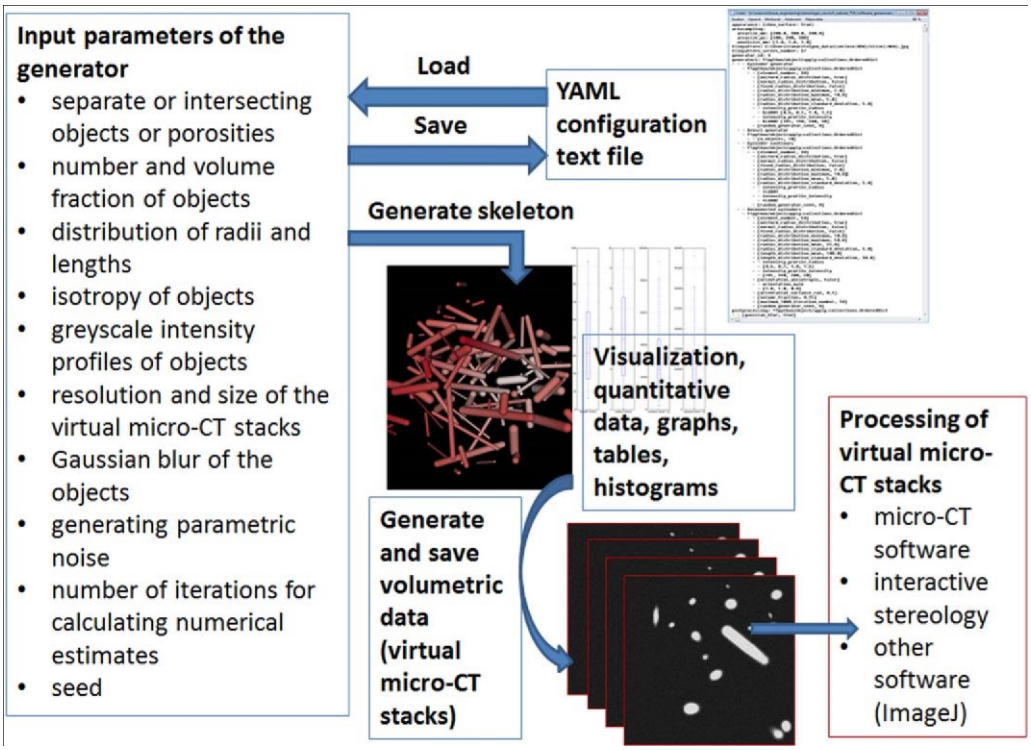

FIGURE 1 Main steps during the setting, generation, and processing of the fibrillar and porous three-dimensional objects and corresponding virtual micro-CT stacks. The user sets the required input parameters (see Table 2 for details) either manually or from a previously saved YAML configuration text file. The skeleton of the objects is generated together with a quantitative description of the objects (volumes, surfaces, and lengths), and the data can be visually checked by the user in the form of three-dimensional skeletons. Once the data meets the required settings, full volumetric data are generated and saved to disk as image sequences mimicking micro-CT stacks together with a three-dimensional model (VTK format) and tables containing all the morphometric results (CSV files). The resulting virtual micro-CT stacks can be loaded into any type of software supporting DICOM or JPEG image stacks [Color figure can be viewed at wileyonlinelibrary.com]

3.4 | Evaluating known morphometric values with analysis based on thresholding on the micro-CT console

For testing the sensitivity of the segmentation procedures using the SkyScan Bruker console micro-CT software, 40 image stacks were generated, representing low to high numbers of objects (Figure 5a), isotropy of objects (Figure 5b), resolution of stacks (Figure 5c), and noise (Figure 5d). After processing these phantom stacks (see Figure 6 for the main steps), situations leading to possible bias were identified (Figure 7). This included thresholding of the gradual transition of grayscale values between the objects and their background (Figure 7a), reduction of object count caused by peripheral sections of objects (Figure 7b), occasionally colliding objects (Figure 7c), and fragmentation due to binarization (Figure 7d).

There was on overall good agreement between the known surface and volume densities of generated objects and the results obtained on the micro-CT console within most of the range of values typical for biomaterials (Figure 8a,b). As shown in the Bland-Altman plots (Figure 8c, d), the disagreement between both measures gradually increased with increasing values of the densities.

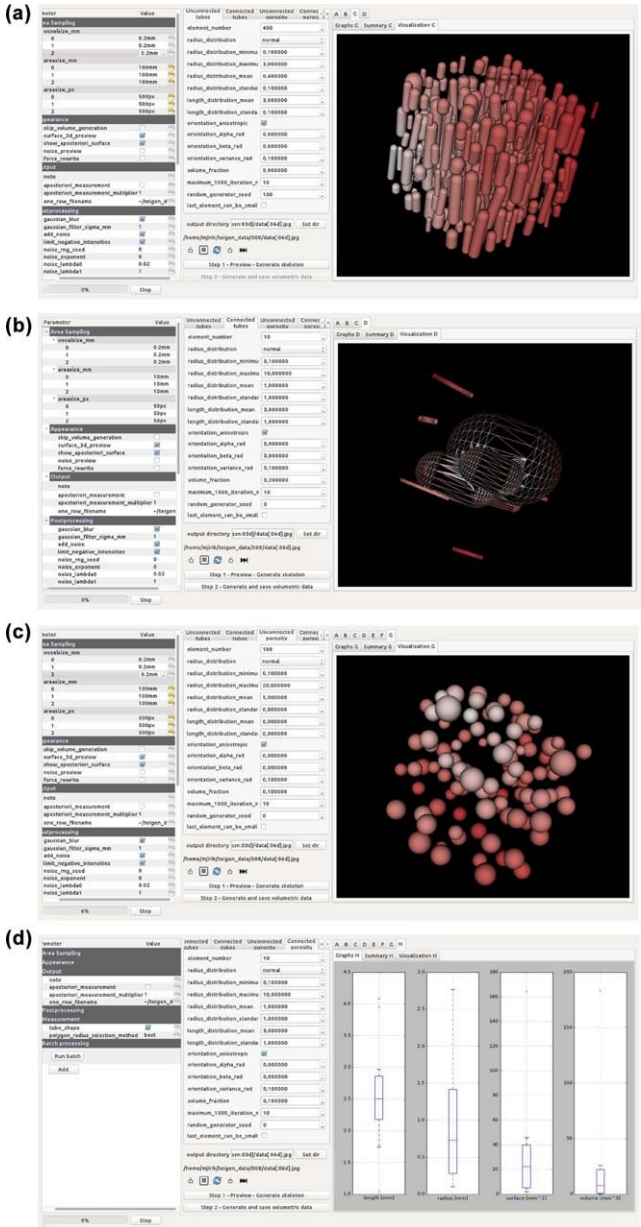

FIGURE 2 Graphical user interface of the four types of generators in the TeIGen software. (a) Generating unconnected tubes, in this example with a highly anisotropic orientation. (b) Generating connected (colliding) tubes, in this example within a wide range of diameters. (c) Generating unconnected porosities, which may have shape of spheres or tubes. (d) Generating connected (overlapping) porosities, overview of morphometric data on length, radius, surface, and volume distribution in the preview window [Color figure can be viewed at wileyonlinelibrary.com]

A detailed analysis of sensitivity of the thresholding upon various values of parameters of generated testing image sets revealed that the changes in object count and the value of isotropy did not affect the accuracy of the micro-CT quantification (Figure 9a,b). The number of objects was underestimated by the micro-CT, and the volumes, surfaces, and length densities had a tendency toward being overestimated. The size of the error

significantly increased with decreasing resolution when the voxel size exceeded 1/10 of the typical object size (Figure 9c), which simulated the effect of the smallest details that could still be reliably quantified. Similarly, the results became unreliable when the standard deviation of the noise intensity (mean5 0) exceeded 37 arbitrary units, and more filtering and higher threshold values were necessary (see Methods).

3.5 | Examples of practical applications

Verification of micro-CT analysis results of specimen microstructure is hard to achieve or even not possible as was mentioned in 1.3. TeIGen software enables evaluation of micro-CT analysis accuracy, image processing effect and bias quantification. Despite the fact, that 3D structures generated by TeIGen are simplification of studied specimen, it provides important and unique information, which may improve decision making in image processing and analyzes understanding. The benefit of using the TeIGen software will be illustrated in three examples.

3.5.1 | Evaluation of global thresholding effect

A fundamental approach in image thresholding is the use of Global threshold. Separating objects from their background requires a manual selection of grayscale value, which is usually based on operator's subjective assessment. Since there is a gradual transition between object and background, this decision often lacks accuracy and repeatability (typical situations are shown in Figure 10a,b). A solution is as follows: First, TeIGen software is employed for generating a dataset with a known structure similar to the specimen under study. Second, a series of different global thresholding values are applied for binarization using the micro-CT analysis. Third, the results of the micro-CT analysis are compared with known structural parameters generated in the first step. Four, the most accurate settings are used for further specimen analysis and bias introduced by micro-CT analysis is quantified (e.g., discrepancy between objects volume and surface accuracy). An example of such a simple analysis which required approximately 20 min of work is shown in Table 3.

3.5.2 | Effect of image noise quantification

Image noise is found in all micro-CT scans. However, the effect of image noise on results is usually not considered. TeIGen software is used for generating dataset of structures similar to studied specimen with similar level of image noise (Figure 6, see also section 4.1.4). By analyzing the same dataset with and without applying noise reduction algorithms, any bias introduced by noise and micro-CT analysis is quantified, because the impact of noise reduction and filtering is compared with the known structural parameters generated by the TeiGen software.

3.5.3 | Image 2D binarization did introduce bias into quantification of object number in isotropic tubular structures

Tissue engineering scaffold based on microfibers is subjected to microCT 3D analysis. 2D or 3D threshold is considered. Assessment of thresholding resulted in a significant overestimation of number of objects (Figure 7d, see also section 4.1.2) as well as inaccurate surface and volume estimates. In this case, using a three-dimensional thresholding was justified despite its computational time costs, as it provided more accurate results.

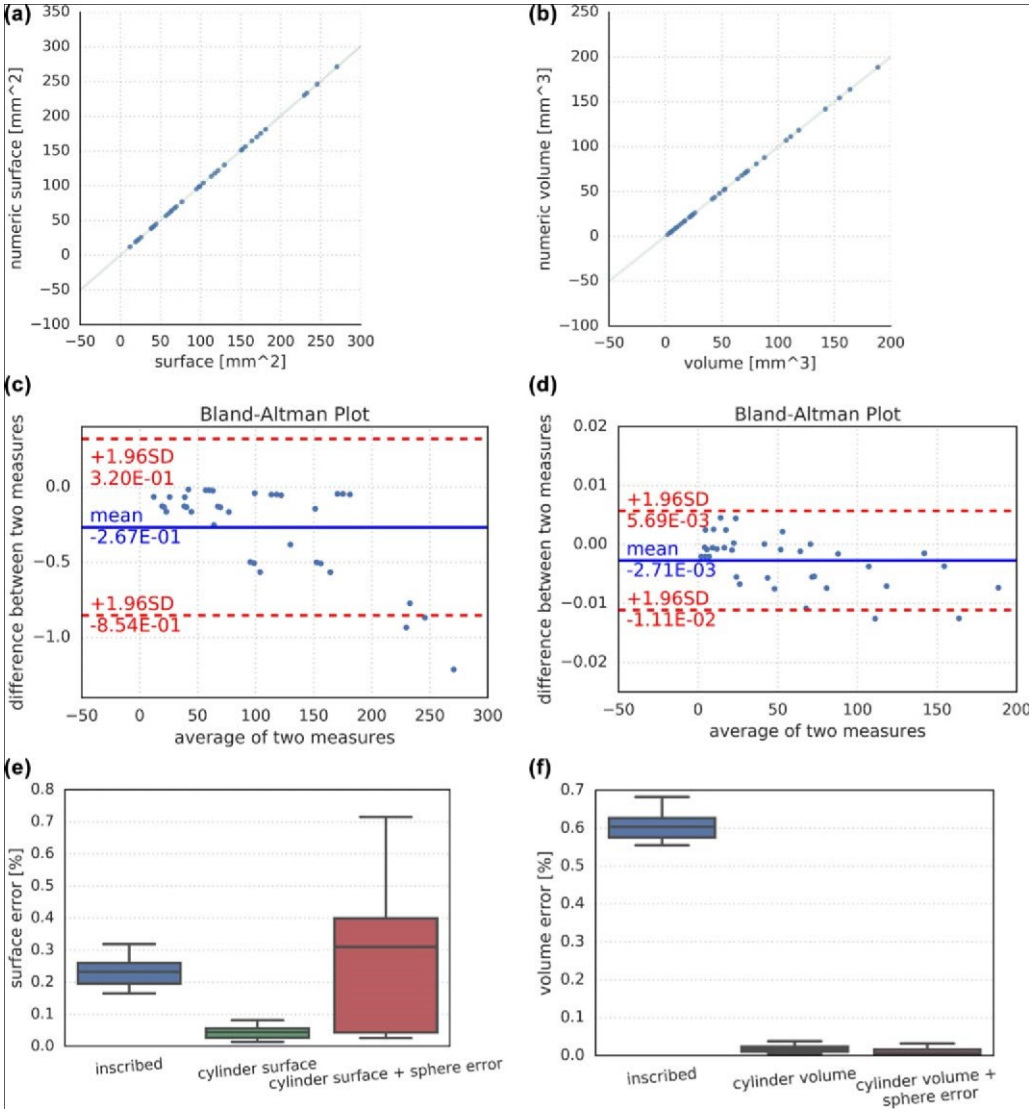

FIGURE 3 Comparing known volumes and surfaces with numerically estimated values. The source data for the graphs are available as Supporting Information S1. (a) Correlation scatter plot displaying the numerically estimated surfaces (Y-axis) against the precisely known surfaces (X-axis) of testing objects. (b) Correlation scatter plot displaying the numerically estimated volumes (Y-axis) against the precisely known volumes (X-axis) of testing objects. (c) Bland-Altman plot displaying the agreement between the numerically estimated surfaces and known surfaces of testing objects. The difference between both values (Y-axis) is plotted against their average (X-axis). The mean difference is shown as a blue line accompanied by a 61.96 standard deviation of the difference. (d) Bland-Altman plot (Altman and Bland, 1983) displaying the agreement between the numerically estimated volumes and known volumes of testing objects. The difference between both values (Y-axis) is plotted against their average (X-axis). The mean difference is shown as a blue line accompanied by a 61.96 standard deviation of the difference. (e) Box plot showing the impact of three methods used for compensation of the surface errors. (f) Box plot showing the impact of three methods used for compensation of the volume errors. In E and F, the relative error was calculated as 1003(value-numerical estimate)/value. The box spans the lower limits of the 2nd quartile (Q2) and the upper limits of the 3rd quartile (Q3), and the whiskers span the Q1-1.53(Q3-Q1) and Q3 1 1.53(Q3-Q1) values (Q1 is

effect based on subjective visual evaluation is usually the 1st quartile) [Color figure can be viewed at wileyonlinelibrary.com] insufficient and inaccurate.

To improve analysis, TeIGen software is applied to generate dataset of tubular structures with known parameters. For example, a two-dimensional

4 | DISCUSSION

4.1 | Image processing prior to micro-CT 3D analysis

4.1.1 | Image processing optimization: Aims and basics

Image processing optimization was based on many preliminary analyzes. We aimed to find a simple process (low number of variables

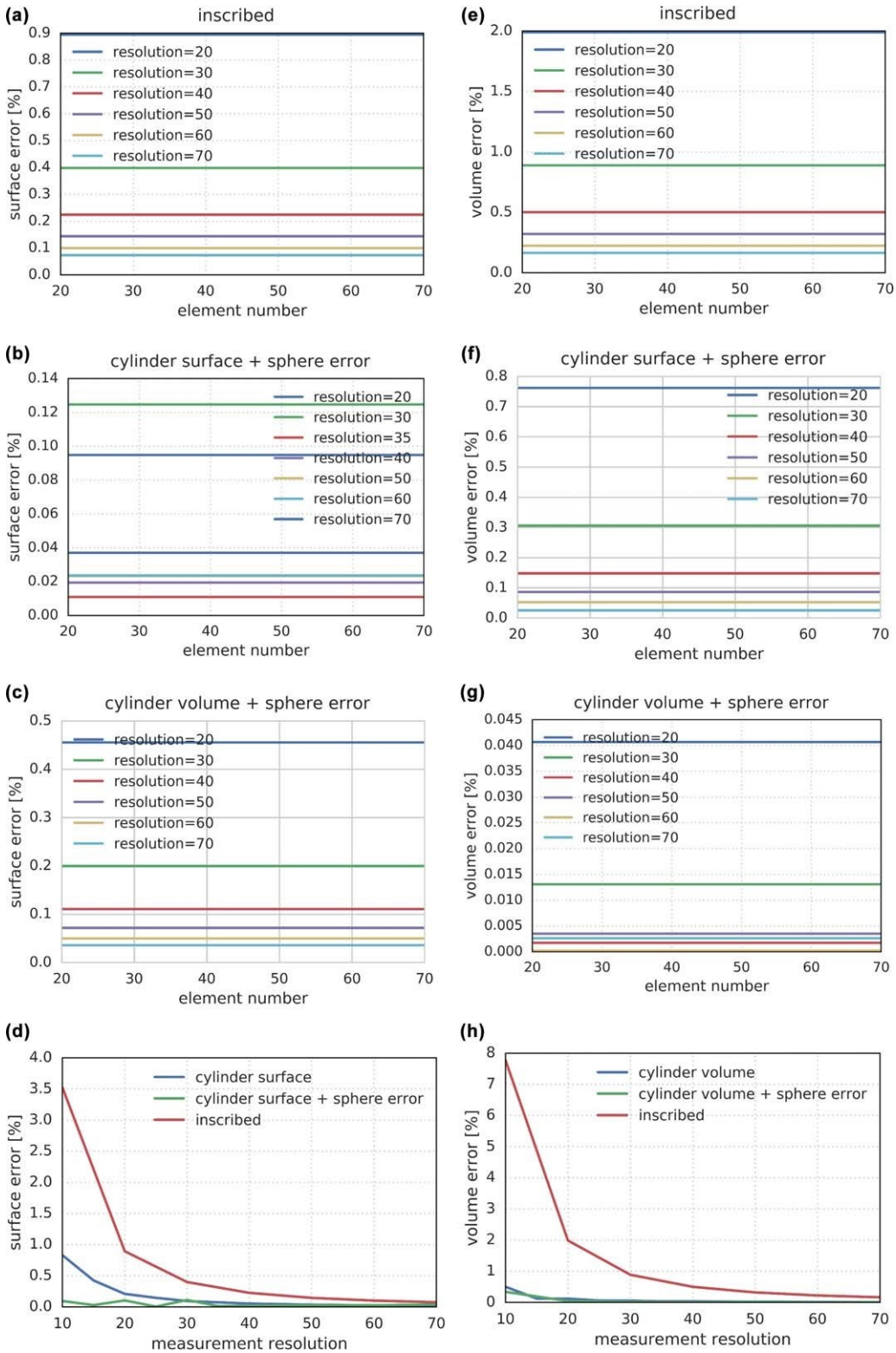

FIGURE 4 Analysis of the sensitivity of surface errors (a–d) and volume errors (e–h) to the number of generated objects (element number, a–c, e–g) and resolution at which the numerical estimates of the surface and volume were performed (d, h). The relative error plotted on the Y-axis was calculated as 1003(true value-numerical estimate)/value. The results are displayed without compensation (a,e) and for several methods of error compensation described in the Methods, namely: a,e—surface and volume error when no compensation is used (the colored lines show various resolutions), b,d—cylinder surface and sphere errors are compensated, c,g—cylinder volume and sphere errors are compensated. d,h—surface and volume measurement errors depending on the measurement resolution [Color figure can be viewed at wileyonlinelibrary.com]

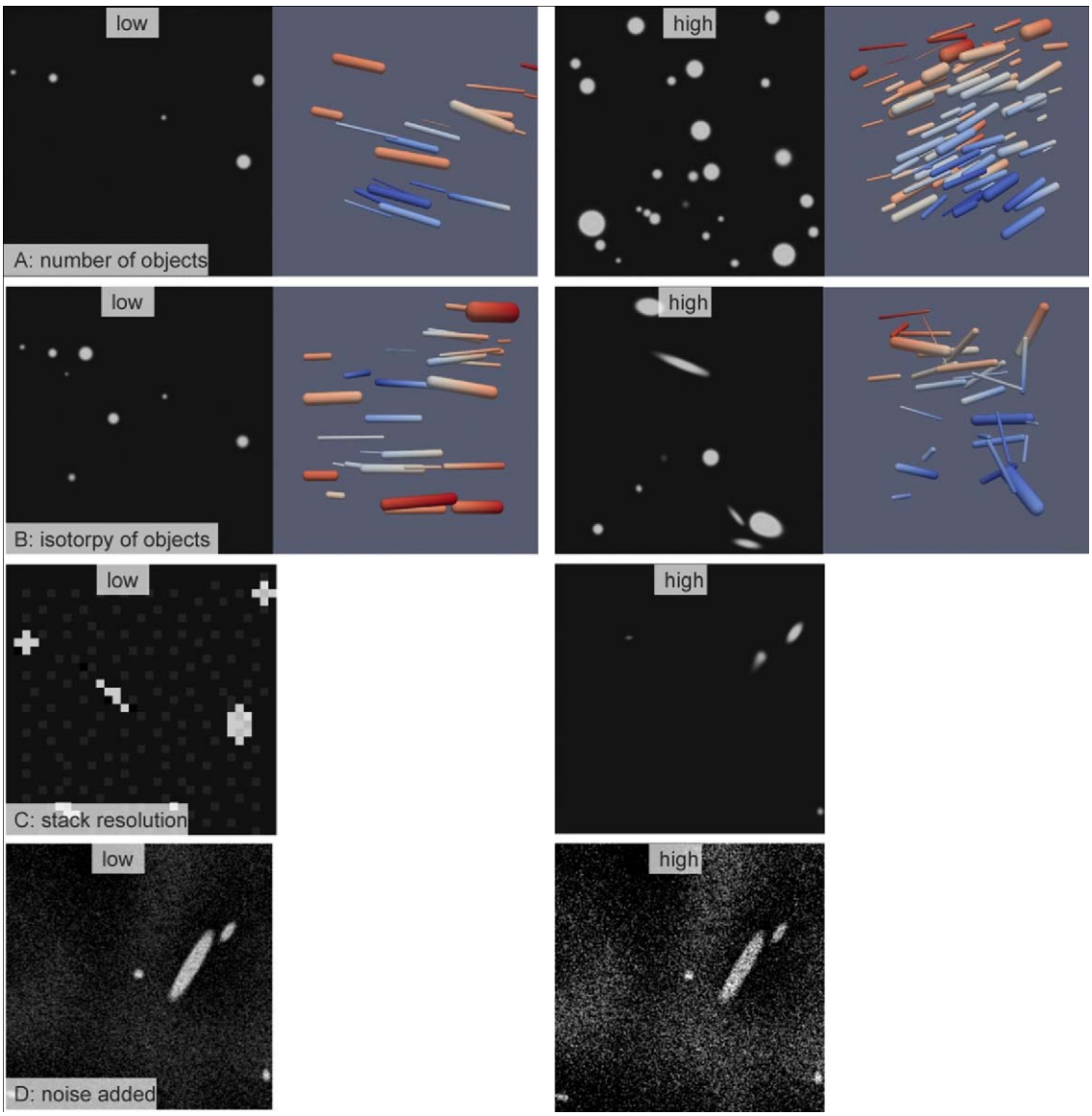

FIGURE 5 Examples of structures generated with various settings of parameters. For every parameter, ten sets of images were generated with values increasing from relatively low to relatively high, namely: (a) number of objects, (b) isotropy of objects, (c) resolution of image stacks, and (d) amount of noise added to the image data. In a-b, both two-dimensional sections and three-dimensional views are presented
[Color figure can be viewed at wileyonlinelibrary.com]

influencing outcomes and convenient time efficacy) with satisfactory and reproducible results in all variable parameters of tested datasets. Datasets with the variable count were generally uncomplicated compared to isotropy, noise, and resolution, where we encountered more complications that had to be managed.

Image processing modifications by CTAn software were often performed based on subjective assessment by an experienced micro-CT user. This approach is very common in micro-CT analysis (especially in life sciences applications), and therefore it has been chosen for our study. However, this is considered one of the major drawbacks of micro-CT analysis. Reduction of subjectivity was reached by an automated threshold procedure and object count evaluation, which will be described further. This was achievable when assessing various values of object count, isotropy

datasets, whereas noise and resolution dataset evaluation was more influenced by subjectivity because individualization of the image processing approach was needed.

Object number count was important in process optimization. A user performing micro-CT analysis would not be aware of dataset parameters generated by TeIGen software. Therefore, the object number count is the only parameter where differences between analysis results and dataset 3D visualization (CTVox, Bruker) are noticeable. There is no option for the evaluation of the other parameters (e.g., volume, surface, length) from this point of view.

The following procedures were used in the image processing optimization process. A universally accurate procedure ("standard" procedure) was found for count and isotropy. For resolution and noise variables, an individual approach had to be employed. Standard procedure was based of image filtering (Gaussian blur in 3D, radius5 2 less than 50 voxels), because some datasets had a gray pixel pattern on the background, and in some cases, they were evaluated as the objects using automatic binarization (Figure 7b). This pattern can imitate image noise in real micro-CT data. An automatic Otsu threshold in 3D was used for image binarization to reduce the influence of subjectivity. A despeckle operation in 3D was performed (remove white speckles less than 12 voxels—more in 4.1.2).

4.1.2 | Number of objects and its variability

Object number count was the only dataset parameter that could be employed in image processing optimization. Reduction of the object count number was observed in many cases, but usually less than 10% of the expected object count. Two causes were identified and explored. First, many datasets presented few relatively small objects, which were presented within a volume of interest only by their edge, so their grayscale values were not sufficient for recognition as an object. We have to consider that the transition from an object to the background is gradual, as we can see in the profile line (Figure 7a,b). In such objects, Gaussian filtering can even reduce their grayscale value, thus increasing the probability of being eliminated by binarization. Second, collision between objects was occasionally observed (Figure 7c), so two former objects were recognized as one. TeIGen should prevent these situations; however, regarding Figure 7a, we can estimate that two objects can be connected just by a gradual transition from object to background, even though their "core" structures are separate. In addition, Gaussian blur can enhance object collisions by creating a connection between the transition areas of two objects.

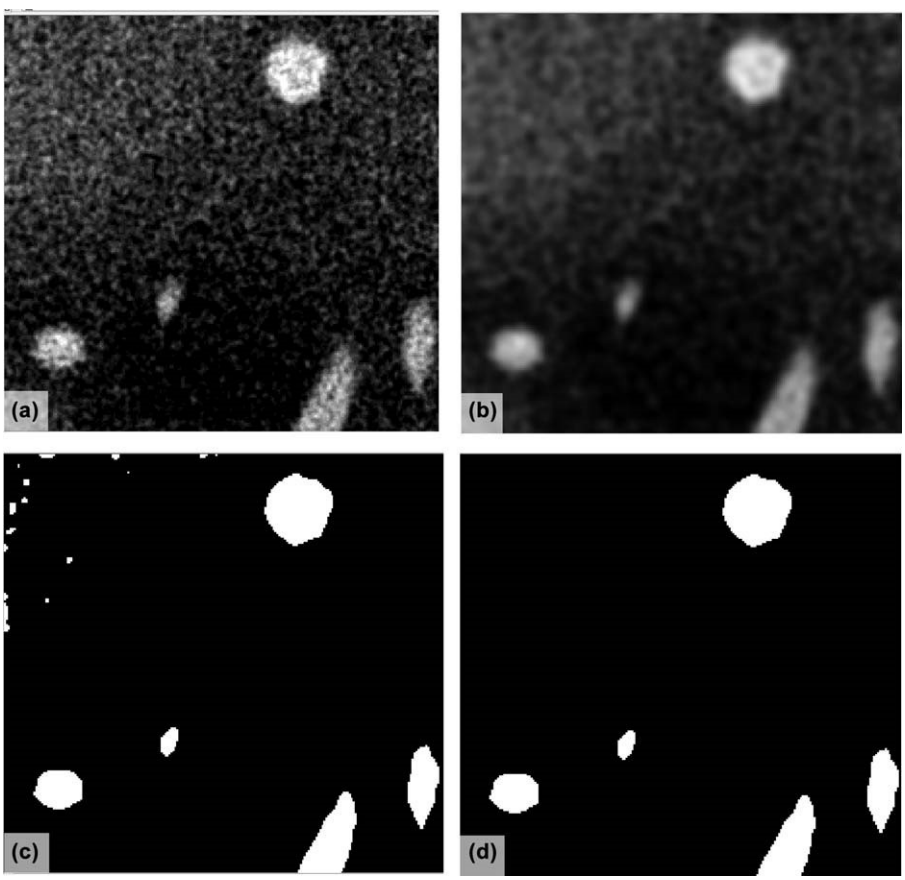

FIGURE 6 Main steps during the image processing of the virtual CT image stacks prior to analysis using the SkyScan 1272 (Bruker) console software. (a) Grayscale cross-section image (NOISE dataset). (b) Application of Gaussian blur in 3D. (c) Image after the binarization procedure (Global threshold). There are white speckles in the upper left corner as a result of image noise. We can observe irregular shapes of all objects as a result of noise and object interaction. (d) Image after performing a despeckle operation in 3D (remove white speckles of

In contrast, the object count number increase was usually more substantial, i.e., from tens to hundreds of percent of the expected object count. Several causes were identified. In preliminary evaluation of an isotropy dataset, we found that objects with relatively small diameter that are almost parallel to the transversal plane were fragmented by the binarization process in 2D (tested for better time efficacy) into many smaller objects (Figure 7d). These objects could be roughly divided into two groups: small objects with volumes of a few voxels and large objects of higher volume but still much smaller than generated objects. These isolated voxels may be connected to the original object by a side or vertex; however, this is not sufficient to be recognized as one object since object voxels are, in CTAn, considered to be connected only when they are in contact via their faces. We decided to employ automatic Otsu thresholding in 3D, which led to significant improvement. However, the object count number was still considered to be noise and removed by a despeckle operation in 3D (remove white speckles of less than 12 voxels). Modification of these two processes led to accurate dataset analysis regarding object number count.

4.1.3 | Resolution parameter and image processing

In resolution variable datasets (pixel size from 10 mm to 500 mm in a 10 3 10 3 10-mm^3 volume), we observed an increase of the object number count with an increase of pixel size. Substantial changes resulted from a shift from 100 mm to 200 mm for pixel size. Objects with defined parameters are generated by TeIGen software and subsequently voxelized. In lower resolution, objects can be fragmented as mentioned above (4.1.2). We did not succeed in finding a solution for image processing using CTAn for a pixel size of 200 mm or more for 10 3 10 3 10-mm^3 dataset volumes. An optimization process regarding object count evidently led to unacceptable

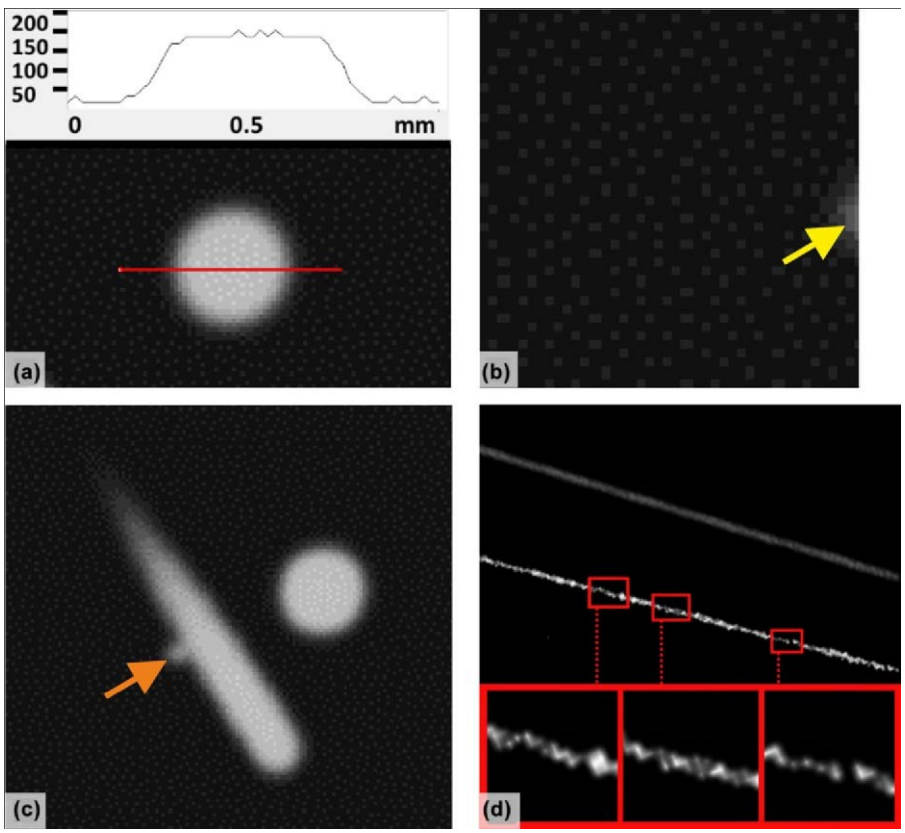

FIGURE 7 Illustration of situations leading to bias in analysis during the image processing. (a) Profile line (red line) presenting the image grayscale value (0–255). A gradual transition is apparent, which is similar to real micro-CT data. This phenomenon is a fundamental problem in image binarization. (b) Object count reduction caused by the peripheral section of an object (yellow arrow), where the grayscale value is not sufficient to be evaluated as an object by the automatic threshold. A pattern of gray pixels is visible in the background; in some datasets, they were recognized as an object, and thus they have to be eliminated by a filtering procedure. (c) Object count reduction caused by the collision of two objects (orange arrow). These are connected by their transition areas even though their core structures are separate. (d) Object count reduction caused by object fragmentation by the binarization process (especially in 2D). The upper object presents a grayscale 3D model (CTVox), and the lower object is the same object after automatic image binarization in 2D; three areas are enlarged to depict fragmentation. According to Individual Object Analysis, there are 37 objects (!) from the original one [Color figure can be viewed at wileyon-
much higher linelibrary.com]

than expected. Individual Object Analysis was performed in 3D, and object volume distribution was achieved and examined. We found that a great number of objects are below 12 voxels in volume, and thus they were

changes in object volume and vice versa. The pixel size value had to be considered for the parameter of filtering and despeckle operations in means of reduction of its value; for a pixel size of 80 mm or more, these operations were not applied.

4.1.4 | Noise parameter and image processing

Noise datasets (Figure 6a) needed higher individualization (and thus a more subjective approach) since these presented (together with resolution datasets) the most variable image data. Because of this, comparison with datasets processed by the "standard" approach is less applicable. The main problem was the gradual decrease of the signal to noise ratio in image data, so the outcome is always a compromise between noise reduction and object number and volume preservation. Filtration was achieved by Gaussian blur in 3D and was used with a gradual increase of the radius from 2 to 5 voxels (Figure 6b). An automatic Otsu threshold in 3D failed to provide reliable binarization because, in some datasets, noise was recognized as an object. A global threshold had to be employed with a progressive increase in the lower threshold value from 87 to 135 as the noise was intensified (Figure 6c). Interaction between noise and generated objects can lead to an alteration of volume, surface and object shape, which is noticeable in Figure 6c. A higher threshold value resulted in a reduction in object number count and object volume. A despeckle operation was performed with an increase of defined volume (removing white speckles less than: from 12 to 250 mm; Figure 6d).

4.2 | Novelty of the present approach

When compared to the ImageJ plugins mentioned in 1.3., the TeIGen software allows for generating 3D objects as test images. When compared with the Gensei software (Cimrman, 2010), TeIGen provides colliding and noncolliding fibrous structures, the geometric characteristics of which can be set by the user. Moreover, TeIGen generates also porosities and allows for modeling various types of realistic noise. The application includes both graphical user interface with 3D visualization which facilitates data preparation, as well as batch processing option.

It is recommended that the user performs a real object analysis first, using a micro-CT or scanning electron microscopy, thus estimating the typical range of the quantitative characteristics (i.e., total volumes, surfaces, lengths, and number of objects inside ROI). However, the error between the true and estimated data is unknown. In the second step, the data are used as input data of the TeIGen software defining the objects to be generated. In this second step, phantom objects with geometrical properties statistically similar to the real material are generated, but this time, the geometrical characteristics are precisely known. In the third step, the measurement of these phantom data is repeated and the error between the true known and estimated data is quantified. This can be used for calibration of the whole measurement and for identifying any major sources of bias.

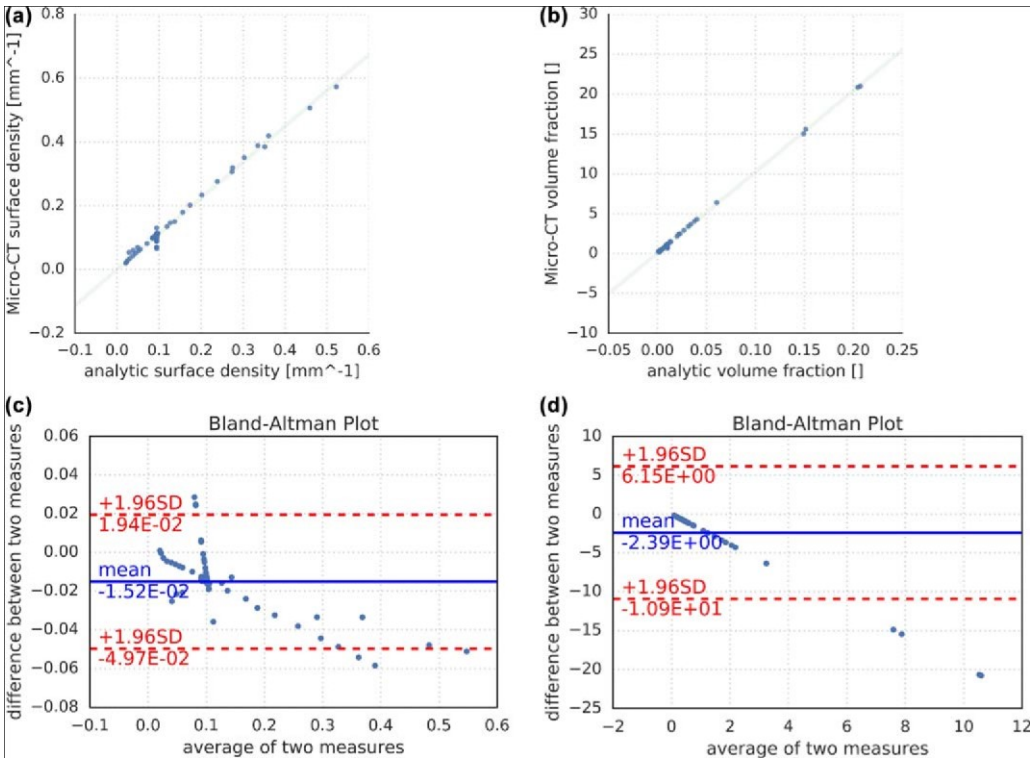

FIGURE 8 Comparing known surface and volume densities of generated objects with the results obtained after thresholding on the microCT console. The source data for the graphs are provided as Supporting Information S2. Data sets with known surface and volume densities were processed by the micro-CT software as described above. (a,b) correlation scatter plots displaying the values from micro-CT (Y-axis) against the precisely known surface and volume densities (X-axis) of testing objects. (c,d) Bland-Altman plots displaying the agreement between the surface and volume densities estimated on micro-CT and known values of the same testing objects. The difference between both values (Y-axis) is plotted against their average (X-axis). The mean difference is shown as a blue line accompanied by a 61.96 standard deviation of the difference [Color figure can be viewed at wileyonlinelibrary.com]

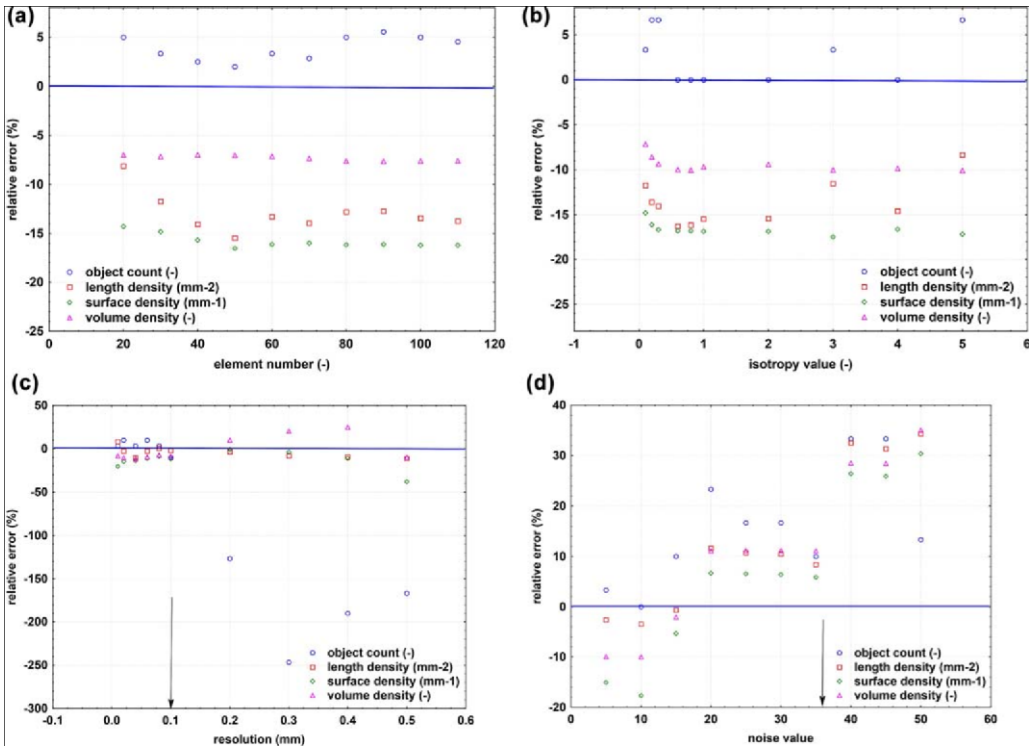

FIGURE 9 Analysis of the sensitivity of the thresholding to various values of parameters in generated image sets. Data sets with known numbers of objects, length densities, surface densities, and volume densities were processed by the micro-CT software as described above. After the morphometry on the micro-CT console was done, the relative errors (Y-axis) were calculated as 1003(true value-numerical estimate)/value and plotted against gradually changing values of the number of objects (a), isotropy (b), image resolution (c), and noise value (d). (a) Various object counts did not affect the size of the relative error. While the numbers of objects were underestimated by the microCT, the volumes, lengths and surfaces were slightly overestimated. (b) The value of isotropy did not affect the size of the error. (c) The size of the error dramatically increased when the voxel size exceeded 0.1 mm (arrow) in virtual stacks of 10 3 10 3 10 mm containing objects with a mean diameter of 1 mm. (d) The size of the error increased when the noise value exceeded 37 (arrow) [Color figure can be viewed at wileyonlinelibrary.com]

In general, using traceable standard reference materials has always belonged to good laboratory practice. The TeIGen software offers a solution by generating virtual standard reference materials. These might either mimic the real materials or be generated according to the best qualified estimates currently available.

4.3 | Further development of the TeIGen software and its relevance to manufacturing and characterization of biomaterials

Further development of the TeIGen software incorporates improvements in the highest values of filling the space with unconnected objects of increasing volume fraction. This task has theoretical limits that cannot be exceeded (Zidek et al., 2016), but the present algorithm starts to require unacceptable computational time costs when reaching the value of approx. 30% volume fraction. Should more space be filled with the tubes, collisions have to be allowed in the settings.

Another challenge for the future would be using the sections of generating objects to simulate the optimum sampling of numbers of image sections and their thicknesses. The TeIGen software can become a useful tool for planning of the sampling design of studies in microscopy, including manual and interactive measurements of objects with known size, where the research aim is to find the number and thickness of sections that are necessary for reliable measurements of numbers, surfaces, and volumes of tubular or spherical objects in studies using stereological counting rules (Mouton et al., 2017).

We greatly acknowledge the wide use of the ImageJ software (Schneider et al., 2012) and its contribution to the scientific community worldwide. Although ImageJ currently supports Python scripting, it

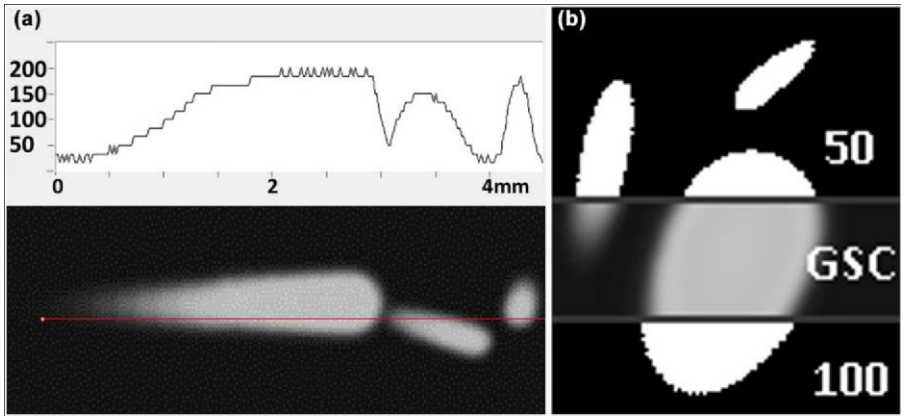

FIGURE 10 Illustration of global thresholding effect. (a) Profile line cutting tubular structures with grayscale value. (b) Different global threshold values (50 and 100; values were chosen to provide apparent differences in this figure) combined with original grayscale image (GSC). Binarized structures appear larger or smaller based on threshold value used [Color figure can be viewed at wileyonlinelibrary.com] TABLE 3 Example of practical application of the TeIGen software

	Object number	Tot.V. (mm^3)	M.Obj.V. (mm^3)	Tot.S. (mm^2)	M.Obj.S. (mm^2)
TeiGen (true value)	30	11.33	0.38	113.39	3.78
Global threshold 5 50	28	16.00	0.57	136.89	4.89
Global threshold 5 75	30	12.42	0.41	116.20	3.87
Global threshold 5 100	29	10.33	0.36	102.17	3.52

Illustration of the effect of Global threshold used during micro-CT processing on analysis results in selected parameters: Tot.V.—total volume of all objects, M.Obj.V.—mean object volume, Tot.S.—total surface of all objects, M.Obj.S.—mean object surface. For details see Figure 10 and section 3.5.
This analysis required approximately 20 min of time and revealed the preferred Global threshold settings 5 75.

currently does not allow for using libraries that are not part of the language kernel (for example, scipy, numpy, scikit-image librares, and several others). Should the ImageJ support these libraries in the future, the TeiGen software can be incorporated as an ImageJ plugin, thus benefiting from the ImageJ interface and a plethora of other functions. At present TeIGen can cooperate with ImageJ by reading and saving image data from/into the commonly supported file formats.

5 | CONCLUSION

Open-source software for the generation of three-dimensional models of fibrous and porous structures with known volumes, surfaces, lengths and object counts was developed and made freely available to the scientific community. This study provides a software tool for calibrating quantitative micro-CT assessments by producing and saving virtually generated image datasets with known morphometric data on noncolliding tubes, colliding tubes, or material porosities. This tool is useful for identifying combinations of object and image stack properties, which may easily lead to biased results using thresholding procedures of fibrous biomaterials in microCT. Some of these situations were extensively tested in the present article to help users of micro-CT understand where errors can occur, ensuring that micro-CT segmentation procedures can be proved to be valid and correct. We identified combinations of object and image stack properties that may easily lead to biased results using thresholding procedures in microCT. A solution to this problem could be more frequent application of design-based stereological methods during micro-CT analyzes. This method is openly available to researchers involved in morphometry of three-dimensional fibrillar and porous structures in micro-CT scans.

HUMAN AND ANIMAL RIGHTS STATEMENT

This article does not contain any studies with human participants or animals performed by any of the authors. This article does not contain patient data.

ACKNOWLEDGMENTS

The authors thank the following research projects. ZT, PS, and MHK were supported by AZV MZ CR Project No. 15–25813A. MJ, TK, AM, PT, PS, MHK, and MK were also supported by the National Sustainability Program I (NPU I) Nr. LO1503 provided by the Ministry of Education, Youth and Sports of the Czech Republic, by the Progres Q39 and Progres Q29/LF1 (MB) projects of the Charles University, and by the SVV 260390/2017 and SVV 260392/2017 projects of the Charles University. PK was supported by project LO1506 of the Czech Ministry of Education, Youth and Sports under program NPU I. ZT was also supported by the Ministry of Education, Youth

and Sports under the project FIND No. CZ.02.1.01/0.0/0.0/16_019/0000787. The micro-CT part of the study is a result of the project implementation: "Technological development of post doc programs," registration number CZ.1.05/41.00/16.0346, supported by Research and Development for Innovations Operational Programme (RDIOP) co-financed by the European regional development fund and the state budget of the Czech Republic. MJ and ZT were also supported by the Charles University Research Centre program UNCE/MED/006 University Center of Clinical and Experimental Liver Surgery.

CONFLICT OF INTEREST

The authors declare that they have no conflicts of interest.

ORCID

Zbynek Tonar http://orcid.org/0000-0002-7200-9894

REFERENCES

Altman, D. G., & Bland, J. M. (1983). Measurement in medicine: The analysis of method comparison studies. The Statistician, 32(3), 307–317.

Baddeley, A., & Jensen, E. B. (2004). Stereology for statisticians. Boca Raton: Chapman & Hall/CRC.

Bruker Corporation. (2017). Morphometric parameters measured by SkyscanTM CT-analyser software. Billerica: Bruker Corporation.

Buie, H. R., Campbell, G. M., Klinck, R. J., MacNeil, J. A., & Boyd, S. K. (2007). Automatic segmentation of cortical and trabecular compartments based on a dual threshold technique for in vivo micro-CT bone analysis. Bone, 41(4), 505–515.

Burey, A., Dos Reis, P. J., Santana, Vicentin B. L., Dezan Garbelini, C. C., Grama Hoeppner, M., & Appoloni, C. R. (2018). Polymerization shrinkage and porosity profile of dual cure dental resin cements with different adhesion to dentin mechanisms. Microscopy Research and Technique, 71(1), 88–96.

Burey, A., Dos Reis, P. J., Santana Vicentin, B. L., Dezan Garbelini, C. C., Grama Hoeppner, M., & Appoloni, C. R. (in press). Polymerization shrinkage and porosity profile of dual cure dental resin cements with different adhesion to dentin mechanisms. Microscopy Research and Technique. https://doi.org/10.1002/jemt.22960.

Burghardt, A. J., Kazakia, G. J., & Majumdar, S. (2007). A local adaptive threshold strategy for high resolution peripheral quantitative computed tomography of trabecular bone. Annals of Biomedical Engineering, 35(10), 1678.

Cimrman, R. (2010). Gensei – GENerate serial images. Retrieved from https://github.com/rc/gensei

De Souza, E. T., Nunes Tameirao, M. D., Roter, J. M., De Assis, J. T., De Almeida Neves, A., & De-Deus, G. A. (2013). Tridimensional quantitative porosity characterization of three set calcium silicate-based repair cements for endodontic use. Microscopy Research and Technique, 76(10), 1093–1098.

Draenert, M. E., Draenert, A. I., Forriol, F., Cerler, M., Kunzelmann, K. H., Hickel, R., & Draenert, K. (2012). Value and limits of m-CT for nondemineralized bone tissue processing. Microscopy Research and Technique, 75(4), 416–424.

Gomez, S., Vlad, M. D., L opez, J., & Fern andez, E. (2016). Design and properties of 3D scaffolds for bone tissue engineering. Acta Biomaterialia, 42, 341–350.

Gomez, S., Vlad, M. D., L opez, J., Navarro, M., & Fern andez, E. (2013). Characterization and three-dimensional reconstruction of synthetic bone model foams. Materials Science & Engineering. C, Materials for Biological Applications, 33(6), 3329–3335.

Hara, T., Tanck, E., Homminga, J., & Huiskes, R. (2002). The influence of microcomputed tomography threshold variations on the assessment of structural and mechanical trabecular bone properties. Bone, 31(1), 107–109.

Hildebrand, T., & Ruegsegger, P. (2003). A new method for the model independent assessment of thickness in three dimensional images. Journal of Microscopy, 185, 67–75.

Ho, S. T., & Hutmacher, D. W. (2006). A comparison of micro CT with other techniques used in the characterization of scaffolds. Biomaterials, 27(8), 1362–1376.

Horakova, J., Mikes, P., Saman, A., Svarcova, T., Jencova, V., Suchy, T., ... Prochazkova, R. (2018). Comprehensive assessment of electrospun scaffolds hemocompatibility. Materials Science & Engineering. C, Materials for Biological Applications, 82, 330–335.

Jimenez, P., Thomas, F., & Torras, C. (2001). 3D collision detection: A survey. Computers & Graphics, 25, 269–285.

Jirík, M. (2017). Teigen – TEst Image GENerator software. Retrieved from https://mjirik.github.io/teigen/

Jirík, M., & Tonar, Z. (2018). User manual for the Teigen – TEst Image GENerator software. Retrieved from https://github.com/mjirik/teigen/blob/master/user_manual.md

Jirík, M., Tonar, Z., Kralíčkova, A., Eberlova, L., Mírka, H., Kochova, P., ... Liska, V. (2016). Stereological quantification of microvessels using semiautomated evaluation of X-ray microtomography of hepatic vascular corrosion casts. International Journal of Computer Assisted Radiology and Surgery, 11(10), 1803–1819.

Jones, A. C., Arns, C. H., Sheppard, A. P., Hutmacher, D. W., Milthorpe, B. K., & Knackstedt, M. A. (2007). Assessment of bone ingrowth into porous biomaterials using Micro-CT. Biomaterials, 28 (15), 2491–2504.

Karageorgiou, V., & Kaplan, D. (2005). Porosity of 3D biomaterial scaffolds and osteogenesis. Biomaterials, 26(27), 5474–5491.

Kochova, P., Cimrman, R., Janaček, J., Witter, K., & Tonar, Z. (2011). How to asses, visualize and compare the anisotropy of linear structures reconstructed from optical sections - a study based on histopathological quantification of human brain microvessels. Journal of Theoretical Biology, 286(1), 67–78.

Landis, E. N., & Keane, D. T. (2010). X-ray microtomography. Materials Characterization, 61(12), 1305–1316.

Lorensen, W. E., & Harvey, E. C. (1987). Marching cubes: A high resolution 3d surface construction algorithm. ACM Siggraph Computer Graphics, 21(4), 163–169.

Maia, R. S., Jacob, C., Hara, A. K., Silva, A. C., Pavlicek, W., & Ross, M. J. (2015). An algorithm for noise correction of dual-energy computed tomography material density images. International Journal of Computer Assisted Radiology and Surgery, 10(1), 87–100.

Montufar, E. B., Vojtova, L., Celko, L., & Ginebra, M. P. (2017). Calcium phosphate foams: Potential scaffolds for bone tissue modeling in three dimensions. Methods in Molecular Biology (Clifton, N.J.), 1612, 79–94.

Moore, M., & Wilhelms, J. (1988). Collision detection and response for computer animation. Computer Graphics, 22(4), 289–298.

Mouton, P. R. (2002). Principles and practices of unbiased stereology. An introduction for bioscientists. Baltimore: The Johns Hopkins University Press.

Mouton, P. R., Phoulady, H. A., Goldgof, D., Hall, L. O., Gordon, M., & Morgan, D. (2017). Unbiased estimation of cell number using the automatic optical fractionator. Journal of Chemical Neuroanatomy, 80, A1–A8.

Neves, A. A., Coutinho, E., Alves, H. D., & de Assis, J. T. (2015). Stress and strain distribution in demineralized enamel: A micro-CT based finite element study. Microscopy Research and Technique, 78(10), 865–872.

Otsu, N. (1979). A threshold selection method from gray-level histograms. IEEE Transactions on Systems, Man, and Cybernetics, 9(1), 62–66.

Parkinson, I. H., Badiei, A., & Fazzalari, N. L. (2008). Variation in segmentation of bone from micro-CT imaging: Implications for quantitative morphometric analysis. Australasian Physical & Engineering Sciences in Medicine, 31(2), 160–164.

Particelli, F., Mecozzi, L., Beraudi, A., Montesi, M., Baruffaldi, F., & Viceconti, M. (2012). A comparison between micro-CT and histology for the evaluation of cortical bone: Effect of polymethylmethacrylate embedding on structural parameters. Journal of Microscopy, 245(3), 302–310.

Plencner, M., East, B., Tonar, Z., Otahal, M., Prosecka, E., Rampichova, M., ... Amler, E. (2014). Abdominal closure reinforcement by using polypropylene mesh functionalized with poly-e-caprolactone nanofibers and growth factors for prevention of incisional hernia formation. International Journal of Nanomedicine, 9, 3263–3277.

Prosecka, E., Rampichova, M., Litvinec, A., Tonar, Z., Kralíčkova, M., Vojtova, L., ... Amler, E. (2015). Collagen/hydroxyapatite scaffold enriched with polycaprolactone nanofibers, thrombocyte-rich solution and mesenchymal stem cells promotes regeneration in large bone defect in vivo. Journal of Biomedical Materials Research Part A, 103(2), 671–682.

Pyka, G., Kerckhofs, G., Schrooten, J., & Wevers, M. (2014). The effect of spatial micro-CT image resolution and surface complexity on the morphological 3D analysis of open porous structures. Materials Characterization, 87, 104–115.

Rau, T. S., Wurfel, W., Lenarz, T., & Majdani, O. (2013). Three-dimen-€ sional histological specimen preparation for accurate imaging and spatial reconstruction of the middle and inner ear. International Journal of Computer Assisted Radiology and Surgery, 8(4), 481–509.

Remy, E., & Thiel, E. (2002). Medial axis for chamfer distances: Computing look-up tables and neighbourhoods in 2D or 3D. Pattern Recognition Letters, 23(6), 649–661.

Schladitz, K. (2011). Quantitative micro-CT. Journal of Microscopy, 243(2), 111–117.

Schneider, C. A., Rasband, W. S., & Eliceiri, K. W. (2012). NIH Image to ImageJ: 25 years of image analysis. Nature Methods, 9(7), 671–675.

Schroeder, W. J., Avila, L. S., & Hoffman, W. (2000). Visualizing with VTK: A tutorial. IEEE Computer Graphics and Applications, 20(5), 20–27.

Schroeder, W., Martin, K. M., & Lorensen, W. E. (1998). The visualization toolkit (2nd ed.): An object-oriented approach to 3D graphics. Upper Saddle River: Prentice-Hall.

Shen, H., Nutt, S., & Hull, D. (2004). Direct observation and measurement of fiber architecture in shor fiber-polymer composite foam through micro-CT imaging. Composites Sci Technol, 64(13–14), 2113– 2120.

Shepp, L. A., & Logan, B. F. (1974). The Fourier reconstruction of a head section. IEEE Transactions on Nuclear Science, 21(3), 21–43.

Stock, S. R. (2009). MicroComputed tomography methodology and applications. Boca Raton: CRC Press.

Stoyan, D., Kendall, W. S., & Mecke, J. (1995). Stochastic geometry and its applications. New York: John Wiley & Sons.

Suchy, T., Supov a, M., Sauerova, P., Verdanova, M., Sucharda, Z., Ryglova, S., ... Kalbačova, M. H. (2015). The effects of different cross-linking conditions on collagen-based nanocomposite scaffoldsan in vitro evaluation using mesenchymal stem cells. Biomedical Materials (Bristol, England), 10(6), 065008.

Szentivanyi, A., Chakradeo, T., Zernetsch, H., & Glasmacher, B. (2011). Electrospun cellular microenvironments: Understanding controlled release and scaffold structure. Advanced Drug Delivery Reviews, 63(4– 5), 209–220.

Tonar, Z., Khadang, I., Fiala, P., Nedorost, L., & Kochova, P. (2011). Quantification of compact bone microporosities in the basal and alveolar portions of the human mandible using osteocyte lacunar density and area fraction of vascular canals. Annals of Anatomy, 193(3), 211–219.

Tonar, Z., Kochova, P., Cimrman, R., Witter, K., Janacek, J., & Rohan, V. (2011). Microstructure oriented modelling of hierarchically perfused porous media for cerebral blood flow evaluation. Key Engineering Materials, 465, 286–289.

Yan, Y. B., Qi, W., Qiu, T. X., Teo, E. C., & Lei, W. (2012). The effect of threshold value on the architectural parameters and stiffness of human cancellous bone in micro-CT analysis. Journal of Mechanics in Medicine and Biology, 12(05), 1250092.

Zhang, J., Yan, C. H., Chui, C. K., & Ong, S. H. (2010). Fast segmentation of bone in CT images using 3D adaptive thresholding. Computers in Biology and Medicine, 40(2), 231–236.

Zhong, S., Zhang, Y., & Lim, C. T. (2012). Fabrication of large pores in electrospun nanofibrous scaffolds for cellular infiltration: A review. Tissue Engineering Part B, Reviews, 18(2), 77–87.

Zidek, J., Vojtova, L., Abdel-Mohsen, A. M., Chmelik, J., Zikmund, T., Brtnikova, J., ... Kaiser, J. (2016). Accurate micro-computed tomography imaging of pore spaces in collagen-based scaffold. Journal of Materials Science: Materials in Medicine, 27(6), 110.

SUPPORTING INFORMATION

Additional Supporting Information may be found online in the supporting information tab for this article.

How to cite this article: Jiríik M, Bartos M, Tomasek P, et al. Generating standardized image data for testing and calibrating quantification of volumes, surfaces, lengths, and object counts in fibrous and porous materials using X-ray microtomography. Microsc Res Tech. 2018;81:551–568. https://doi.org/10.1002/ jemt.23011

BRING YOUR CAREER TO THE NEXT LEVEL IN 2020...

We've expanded our course selection...again!
We now have even more offerings, led by our certified faculty. Maximize your skill and knowledge sets with our...

- Educational Workshops
- Corporate Training
- Group Training
- Private Training
- Equipment Demonstrations

See our website for more information...
www.emsmicroscopyacademy.com

Biological TEM Workshop

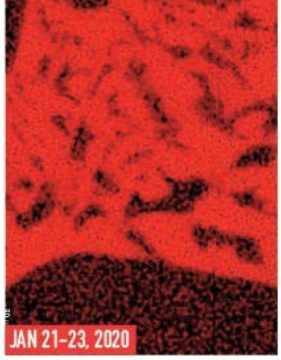

X-Ray Microanalysis Workshop

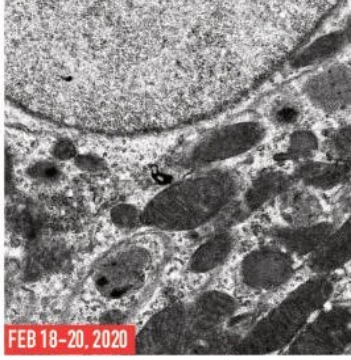

Automated and Rapid Specimen Processing for Electron Microscopy Workshop

Materials Ultramicrotomy
Preparatory Session on FEB 24 for those unfamiliar with microtomy.

Introduction to Microscopy Techniques Workshop

Biological SEM Workshop

Cryo SEM Workshop

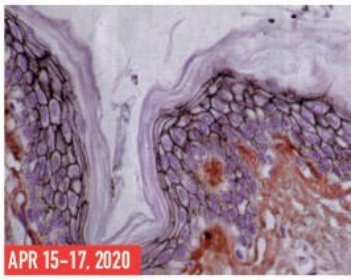

Aurion Immunogold Silver Staining

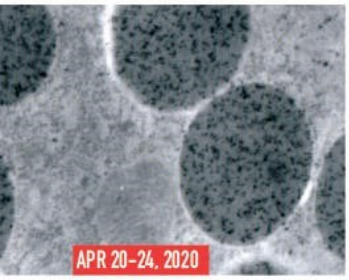

Cryosectioning/Immunogold Workshop

Introduction to Microscopy Techniques Workshop

X-Ray Microanalysis Workshop

Microscopy: The Complete Image
June Session

Microscopy: The Complete Image
July Session

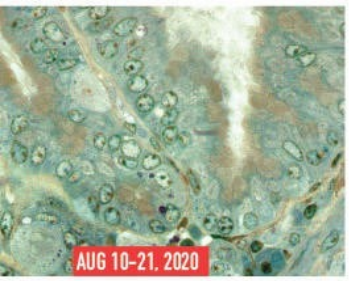

Microscopy: The Complete Image
August Session

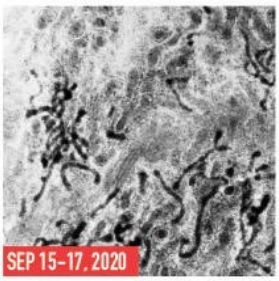

Introduction to Microscopy Techniques Workshop

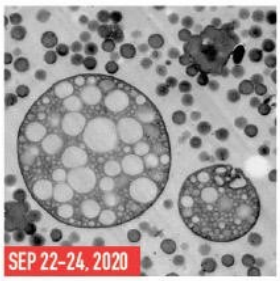

Materials Ultramicrotomy
Preparatory Session on SEP 21 for those unfamiliar with microtomy.

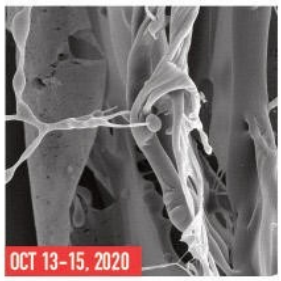

Cryo SEM Workshop

Biological SEM Workshop

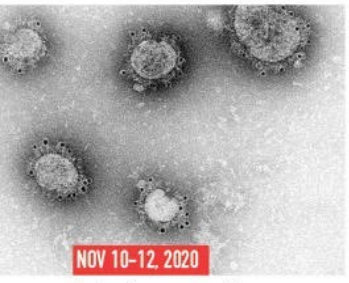

Aurion Immunogold Silver Staining

Biological TEM Workshop

SIGN UP FOR A CLASS TODAY, OR SUGGEST A COURSE THAT YOU WANT...

EMS Microscopy Academy

...ENDLESS POSSIBILITIES

www.emsmicroscopyacademy.com

Electron Microscopy Sciences • 1560 Industry Road, Hatfield, PA 19440 • **phone:** 215-412-8400 • **email:** info@emsdiasum.com

PLOS ONE

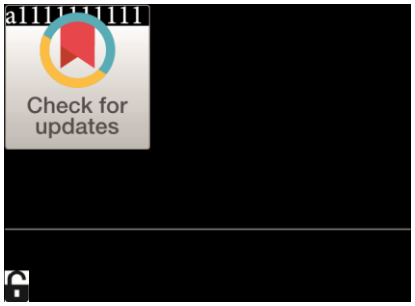

Citation: Blassova T, Tonar Z, Tomasek P, Hosek P, Hollan I, Treska V, et al. (2019) Inflammatory cell infiltrates, hypoxia, vascularization, pentraxin 3 and osteoprotegerin in abdominal aortic aneurysms – A quantitative histological study. PLoS ONE 14(11): e0224818. https://doi.org/10.1371/journal.pone.0224818

Editor: Helena Kuivaniemi, Stellenbosch University
Faculty of Medicine and Health Sciences, SOUTH
AFRICA

Received: June 7, 2019

Accepted: October 22, 2019

Published: November 8, 2019

DataAvailabilityStatement: All relevant data are within the manuscript and its Supporting Information files.

Funding: This work was mainly supported by the
Ministry of Health of the Czech Republic, Project No. AZV 15-32727A. The study received additional support from the National Sustainability Program I No. LO1503, from the Charles University Research Fund – Progres Q39, by project No. CZ.02.1.01/ RESEARCH ARTICLE

Inflammatory cell infiltrates, hypoxia, vascularization, pentraxin 3 and osteoprotegerin in abdominal aortic aneurysms – A quantitative histological study

Tereza Blassova[1]*, Zbynek Tonar[1], Petr Tomasek[1], Petr Hosek[1], Ivana Hollan[2,3], Vladislav Treska[4], Jiri Molacek[4]

1 Department of Histology and Embryology and Biomedical Centre, Faculty of Medicine in Pilsen, Charles University, Pilsen, Czech Republic, **2** Hospital for Rheumatic Diseases, Lillehammer, Norway, **3** Department of Medicine, Brigham and Women's Hospital, Boston, Massachusetts, United States of America,
4 Department of Vascular Surgery, University Hospital in Pilsen, Faculty of Medicine in Pilsen, Charles University, Pilsen, Czech Republic

* tereza.blassova@lfp.cuni.cz

Abstract

Information about the tissue characteristics of abdominal aortic aneurysms (AAAs), some of which may be reflected in the serum, can help to elucidate AAA pathogenesis and identify new AAA biomarkers. This information would be beneficial not only for diagnostics and follow-up but also for potential therapeutic intervention. Therefore, the aim of our study was to compare the expression of structural proteins, immune factors (T and B lymphocytes, macrophages, neutrophils and pentraxin 3 (PTX3)), osteoprotegerin (OPG), microvessels and hypoxic cells in AAA and nonaneurysmal aortic walls. We examined specimens collected during surgery for AAA repair (n = 39) and from the abdominal aortas of kidney donors without AAA (n = 8). Using histochemical and immunohistochemical methods, we quantified the areas positive for smooth muscle actin, desmin, elastin, collagen, OPG, CD3, CD20, MAC387, myeloperoxidase, PTX3, and hypoxia-inducible factor 1-alpha and the density of CD31-positive microvessels. AAA samples contained significantly less actin, desmin, elastin and OPG, more collagen, macrophages, neutrophils, T lymphocytes, B lymphocytes, hypoxic cells and PTX3, and a greater density of vasa vasorum (VV) than those in non-AAA samples. Hypoxia positively correlated with actin and negatively correlated with collagen. Microvascular density was related to inflammatory cell infiltrates, hypoxia, PTX3 expression and AAA diameter. The lower OPG expression in AAAs supports the notion of its protective role in AAA remodeling. AAA contained altered amounts of structural proteins, implying reduced vascular elasticity. PTX3 was upregulated in AAA and colocalized with inflammatory infiltrates. This evidence supports further evaluation of PTX3 as a candidate marker of AAA. The presence of aortic hypoxia, despite hypervascularization, suggests that

hypoxiainduced neoangiogenesis may play a role in AAA pathogenesis. VV angiogenesis of the AAA wall increases its vulnerability.

0.0/0.0/16_019/0000787 "Fighting INfectious Diseases" and No. CZ.02.1.01/0.0/0.017_048/0007280 "Application of Modern Technologies in Medicine and Industry", awarded by the Ministry of Education, Youth and Sport of the Czech Republic, financed by European Regional Development Fund.

Competinginterests: The authors have declared that no competing interests exist.

Introduction

Abdominal aortic aneurysms (AAAs) occur in 1–7% of the population over 50 years of age [1]. The pathomechanisms underlying the development of AAAs and AAA instability, which may induce AAA disruption, are still unclear. Therefore, the prevention and treatment of AAAs are insufficient. Furthermore, tools for monitoring AAAs and predicting their complications are limited.

Thus, it is important to identify the crucial structural changes and processes that lead to the development of AAAs and AAA instability. Some of these may be reflected in the serum, serve as biomarkers for diagnosing and monitoring AAAs, and predict their complications. Moreover, improved insights into the pathophysiological processes may help to identify novel therapeutic targets.

AAAs are characterized by decreased vascular elasticity. There are theories that inflammation and changes in microcirculation can contribute to the vascular remodeling of aneurysms [2–5]. Aortic inflammatory cells (T and B lymphocytes) and endothelial cells from invading neovessels express matrix metalloproteinases (MMP) and may substantially contribute to aneurysm instability [6]. Nonetheless, there have been inconsistent results regarding the vascularization of AAAs; while a study by Eberlova´ revealed lower microvascular density in AAAs, Rodella found a higher density of microvessels in the AAA aorta compared to the non-AAA aorta [2,4].

Among the factors that may be involved in the pathogenesis of AAAs are osteoprotegerin (OPG) and pentraxin 3 (PTX3). PTX3 is a molecule of the innate immune system that protects against infections, participates in the clearance of apoptotic cells, modulates inflammation and angiogenesis, and participates in extracellular matrix formation. PTX3 belongs to the same protein family as C-reactive protein (CRP). However, in contrast to CRP, it is produced locally in the inflamed tissue and in neutrophils [7]. There are indications that PTX3 may be superior to CRP as a biomarker of atherosclerotic cardiovascular diseases (CVD) (including acute coronary syndromes), possibly due to its ability to reflect vascular inflammation and due to the speed of its response [8–10]. Interestingly, the role of PTX3 in CVD may be protective, and PTX3 may represent a relevant therapeutic target [11,12]. Nevertheless, there is currently minimal knowledge about the role of PTX3 in AAAs.

OPG, a key regulator of bone remodeling, has also been implicated in the immune response and vascular diseases. OPG is secreted by osteoblasts, endothelial cells, human aortic vascular smooth muscle cells (VSMCs), dendritic cells, lymphocytes and plasma cells [13]. OPG inhibits vascular calcification by regulating the procalcific effects of receptor activator of nuclear factor kappa-B ligand in VSMCs [14,15]. The role of OPG in CVD has not yet been fully clarified. Clinical studies have shown that high OPG levels are related to the presence and progression of CVD, including AAAs [13,16,17]. However, animal models point to a protective role of OPG in CVD [18,19].

In order to improve insights into vessel wall alterations in AAAs, we compared the expression of structural proteins, osteoprotegerin, and pentraxin 3 and the presence of immune factors (T and B lymphocytes, neutrophils and macrophages), microvessels and hypoxic cells in AAA and non-aneurysmal aortic walls and to explore their relationships.

Materials and methods

Patients

In this study, we examined aortic tissue removed during open surgical repair of AAA from 39 patients, and corresponding aortic specimens from 8 individuals—cadaveric organ donors without aortic aneurysms. In the AAA group, the inclusion criteria were a diagnosis of AAA and open surgery at University Hospital in Pilsen. The exclusion criteria were malignancy in the anamnesis, infection or autoimmune disease, and renal and hepatic dysfunction. There

were no inflammatory AAAs in our group of patients as well as no familial AAAs. Also all AAAs were non-ruptured. Control samples were from heart-beating donors after brain death diagnosed. The samples were taken together with other organs for transplantation according to the Transplantation Act valid in the Czech Republic. Thus, the samples did not suffer any warm ischemia. The aortas were flushed with a perfusion solution together with the organs, and immediately after explantation they were fixed in formalin solution. This study conforms to the principles outlined in the Declaration of Helsinki. The study was approved by the Ethical Committee of University Hospital and the Faculty of Medicine of Charles University in Pilsen on 12th August 2014, and all the AAA patients gave written informed consent.

Histological analysis

The specimens were fixed in formalin and embedded in paraffin, and each was cut into 28 serial 4-μm thick histological sections. The sections were stained using a battery of 14 methods to assess of overall morphology and markers of main tissue components, immune factors, hypoxia, osteoprotegerin and microvessels (Table 1). General protocol for immunohistochemical methods can be find here: dx.doi.org/10.17504/protocols.io.7uxhnxn. S1 Table provides details regarding the antibodies and pretreatment used in the immunohistochemical methods. The immunohistochemical reactions were visualized with diaminobenzidine (DAB+, Liquid; DakoCytomation, Glostrup, Denmark). The immunohistochemical sections were counterstained with Gill's haematoxylin.

For each staining method, 4 micrographs were randomly collected in a systematic and uniform manner; resulting in total 56 micrographs for each sample. We used 20× and 40× objectives mounted on an Olympus BX51 microscope to take the photomicrographs (see S2 Table). The unbiased sampling of the micrographs of the sections was performed as described in our

Table 1. Histological staining methods used in the study.

Staining	Purpose and visualization of aortic wall components
Hematoxylin-eosin [20]	Overall morphology of the aortic wall
Verhoeff's hematoxylin and green trichrome [21]	Overall morphology, differentiating connective tissue, smooth muscle
Picrosirius red (Direct Red 80, Sigma Aldrich, Munich, Germany) [22]	Type I and type III collagen when observed under circularly polarized light
Orcein (Tanzer's orcein, Bowley Biochemical Inc., Danvers, MA, USA)	Elastic membranes, elastic fibres
Immunohistochemical detection of alpha-smooth muscle actin	Contractile phenotype of vascular smooth muscle cells
Immunohistochemical detection of desmin	Contractile phenotype of vascular smooth muscle cells
Immunohistochemical detection of MAC387	Macrophages infiltrating the aortic wall
Immunohistochemical detection of myeloperoxidase	Neutrophilic granulocytes infiltrating the aortic wall
Immunohistochemical detection of CD3	T-lymphocytes

Immunohistochemical detection of CD20	B-lymphocytes
Immunohistochemical detection of CD31	Endothelium of vasa vasorum
Immunohistochemical detection of HIF 1-alpha	Hypoxia-inducible factor 1-alpha, a marker of tissue hypoxia
Immunohistochemical detection of Pentraxin-3	Pentraxin 3, a protein produced in response to inflammatory signals
Immunohistochemical detection of Osteoprotegerin	Osteoprotegerin, a calcium controlling protein

https://doi.org/10.1371/journal.pone.0224818.t001

previous studies on the aorta [23,24]. Briefly, starting in a randomly selected part of a histological section, the *(x, y)* distances between 4 micrographs uniformly covered the entire circumference of the tunica media, including the image fields bordering the adventitia or the lumen. This resulted in a fair sampling of the image fields, in which all of the components and structures were selected with a probability proportional to their areas on the histological slide. To quantify collagen by microscopy, we used a circular polarizing filter (Hama, Monheim, Germany) crossed with a quarter wave λ/4 filter below the analyser filter (U-GAN, Olympus, Tokyo, Japan) mounted on an Olympus CX41 microscope (Olympus, Tokyo, Japan). The advantages of this method are described elsewhere [22].

Histological quantification was performed as described previously [2,23–28]. Briefly, a stereological point grid (the PointGrid module of Ellipse software (ViDiTo, Kosˇice, Slovakia), cf. [29]) was loaded and randomly superposed on the micrographs to quantify the area of actin, desmin, elastin, collagen staining and the immunopositivity of macrophages, neutrophils, T lymphocytes, B lymphocytes, hypoxic cells, PTX3, and OPG. The number of points that intersected the structure of interest was counted. The point grid method allowed for individual corrections of the reference space (i.e., tunica media or adventitia) for any possible artefacts, microcracks or the presence of the lumen vs. the vessel wall. Whenever possible, the entire wall was used as a meaningful reference space [30]. The area for each parameter was calculated for each protein by dividing the number of grid lines intersecting the structure of interest by the number of grid lines intersecting the reference space of the vascular wall, and the result was multiplied by 100. The vascularization of the wall was quantified using an unbiased counting frame positioned on the micrographs. The number of CD31-positive vasa vasorum (VV) profiles was divided by the sum of the areas of the counting frame and expressed as a two-dimensional density of microvessels (Q_A, quantity per area).

Statistics

In some cases, the surgeon took two samples from one patient. We processed both samples and used the average results for the statistical analysis. We used the chi-square test to assess differences in proportions among the groups. We compared continuous nonnormally distributed variables by the Mann-Whitney-Wilcoxon test. Correlations were assessed using the Spearman correlation coefficient and Kendall's tau coefficient. All tests were two-sided and performed with the Statistica Base 11 package (StatSoft, Inc., Tulsa, OK, USA). The level of statistical significance was set at 0.05. False discovery rate (FDR) was controlled using the

Benjamini-Hochberg procedure carried out upon the results of all significance test performed within the study. At the baseline significance level of 0.05, the estimated FDR is 20%, indicating 80% of the presented significant results to be true positives. A conservative overall FDR of 5% would require the individual significance level of 0.005.

The complete primary morphometric data from our samples (see S3 Table) have been made publicly available for further analyses.

Results

Characteristics of the examined individuals are presented in Table 2. The AAA group showed a trend toward a higher proportion of males and a significantly higher mean age.

Comparisons of AAA and non-AAA samples are summarized in Table 3. AAA samples contained significantly less actin, desmin, elastin (Fig 1) and osteoprotegerin, more collagen, macrophages, neutrophils, T lymphocytes, B lymphocytes, hypoxic cells and PTX3, and a greater density of VV (Fig 2) than did non-AAA samples. Microvascular density was related to inflammatory cell infiltrates, PTX3 expression and hypoxia.

Table 2. Data of patients.

	AAA patient (n = 39)	Control group (n = 8)	p value
Male n (%)	32 (82%)	4 (50%)	0.057
Age (years)	70 (6.7)	51 (10.4)	0.00024
Average size of aneurysm (mm)	55 (11.8)	Not applicable	
Diabetes mellitus	8 (18%)	1 (13%)	NS
Hypertension	27 (61%)	3 (38%)	NS
Ischemic heart disease	18 (41%)	2 (25%)	NS
Peripheral artery disease	12 (27%)	4 (50%)	NS
Smoker—current	22 (56%)	3 (38%)	NS
Smoker—former	9 (23%)	2 (25%)	NS
Non-smoker	8 (21%)	3 (38%)	NS

Values are the median (SD) or frequency (relative frequency). NS–not significant.

https://doi.org/10.1371/journal.pone.0224818.t002

The correlations among the quantitative parameters among AAA patients are presented in Fig 3 and those among all examined individuals are presented in Fig 4.

Microvascular density was moderately positively correlated with hypoxia, neutrophils, macrophages, B lymphocytes and the clinically measured size of aneurysms in all samples and with neutrophils, macrophages, B lymphocytes and the aneurysm size in AAA samples.

OPG was positively moderately correlated with actin and elastin in all samples. OPG was positively moderately correlated with macrophages and B lymphocytes in the wall of AAA.

Markers of hypoxic cells were positively moderately correlated with neutrophils, T and B lymphocytes and patient age in all samples, while in AAA samples, the hypoxic cells were moderately positively correlated with actin and negatively correlated with collagen.

Men had fewer hypoxic cells than women (p = 0.001) in the AAA samples. Age had only a weak effect on the vascular density (r = 0.3; p = 0.032) in AAA samples. There was no influence of smoking on the evaluated histological parameters. The qualitative histological findings are

Table 3. Testing the differences between the AAA vs. the non-AAA samples of aortic wall.

	AAA			Non AAA			
Parameter	**Median**	**Lower Quartile**	**Upper Quartile**	**Median**	**Lower Quartile**	**Upper Quartile**	**p-value**
A_A*(actin,int+media)*	2.1	1.8	3.1	15.3	11.1	17.0	0.000013
A_A*(desmin,int+media)*	0.3	0.1	0.4	0.6	0.4	0.7	0.025
A_A*(elastin,int+media)*	0.8	0.2	1.4	3.9	3.1	5.2	0.00015
A_A*(collagen,int+media)*	9.0	3.2	13.4	1.2	0.7	5.1	0.0034
A_A*(MAC387, wall)*	1.2	0.9	1.8	0.7	0.5	1.0	0.039
A_A*(myeloperoxidase, wall)*	2.5	2.0	3.0	1.2	1.0	2.6	0.046
A_A*(CD3, wall)*	0.4	0.3	0.5	0.2	0.1	0.3	0.009
A_A*(CD20, wall)*	0.7	0.4	1.0	0	0	0.2	0.0001
A_A*(HIF 1-alpha, wall)*	0.9	0.6	1.0	0.3	0.2	0.4	0.001
A_A*(osteoprotegerin, wall)*	0.6	0.5	0.9	1.4	1.3	1.8	0.001
A_A*(pentraxin-3, wall)*	0.7	0.5	0.9	0.4	0.3	0.5	0.007
Q_A*(CD31-positive microvessels,wall)* (mm^{-2})	74.4	52.4	98.1	37.2	24.5	38.9	0.0006

A_A*(component, space)*: Area fraction of the respective components within their reference spaces (%); Q_A: number of microvessel profiles per section area; *int+media*: data pooled from the intima and media; *wall*: data pooled the wall (i.e., from intima, media and adventitia). The abbreviations of all the parameters are explained in S2 Table.

https://doi.org/10.1371/journal.pone.0224818.t003

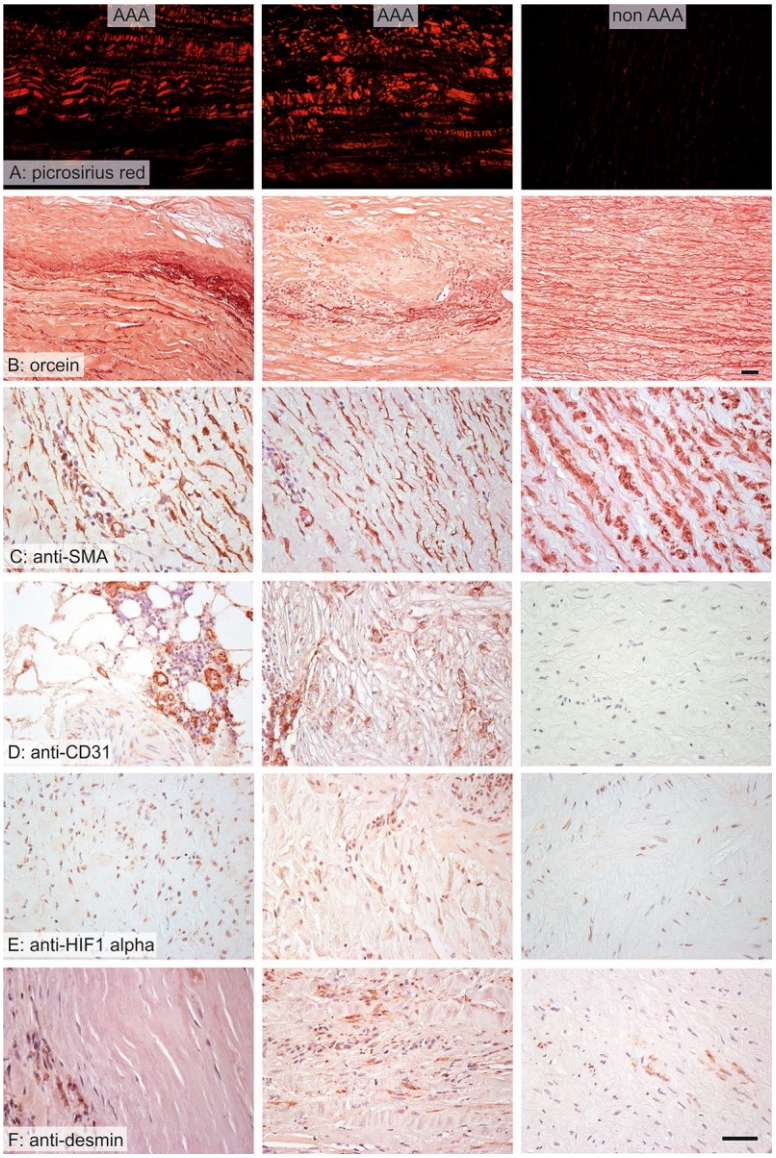

Fig 1. Wall composition in AAA (left and middle columns) and non-AAA samples (right column). In the AAA samples, the collagen was more abundant (A), the elastin was partially or mostly destroyed (B), the wall contained more vasa vasorum (D), expressed more hypoxia markers (E) and less contractile phenotype of vascular smooth muscle (C, F). Stained with picrosirius red (A), orcein (B), and immunohistochemistry with anti-smooth muscle actin antibody (C) for visualization of the contractile phenotype of vascular smooth muscle cells, anti-CD31 (D) for visualization of endothelium, anti-HIF 1-alpha (E) for visualization of tissue hypoxia and anti-desmin (F) for visualization of the contractile phenotype of vascular smooth muscle cells; nuclei were stained with Gill's hematoxylin; scale bar 50 μm.

https://doi.org/10.1371/journal.pone.0224818.g001

shown as a composite in Fig 5. Our primary data from histological quantitative analysis are shown in S3 Table.

Discussion

The aim of this study was to identify markers to recognize the presence and vulnerability of AAA because screening is not performed using Ultrasonography or Computer Tomography in most countries. Our AAA samples contained a higher microvessel density than non-AAA

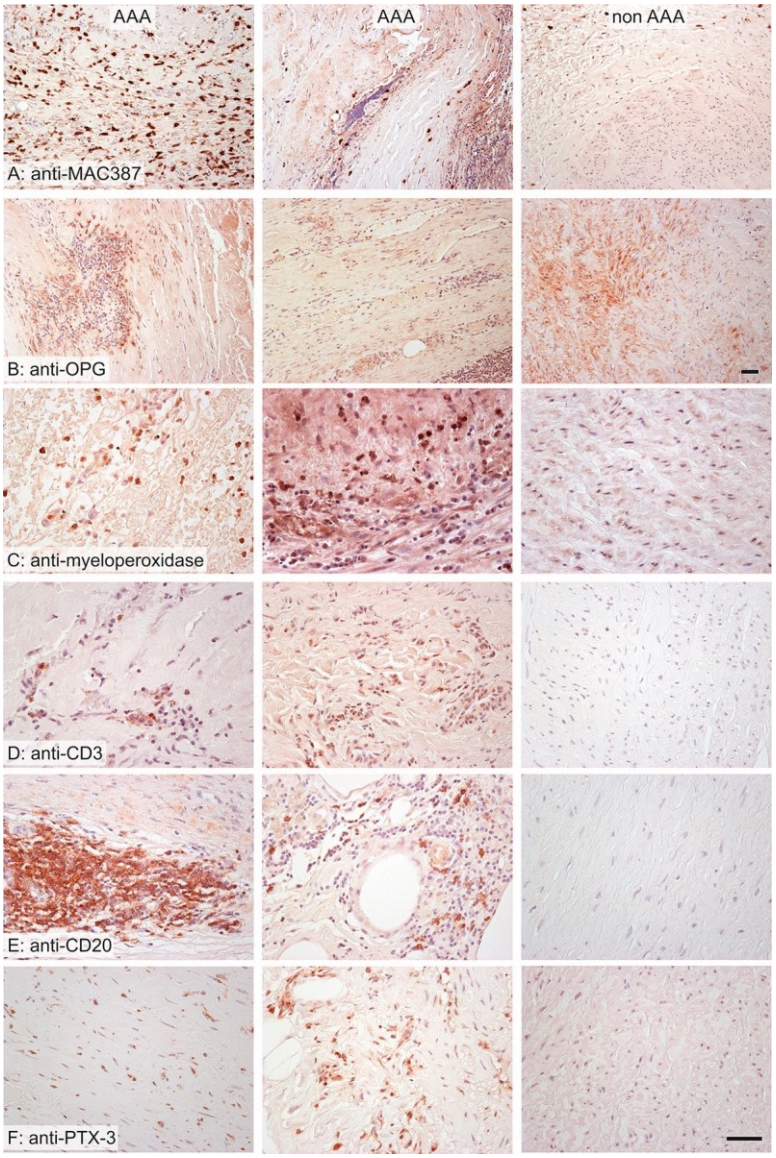

Fig 2. Wall composition in AAA (left and middle column) and non-AAA samples (right column). The AAA samples were more infiltrated by macrophages (A), neutrophils (B), T lymphocytes (D) and B lymphocytes (E). The distribution of osteoprotegerin (OPG) was more diffuse in non-AAA (C). The expression of pentraxin 3 was greater in AAA samples (F). Stained immunohistochemistry with anti-MAC387 antibody (A) for visualization of macrophages, anti-osteoprotegerin (B), anti-myeloperoxidase (C) for visualization of neutrophilic granulocytes, anti-CD3 (D) for visualization of T lymphocytes, anti-CD20 (E) for visualization of B lymphocytes, anti-pentraxin 3 (F); nuclei were stained with Gill's hematoxylin; scale bar 50 μm.

https://doi.org/10.1371/journal.pone.0224818.g002

samples, which is in accordance with the findings of Rodella *et al*. [4]. As in the study by Eberlova´ *et al*., the microvessel density was correlated with the AAA diameter and the inflammatory infiltrates [2]. The number of microvessel profiles correlated positively with hypoxia and immune factors (B lymphocytes, macrophages, neutrophils and PTX3). The number of microvessel profiles correlated positively with hypoxia and immune factors (B lymphocytes, macrophages, neutrophils and PTX3). This correlation might be due to the stimulating effects of inflammatory and hypoxic states on angiogenesis [31]. In human AAA, the adventitial VV has been observed to be stenotic in both small and large AAA, with the sac tissue in these AAA

	A_A (desmin, int+media)	A_A (elastin, int+media)	A_A (collagen, int+media)	A_A (MAC387, wall)	A_A (myeloperoxidase, wall)	A_A (CD3, wall)	A_A (CD20, wall)	A_A (HIF 1-alpha, wall)	A_A (osteoprotegerin, wall)	A_A (pentraxin-3, wall)	Q_A (CD31-positive microvessels, wall) (mm^{-2})	Average size of aneurysm (mm)
A_A (actin,int+media)	0.11	0.08	**-0.33**	0.02	0.23	-0.10	-0.16	**0.35**	0.18	-0.03	0.08	0.27
A_A (desmin,int+media)	-	0.12	0.03	0.11	0.21	0.04	0.04	0.25	0.10	**0.47**	0.14	-0.01
A_A (elastin,int+media)	-	-	-0.16	0.05	-0.03	-0.09	-0.11	0.21	0.15	-0.05	0.08	0.04
A_A (collagen,int+media)	-	-	-	0.05	-0.03	-0.07	0.16	**-0.33**	-0.10	0.24	-0.03	0.05
A_A (MAC387, wall)	-	-	-	-	**0.34**	0.14	**0.41**	0.07	**0.40**	0.02	**0.41**	0.16
A_A (myeloperoxidase, wall)	-	-	-	-	-	0.03	0.26	0.22	0.11	0.21	**0.41**	0.08
A_A (CD3, wall)	-	-	-	-	-	-	0.17	0.07	0.32	0.08	-0.01	0.3
A_A (CD20, wall)	-	-	-	-	-	-	-	0.15	**0.37**	0.06	**0.44**	0.13
A_A (HIF 1-alpha, wall)	-	-	-	-	-	-	-	-	0.19	0.26	0.24	-0.01
A_A (osteoprotegerin, wall)	-	-	-	-	-	-	-	-	-	0.21	0.25	0.18
A_A (pentraxin-3, wall)	-	-	-	-	-	-	-	-	-	-	**0.39**	0.22
Q_A (CD31-positive microvessels, wall) (mm^{-2})	-	-	-	-	-	-	-	-	-	-	-	**0.5**

Fig 3. Correlations of the examined histological parameters, in AAA samples. All correlations significant at p<0.05 are highlighted in boldface. A_A*(component, space)*: Area fraction of the respective components within their reference spaces; Q_A: number of microvessel profiles per section area; *int+media*: data pooled from the intima and media; *wall*: data pooled from the wall (i.e., from intima, media and adventitia). Abbreviations of all the examined parameters are explained in S2 Table.

https://doi.org/10.1371/journal.pone.0224818.g003

being ischemic and hypoxic. Hypoperfusion of the vascular wall vessel could have critical effects on the development of infrarenal AAA [5]. This hypothesis was verified in a rodent model of AAA when VV blood flow was blocked through the tight ligation of the aorta over the catheter [32]. However, the reason for ischemia formation is still unclear. There were indications that the reduced oxygenation of the aortic wall might be due to reduced oxygen diffusion from the lumen due to intraluminal thrombus (ILT) [33]. Notably, more recent analyses indicate that changes in adventitial VV occurred, irrespective of the presence of ILT. Adventitial VV may play an independent role in the perfusion and oxygenation of the aortic wall, with VV stenosis contributing to the ischemia of the aortic wall itself [34]. Furthermore, increased aortic stiffness and hypertension may narrow the lumen of VV. Greater vascular density in AAA was found in older AAA patients. This result is in accordance with the findings [35] that showed an increased VV diameter and area within thoracic aorta in aged subjects. The AAA samples contained a greater number of hypoxic cells than did the non-AAA samples. The number of hypoxic cells correlated positively with immune factors (T and B lymphocytes and neutrophils). There are indications from other research that HIF 1-alpha is pivotal for AAA progression toward rupture [36]. Several factors related to aneurysm susceptibility (including angiotensin II and nicotine) cause the upregulation of MMP-2 and

MMP-9 through aberrantly induced HIF 1-alpha and promote aneurysmal progression [37]. We demonstrated that men

	A_A(desmin, int+media)	A_A(elastin, int+media)	A_A(collagen, int+media)	A_A(MAC387, wall)	A_A(myeloperoxidase, wall)	A_A(CD3, wall)	A_A(CD20, wall)	A_A(HIF 1-alpha, wall)	A_A(osteoprotegerin, wall)	A_A(pentraxin-3, wall)	Q_A(CD31-positive microvessels, wall) (mm^{-2})	Average size of aneurysm (mm)
A_A(actin,int+media)	**0.32**	**0.42**	**-0.49**	-0.2	-0.06	**-0.31**	**-0.47**	-0.08	**0.41**	-0.27	-0.31	0.27
A_A(desmin,int+media)	-	**0.3**	-0.17	-0.11	0.06	-0.05	-0.18	0.06	0.24	0.27	-0.12	0.09
A_A(elastin,int+media)	-	-	**-0.37**	-0.13	-0.20	**-0.32**	**-0.39**	-0.15	**0.36**	-0.26	-0.26	0.09
A_A(collagen,int+media)	-	-	-	0.22	0.16	0.18	**0.39**	-0.01	-0.26	**0.38**	0.21	0.05
A_A(MAC387, wall)	-	-	-	-	**0.45**	0.15	**0.49**	0.16	0.17	0.15	**0.43**	0.26
A_A(myeloperoxidase, wall)	-	-	-	-	-	0.21	**0.41**	**0.35**	-0.04	**0.39**	**0.42**	0.12
A_A(CD3, wall)	-	-	-	-	-	-	**0.36**	**0.35**	0.02	**0.31**	0.22	0.21
A_A(CD20, wall)	-	-	-	-	-	-	-	**0.4**	-0.04	**0.3**	**0.61**	0.12
A_A(HIF 1-alpha, wall)	-	-	-	-	-	-	-	-	-0.1	**0.44**	**0.41**	0.02
A_A(osteoprotegerin, wall)	-	-	-	-	-	-	-	-	-	-0.01	-0.07	0.15
A_A(pentraxin-3, wall)	-	-	-	-	-	-	-	-	-	-	**0.45**	0.09
Q_A(CD31-positive microvessels, wall) (mm^{-2})	-	-	-	-	-	-	-	-	-	-	-	**0.5**

Fig 4. Correlations of the examined histological parameters, in all samples. All correlations significant at p<0.05 are highlighted in boldface. A_A*(component, space)*: Area fraction of the respective components within their reference spaces; Q_A: number of microvessel profiles per section area; *int+media*: data pooled from the intima and media; *wall*: data pooled from the wall (i.e., from intima, media and adventitia). The abbreviations of all the parameters are explained in S2 Table.

https://doi.org/10.1371/journal.pone.0224818.g004

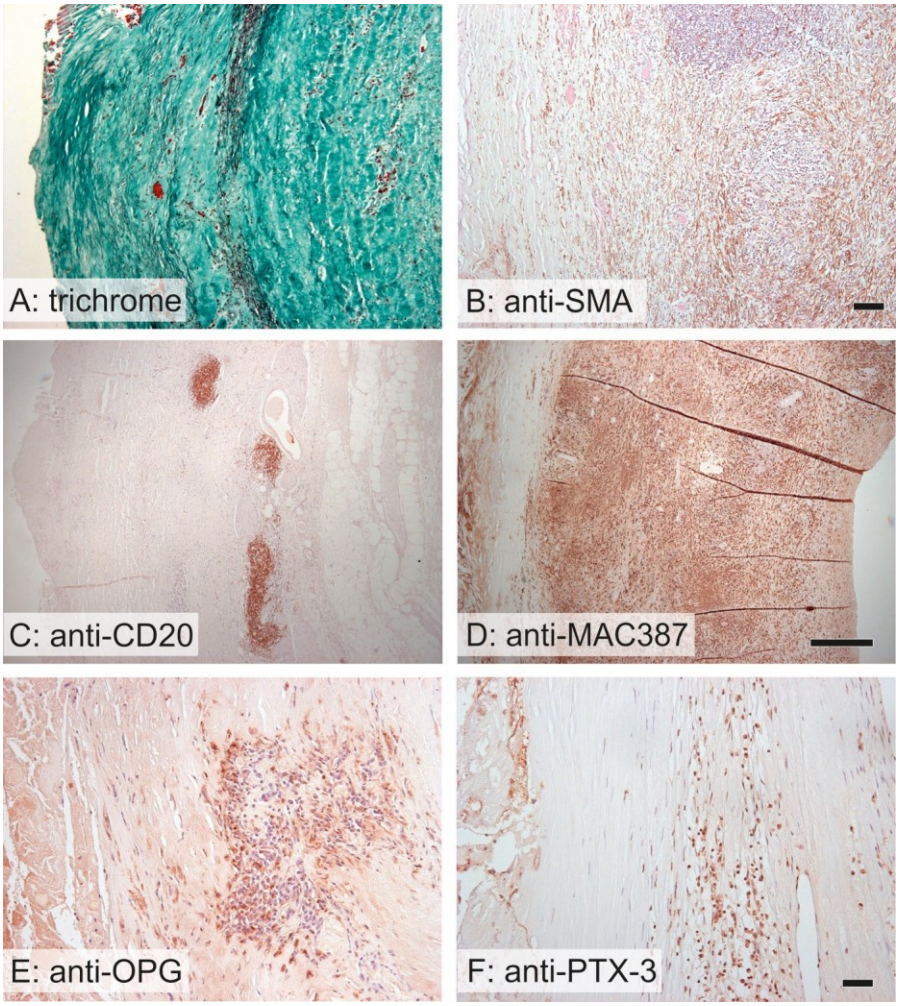

Fig 5. Qualitative findings in AAA samples. A—The basic pattern of the aortic wall was destroyed by newly formed vessels surrounded by inflammatory infiltrates. The elastin fibers (black) were compressed and destroyed. B–The inflammatory cells penetrated among the smooth muscle cells (brown) into the tunica media. C–Lymphocytes (brown) occurred mostly in aggregates resembling lymphoid follicles. D—Rarely, the macrophages (brown) penetrated diffusely the whole wall of the AAA. E–The expression of osteoprotegerin (brown) occurred mostly in the areas infiltrated by leukocytes. F–Similarly, the positivity of pentraxin 3 (brown) also occurred in areas infiltrated by leukocytes. Stained with Verhoeff's hematoxylin and green trichrome (A) and immunohistochemistry with an antibody against smooth muscle actin (B) for visualization of the contractile phenotype of vascular smooth muscle cells, anti-CD20 (C) for visualization of B lymphocytes, anti-MAC387 (D) for visualization of macrophages, antiosteoprotegerin (anti-OPG) (E) and anti-pentraxin 3 (anti-PTX3) (F); nuclei were stained with Gill's hematoxylin; scale bar 100 μm (A, B), 500 μm (C, D) and 50 μm (E, F).

https://doi.org/10.1371/journal.pone.0224818.g005

had fewer hypoxic cells than women in AAA patients. In a study of samples from patients with pulmonary arterial hypertension, the expression of HIF 1-alpha was higher in female than in male pulmonary artery smooth muscle cells [38]. There are differences in HIF 1-alpha signaling between female and male vascular smooth muscle cells [38]. This difference should be analyzed futher, since these findings could be useful for understanding the pathomechanisms of AAA in different genders.

We demonstrated a statistically significantly higher expression of PTX3 in AAA than in non-AAA patients. The PTX3 correlated positively with collagen, hypoxia and immune cells (T and B lymphocytes and neutrophils). These results corresponded with the findings from studies in which the parameters from AAA were compared to samples of ascending aorta without AAA [39,40]. The findings from these studies were not compared with other structural components of AAA tissue. These authors also analyzed PTX3 serum levels. There was no difference between the serum levels of AAA and non-AAA patients. PTX3 expression negatively correlated with the maximum diameter of the aneurysm [39]. In a recent study, PTX3 serum levels in AAA patients were higher than those in non-AAA patients. Serum levels were AAA diameter-independent [41]. The PTX3 expression in our tissue samples also did not correlate with aneurysm diameter. Peak levels of PTX3 in patients with acute aortic dissection were associated with the amount of transient pleural fluid accumulation, which may be associated with inflammatory vascular permeability [42]. Based on our results, we hypothesized that PTX3 might play a role in the pathogenesis of AAA. However, the histological analysis reflected the outcome of the AAA remodeling. Therefore, more evidence is necessary.

The structure of PTX3 is similar to that of CRP, which is from the same pentraxin superfamily. CRP was also suggested as a biomarker of AAA [43–46]. In contrast to PTX3, which is expressed in circulating neutrophils as well as a variety of cells in inflamed tissue (including endothelial cells, fibroblasts, VSMCs and inflammatory cells) [40,47,48]. CRP is synthesized by hepatocytes upon stimulation by systemic proinflammatory cytokines. Therefore, PTX3 is a more accurate marker of the actual inflammatory state and mirrors local inflammation that does not necessarily lead to an increase in systemic cytokines (e.g., in vascular inflammation, even without systemic inflammation) [49]. PTX3 is also less influenced by total cholesterol, high-density lipoprotein, hemoglobin, smoking, obesity or gender [49,50]. Our study provides evidence of the distribution of PTX3, OPG and hypoxic

cells within AAAs, but further analyses relating histological data to biochemical markers are needed.

The AAA samples contained less elastin and more macrophages, neutrophils, T and B lymphocytes and a greater density of VV. These data support the finding of the increasing gene expression of MMP-9, which degrades elastin and plays a role in the proliferation and migration of VSMCs, and intercellular adhesion molecule-1, which promotes leukocyte adhesion to and migration through endothelial cells [6,51].

The AAA samples contained a smaller amount of OPG. These findings from our quantitative analyses support a potential preventive effect of OPG [19].

A limitation of the present study is that the results were based on AAA samples harvested during an open surgical repair of AAA sac. However, many AAA patients undergo endovascular aortic repair [52], where no morphological tissue samples can be removed for research purposes. Moreover, also harvesting of control samples of healthy aorta from organ donors has limitations as the interest of the waiting organ recipients is prioritized over harvesting of samples for research purposes. In addition, bias may have been introduced since the morphometry of our samples was based on 1–2 histological sections per each quantitative parameter. Also, our quantification used two-dimensional routine sections only, whereas some structures (e.g. the vasa vasorum) are three-dimensional and would require more sophisticated quantification techniques, e.g. confocal microscopy or X-ray microtomography. Moreover, also the present study relies on histological analysis, but its conclusions should be further verified using established quantitative techniques (Enzyme-Linked Immunosorbent Assay or western blots) to demonstrate the differences in protein expression more convincingly.

Conclusion

AAA tissue samples contained significantly less actin, desmin, elastin and osteoprotegerin, more collagen, macrophages, neutrophils, T lymphocytes, B lymphocytes, hypoxic cells and PTX3, and a greater density of VV than did non-AAA samples. PTX3 and hypoxia correlated with each other and with T and B lymphocytes and neutrophils. Microvascular density was related to inflammatory cell infiltrates, PTX3 expression, hypoxia and average size of aneurysms. AAA contained altered amounts of structural proteins, implying reduced vascular elasticity. This remodeling of the AAA wall occurred under significant tissue hypoxia, despite a greater density of microvessels than of non-aneurysmal aorta. PTX3 was upregulated in AAA, and its colocalization with the inflammatory infiltrates supports the theory of a potential role for PTX3 as a marker of vascular inflammation. The presence of aortic hypoxia, despite hypervascularization, suggests hypoxia-induced neoangiogenesis that may play a role in AAA pathogenesis. VV angiogenesis of the AAA wall increases its vulnerability.

Supporting information

S1 Table. Primary antibodies used for immunohistochemistry.
(DOC)

S2 Table. Quantitative parameters used for morphometry of the aortic wall.
(DOC)

S3 Table. Primary data from analysis.
(XLS)

Author Contributions

Formal analysis: Petr Hosek.

Investigation: Tereza Blassova, Zbynek Tonar, Vladislav Treska.

Methodology: Tereza Blassova, Petr Tomasek.

Supervision: Jiri Molacek.

Writing – original draft: Tereza Blassova, Zbynek Tonar, Ivana Hollan.

References

1. Ku¨hnl A, Erk A, Trenner M, Salvermoser M, Schmid V, Eckstein H-H. Incidence, Treatment and Mortality in Patients with Abdominal Aortic Aneurysms: An Analysis of Hospital Discharge Data from 2005–
2014. Dtsch Aerzteblatt Online. 2017; https://doi.org/10.3238/arztebl.2017.0391 PMID: 28655374
2. Eberlova´ L, Tonar Z, Witter K, Kř´ız˘kova´ V, Nedorost L, Korabečna´ M, et al. Asymptomatic Abdominal Aortic Aneurysms Show Histological Signs of Progression: a Quantitative Histochemical Analysis.
Pathobiol J Immunopathol Mol Cell Biol. 2013; 80: 11–23. https://doi.org/10.1159/000339304 PMID: 22797551
3. Billaud M, Hill JC, Richards TD, Gleason TG, Phillippi JA. Medial Hypoxia and Adventitial Vasa Vasorum Remodeling in Human Ascending Aortic Aneurysm. Front Cardiovasc Med. 2018; 5. https:// doi.org/10.3389/fcvm.2018.00124 PMID: 30276199
4. Rodella LF, Rezzani R, Bonomini F, Peroni M, Cocchi MA, Hirtler L, et al. Abdominal Aortic Aneurysm and Histological, Clinical, Radiological Correlation. Acta Histochem. 2016; 118: 256–262. https://doi. org/10.1016/j.acthis.2016.01.007 PMID: 26858185
5. Tanaka H, Zaima N, Sasaki T, Sano M, Yamamoto N, Saito T, et al. Hypoperfusion of the Adventitial Vasa Vasorum Develops an Abdominal Aortic Aneurysm. PloS One. 2015; 10: e0134386. https://doi. org/10.1371/journal.pone.0134386 PMID: 26308526
6. Reeps C, Pelisek J, Seidl S, Schuster T, Zimmermann A, Kuehnl A, et al. Inflammatory Infiltrates and Neovessels Are Relevant Sources of MMPs in Abdominal Aortic Aneurysm Wall. Pathobiol J Immunopathol Mol Cell Biol. 2009; 76: 243–252. https://doi.org/10.1159/000228900 PMID: 19816084
7. Cieślik P, Hrycek A. Long Pentraxin 3 (PTX3) in the Light of Its Structure, Mechanismof Action and Clinical Implications. Autoimmunity. 2012; 45: 119–128. https://doi.org/10.3109/08916934.2011.611549 PMID: 21988562
8. Bonacina F, Baragetti A, Catapano AL, Norata GD. Long Pentraxin 3: Experimental and Clinical Relevance in Cardiovascular Diseases. Mediators Inflamm. 2013; 2013: 1–10. https://doi.org/10.1155/2013/ 725102 PMID: 23690668
9. Yigit S, Sari S, Canbolat IP, Arat Ozkan A, Ersanli MK, Gurmen T. Pentraxin-3 a Novel Biomarker for Predicting Coronary Artery Disease. Eur Heart J. 2013; 34: P3108–P3108. https://doi.org/10.1093/ eurheartj/eht309.P3108
10. Buda V, Andor M, Tomescu MC, Cristescu C, Voicu M, Citu I, et al. P2637ACE Inhibitors and ARBs Decrease More Powerful the PTX-3 Plasma Levels of Hypertensive Patients with Endothelial Dysfunction Compared with Other Anti-Hypertensive Drugs, in a Chronic Treatment. Eur Heart J. 2017; 38. https://doi.org/10.1093/eurheartj/ehx502.P2637

11. Nakamura A, Miura S, Shiga Y, Norimatsu K, Miyase Y, Suematsu Y, et al. Is Pentraxin 3 a Biomarker, a Player, or Both in the Context of Coronary Atherosclerosis and Metabolic Factors? Heart Vessels. 2015; 30: 752–761. https://doi.org/10.1007/s00380-014-0553-0 PMID: 25048680

12. Norata GD, Garlanda C, CatapanoAL. The Long Pentraxin PTX3: A Modulator of the Immunoinflammatory Response in Atherosclerosis and Cardiovascular Diseases. Trends Cardiovasc Med. 2010; 20: 35–40. https://doi.org/10.1016/j.tcm.2010.03.005 PMID: 20656213

13. Koole D, Hurks R, Schoneveld A, Vink A, Golledge J, Moran CS, et al. Osteoprotegerin Is Associated with Aneurysm Diameter and Proteolysis in Abdominal Aortic Aneurysm Disease. Arterioscler Thromb Vasc Biol. 2012; 32: 1497–1504. https://doi.org/10.1161/ATVBAHA.111.243592 PMID: 22516062

14. Callegari A, Coons ML, Ricks JL, Rosenfeld ME, Scatena M. Increased Calcification in Osteoprotegerin-Deficient Smooth Muscle Cells: Dependence on Receptor Activator of NF-κB Ligand and Interleukin 6. J Vasc Res. 2014; 51: 118–131. https://doi.org/10.1159/000358920 PMID: 24642764

15. Morony S, Tintut Y, Zhang Z, Cattley RC, Van G, Dwyer D, et al. Osteoprotegerin Inhibits Vascular Calcification without Affecting Atherosclerosis in Ldlr(-/-) Mice. Circulation. 2008; 117: 411–420. https://doi. org/10.1161/CIRCULATIONAHA.107.707380 PMID: 18172035

16. Jono S, Ikari Y, Shioi A, Mori K, Miki T, Hara K, et al. Serum Osteoprotegerin Levels Are Associated with the Presence and Severity of Coronary Artery Disease. Circulation. 2002; 106: 1192–1194. https:// doi.org/10.1161/01.cir.0000031524.49139.29 PMID: 12208791

17. Moran CS, McCann M, Karan M, Norman P, Ketheesan N, Golledge J. Association of Osteoprotegerin With Human Abdominal Aortic Aneurysm Progression. Circulation. 2005; 111: 3119–3125. https://doi. org/10.1161/CIRCULATIONAHA.104.464727 PMID: 15939823

18. Bennett BJ, Scatena M, Kirk EA, Rattazzi M, Varon RM, Averill M, et al. Osteoprotegerin Inactivation Accelerates Advanced Atherosclerotic Lesion Progression and Calcification in Older ApoE-/- Mice. Arterioscler Thromb Vasc Biol. 2006; 26: 2117–2124. https://doi.org/10.1161/01.ATV.0000236428.91125.e6 PMID: 16840715

19. Bumdelger B, Kokubo H, Kamata R, Fujii M, Yoshimura K, Aoki H, et al. Osteoprotegerin Prevents Development of Abdominal Aortic Aneurysms. PloS One. 2016; 11: e0147088. https://doi.org/10.1371/ journal.pone.0147088 PMID: 26783750

20. Bancroft JD, Gamble M. Theory and Practice of Histological Techniques. [Edinburgh]: Churchill Livingstone; 2008.

21. Kocova´ J. Overall Staining of Connective Tissue and the Muscular Layer of Vessels. Folia Morphol. 1970; 18: 293–295.

22. Rich L, Whittaker P. Collagen and Picrosirius Red Staining: a Polarized Light Assessment of Fibrillar Hue and Spatial Distribution. Braz J Morphol Sci. 2005; 2005: 97–104.

23. Kubı´kova´ T, Kochova´ P, Bra´zdil J, S˘patenka J, Burkert J, Kra´lı´čkova´ M, et al. The Composition and Biomechanical Properties of Human Cryopreserved Aortas, Pulmonary Trunks, and Aortic and Pulmonary Cusps. Ann Anat—Anat Anz. 2017; 212: 17–26. https://doi.org/10.1016/j.aanat.2017.03.004 PMID: 28434910

24. Tonar Z, Toma´s˘ek P, Loskot P, Jana´ček J, Kra´lı´čkova´ M, Witter K. Vasa Vasorum in the Tunica Media and Tunica Adventitia of the Porcine Aorta. Ann Anat—Anat Anz. 2016; 205: 22–36. https://doi.org/10. 1016/j.aanat.2016.01.008 PMID: 26844625

25. Houdek K, Mola´ček J, Třes˘ka V, Kř´ız˘kova´ V, Eberlova´ L, Boudova´ L, et al. Focal Histopathological Progression of Porcine Experimental Abdominal Aortic Aneurysm is Mitigated by Atorvastatin. Int Angiol J Int Union Angiol. 2013; 32: 291–306.

26. Mouton PR. Principles and Practices of Unbiased Stereology: an Introduction for Bioscientists. Baltimore: Johns Hopkins University Press; 2002.

27. Tonar Z, Kubı´kova´ T, Prior C, Demje´n E, Lis˘ka V, Kra´lı´čkova´ M, et al. Segmental and Age Differences in the Elastin Network, Collagen, and Smooth Muscle Phenotype in the Tunica Media of the Porcine

Aorta. Ann Anat Anat Anz Off Organ Anat Ges. 2015; 201: 79–90. https://doi.org/10.1016/j.aanat.2015.05.005 PMID: 26232584

28. Tonar Z, Egger GF, Witter K, Wolfesberger B. Quantification of Microvessels in Canine Lymph Nodes. Microsc Res Tech. 2008; 71: 760–772. https://doi.org/10.1002/jemt.20619 PMID: 18615685

29. Howard V, Reed MG. Unbiased Stereology: Three-Dimensional Measurement in Microscopy. Liverpool: QTP; 2010.

30. Witter K, Tonar Z, Scho¨pper H. How many Layers has the Adventitia?—Structure of the Arterial Tunica Externa Revisited. Anat Histol Embryol. 2017; 46: 110–120. https://doi.org/10.1111/ahe.12239 PMID: 27282337

31. Holmes DR, Liao S, Parks WC, Thompson RW. Medial Neovascularization in Abdominal aortic Aneurysms: a Histopathologic Marker of Aneurysmal Degeneration with Pathophysiologic Implications. J Vasc Surg. 1995; 21: 761–771; discussion 771–772. https://doi.org/10.1016/s0741-5214(05)80007-2 PMID: 7539511

32. Tanaka H, Unno N, Yata T, Kugo H, Zaima N, Sasaki T, et al. Creation of a Rodent Model of Abdominal Aortic Aneurysm by Blocking Adventitial Vasa Vasorum Perfusion. J Vis Exp. 2017; https://doi.org/10. 3791/55763 PMID: 29155740

33. Vorp DA, Lee PC, Wang DH, Makaroun MS, Nemoto EM, Ogawa S, et al. Association of Intraluminal Thrombus in Abdominal Aortic Aneurysm with Local Hypoxia and Wall Weakening. J Vasc Surg. 2001; 34: 291–299. https://doi.org/10.1067/mva.2001.114813 PMID: 11496282

34. Tanaka H, Zaima N, Sasaki T, Hayasaka T, Goto-Inoue N, Onoue K, et al. Adventitial Vasa Vasorum Arteriosclerosis in Abdominal Aortic Aneurysm. PloS One. 2013; 8: e57398. https://doi.org/10.1371/ journal.pone.0057398 PMID: 23460850

35. Popescu MR, Butcovan D, Folescu R, Motoc A, Zamfir CL. Thoracic Aorta Dissection—Assessment of Aortic Adventitia Involvement. Rom J Leg Med. 2013; 21: 207–2014. doi: 0.4323/rjlm.2013.207

36. Ga¨bel G, Northoff BH, Weinzierl I, Ludwig S, Hinterseher I, Wilfert W, et al. Molecular Fingerprint for Terminal Abdominal Aortic Aneurysm Disease. J Am Heart Assoc. 2017; 6. https://doi.org/10.1161/JAHA.117.006798 PMID: 29191809

37. Tsai S-H, Huang P-H, Hsu Y-J, Peng Y-J, Lee C-H, Wang J-C, et al. Inhibition of Hypoxia Inducible Factor-1α Attenuates Abdominal Aortic Aneurysm Progression through the Down-Regulation of Matrix Metalloproteinases. Sci Rep. 2016; 6: 28612. https://doi.org/10.1038/srep28612 PMID: 27363580

38. Docherty CK, Nilsen M, MacLean MR. Influence of 2-Methoxyestradiol and Sex on Hypoxia-Induced Pulmonary Hypertension and Hypoxia-Inducible Factor-1-α. J Am Heart Assoc. 2019; 8: e011628. https://doi.org/10.1161/JAHA.118.011628 PMID: 30819028

39. Sawada H, Naito Y, Oboshi M, Iwasaku T, Morisawa D, Okuhara Y, et al. Pentraxin 3 Expression in Human Abdominal Aortic Aneurysm. Circulation. 2014; 2014: A15060.

40. Sawada H, Naito Y, Oboshi M, Soyama Y, Nishimura K, Eguchi A, et al. Increment of Pentraxin3 Expression in Abdominal Aortic Aneurysm. Int J Cardiol. 2015; 195: 281–282. https://doi.org/10.1016/j. ijcard.2015.05.177 PMID: 26056957

41. Molacek J, Treska V, Zeithaml J, Hollan I, Topolcan O, Pecen L, et al. Blood Biomarker Panel Recommended for Personalized Prediction, Prognosis, and Prevention of Complications Associated with Abdominal Aortic Aneurysm. EPMA J. 2019; 10: 125–135. https://doi.org/10.1007/s13167-019-00173-2 PMID: 31258818

42. Arao K, Fujiwara T, Taniguchi Y, Jinnouchi H, Sasai H, Matsumoto M, et al. Implications of Pentraxin 3 Levels in Patients with Acute Aortic Dissection. Heart Vessels. 2015; 30: 211–217. https://doi.org/10.1007/s00380-014-0470-2 PMID: 24474442

43. Folsom Aaron R., Yao Lu, Alonso Alvaro, Lutsey Pamela L., Missov Emil, Lederle Frank A., et al. Circulating Biomarkers and Abdominal Aortic Aneurysm Incidence. Circulation. 2015; 132: 578–585. https:// doi.org/10.1161/CIRCULATIONAHA.115.016537 PMID: 26085454

44. Henriksson AE, Lindqvist M, Sihlbom C, Bergstro¨m J, Bylund D. Identification of Potential Plasma Biomarkers for Abdominal Aortic Aneurysm Using Tandem Mass Tag Quantitative Proteomics. Proteomes.
2018; 6. https://doi.org/10.3390/proteomes6040043 PMID: 30340394

45. Moris D, Mantonakis E, Avgerinos E, Makris M, Bakoyiannis C, Pikoulis E, et al. Novel Biomarkers of Abdominal Aortic Aneurysm Disease: Identifying Gaps and Dispelling Misperceptions. BioMed Res Int. 2014; 2014: 1–13. https://doi.org/10.1155/2014/925840 PMID: 24967416

46. Urbonavicius S, Urbonaviciene G, Honore´ B, Henneberg EW, Vorum H, Lindholt JS. Potential Circulating Biomarkers for Abdominal Aortic Aneurysm Expansion and Rupture—a Systematic Review. Eur J Vasc Endovasc Surg. 2008; 36: 273–280. https://doi.org/10.1016/j.ejvs.2008.05.009 PMID: 18639476

47. Fornai F, Carrizzo A, Forte M, Ambrosio M, Damato A, Ferrucci M, et al. The Inflammatory Protein Pentraxin 3 in Cardiovascular Disease. Immun Ageing A. 2016; 13: 25. https://doi.org/10.1186/s12979-0160080-1 PMID: 27559355

48. Cabiati M, Svezia B, Verde A, Caselli C, Del Ry S. P3401Pentraxin 3, a Novel Inflammatory Marker in Heart Failure Patients: Its Expression in Circulating Leukocytes as a Function of Clinical Severity. Eur Heart J. 2017; 38. https://doi.org/10.1093/eurheartj/ehx504.P3401

49. Liu H, Guan S, Fang W, Yuan F, Zhang M, Qu X. Associations Between Pentraxin 3 and Severity of Coronary Artery Disease. BMJ Open. 2015; 5: e007123. https://doi.org/10.1136/bmjopen-2014-007123 PMID: 25854969

50. Kinoshita M, Yokote K, Arai H, Iida M, Ishigaki Y, Ishibashi S, et al. Japan Atherosclerosis Society (JAS) Guidelines for Prevention of Atherosclerotic Cardiovascular Diseases 2017. J Atheroscler Thromb.
2018; 25: 846–984. https://doi.org/10.5551/jat.GL2017 PMID: 30135334

51. Armstrong PJ, Johanning JM, Calton WC, Delatore JR, Franklin DP, Han DC, et al. Differential Gene Expression in Human Abdominal Aorta: Aneurysmal versus Occlusive Disease. J Vasc Surg. 2002; 35:
346–14. https://doi.org/10.1067/mva.2002.121071 PMID: 11854734

52. Patel R, Sweeting MJ, Powell JT, Greenhalgh RM. Endovascular Versus Open Repair of Abdominal Aortic Aneurysm in 15-years' Follow-up of the UK Endovascular Aneurysm Repair Trial 1 (EVAR Trial
1): a Randomised Controlled Trial. The Lancet. 2016; 388: 2366–2374.
https://doi.org/10.1016/S01406736(16)31135-7

Annals of Anatomy 228 (2020) 151434

Contents lists available at ScienceDirect

Annals of Anatomy

journal homepage: www.elsevier.com/locate/aanat

RESEARCH ARTICLE

Histological mapping of porcine carotid arteries—An animal model for the assessment of artificial conduits suitable for coronary bypass grafting in humans

Petr Tomásek[a,b], Zbynek Tonar[a,*], Martina Grajciarová[a], Tomás Kural[a], Daniel Turek[c,d], Jana Horáková[e], Richard Pálek[f], Lada Eberlová[g], Milena Králícková[a], Václav Liska[f]

[a] Department of Histology and Embryology and Biomedical Center, Faculty of Medicine in Pilsen, Charles University, Karlovarska 48, 30166 Pilsen, Czech Republic [b] Department of Forensic Medicine, Second Faculty of Medicine, Charles University and Na Bulovce Hospital, Budinova 2, 18081 Prague, Czech Republic [c] First Faculty of Medicine, Charles University in Prague, Katerinska 32, 12108 Prague 2, Czech Republic [d] Department of Cardiac Surgery, Institute for Clinical and Experimental Medicine, Videnska 1958/9, 14021 Prague, Czech Republic

[e] Department of Nonwovens and Nanofibrous Materials, Faculty of Textile Engineering, Technical University of Liberec, Studentska 2, 46117 Liberec, Czech Republic [f] Department of Surgery and Biomedical Center, Faculty of Medicine in Pilsen, Charles University, Husova 3, 30605 Pilsen, Czech Republic [g] Department of Anatomy, Faculty of Medicine in Pilsen, Charles University, Karlovarska 48, 30166 Pilsen, Czech Republic

article info

Article history:
Received 8 July 2019
Received in revised form
12 September 2019 Accepted 11 October 2019

Keywords:
Bypass grafting
Cardiac surgery
Carotid artery
Coronary arteries
Internal thoracic artery
Pig
Stereology

abstract

Background: Using animal models in experimental medicine requires mapping of their anatomical variability. Porcine common carotid arteries (CCA) are often preferred for the preclinical testing of vascular grafts due to their anatomical and physiological similarity to human small-diameter arteries. Comparing the microscopic structure of animal model organs to their human counterparts reveals the benefits and limitations of translational medicine.

Methods: Using quantitative histology and stereology, we performed an extensive mapping of the regional proximodistal differences in the fractions of elastin, collagen, and smooth muscle actin as well as the intima-media and wall thicknesses among 404 segments (every 1 cm) of porcine CCAs collected from male and female pigs (n = 21). We also compared the microscopic structure of porcine CCAs with segments of human coronary arteries and one of the preferred arterial conduits used for the coronary artery bypass grafting (CABG), namely, the internal thoracic artery (ITA) (n = 21 human cadavers).

Results: The results showed that the histological structure of left and right porcine CCA can be considered equivalent, provided that gross anatomical variations of the regular branching patterns are excluded. The proximal elastic carotid (51.2% elastin, 4.2% collagen, and 37.2% actin) transitioned to more muscular middle segments (23.5% elastin, 4.9% collagen, 54.3% actin) at the range of 2–3 centimeters and then to even more muscular distal segments (17.2% elastin, 4.9% collagen, 64.0% actin). The resulting morphometric data set shows the biological variability of the artery and is made available for biomechanical modeling and for performing a power analysis and calculating the minimum number of samples per group when planning further experiments with this widely used large animal model.

Conclusions: Comparison of porcine carotids with human coronary arteries and ITA revealed the benefits and the limitations of using porcine CCAs as a valid model for testing bioengineered small-diameter CABG vascular conduits. Morphometry of human coronary arteries and ITA provided more realistic data for tailoring multilayered artificial vascular prostheses and the ranges of values within which the conduits should be tested in the future. Despite their limitations, porcine CCAs remain a widely used and well characterized large animal model that is available for a variety of experiments in vascular surgery.

1. Introduction

Using animal models in experimental medicine requires mapping of their anatomical variability. This is an necessary condition

* Corresponding author.
E-mail address: tonar@lfp.cuni.cz (Z. Tonar).

https://doi.org/10.1016/j.aanat.2019.151434

for performing a power analysis to justify the numbers of animals and biological samples required for detecting any biological effects targeted in the experiment. Comparing the microscopic structure of animal model organs to their human counterparts reveals the benefits and limitations of translational medicine. This approach is needed for a realistic interpretation of the results gained in animal models and for bridging the gaps between experimental medicine and possible benefits for human patients where translational research is concerned (Lossi et al., 2016). One of the important issues in vascular medicine is the manufacturing of bioengineered vascular grafts for coronary artery bypass grafting (CABG), their optimization (Szafron et al., 2019) and their testing in animal models. The present study was motivated by the lack of quantitative data mapping the microscopic structure of one of the important models in vascular surgery, namely, the porcine common carotid artery (CCA).

1.1. Porcine CCA as a animal models in experimental studies

The porcine CCA is often preferred for the preclinical testing of vascular grafts due to its anatomical and physiological similarity to human small-diameter arteries (García et al., 2011). Porcine CCAs are currently often used as an experimental model in vascular surgery, such as designing stents used in the treatment of CCA obstruction or stenosis and in acute ischemic stroke (Fong et al., 2017; Jiang et al., 2016; Nikoubashman et al., 2018; Stewart et al., 2017; Sun et al., 2019; Zhou et al., 2016). To date, porcine CCAs have been used for testing various types of bioengineered vascular grafts, such as polytetrafluoroethylene (PTFE) and electrospun poly--caprolactone nanofibers (PCL) (Kritharis et al., 2012; Jaramillo et al., 2018; Mrowczynski et al., 2014; Tzchori et al., 2018).

The CCA is a paired artery located in the area of the neck vertebrae approximately 2–2.5 cm under the skin (Anderson et al., 2018). Both arteries originate from the brachiocephalic trunk, which in turn stems from the aortic arch (Dondelinger et al., 1998; Popesko, 1978). The CCA passes along the ventral surface from its source of origin and then through the dorsolateral surface of the trachea. The recurrent laryngeal nerve is on the ventral side of the CCA, the vagosympathetic trunk is on the dorsal side and the internal jugular vein is on the lateral side (Popesko, 1978). CCA branching occurs in the following order: caudal thyroid artery (which is only on the left side), cranial thyroid artery, cranial laryngeal artery, internal carotid artery and external carotid artery (Popesko, 1978). In adult pigs, the proximal diameter is approximately 5–6 mm (Dondelinger et al., 1998; García et al., 2011).

From an anatomical and surgical point of view there are several advantages, such as easy surgical access with the possibility of using the same surgical instruments and suture materials as employed in humans (Anderson et al., 2018). Porcine CCA is easily accessible for catheterization (Dondelinger et al., 1998). The sufficient length of porcine CCA with minimum branching makes the implantation of grafts feasible. The patency of the grafts can be easily monitored using Doppler USG sonography (Anderson et al., 2018). Porcine CCA exhibits a comparable pressure resistance to that of autologous grafts for CABG, namely, the human saphenous veins (Negishi et al., 2011).

From the viewpoint of histology, the proximal porcine CCA was reported to contain more elastin than its distal segments (Sokolis et al., 2011; García et al., 2013, 2011). Distally, elastin is substituted by smooth muscle cells (García et al., 2013, 2011; Weizsäcker et al., 2014).

1.2. Autologous conduits for CABG

CABG is the most common cardiac surgery procedure performed worldwide. Appropriate graft selection, in addition to precise surgical techniques, is essential to acquire good long-term results. The severity of natural vessel stenosis and capacious (ample) target vessel run-off are among the well-known factors determining long-term graft patency. In terms of patients' 10-year survival, the superiority of the left internal thoracic artery (ITA) anastomozed to the left anterior descending coronary artery (LAD; anterior interventricular branch of the left coronary artery) was proven more than 30 years ago (Loop et al., 1986), and left ITA to LAD grafting remains the cornerstone of modern coronary bypass surgery. ITA, as a small-diameter elastic type artery, is known to be resistant to vasospasms, neointimal hyperplasia and atherosclerosis due to a considerable production of anti-inflammatory and vasoactive substances, especially nitric oxide (Sisto and Isola, 1989; Wharton et al., 1994; Otsuka et al., 2013). According to a functional classification of arterial grafts, the ITA is a somatic artery with considerable amounts of elastic lamellae and with a lower tendency towards spasticity than other autologous conduits used for CABG (He, 2013). Other commonly used autologous grafts include radial artery (Gaudino et al., 2005), saphenous veins (Yazdani et al., 2013), the right gastroepiploic artery (Martínez-González et al., 2017) and some other rarely used alternative grafts used in patients with a complete lack of suitable conduits (Losko et al., 2016).

1.3. Tissue-engineered small diameter vascular grafts

Blood vessel replacement with a small-diameter (<6 mm) graft represents the holy grail of peripheral vascular surgery (Kakisis et al., 2005). Various materials and production techniques have been developed in the search for vascular prostheses (Chlupac et al., 2009; Naito et al., 2011; Pashneh-Tala et al., 2016; Ong et al., 2017). Prostheses based on polyethylene terephthalate (PETE), PTFE or polyurethane work well in the replacement of vessels with large diameters. When such prostheses are used as a small-diameter replacement, an unfavorable healing process has been described in terms of thrombogenicity as a reason for the lack of endothelium together with anastomotic intimal hyperplasia caused by local changes in blood flow (Sarkar et al., 2007; Chlupac et al., 2009). Therefore, novel biodegradable materials based on, for example, polyesters (de Valence et al., 2012a,b; Tara et al., 2014), collagen (Menasche et al., 1984), elastin (Wise et al., 2011; Koens et al., 2015) and silk fibroin (Wang et al., 2010; McClure et al., 2012) are under development of ideal vascular grafts. These materials generally support the endothelialization of the inner surface of the prosthesis, ensuring a long-term nonthrombogenic surface, facilitating healing and enabling the regeneration of functional vessels. However, degradation happens concurrently with the healing process, which is difficult to predict.

In addition to the degradation process and its function under in vivo conditions that ensures the ability to remodel, other structural and functional parameters of vascular grafts must be carefully considered. From the viewpoint of mechanics, vessel replacements must be compliant and possess sufficient burst strength. For surgical handling, suture retention strength is required. A comparison of the mechanical properties of clinically available grafts and human vessels is reported in a study by Johnson et al. (2015). Last but not least, the prosthesis has to be easily handled during surgeries and be immediately available in various sizes. The production cost should be economically favorable, and its storage should be uncomplicated and long-term (Arrigoni et al., 2006).

Bioengineered vascular prostheses can also be modified by the addition of various active substances, such as growth factors (Shin et al., 2012; Wang et al., 2017), heparin (Liu et al., 2014; Qiu et al., 2017), and nitric oxide donors (Koh et al., 2013; Rychter et al., 2016).

Another strategy of producing artificial small-diameter grafts suitable for CABG relies on decellularized conduits (e.g., Lawson et al., 2016; Lindsey et al., 2017). Regardless of the manufacturing strategy, the performance of newly developed grafts is tested in animal models such as rats, rabbits, pigs and sheep (Byrom et al., 2010). Replacement of the carotid artery in a porcine model was used in studies of tissue-engineered vascular grafts prepared from decellularized arteries (Quint et al., 2011; Dahan et al., 2017) or electrospun PCL vascular grafts (Mrowczynski et al., 2014). The ideal vascular graft for clinical application in CABG should have the following attributes: adequate handling characteristics for surgical implantation, ability to maintain the diameter in stress conditions (resistance to kinking, and bending), routing compliance for sequential anastomosis construction, capability to withstand systemic pressure changes over a long time period, low rates of thromboembolic events in low-flow, low-diameter conditions, and low susceptibility to competitive flow. Following implantation, the graft should have growth potential and resistance to infection.

The graft is supposed to be capable of remodeling, responding to a variety of stimuli similarly to a native vessel. The manufacturing range of the conduits required for CABG is expected to be 3–5 mm in diameter to meet the needs of various coronary regions, with acceptable short- and long-term patency comparable at least with saphenous vein grafts. However, proportions between the size of grafts and the native vessels are still under debate (Best et al., 2018).

1.4. Aims of the study

To the best of our knowledge, no quantitative histological studies are available that demonstrate how the microscopic structure changes along the macroscopic segments of the relatively long CCA. Moreover, we found no quantitative evidence comparing the histological structure of various segments of porcine CCAs with human coronary arteries or with arteries most frequently used as autologous grafts. Significant differences should be expected between the structure of coronary arteries of elderly humans, i.e., the vessels to which the conduits should be applied in patients undergoing CABG, and the porcine carotids as their animal model in relatively young pigs. At the same time, manufacturing porous and multilayered nanofibrous vascular prostheses prepared for in vivo studies in pigs would greatly benefit from morphometry showing the composition and proportions of real blood vessels in humans.

The first aim was to map the differences in the fraction of elastin, collagen, and smooth muscle actin within the intima and media, as well as the intima-media thickness and wall thickness among the segments of porcine CCAs on both the right and left sides. The second aim was to compare the microscopic structure of porcine CCAs with human coronary arteries and one of the preferred arterial conduits, namely, the ITA. These differences should reveal the limitations of using porcine CCAs as a valid model for testing CABG conduits and reveal the ranges of values within which the conduits should be tested in the future.

2. Materials and methods

2.1. Collecting porcine CCAs

Whole CCAs (n = 41) and adjacent arterial branches were obtained from 21 healthy male and female Prestice Black-Pied pigs (Vrtkova, 2015) aged 12–21 weeks and weighing 20–65 kg (35.8 ± 13.3 kg, mean ± SD). The female pigs (n = 12) were, on average, aged 17.3 ± 3 weeks and weighed 40.7 ± 14.5; the male pigs (n = 9) were aged 14.6 ± 2.7 weeks and weighed 39.2 ± 7.2 kg. The animals were part of other research projects on experimental liver surgery and projects approved for training on surgical skills. All the projects numbers (MSMT-42178/2015-4, MSMT-29543/2015-6, MSMT-32067/2015-5) were approved by the local ethical authorities and by the Faculty Committee for the Prevention of Cruelty to Animals. All the animals received humane care in compliance with the European Convention on Animal Care at the Experimental Surgery Facility, Biomedical Center, Faculty of Medicine in Pilsen, Charles University. As described previously (Junatas et al., 2017), the animals were premedicated (with atropine, ketamine and azaperone), anaesthetized (with propofol and fentanyl), relaxed (with pancuronium), intubated, and mechanically ventilated. Fluid infusion and volume restoration were provided (Plasmalyte solution and Gelofusine solution; B-Braun AG, Melsungen, Germany). The animals were sacrificed under anesthesia by administration of cardioplegic potassium chloride solution. Immediately after sacrifice, both left and right CCAs were dissected as shown in Fig. 1A. This resulted in 21 left CCAs and 20 right CCAs (i.e., 20 pairs of right and left CCAs plus one additional left CCA, because the preparation of the right side resulted in a damaged sample in one animal). After dissection, the arteries were photographed and then rinsed, perfused, and immersed in 10% neutral buffered formalin solution. For further histological analyses, each CCA was exhaustively cut into a series of 1-cm long segments, which were consecutively numbered in the proximodistal direction (Fig. 1A). As the length of the CCA varied between 8–13 cm, also the number of segments ranged between 8 and 13 (Supplement 1); each of these segments was examined separately using histology.

2.2. Collecting segments of coronary arteries from human cadavers

Vascular segments representing three human coronary arteries were obtained from 21 human cadavers aged 57–78 years (n = 14 females aged 64.8 ± 5.6 years; n = 7 males aged 71.6 ± 6.5 years) dissected during 2017 at the Department of Forensic Medicine, Second Faculty of Medicine, Charles University. The male-to-female ratio was 2:1 as common in patients undergoing CABG. Collection of samples of organs routinely reviewed during a forensic autopsy is permitted according to the Czech law for educational and scientific purposes. The postmortem interval ranged from 9 to 59 h (29.4 ± 16.3 h). If there was any apparent autolysis detected during the autopsy, the sample was excluded. The immediate cause of death was not taken into account. Although there were no macroscopically injured coronary arteries, all hearts damaged by trauma were excluded.

From the hearts dissected from the thoracic cavities, segments of coronary arteries were taken according to the sampling scheme shown in Fig. 1B–E. From the human left coronary artery (LCA), samples were taken and labeled from the circumflex branch (A1), from the left marginal branch (A2), from the anterior interventricular branch (B1), and from the diagonal branch (B2). From the human right coronary artery (RCA), samples were taken on the right border of the heart (C1), from the posterior interventricular branch (C2), and from the right posterolateral branch (C3). In most of the deceased individuals, circular samples were cut off perpendicularly to the long axis, but if it was necessary (for operational reasons) to collect the samples after the autopsy, the transversal cuts from longitudinally cut coronary arteries were taken perpendicularly to the longitudinal axis of the artery. The arterial segments were fixed in neutral 10% formaldehyde. Only hearts with typical anatomical arrangements of coronary arteries were examined, while the hearts of several individuals with undeveloped posterolateral branches were omitted.

2.3. Collecting segments of ITA from human cadavers

From every individual from whom the samples of coronary arteries were collected, either the whole left ITA was dissected out with the adjacent part of subclavian artery or a stitch mark was made to unambiguously identify the proximal end of the artery for

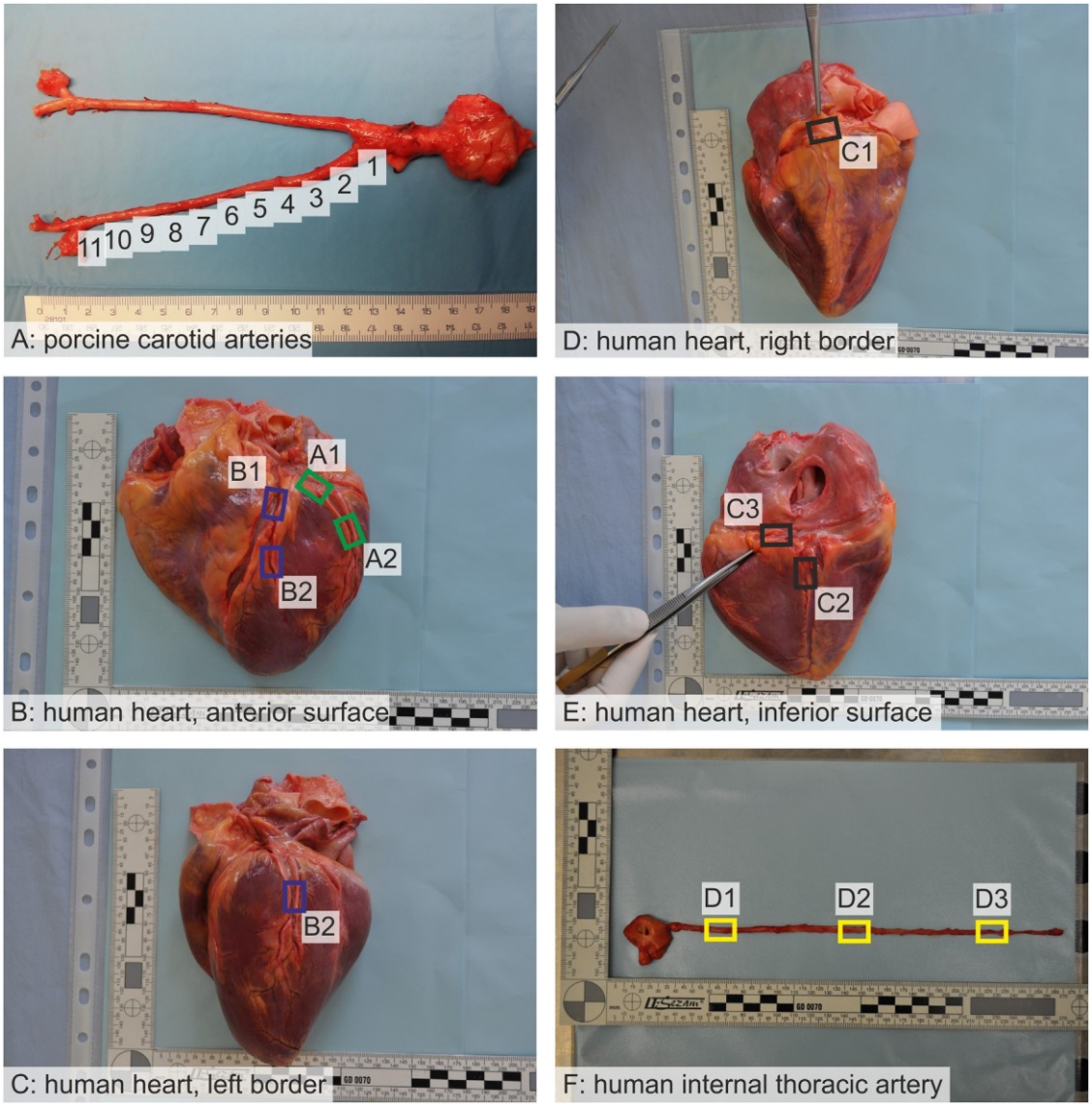

Fig.1.Positionandsamplingofthearterialsegmentsunderstudy.(A)Porcinecarotidarteries,ventralview.Theproximodistalsegmentswerelabeled1–11(shownin therightcarotidarteryonly).(B)Fromthehuman leftcoronaryartery(h-LCA),samplesweretakenandlabeledfromthecircumflexbranch(A1),fromtheleftmarginal branch(A2),fromtheanteriorinterventricularbranch(B1)andfromthediagonalbranch(B2).(C) Thepositionofthesampletakenfromthediagonalbranchoftheanterior interventricularbranchisshownfromanotherviewasthediagonalbranchrunsacrosstheleftventricletowardstheapexoftheheart.(D)From thehumanrightcoronary artery(h-RCA),labeledsamples(C1)weretakenfromtherightborderoftheheart.(E)Moresamplesrepresentingtheh-RCAcamefromtheposteriorinterventricularbranch (C2)andfrom therightposterolateralbranch(C3).(F)Thehumanleftinternalthoracicarterywasrepresentedbythreearterialsegments:themiddleoftheproximalthird (D1),middlethird(D2),andthedistalthird(D3).

sampling. Three segments were taken for histological examination (Fig. 1F), representingtheproximalthird(D1),themiddlethird (D2),andthedistalthird(D3)of theartery.

2.4. Histologicalsectioningandstaining

Each arterial segment was and processed in the Leica TP1020 tissue processor (Leica Biosystems GmbH, Nussloch, Germany) and embedded into paraffin. Fourteen serial histological sections per arterial segment were cut (section thickness of 5 m, Leica RM2255 microtome) perpendicular to the longitudinal axis of each artery. The sections were mounted on histological slides, deparaffinized, and rehydrated. Sections were stained using a set of five staining methods for assessment of overall morphology and wall thickness (hematoxylin-eosin; Verhoeff's hematoxylin and green trichrome), and analysis of main tissue components (orcein stain forelastin;picrosiriusredstainforcollagen;immunohistochemicaldetectionof -smooth muscle actin a vascular smooth muscle marker). The number of sections per stain as well as the details on the staining methods, including the manufacturers, are summarized in Table 1. For immunohistochemical detection of actin, the slides were incubated at 4◦C overnight with Monoclonal Mouse Anti-Human Smooth Muscle Actin antibody, Clone 1A4 DakoCytomation (Glostrup, Denmark), using a 1:500 dilution. This reaction was preceded by a heat-induced epitope retrieval process using Epitope Retrieval Solution pH 9 (Novocastra Leica, Leica Biosystems GmbH, Nussloch, Germany) for five minutes. Visualization of the immunohistochemical reaction was based on diaminobenzidine (DAB+, Liquid; DakoCytomation). Immunohistochemical sections were counterstained with Gill's hematoxylin. All sections were dehydrated in graded ethanol solutions and mounted with a xylene-soluble medium.

Table 1
Histological staining methods used in the study.

Staining	Purpose and visualization of aortic wall components	Number of sections stained
Hematoxylin-eosin (Bancroft and Stevens, 1996)	Overall morphology of the arterial wall	4
Verhoeff's hematoxylin and green trichrome (Kochová, 1970)	Overall morphology, differentiating connective tissue, smooth muscle, measurement of the intima-media and wall thicknesses	4
Picrosiriusred (Direct Red 80, Sigma Aldrich, Munich, Germany) (Rich and Whittaker, 2005)	Type I and type III collagen when observed under circularly polarized light	2
Orcein (Tanzer's orcein, Bowley Biochemical Inc., Danvers, MA, USA)	Elastic membranes, elastic fibers	2
Immunohistochemical detection of alpha-smooth muscle actin	Vascular smooth muscle cells	2

2.5. Micrographs

For quantification of elastin, collagen, and actin, four micrographs were taken in a systematic, uniform, random manner per staining method using a 40× objective mounted on an Olympus BX51 microscope (Olympus Optical Co., Ltd., Tokyo, Japan) (Table 2). In this way, representative samples of the intima and media region were further evaluated (Fig. 2A), similar to Tonar et al. (2015). Measurement of the thicknesses was based on two micrographs captured under a 4× objective, where two opposite micrographs were sufficient to represent the whole arterial profile. As the identical sampling of photographs was performed for each of the 614 vascular segments under study, the total number of micrographs used for quantification exceeded 11,000.

2.6. Morphometry of the arterial wall

The area fractions of elastin, collagen, and actin within the tunica intima and tunica media were assessed using a stereological point grid as implemented in the PointGrid module of the Ellipse software (ViDiTo, Slovak Republic), cf. Howard and Reed (1998) as described and thoroughly tested in vascular research previously (Witte et al., 2010; Eberlova et al., 2013; Tonar et al., 2015; Kubíková et al., 2017). For each staining method and arterial segment, a set of four images (Fig. 2A) was loaded, and the point grid was randomly superposed on the set of micrographs. The number of points hitting the highlighted tissue component (Fig. 2B–D) was counted semiautomatically. Preliminary counting was performed using the Threshold function of the PointGrid module, and the status of each point (i.e., counted in or not counted in) was then visually checked and manually corrected, if necessary. The point grid method also allowed for individual corrections of the tunica intima and media for microcracks, folds or any other possible artifacts. At least 150 intersections of the point grid per section and method (Tschanz et al., 2014) were always used for estimating the area fractions. The precision of the point grid estimates was tested and calibrated on standardized image data sets generated with the TeiGen software (Jiríkˇ et al., 2018). The area fraction of elastin, collagen, and actin was then calculated for each staining method by dividing the number of points hitting the tissue component of interest by the number of points hitting the reference space. The reference space was the profile area of the tunica intima and media within the image field. The values from the four micrographs per staining method and vascular segment were averaged. The quantification was performed blindly by two operators (P.T. and Z.T.) who had no knowledge on the biological status of the specimens that were labelled by laboratory codes only. Each of the two observers was trained to achieve low intraobserver variability with a mean intraclass correlation coefficient for repeated estimations above 0.92 according to Shrout and Fleiss (1979). The interobserver variability had a mean intraclass correlation coefficient 0.90.

The combined thickness of the intima and media was measured. Using the linear probes of the Fiji software (Schindelin et al., 2012), the distance between the intimal surface profile and the media adventitia border profile was measured four times in each sample and then averaged (Fig. 2E). Similarly, the wall thickness was measured as the distance between the intimal surface profile and the outermost layer of the compact connective tissue of the vascular tunica externa. To avoid bias, the outer layer of adjacent loose connective tissue was not considered, as this is known to be greatly affected by anatomical dissection (Kim et al., 2015; Witte et al., 2017).

Additionally, a pilot study of the distribution of collagen within the adventitia was done. It was based on three randomly selected porcine CCAs (n = 30 segments) that were compared to three pairs of randomly selected human coronary arteries (n = 21 segments) and three human ITAs (n = 9 segments).

The complete overview of all the quantitative parameters used in this study for morphometry of the arterial segments is provided in Table 2.

2.7. Assessing the atherosclerotic changes in human coronary arteries

To provide a better characterization of the human coronary arteries and ITAs, any findings of atherosclerotic lesions were classified according to Stary et al. (1994) and Stary (2000). Briefly, this protocol included the following stages: 0 — no atherosclerosis or only adaptive thickening of the intima present; I — initial lesions with isolated macrophage foam cells; II — multiple foam cell layers formed; III — isolated extracellular lipid pools; IV — confluent extracellular lipid core formed; V — fibromuscular tissue layers produced; VI — surface defects, thrombosis; VII — predominant calcification; VIII — predominant fibrous tissue changes. The data will be discussed in the context or regarding more realistic expectations when testing vascular grafts with prospective application to coronary arteries.

2.8. Statistics

In total, 404 segments of porcine CCAs, 147 segments of human coronary arteries, and 63 segments of human ITAs were analyzed. For each vascular segment, the values from each set of micrographs (Table 2) were averaged. As Shapiro–Wilk's test showed aberrations from the normal distribution in some of the variables, nonparametric statistics were applied. The Wilcoxon matched pairs test was used to compare the data on the left vs. right CCA of the same porcine individuals. No comparison was possible between male vs. female pigs, as the female individuals were older and had a higher body weight than the male ones. Kruskal–Wallis ANOVA was used to assess the differences between the porcine CCAs, human coronary arterial segments, and human ITA segments. Correlations among the quantitative variables were evaluated using the Spearman correlation coefficient. These tests were used as available in the StatistiCa Base 11 package (StatSoft, Inc., Tulsa, OK, USA). A power analysis according to Chow et al. (2008) was performed to

Table2
Quantitativeparameters used in this study for morphometry of the arterial segments. The magnification of the microscope objective that was used for quantification of each parameter is provided. The number of micrographs that were sampled is shown as well. See also the Section 2. The A_A (collagen, adventitia) was quantified in 30 segments of CCAs and 30 segments of human arteries as a pilot study only.

Quantitative parameter abbreviation and units	Definition, reference area, interpretation and units	Objective used	Micrographs taken
A_A (elastin,int+med)(−)	The area fraction of elastin stained with orcein within the tunica intima and media reference area.	40×	4
A_A (collagen,int+med)(−)	The area fraction of collagen stained with picrosirius red and observed under polarized light within the tunica intima and media reference area.	40×	4
A_A (collagen,adventitia)(−)	The area fraction of collagen stained with picrosirius red and observed under polarized light within the tunica adventitia reference area.	20×	4
A_A (actin,int+med)(−)	The area fraction of-smooth muscle actin stained immunohistochemically within the tunica intima and media reference area.	40×	4
Int+media thickness(IMT)(m)	The combined thickness of the intima and media, measured as the mean distance between the intimal surface profile and the media-adventitia border profile.	4×	2
Wall thickness(WT)(m)	The wall thickness, measured as the mean distance between the intimal surface profile and the outermost layer of the compact connective tissue of the vascular tunica externa.	4×	2

calculate the sample size needed to detect the expected increase or decrease in the fractions of the tunica intima and media in porcine CCAs.

3. Results

3.1. Gross anatomical findings and variations of porcine carotid and adjacent arteries in the present study

The most common branching pattern is shown in Fig. 3A–C. Three out of 21 cases exhibited anatomical asymmetry between the right and left sides. The findings included an aberrant artery branching from the right subclavian artery (Fig. 3D), an aberrant branch (supplying the thyroid gland) originating from the right CCA (Fig. 3E), and double right external carotid arteries (Fig. 3F).

3.2. Right side vs. left side and segmental differences in the microscopic structure of porcine CCAs

The complete morphometric data for all the vascular segments under study are provided in Supplement 1. Comparison of paired right vs. left porcine carotids (Supplement 2) revealed no differences in the area fractions of collagen and actin. No differences were found in the intima media thickness, wall thickness, and IMT/WT ratio. The right porcine CCA showed a greater fraction of elastin than the left CCA (Wilcoxon matched pairs $p = 0.043$). After excluding three animals with gross anatomical variations on the right side from the statistical analysis, there was no difference between the right vs. left side at all.

Comparison along the proximodistal direction revealed considerable differences in the composition of the tunica intima and media among the porcine carotid arterial segments (Fig. 4A). The area fraction of elastin within the media decreased in the proximodistal direction (Kruskal–Wallis ANOVA $p < 0.001$). At the same time, the area fraction of actin increased in the proximodistal direction ($p < 0.001$). The fraction of collagen remained approximately the same along the whole length. The intima-media thickness (Fig. 4B) showed a decrease in the proximodistal direction ($p < 0.001$), but the total wall thickness varied and tended to increase in the distal segments ($p < 0.001$). Thus, the proportion of the intima-media thickness to the total wall thickness decreased in the proximodistal direction ($p < 0.001$).

Table 3 presents descriptive statistics for calculating the minimum number of samples needed to compare two means when performing a power analysis as part of designing future experiments involving porcine carotid arteries. For this purpose, data from the left and right four proximal segments (1-4 cm from the bifurcation), four middle segments (5–8 cm), and four distal segments (9–12 cm) were pooled.

3.3. Differences between porcine CCAs, human coronary arteries and ITAs

An overall comparison shown in Fig. 5 revealed that neither the mean fractions of actin, elastin, and collagen (Fig. 5A) nor the thicknesses of intima + media and the whole wall (Fig. 5B) can be generally considered equivalent between porcine carotids and human coronary or ITAs.

The morphometric findings are also illustrated histologically in Figs. 6–8. While proximal segments of porcine CCAs (Fig. 6A) contained repeating elastic lamellae as the prevailing component of the tunica media, its middle segments showed approximately balanced proportions of elastin and smooth muscle (Fig. 6B). Distal segments consisted mostly of vascular smooth muscle cells (Fig. 6C). Elastin decreased in the proximodistal direction, while actin increased (Fig. 8A–C). The fraction of collagen oscillated around approximately the same values (Fig. 8A–C) along the whole CCA. The human coronary arteries (Fig. 7A–B) very often lacked rotational symmetry; they contained very often eccentric atherosclerotic lesions (see Supplement 2 for detailed scoring of atherosclerosis). The amounts of elastin and actin were lower than those in porcine CCAs, often reduced only to fragments of the inner and outer elastic laminae (Fig. 8D–E). Either the positivity for actin was diffusely lost, or there were larger actin-negative foci. The ITA (Fig. 7C) was mostly free of atherosclerosis or showed not only adaptive thickening of the intima but also retained a regular pattern of elastic lamellae and actin positivity (Fig. 8F). The elastin was well preserved, occurring in the form of repeating concentric lamellae that alternated with smooth muscle cells.

A detailed visualization of the morphometric results in all the vascular segments under study is shown in Fig. 9. Porcine CCAs had a tendency towards containing more elastin (Fig. 9A) and actin (Fig. 9C) than the other vascular segments under study. Unlike the case in human arteries, actin and elastin were the dominant constituents of the intima and media in porcine CCAs (Fig. 9C–E). The thickness of the intima-media, the wall thickness, and the IMT/WT ratio partially overlapped between porcine CCAs and the human LCA, RCA, and ITA arterial segments under study (Fig. 9F–H). The complete data set with all the morphometric results for all of the samples of all arterial segments is provided in Supplement 3.

3.4. Fraction of collagen within Tunica adventitia

The outcome of the pilot study is shown in Fig. 10 (see Supplement 4 for complete primary data) and Supplement 5. The fraction

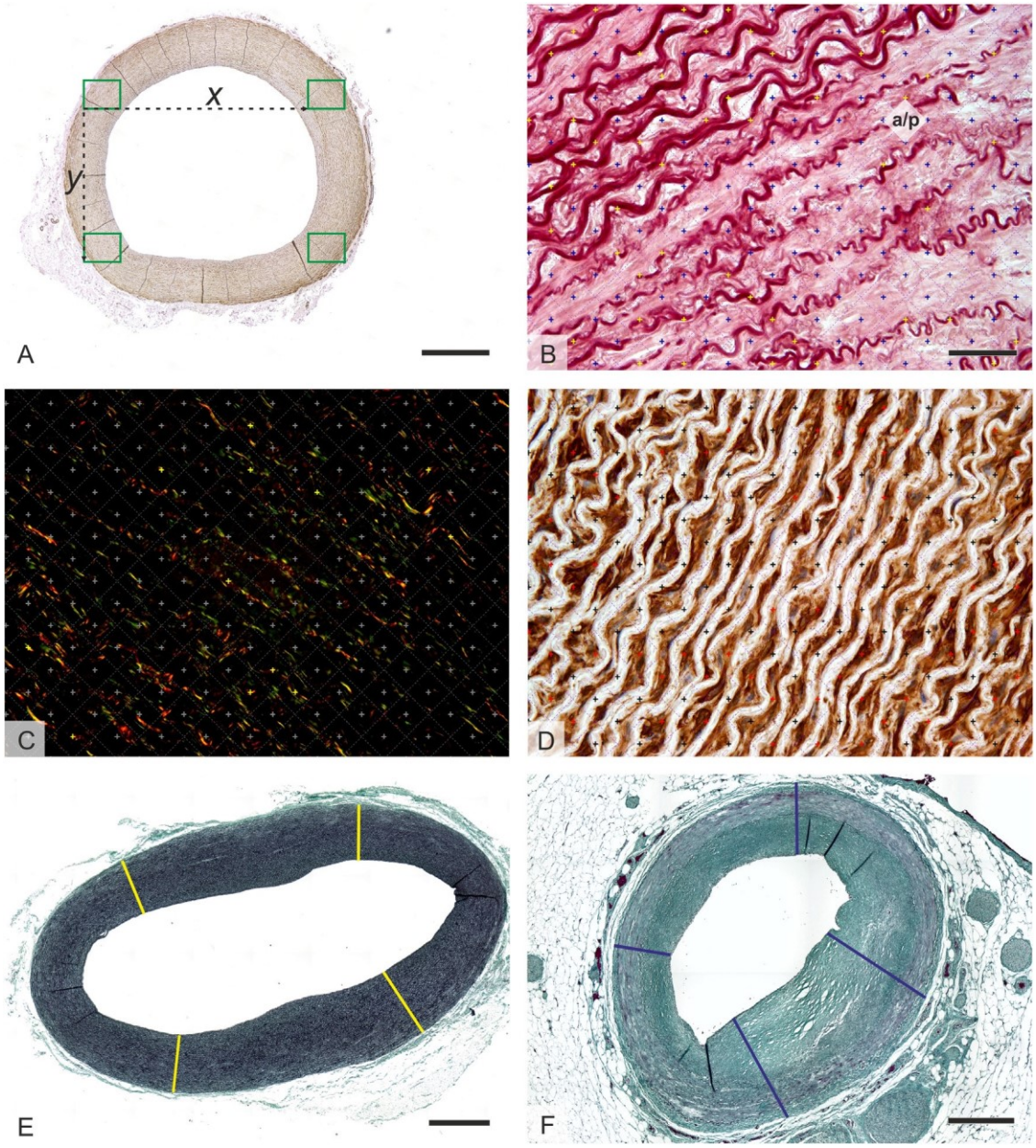

Fig. 2. Histological sampling and quantification of the components and thickness of the arterial segments. (A) Rectangles demonstrate the four micrographs sampled from the reference space of the tunica intima and media for each tissue sample and staining method. The (x,y) distances between the micrographs were uniform in a particular section to cover the entire cross-sectional area of the tunica intima and media, including the image fields bordering either the adventitia or the lumen. The size of the uniform sampling step (x,y) was modified proportionally to the size of any particular vascular segment. (B) A stereological point grid was projected on the micrographs, and the number of points hitting the elastin (highlighted in yellow) was counted. The area associated statistically with each point is labeled as (a/p). The reference area of the tunica intima and media was quantified using the same point grid. (C) The number of points hitting the collagen (highlighted in yellow) was counted as well. (D) The number of points hitting the elastin (highlighted in red) was counted accordingly. (E) The intima-media thickness was measured as the mean distance between the intimal surface profile and the media-adventitia border profile (four equidistant measurements per image, line probes highlighted in yellow). An example is given in the proximal porcine carotid segment. (F) The wall thickness was measured as the mean distance between the intimal surface profile and the outermost layer of the compact connective tissue of the tunica externa. An example is given in the circumflex branch of the human left coronary artery. Immunohistochemical detection of alpha-smooth muscle actin, visualization horseradish peroxidase/diaminobenzidine, and counterstaining with hematoxylin (A, D) orcein stain (B), picrosirius red stain observed under circularly polarized light (C), Verhoeff's hematoxylin and green trichrome (E,F). Scale bar: 1000 m (A,E), 50 m (B–D), and 500 m (F).

of collagen varied within the range of 0.4–0.7 along the whole length of CCA (mean ± SD 0.57 ± 0.08). Human coronary arteries (collagen fraction 0.32 ± 0.12) as well as human ITAs (0.33 ± 0.13) had a tendency towards lower fractions and a greater variability of collagen within adventitia than porcine CCA. The areas occupied by larger vasa vasorum were mostly negative in collagen (Supplement 5).

3.5. Correlation between the quantitative histological parameters

In porcine carotids, the amounts of elastin correlated negatively with collagen (Spearman $R = -0.156$; $p < 0.05$), actin ($R = -0.760$), and positively with the intima-media thickness ($R = 0.302$). In human coronary arteries, elastin correlated positively with actin ($R = 0.230$), but it was statistically independent of actin or intima-

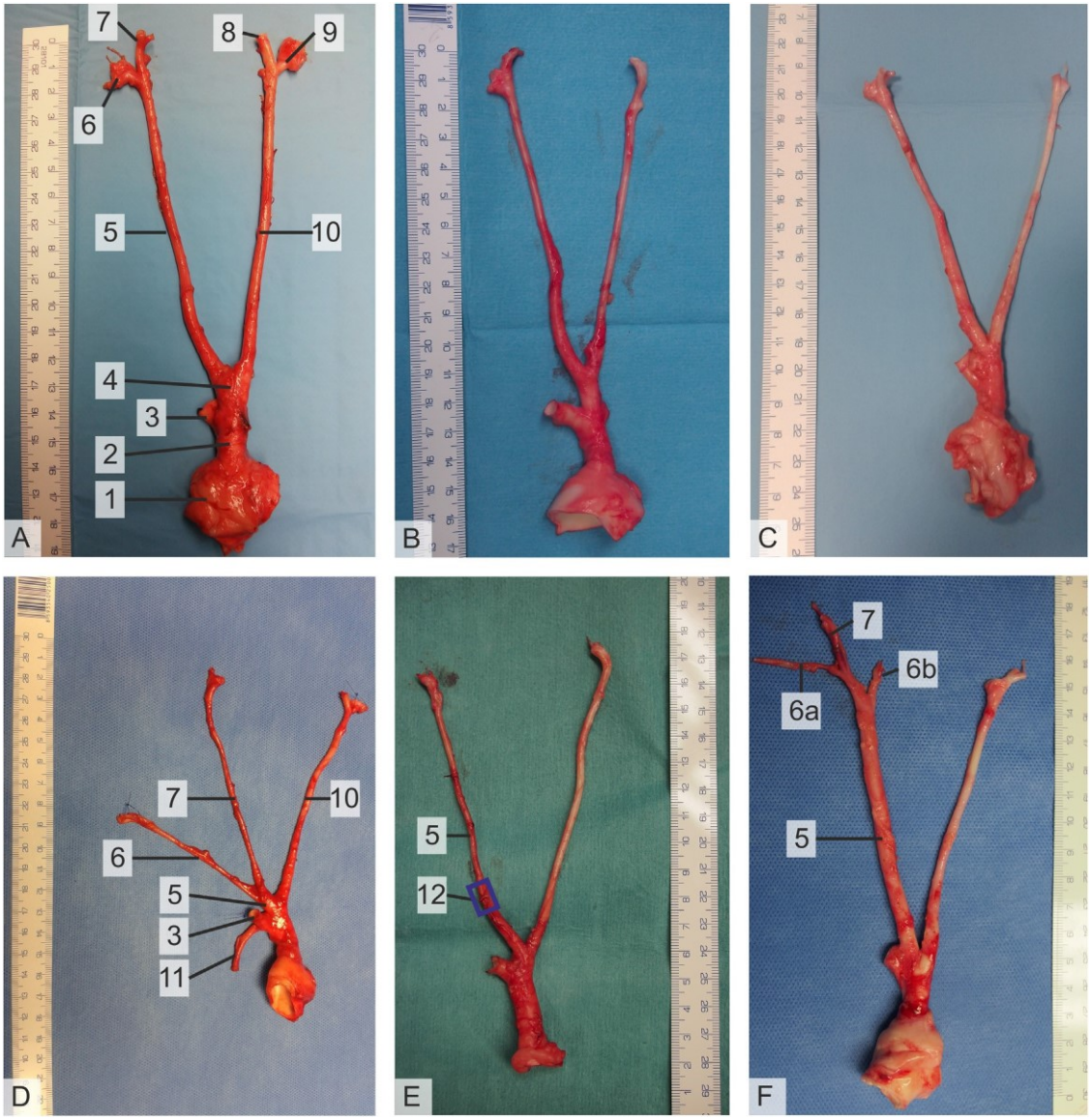

Fig. 3. Gross anatomical findings and variations of porcine common carotid arteries (CCA) and adjacent arteries in the present study. (A) The most common branching pattern, clockwise: aortic arch (1), brachiocephalic trunk (2), right subclavian artery (3), bicarotid trunk (4), right CCA (5), right external carotid artery (6), right internal carotid artery (7), left internal carotid artery (8), left external carotid artery (9), left CCA (10). (B) The same regular branching pattern. (C) The same branching pattern with shorter carotid arteries in a younger individual. (D) Branching pattern with a very short right CCA (5) and a very long right external carotid (6) and right internal carotid (7). Additionally, there was an aberrant artery (11), most likely the residual right aortic arch branching from the right subclavian artery (3). On the left side, the CCA (10) had a regular proportion. (E) An aberrant branch (12, branching site within the blue rectangle) for the thyroid gland originated from the right CCA (5). (F) There were two right external carotid arteries (6a, 6b) branching from the right common carotid (5). One of the right external carotid arteries (6b) originated proximally to the branching of the right internal carotid artery (7).

media thickness. The complete list of correlations for each type of arterial segment is shown in Table 4.

4. Discussion

4.1. Variations in gross anatomy have to be anticipated and considered during experiments

All gross anatomical variations of the regular branching patterns were found on the right side (three animals out of 21, Fig. 3D–F). In particular, the short right common carotid (Fig. 3D) might bias any evaluation of surgical experiments. When testing vascular grafts, a complete anatomical preparation comparable to our study would probably not be performed. Thus, either the external or the internal carotid arteries might be mistaken for the right common carotid, but there would be significant asymmetry when compared to a thicker common carotid on the left side. Another variation that might have an implication for using the common carotid as a model organ would be aberrant branches of the common carotid, such as additional branches supplying the thyroid gland (Fig. 3E). The presence of unexpected extra branching sites might bias any consequent histological morphometric analyses.

The sum of the area fractions of elastin, collagen, and actin was considerably greater in the porcine CCAs than in the human coronary arteries and ITAs. This finding was primarily due to the additional tissue components present in arterial segments of human individuals aged 55–80 years, such as lipid-laden foam cells, extracellular lipids, and cholesterol crystals. Another possible explanation that needs to be confirmed in the future is the potentially larger fraction of glycosaminoglycans in human arteries than in CCAs of relatively young pigs.

Fig. 4. Comparison among the proximal, middle, and distal segments of the porcine common carotid arteries (CCAs). The x-axis shows the proximodistal position of each segment in centimeters. Samples (n=404) from right and left CCAs (n=41) from all the animals (n=21) were pooled in this graph. (A) The area fraction of elastin within the media decreased in the proximodistal direction (Kruskal–Wallis ANOVA $p<0.001$). The area fraction of actin increased in the proximodistal direction ($p<0.001$). The fraction of collagen remained approximately the same along the whole length. (B) The intima-media thickness, the wall thickness (left y-axis), and their mutual ratio (righty-axis) changed considerably along the CCAs ($p<0.001$ in all three parameters). Data are displayed as the means ± standard error of the means. See Supplement 1 for complete

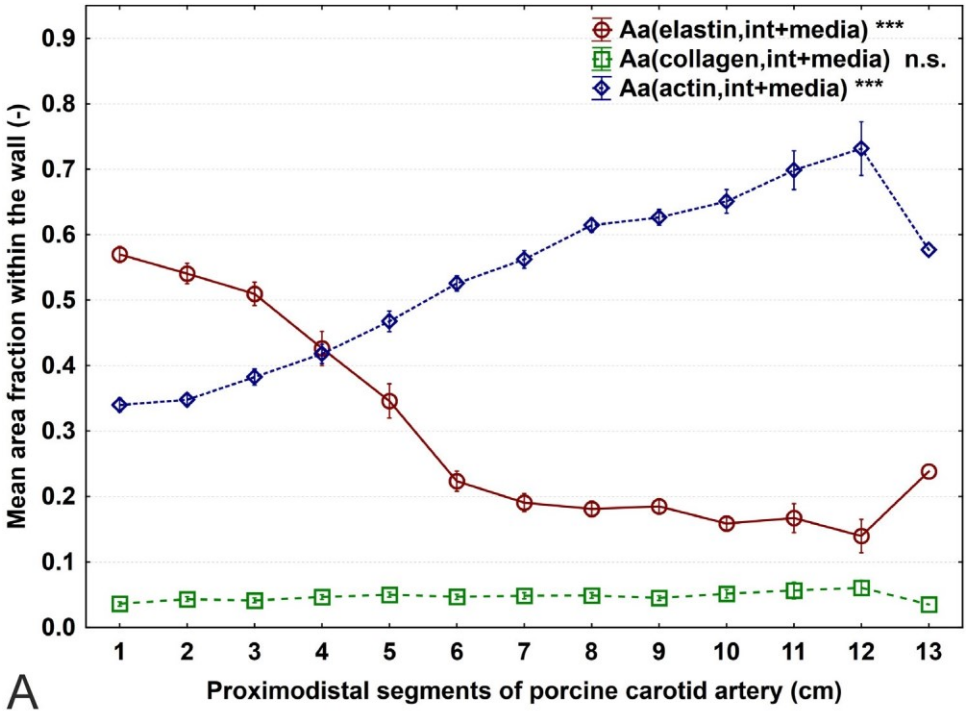

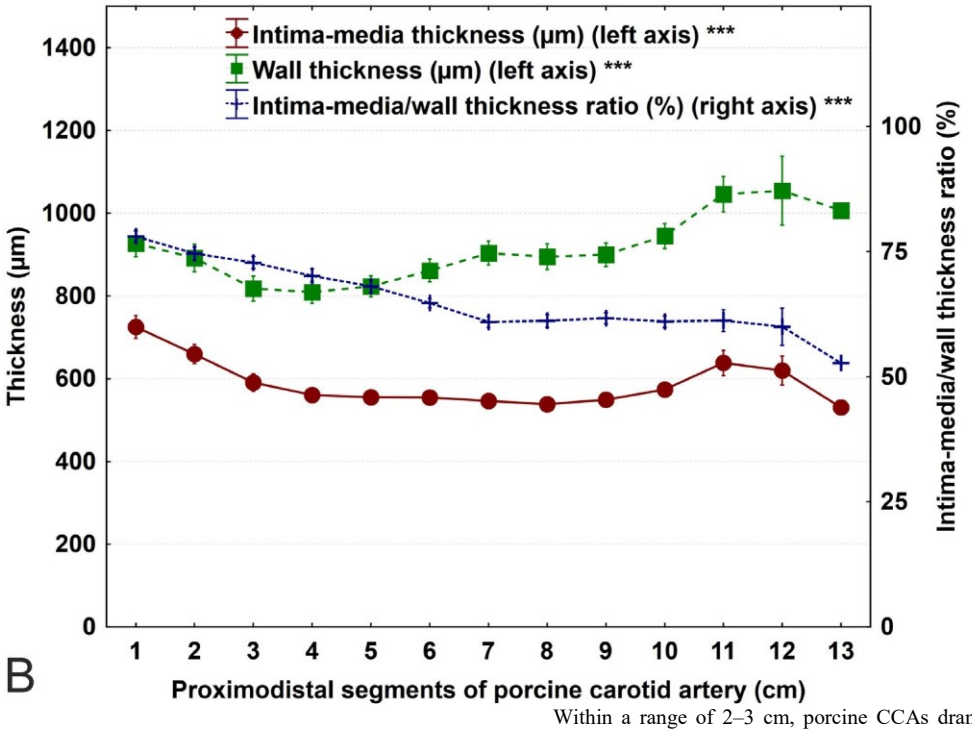

primary data.

4.2. Segmental differences in the porcine CCAs—from elastic to muscular type

Within a range of 2–3 cm, porcine CCAs dramatically changed their phenotype from mostly elastic to mostly muscular (Fig. 4A). Interestingly, some long blood vessels show a considerable uniformity of their microscopic structure along macroscopically long segments, such as vasa vasorum density (Tonar etal., 2012) or smooth muscle distribution (Kochová etal., 2014) along human saphenous veins. Some blood vessels, such as the aorta, show con-

Table3
Descriptivestatisticsforcalculatingtheminimumnumberofsamplesneededtocomparetwomeanswhenperformingapoweranalysisaspartofdesigningfutureexperiments involvingporcinecommoncarotid arteries(CCAs).Forthispurpose,datafromtheleftandrightfourproximalsegments(1–4cmfromthebifurcation),fourmiddlesegments (5–8cm),andfourdistalsegments(9–12cm)werepooled.Themeansand standarddeviationsarerounded.Thenumberofarterialsegments(n)usedforcalculationofeach partisshowninthefirstcolumn.AA(component)representstheareafractionoftherespectivecomponentwithinthe tunicaintimaandmediareferencespaces;IMT,the intima-mediathickness;andWT,thewallthickness.SeeSupplement3forthecompletesetofprimarydata.

SegmentsofporcineCCAs	Quantitativeparameter	Mean	Standarddeviation
Proximalsegments(1–4cm) (n=164segments)	A_A(elastin)(−)	0.512	0.130 0.023
	A_A(collagen)(−)	0.0420.372	0.082
	A_A(actin)(−)	634	157
	IMT(m)		
	WT(m)	862	201
Middlesegments(5–8cm)(n=164 segments)	A_A(elastin)(−)	0.235	0.131
	A_A(collagen)(−)	0.0490.543	0.027
	A_A(actin)(−)	549	0.099
	IMT(m)		104
	WT(m)	871	182
Distalsegments(9–12cm)(n=76 segments)	A_A(elastin)(−)	0.172	0.066 0.027
	A_A(collagen)(−)	0.049	0.086
	A_A(actin)(−)	0.650	92
	IMT(m)	572	
	WT(m)	944	169

Table4
Spearmanrankordercorrelationsbetweenthequantitative neters.

		A_A(collagen)	A_A(actin)	IMT	WT	IMT/WTratio
PorcineCCAsegments (n=404)	A_A(elastin)	−0.156*	[redacted]	0.302*	[redacted]	0.623*
	A_A(collagen)	–		0.191*		−0.105*
	A_A(actin)	–	–	−0.218*	0.139*	−0.564*
	IMT	–	–	–	0.772*	0.252*
	WT	–	–	–	–	−0.363*
Humancoronaryarterysegments(n=147)	A_A(elastin)A_A (collagen)	0.230*	0.058	[redacted]	[redacted]	0.080
		–	0.053			0.232*
	A_A(actin)IMT	–	–	−0.321*	[redacted]	[redacted]
		–	–	–		
	WT	–	–	–	–	0.302*
HumanITAsegments (n=63)	A_A(elastin)	−0.059		0.300*	0.255*	0.083
	A_A(collagen)	–	0.162[redacted]	−0.159	−0.276*	0.182
	A_A(actin)	–	–	0.114	0.028	0.145
	IMT	–	–	–	0.912*	0.200
	WT	–	–	–	–	−0.171

Thedataareshownforeachtypeofarterialsegment.A_A(component)representstheareafractionoftherespectivecomponentwithinthetunicaintimaandmediareference spaces;IMT,theintima-mediathickness; andWT,thewallthickness.Allcorrelationssignificantat$p<0.05$aremarked(*)andtypedinboldface.Theremainingcorrelations werenotstatisticallysignificant($p>0.05$).Autocorrelationsandrepeatingvalues arereplacedbythe(–)sign.CCA—commoncarotidartery.ITA—internalthoracicartery.

siderable changes in their histological and mechanical properties (Sokolis, 2007; Sokolis et al., 2008; Tonar et al., 2016). A regional difference in the composition of blood vessels has consequences on their mechanical properties (Avril et al., 2015). García et al. (2011) suggested that this shift from the elastic to muscular phenotype in a short course determines the biomechanical properties of individual arterial segments in the proximodistal direction, which can significantly affect the results of experiments targeting the biomechanics of these arteries. We believe that the data on the segmental variability of elastin, collagen, and actin content provided in the present study might also partially explain the mechanical properties of various segments of porcine CCAs. The contribution of the three components quantified in the present study to the passive mechanics of porcine CCAs has been experimentally estimated by Kochová et al. (2012). Selective destruction of elastin, collagen, and smooth muscle while measuring the deformation of the outer diameter of pressurized porcine CCAs revealed the range of stresses in which these constituents are responsible for maintaining the pressure/diameter ratio. Destruction of elastin resulted in enlargement of the carotid diameter but not stiffening or softening of the wall as elastic fiber integrity is known for maintaining CCA integrity (Ferruzzi et al., 2016). Destruction of collagen led to loss of stiffness of the carotid wall. Eliminating smooth muscle cells led to enlarge-

ment of the diameter at pressures up to 120 mmHg and mechanical stiffening at higher pressures.

Most of the numerical results in the present study are in good agreement with other publications that applied similar methods and well-documented anatomical sampling of proximodistal position of the CCA samples. Wyatt et al. (2016) reported the CCA wall thickness of 0.86 ± 0.17 mm which matches the 0.87 ± 0.18 mm found in the middle segment in our study (Table 3). The fraction of elastin in the middle segment 26.3 ± 11.5% found by Wyatt et al. (2016) and the values 22 ± 9% published by Kochová et al. (2012) are also very close to our findings (23.5 ± 13.1%). Similarly, the differences in the elastin fraction found in our study between the proximal (51.2 ± 13%) and distal (17.2 ± 7%) CCA segments are in agreement with the values published by García et al. (2011), namely 52.6±6.7% for the proximal segments and 19.6 ± 4.1± for the distal segments. Our results on smooth muscle fraction in proximal CCA (37.2 ± 8.2%) are very close to those found by García et al. (2011) (31.0±3.3%); however, the fraction of smooth muscle in distal CCA was greater in our study (65.0±8.6%) than in the paper by García et al. (2011) (44.3±4.2%).

The fraction of elastin within human coronary arteries in our study (Fig. 9A) overlaps with the range reported by Ozolanta et al. (1998) (7.5–10.02%).

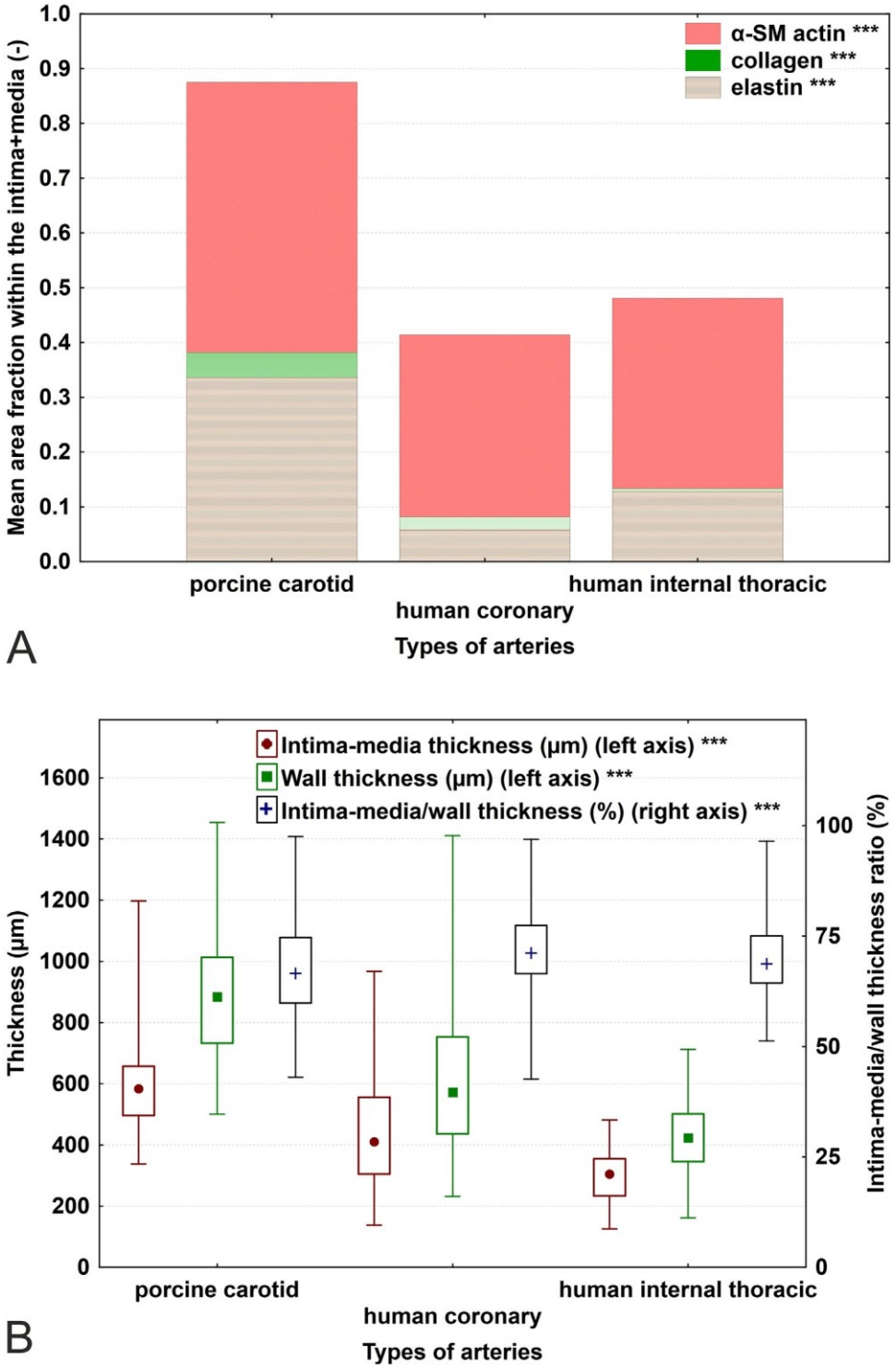

Fig.5.Overallvisualizationoffractionsofactin,collagen,andelastinwithinthetunicaintimaandmediaofporcinecarotidarteries(left),humancoronaryarteries(middle), andhumaninternalthoracicarteries(right). Thesegments fromall the individuals were pooled for the purpose of this comparison. (A) The mean fractions of neither actin, elastin, nor collagen can be considered equivalent among the three groups of arterial segments (Kruskal–Wallis ANOVA $p<0.001$ in all three variables). Data are displayed as cumulations of mean fractions. (B) There were considerable differences in the intima-media thickness, wall thickness, and their ratio when comparing the three groups of arterial segments under study ($p<0.001$). Data are displayed as median values with boxes spanning the upper limits of the first and third quartiles and with whiskers spanning the minimum and maximum values. See Supplement 1 for complete primary data.

4.3. Challenges for manufacturing artificial CABG grafts when proceeding from animal models to human patients

Young porcine animal models are typically used for testing of novel vascular prosthesis as stated in Zilla et al. (2007). In most of studies, 3–6 months old pigs are used (Teebken et al., 2001; Rotmans et al., 2005; Ueberrueck et al., 2005; Quint et al., 2011; Mrowczynski et al., 2014; Koens et al., 2015; Rothuizen et al., 2016; Dahan et al., 2017). Rather than age, their weight is commonly recorded. Implantation period also varies. The majority of studies are short term with final prosthesis assessment after about one month (Rotmans et al., 2005; Quint et al., 2011; Mrowczynski et al.,

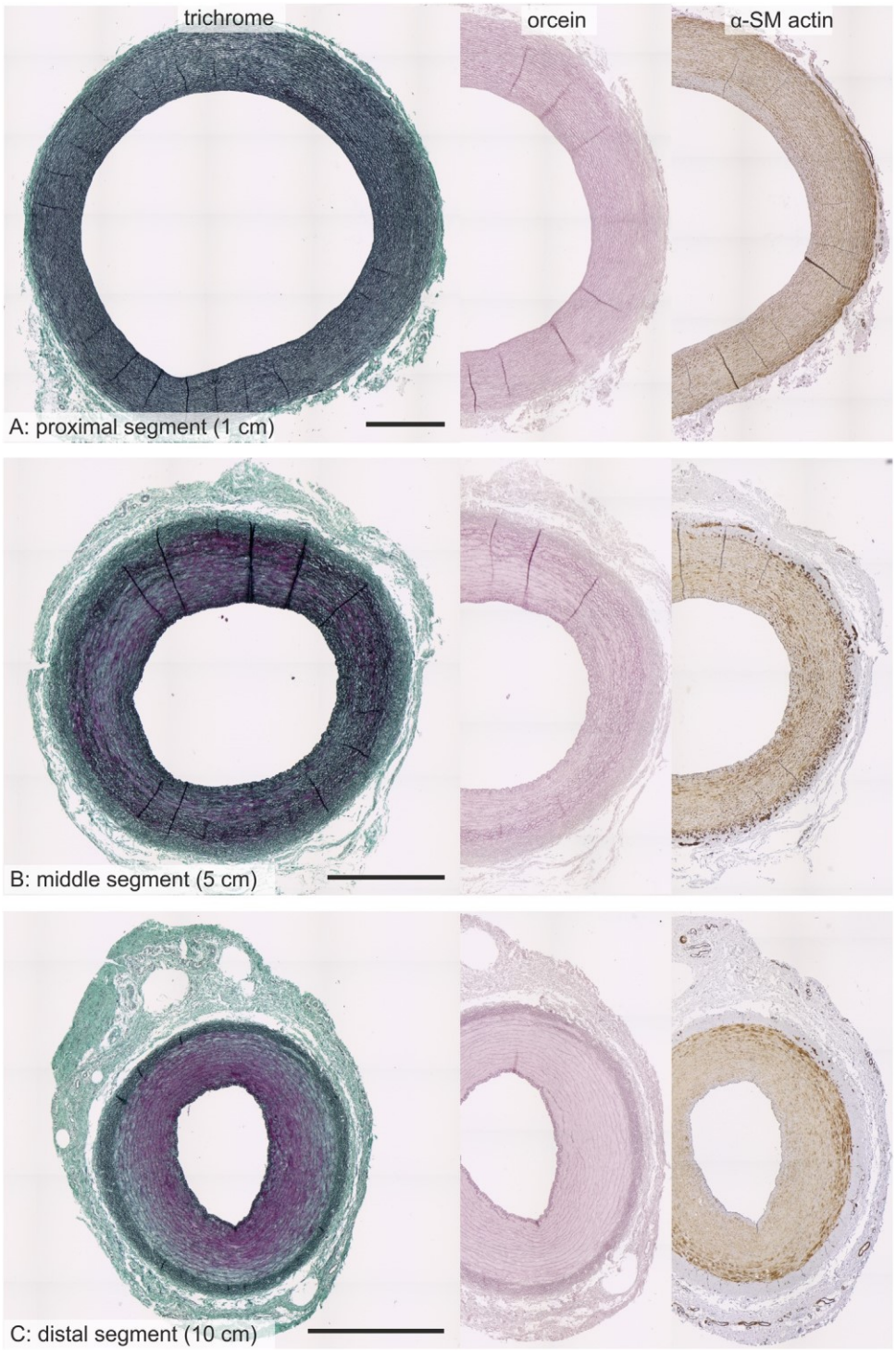

Fig. 6. Comparison of the overall morphology of the proximal, middle, and distal segments of porcine carotid arteries. (A) In proximal segments (1 cm from the bicarotid trunk), repeating elastic lamellae prevailed in the tunica media. (B) In the middle segments (5 cm from the bicarotid trunk), the proportion of elastin and smooth muscle was approximately balanced. (C) In the distal segments (10 cm from the bicarotid trunk), vascular smooth muscle was the prevailing component of the media. Verhoeff's green trichrome (left), orcein stain for elastin (middle), immunohistochemical detection of alpha-smooth muscle actin (right). Scale bar: 1 mm.

2014; Koens et al., 2015; Rothuizen et al., 2016). Long term evaluation was assessed for example for four months (Teebken et al., 2001), or three and six months (Ueberrueck et al., 2005). Interestingly, sex is specified only in some of the cited papers, namely Mrowczynski et al. (2014) used male pigs, whereas Rotmans et al. (2005); Ueberrueck et al. (2005); Koens et al. (2015), and Rothuizen et al. (2016) used female pigs.

Even before the present study, it was obvious that one of the limitations of using porcine CCAs as models for testing vascular grafts intended for human coronary arteries was the discrepancy in age of human patients undergoing CABG vs. relatively low age of animals used as experimental models. The porcine CCAs lacked the histopathological alterations and degenerative changes typical for atherosclerosis common in human patients. The most important challenges to which the bioengineered grafts have to be adapted

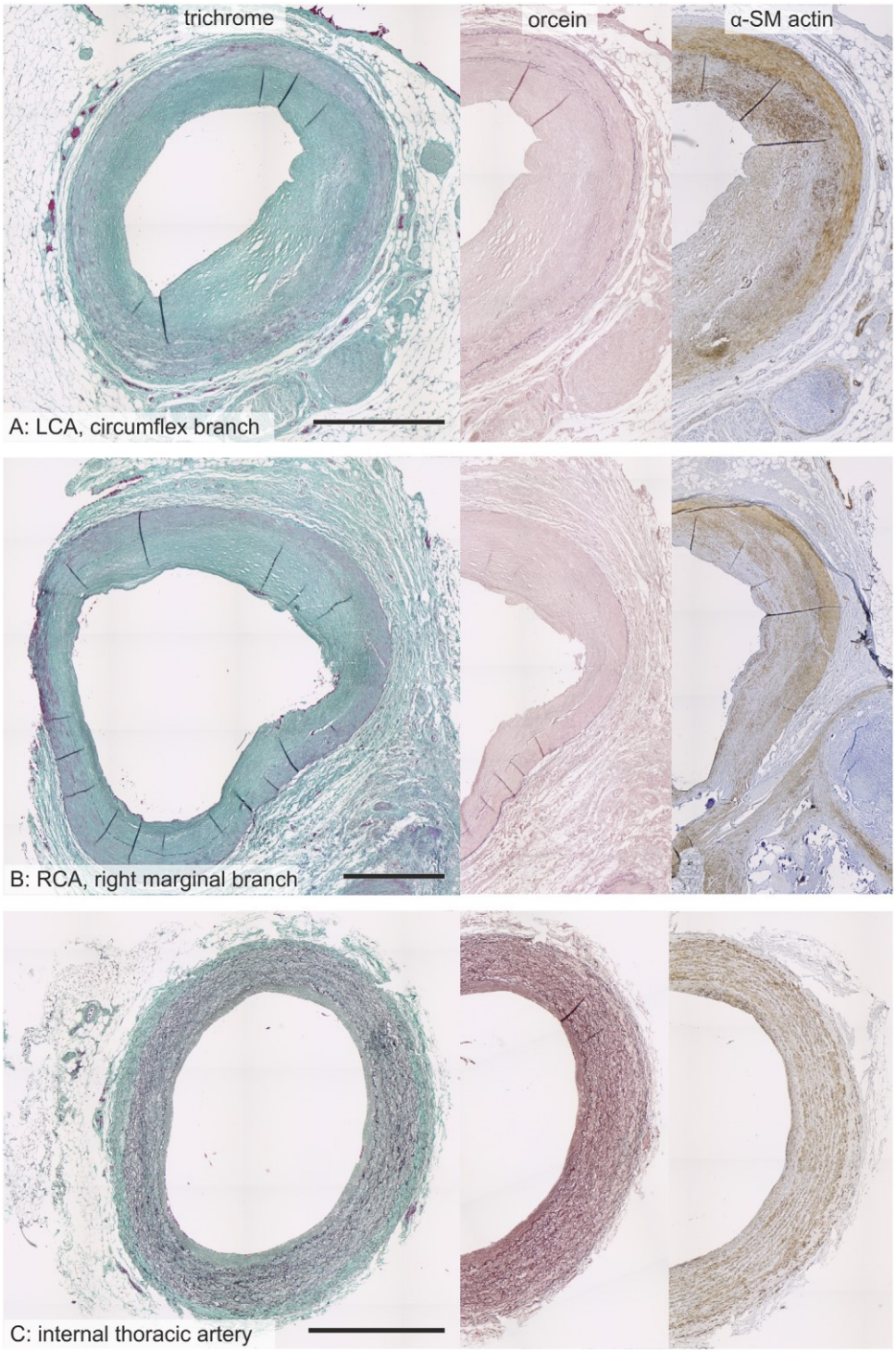

Fig. 7. Examples of the overall morphology of human arteries: arterial segments representing the left coronary artery (LCA), right human coronary artery (RCA), and internal thoracic artery. (A and B) The human coronary arteries often lacked rotational symmetry and often contained eccentric atherosclerotic lesions (see Supplement 2 for detailed scoring of atherosclerosis). The amounts of elastin and actin were lower than those in porcine carotid arteries. Either the positivity for actin was diffusely lost, or there were larger actin-negative foci. (C) The internal thoracic artery was mostly free of atherosclerosis or showed only adaptive thickening of intima. The elastin was well preserved, occurring in the form of repeating concentric lamellae that alternated with smooth muscle cells. Verhoeff's green trichrome (left), orcein stain for elastin (middle), immunohistochemical detection of alpha-smooth muscle actin (right). Scale bar: 1 mm.

even after being successfully tested in porcine carotids are the following: (i) lack of rotational symmetry, which cannot be assumed in human coronary arteries; (ii) focal or diffuse loss of elastin and smooth muscle actin; (iii) the presence of atherosclerotic plaques; (iv) additional presence of other substances that do not occur in model animals, such as deposits of lipids or accumulation of glycosaminoglycans. Additionally, the correlations between the composition and thickness of the arterial wall, which are usually found in healthy arteries (Table 4), are not to be expected in human coronary arteries. However, with the present data mapping the segmental variability, we demonstrated that at least some of the segments of porcine carotids partially overlap with the natural vari-

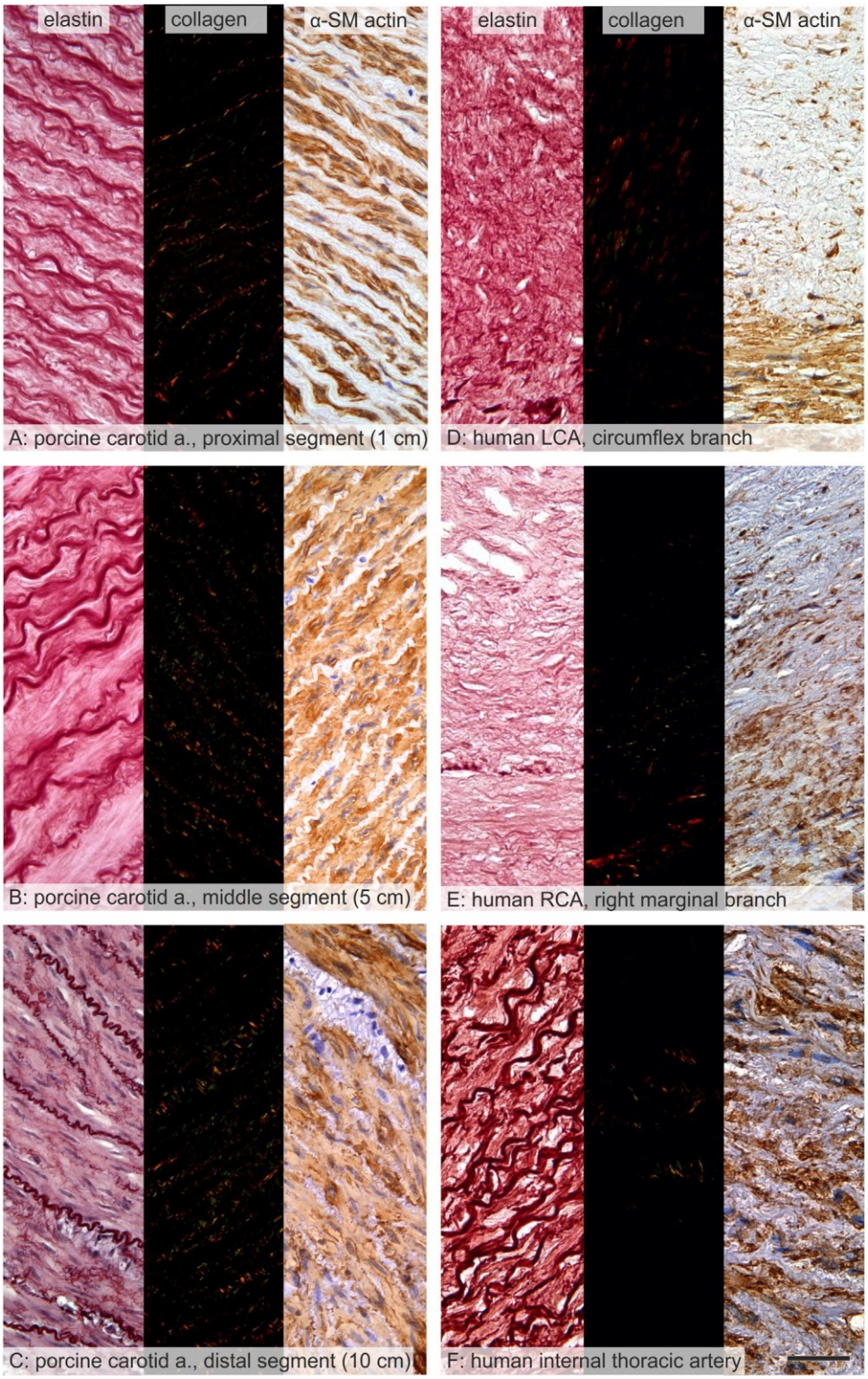

Fig. 8. Elastin, collagen, and actin content in examples of the tunica media of the proximal, middle, and distal segments of porcine carotid arteries (A–C) and in samples of the left human coronary arterial segments (D), right human coronary arterial segments (E), and human internal thoracic arterial segments (F). See Fig. 6 for a detailed quantitative comparison. In carotid arteries (A–C), the arrangement of the tunica media was regular. Elastin (left) decreased in the proximodistal direction, while actin (right) increased. The fraction of collagen (middle) oscillated around approximately the same values. In human coronary arteries (D, E), only fragments of the inner and the outer elastic laminae were found (left), while the internal thoracic arteries showed regular patterns of elastic lamellae (F). Variable areas of the media of the coronary arteries (D, E) contained no smooth muscle (right) but atherosclerotic plaques of various stages (see Supplement 2 for detailed scoring). The internal thoracic artery (F) had a regular pattern of actin positivity. Although the immunohistochemistry provided reliable and unambiguous identification of all the positive areas, it can be noted that porcine CCAs (A–C) that were fixed immediately after harvesting had no background staining at all, while samples of human arteries showed weakly positive counterstaining also in the cytoplasm and extracellular matrix (E–F). Elastin stained with orcein (left); collagen stained with picrosirius red and observed under circularly polarized light (middle); immunohistochemical detection of falpha-smooth muscle actin (right). Scale bar: 30 m.

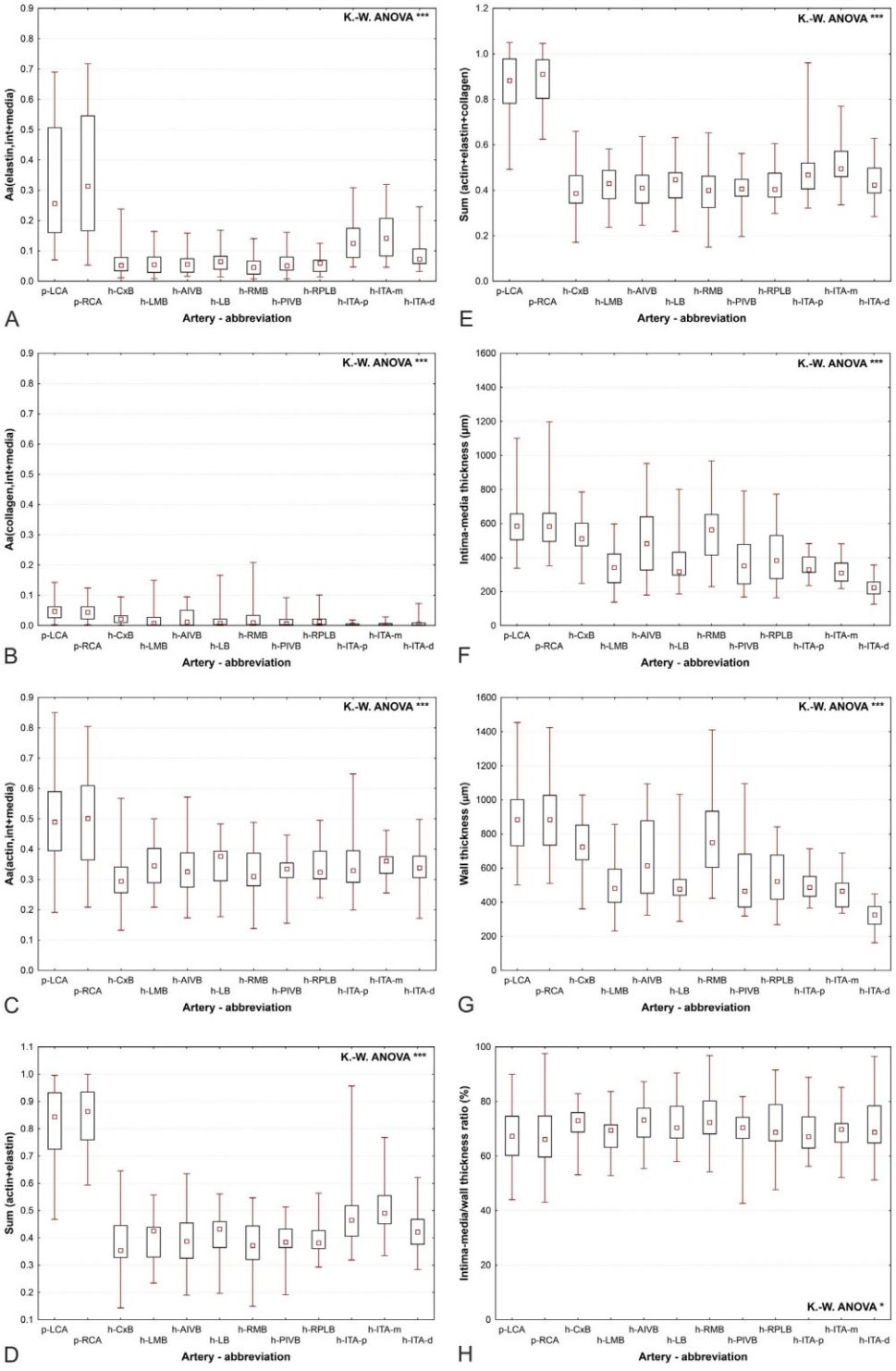

Fig. 9. Detailed visualization of the morphometric results in all the vascular segments under study: Fractions of actin, collagen, and elastin and their sums within the tunica intima and media (A–E); Intima-media thickness (F), wall thickness (G), and their ratio (H). The arterial segments are presented under the following abbreviations: p-LCA — porcine left coronary artery; p-RCA — porcine right carotid artery; h-CxB — (human) circumflex branch; h-LMB – (human) left marginal branch; h-AIVB — (human) anterior interventricular branch; h-LB — (human) lateral branch; h-RCA — (human) right coronary artery; h-RMB — (human) right marginal branch; h-PIVB — (human) posterior interventricular branch; h-RPLB — (human) right posterolateral branch; ITA — (human) internal thoracic artery. Porcine carotid arteries had a tendency towards containing more elastin (A) and actin (C) than the other vascular segments under study. Actin and elastin were the dominant constituents of the intima and media in porcine carotid arteries (C–D), unlike the case in human arteries. The thickness of the intima-media, the wall thickness, and the IMT/WT ratio overlapped between porcine carotid arteries and the remaining arterial segments under study (F–H). Data are displayed as median values with boxes spanning the upper limits of the first and third quartiles and with whiskers spanning the minimum and maximum values. See Supplement 1 for complete primary data. The p-values of the Kruskal–Wallis ANOVA are shown.

ability of human coronary arteries and with the ITA in the fraction of collagen (Fig. 9B), in the intima-media thickness (Fig. 9F), in the wall thickness (Fig. 9H), and in the IMT/WT ratio (Fig. 9H). Despite these limitations, porcine CCAs remain the most widely used and best characterized realistic animal model in studies testing new generations of CABG conduits.

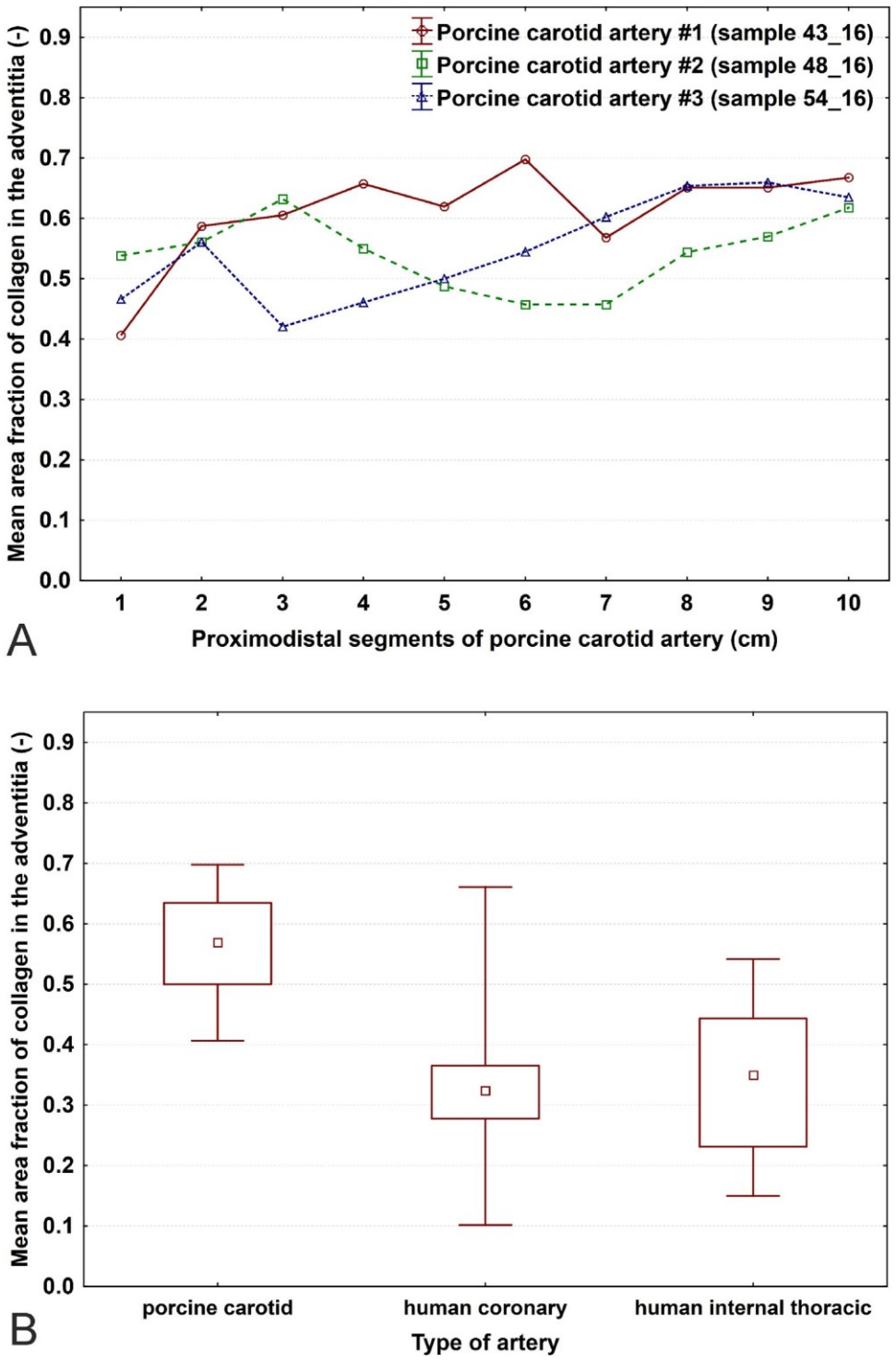

Fig. 10. Visualization of the pilot study on the fraction of collagen within the adventitia based on three randomly selected porcine common carotid arteries (CCAs) (A) and compared to three pairs of randomly selected human coronary arteries and three human internal thoracic arteries (ITAs) (B). (A) Samples (n = 30 segments) from porcine CCAs (n = 3 animals) are displayed. The x-axis shows the proximodistal position of each segment in centimeters. The fraction of collagen varied between the range of 0.4–0.7 along the whole length, the mean values ± SD were 0.61 ± 0.08 (mean ± SD; artery #1), 0.54 ± 0.06 (artery #2), and 0.55 ± 0.09 (artery #3). (B) Comparison between pooled segments of porcine CCAs (left, n = 30 segments), human coronary arteries (middle, n = 21 segments of LCA, CxB, LMB, AIVB, LB, RCA, RMB, PIVB, and RPLB), and human ITAs (n = 9 segments). There was a tendency towards lower fractions and a greater variability of collagen within the adventitia in human coronary arteries (0.32 ± 0.12) and ITAs (0.33 ± 0.13) than in porcine arteries (0.57 ± 0.08). Data are displayed as median values with boxes spanning the upper limits of the first and third quartiles and with whiskers spanning the minimum and maximum values. See Supplement 4 for complete primary data and Supplement 5 for histological findings.

To reflect the requirements listed above, mimicking the natural layered architecture of blood vessels seems to be a solution for the construction of an ideal vascular graft. For example, bilayered grafts have been manufactured by electrospinning of PCL (de Valence et al., 2012a, b). In the inner or outer side of the prosthesis, a barrier layer composed of densely packed small diameter fibers can be added. Vascular prostheses with inner barriers may lead to reduced blood leakage and allow cell invasion from the adventitial side (de Valence et al., 2012a, b). Another recent study reported the fabrication of trilayered grafts (Wu et al., 2018) simulating the

structureofnativebloodvessels.Theinnerlayerwascomposed ofaxiallyaligned fibersmadefrompoly(l-lactide-cocaprolactone) andcollagen,themiddlelayer consistedofcircumferentiallyorientedpoly(lactide-coglycolide)andsilkfibroin yarns,andtheouter layerwascreatedbyrandomfibersmadefrompolymersusedin the luminal side. Such structures exhibited good mechanical properties and promotedendothelialandsmoothmusclecellproliferationin vitro.

Designingartificialvasculargraftsrequiresabasicknowledge oftarget-tissue anatomicalstructure.Especiallyinthecaseofa tissueengineeringapproachwhen mimickingofnativemorphologyistheaim,webelievethateventhoughthedata provided in our study possibly do not represent the whole range of findings in patients undergoing CABG, the primary data provided in Supplement 3 might inspire the manufacturing of bioengineered grafts. For example, the data on the intima-media and the total wall thickness are ready to be used for designing multilayered grafts with the benefits described above. Unfortunately, studies mapping the natural variability of various blood vessels of human potential recipients aregenerallymissingandsoistheircriticalcomparisonwiththe animal modelsusedforpreliminarytesting.

4.4.Practicalstudyimplications

The histological structure of the left and right porcine CCAs (Supplement 1) mightbeconsideredtobeequivalentprovidedthat grossanatomicalvariationsof theregularbranchingpatternsare excluded.Therefore,oneofthesearteriescanbe used as a healthy or sham-operated control in the same animal. This approach of usingthecontralateralCCAasacontrolwasalreadyappliede.g. byKritharisetal. (2012). However, proximal, middle, and distal segments are definitely not mutuallyinterchangeable,anddata acquiredfromeitherofthesesegmentscannot beextrapolatedto theremainingsegments,noteveninthesameanimal.

For further studies that involve assessment of elastin, collagen, or smooth muscleactincontentandthethicknessofthecarotid wall,theminimumnumberof samplespergroupcomparedcanbe calculatedfromTable3.Forexample,when planninganexperiment andexpectingthemeanfractionofactintobedecreasedby 20% in the middle carotid segments (i.e., from 0.543 to 0.427), the minimum numberofsamplesrequiredpergroupwouldbenine,using thetypicaltestpower ˘ = 0.8 (the type II error) and ¸ = 0.05 (type I error) (Chow et al., 2008). Similarly, detectinga25%increaseofthe intima-mediathicknessinproximalsegments(i.e., thickeningfrom 634mto792m)wouldrequire13samples.Thisconsideration is important, especially in pigs, as in a large animal model, where experiments are usually planned with a relatively small number of animals. Calculating the expectednumberofsamplestoprovea scientifichypothesisisalsoanethicalissue asitisessentialforjustifyingthesacrificeoftheanimals—seealsotheprinciplesof the‘3Rs’ (replacement,reduction,andrefinement;Emerson,2010).Moreover, the data provided are available for computer modeling and biomechanical phenotypingofregionalvariationsinthestructural andmechanicalpropertiesof CCA(Bersietal.,2016;Bellinietal., 2017).

Althoughthepilotstudyoncollageninadventitiashowed a tendencytowards its greater fraction in CCA than in human coronary arteries and ITA (Fig. 10, Supplement4),itappearedthatthe quantificationwasinfluencedbythesizeand quantity of larger collagen-negative areas occupied by vasa vasorum and nervi vasorum (see Supplement 5). We suggest that a biologically meaningful assessmentofadventitiashouldcontainalsoquantificationofthe densityandsize ofvasa vasorum(Tonaretal.,2012)andnervi vasorum(Nedorostetal.,2013).It showed that the analysis of adventitia would deserve a more complex study that goes far beyond aims and ambitions of the present paper. Moreover, the “no-touch”harvestingtechniquethatpreservesmostoftheadventitia(Dreifaldtetal., 2011) is strongly recommended. This would also make possible to quantify the totalcontentofthewallconstituents,includingthe adventitia.

4.5.Studylimitationsandremarksonthemethods

Although the present study presents, to our knowledge, the largest collection mappingthebiologicalvariabilityofporcineCCA publishedsofar,agegroupsinboth sexesarenotrepresented inawayallowingfortestinghowthesevariablesareaffecting the structure of porcine CCA. The morphometric data come from formalin-fixed paraffin sections. While the fractions of elastin, collagen, and actin are not biased by tissueshrinkage,thedataonthe intima-mediaandwallthicknessarebiasedbyatleast two factors: (i) tissue shrinkage during processing and (ii) postmortem spasm of the arteries. Theoretically, this could be partially avoided using perfusion fixation under meanarterialpressureinthefuture.

Another limitation appears when looking at the sums of the fractions of elastin, collagen, and actin within the tunica media of the porcine carotids (Fig. 9E) and the primary data in Supplement 3. The summed fractions of the three components exceeded the theoretical maximum value of 1.00 by 0.003–0.049 in 46 out of 614 measurements. This finding suggests that the fraction of some of the components was rather overestimated than underestimated. However, this relative error ranging between 0.3–4.9% probably did not bias the whole study, as none of the conclusions weredrawn fromtheborderlineofstatisticalsignificance.

The present literature (including our paper) mostly lacks data on glycosaminoglycans as a part of testing vascular grafts. Analyses of glycosaminoglycans seem to be underestimated despite their relevance to manufacturing of decelluarized arterial grafts (Liao et al., 2009), neointimal formation (Tang et al., 2010), promoting of hemocompatibility and endothelization (Lu et al., 2013), or intravascular metabolism of antithrombogenic molecules (Klement etal.,2010).Atleastthefollowingtypesofglycosaminoglycans shouldbe analyzed in the future: hyaluronic acid, heparan sulphate, dermatan sulphate, and chondroitinsulphate(Stevensetal.,1976; Malfait,2018).

5.Conclusion

Segmental differences and the biological variability in the fractions of elastin, collagen, actin, and in the intima-media thickness and wall thickness were mapped histologically in porcine CCAs. Left and right porcine CCAs can be considered equivalent, but the proximal elastic carotid transitions in the range of 2–3 cm to more muscular middle and distal segments, which are not interchangeable. The resulting morphometric data set shows the biological variability of the artery and is made available for biomechanical modeling and for performing a power analysis and calculating the minimum number of samples per group when planning further experimentswiththiswidelyusedlargeanimalmodel.

Comparison of porcine carotids with human coronary arteries and one of the preferred arterial autologous conduits for CABG, namely, the ITA, revealed the limitations of using porcine CCAs as a valid model for testing bioengineered small-diameter CABG vascular conduits. Morphometry of human coronary arteries and ITA provided more realistic data for tailoring multilayered artificial vascular prostheses and the ranges of values within which the conduits should be tested in the future. Despite their limitations, porcine CCAs remain a widely used, well-characterized large animal model available for a variety of experiments in vascular surgery.

Ethicalstatement

The authors of the manuscript entitled “Histological mapping of porcine carotid arteries — an animal model for the assessment of artificial conduits suitable for coronarybypassgraftinginhumans” byPetrTomasek,ZbynekTonar,TomasKural, Martina Grajciarova, Daniel Turek, Jana Horakova, Richard Palek, Lada Eberlova, Milena Kralickova, and Vaclav Liska, would like to provide the following ethical statement:

Referringtosamplesofporcinecommoncarotidarteries

Whole carotid arteries (n = 41) and adjacent arterial branches were obtained from 21 healthy male and female Prestice Black Pied pigs aged 12–21 weeks and weighing 20–65 kg (35.8 ± 13.3 kg, mean ± SD). All the animals were part of other research projects onexperimentalliversurgeryandprojectsapprovedfortraining onsurgical skills. All the projects numbers (MSMT-42178/20154, MSMT-29543/2015-6, MSMT-32067/2015-5) were approved by the local ethical authorities and by the

Faculty Committee for the Prevention of Cruelty to Animals. All the animals received humane care in compliance with the European Convention on Animal Care at the Experimental Surgery Facility, Biomedical Center, Faculty of Medicine in Pilsen, Charles University.

Referring to samples of coronary and internal thoracic arteries obtained from human cadavers

Vascular segments representing three human coronary arteries were obtained from 21 human cadavers aged 57–78 years (n = 14 females aged 64.8 ± 5.6 years; n = 7 males aged 71.6 ± 6.5 years) dissected during 2017 at the Department of Forensic Medicine, Second Faculty of Medicine, Charles University. Collection of samples of organs routinely reviewed during a forensic autopsy is permitted according to the Czech law for educational and scientific purposes. We hold the greatest respect for the individuals from whom the samples of coronary arteries and internal thoracic arteries were taken, thus furthering our knowledge of the human body.

Acknowledgments

We hold the greatest respect for the individuals from whom the samples of coronary arteries and ITAs were taken, thus furthering our knowledge of the human body.

This study was supported by the National Sustainability Program I (NPU I) Nr. LO1503 provided by the Ministry of Education, Youth and Sports of the Czech Republic and by the Charles University Research Fund (Progres Q39). The study also received support from the Ministry of Education, Youth and Sports under the project FIND No. CZ.02.1.01/0.0/0.0/16019/0000787. R.P. and V.L. were supported by the European Regional Development Fund-Project "Application of Modern Technologies in Medicine and Industry" (No. CZ.02.1.01/0.0/0.0/17 _ 048/0007280).

JH was supported by the Ministry of Health of the Czech Republic (Grant no: 15-29241A).

Skillful technical support from Ms. Marketa Slajerova is gratefully acknowledged.

Appendix A. Supplementary data

Supplementary material related to this article can be found, in the online version, at doi:https://doi.org/10.1016/j.aanat.2019. 151434.

References

Anderson, J.H., Taggart, N.W., Edgerton, S.L., Cantero Peral, S., Holst, K.A., Cetta, F., Wanek Program Preclinical Pipeline, 2018. Ultrasound guided percutaneous common carotid artery access in piglets for intracoronary stem cell infusion. Lab. Anim. 52, 88–92.

Arrigoni, C.h., Camozzi, D., Remuzzi, A., 2006. Vascular tissue engineering. Cell Transplant. 15, S119–S125.

Avril, S., Bersi, M.R., Bellini, C., Genovese, K., Humphrey, J.D., 2015. Regional identification of mechanical properties in arteries. Comput. Methods Biomech. Biomed. Eng. 8 (Suppl. 1), 1874–1875.

Bancroft, J.D., Stevens, A., 1996. Theory and practice of histological techniques. Churchill Livingstone, New York.

Bellini, C., Caulk, A.W., Li, G., Tellides, G., Humphrey, J.D., 2017. Biomechanical phenotyping of the murine aorta: what is the best control? J. Biomech. Eng. 139, 4.

Bersi, M.R., Bellini, C., Di Achille, P., Humphrey, J.D., Genovese, K., Avril, S., 2016. Novel methodology for characterizing regional variations in the material properties of murine aortas. J. Biomech. Eng. 138, 7.

Best, C., Fukunishi, T., Drews, J., Khosravi, R., Hor, K., Mahler, N., Yi, T., Humphrey, J.D., Johnson, J., Breuer, C.K., Hibino, N., 2018. Oversized biodegradable arterial grafts promote enhanced neointimal tissue formation. Tissue Eng. A 24, 1251–1261.

Byrom, M.J., Bannon, P.G., White, G.H., Ng, M.K., 2010. Animal models for the assessment of novel vascular conuits. J. Vasc. Surg. 52, 176–195.

Chlupac, J., Filova, E., Bacakova, L., 2009. Blood vessel replacement: 50 years of development and tissue engineering paradigms in vascular surgery. Physiol. Res. 58, 119–139.

Chow, S.C., Wang, H., Shao, J., 2008. Sample Size Calculations in Clinical Research, second edition. Chapman & Hall/CRC Biostatistics Series, Boca Raton.

Dahan, N., Sarig, U., Bronshtein, T., Baruch, L., Karram, T., Hoffman, A., Machluf, M., 2017. Dynamic autologous reendothelialization of small-caliber arterial extracellular matrix: a preclinical large animal study. Tissue Eng. A 23, 69–79.

de Valence, S., Tille, J.C., Giliberto, J.P., Mrowczynski, W., Gurny, R., Walpoth, B.H., Moller, M., 2012a. Advantages of bilayered vascular grafts for surgical applicability and tissue regeneratinon. Acta Biomater. 8, 3914–3920.

de Valence, S., Tille, J.C., Mugnai, D., Mrowczynski, W., Gurny, R., Moller, M., Walpoth, B.H., 2012b. Long term performance of polycaprolactone vascular grafts in a rat abdominal aorta replacement model. Biomaterials 33, 38–47.

Dondelinger, R.F., Ghysels, M.P., Brisbois, D., Donkers, E., Snaps, F.R., Saunders, J., Deviere, J., 1998. Relevant radiological anatomy of the pig as a training model in interventional radiology. Eur. Radiol. 8, 1254–1273.

Dreifaldt, M., Souza, D.S., Loesch, A., Muddle, J.R., Karlsson, M.G., Filbey, D., Bodin, L., Norgren, L., Dashwood, M.R., 2011. The "no-touch" harvesting technique for vein grafts in coronary artery bypass surgery preserves an intact vasa vasorum. J. Thorac. Cardiovasc. Surg. 141, 145–150.

Eberlova, L., Tonar, Z., Witter, K., Krizkova, V., Nedorost, L., Korabecna, M., Tolinger, P., Kocova, J., Boudova, L., Treska, V., Houdek, K., Molacek, J., Vrzalova, J., Pesta, M., Topolcan, O., Valenta, J., 2013. Asymptomatic abdominal aortic aneurysms show histological signs of progression: a quantitative histochemical analysis. Pathobiology 80, 11–23.

Emerson, M., 2010. Refinement, reduction and replacement approaches to in-vivo cardiovascular research. Br. J. Pharmacol. 161, 749–754.

Ferruzzi, J., Bersi, M.R., Mecham, R.P., Ramirez, F., Yanagisawa, H., Tellides, G., Humphrey, J.D., 2016. Loss of elastic Fiber integrity compromises common carotid artery function: implications for vascular aging. Artery Res. 14, 41–52.

Fong, P.-Y., Chuang, W.-Y., Huang, Y.-Z., Chang, C.-H., 2017. Safety of carotid artery stent in repetitive transcranial magnetic stimulation—the histopathological proof from swine carotid artery. Neurosci. Lett. 657, 194–198.

García, A., Martínez, M.A., Pena, ˜E., 2013. Determination and modeling of the inelasticity over the length of the porcine carotid artery. J. Biomech. Eng. 135, 31004.

García, A., Pena, E., Laborda, A., Lostalé, F., DeGregorio, M.A., Doblaré, M., Martínez, M.A., 2011. Experimental study and constitutive modelling of the passive mechanical properties of the porcine carotid artery and its relation to histological analysis: implications in animal cardiovascular device trials. Med. Eng. Phys. 33, 665–676.

Gaudino, M., Prati, F., Caradonna, E., Trani, C., Schiavoni, G., Glieca, F., Possati, G., 2005. Implantation in the coronary circulation induces morphofunctional transformation of radial grafts from muscular to elastomuscular. Circulation 112 (Suppl. 9), I208–I211.

He, G.W., 2013. Arterial grafts: clinical classification and pharmacological management. Ann. Cardiothorac. Surg. 2, 507–518.

Howard, C.V., Reed, M.G., 1998. Unbiased Stereology. Three-dimensional Measurement in Microscopy. Springer, New York.

Jaramillo, J., Valencia-Rivero, K.T., Cedano-Serrano, F.J., López, R., Sandoval, N., Briceno, ˜J.C., 2018. Design and evaluation of a structural reinforced small intestinal submucosa vascular graft for hemodialysis access in a porcine model. ASAIO J. 64, 270–277.

Jiang, Y., Li, Y., Xu, X., Yu, Y., Liu, W., Liu, X., 2016. An in vitro porcine model evaluating a novel stent retriever for thrombectomy of the common carotid artery. Catheter. Cardiovasc. Interv. Off. J. Soc. Card. Angiogr. Interv. 87, 457–464.

Jirík, ˚M., Bartos, ˚M., Tomásek, ˚P., Malecková, ˚A., Kural, T., Horáková, J., Lukás, ˚D., Suchy, ´T., Kochová, P., Hubálek Kalbácová, ˚M., Králícková, ˚M., Tonar, Z., 2018. Generating standardized image data for testing and calibrating quantification of volumes, surfaces, lengths, and object counts in fibrous and porous materials using X-ray microtomography. Microsc. Res. Tech. 81, 551–568.

Johnson, J., Ohst, D., Hettercheidt, S., Jones, M., 2015. Development of novel, bioresorbable, small-diameter electrospun vascular grafts. J. Tissue Sci. Eng. 6, 1–7.

Junatas, K.L., Tonar, Z., Kubíková, T., Liska, ˚V., Pálek, R., Mik, P., Králícková, ˚M., Witter, K., 2017. Stereological analysis of size and density of hepatocytes in the porcine liver. J. Anat. 230, 575–588.

Kakisis, J.D., Liapis, C.D., Breuer, C., Sumpio, B.E., 2005. Artificial blood vessel: the Holy Grail of peripheral vascular surgery. J. Vasc. Surg. 41, 349–354.

Kim, E.K., Maldonado, A.A., Jeong, W.S., Hong, J.P., Song, D.H., 2015. Microvascular vessel preparation: what are we really removing during adventitial stripping? J. Plast. Reconstr. Aesthet. Surg. 68, 1568–1573.

Klement, P., Berry, L.R., Liao, P., Wood, H., Tressel, P., Smith, L.J., Haque, N., Weitz, J.I., Hirsh, J., Paredes, N., Chan, A.K., 2010. Antithrombin-heparin covalent complex reduces microemboli during cardiopulmonary bypass in a pig model. Blood 116, 5716–5723.

Kocova, J., 1970. Overall staining of connective tissue and the muscular layer of vessels. Fol. Morphol. 18, 293–295.

Kochová, P., Kuncová, J., Svíglerová, J., Cimrman, R., Miklíková, M., Liska, ˚V., Tonar, Z., 2012. The contribution of vascular smooth muscle, elastin and collagen on the passive mechanics of porcine carotid arteries. Physiol. Meas. 33, 1335–1351.

Kochová, P., Witter, K., Tonar, Z., 2014. Distribution of orientation of smooth muscle bundles does not change along human great and small varicose veins, Ann. Anat. 196, 67–74.

Koens, M.J., Krasznai, A.G., Hanssen, A.E., Hendriks, T., Praster, R., Daamen, W.F., van der Vliet, J.A., van Kuppevelt, T.H., 2015. Vascular replacement using a layered elastin-collagen vascular graft in a porcine model: one week patency versus one month occlusion. Organogenesis 11, 105–121.

Koh, A., Carpenter, A.W., Slomberg, D.L., Schoenfisch, M.H., 2013. Nitric oxide releasing silica nanoparticle-doped polyurethane electrospun fibers. ACS Appl. Mater. Interfaces 5, 7956–7964.

Kritharis, E.P., Giagini, A.T., Kakisis, J.D., Dimitriou, C.A., Stergiopulos, N., Tsangaris, S., Sokolis, D.P., 2012. Time course of flow-induced adaptation of carotid artery biomechanical properties, structure and zero-stress state in the arteriovenous shunt. Biorheology 49, 65–82.

Kubíková, T., Kochová, P., Brázdil, J., Spatenka, ˘ J., Burkert, J., Králícková, ˘ M., Tonar, Z., 2017. The composition and biomechanical properties of human cryopreserved aortas, pulmonary trunks, and aortic and pulmonary cusps. Ann. Anat. 212, 17–26.

Lawson, J.H., Glickman, M.H., Ilzecki, M., Jakimowicz, T., Jaroszynski, A., Peden, E.K., Pilgrim, A.J., Prichard, H.L., Guziewicz, M., Przywara, S., Szmidt, J., Turek, J., Witkiewicz, W., Zapotoczny, N., Zubilewicz, T., Niklason, L.E., 2016. Bioengineered human acellular vessels for dialysis access in patients with end-stage renal disease: two phase 2 single-arm trials. Lancet 387, 2026–2034.

Liao, D., Wang, X., Lin, P.H., Yao, Q., Chen, C.J., 2009. Covalent linkage of heparin provides a stable anti-coagulation surface of decellularized porcine arteries. J. Cell. Mol. Med. 13, 2736–2743.

Lindsey, P., Echeverria, A., Cheung, M., Kfoury, E., Bechara, C.F., Lin, P.H., 2017. Lower extremity bypass using bovine carotid artery graft (artegraft): an analysis of 124 cases with long-term results. World J. Surg. 42, 295–301.

Liu, T., Liu, Y., Chen, Y., Liu, S., Maitz, M.F., Wang, X., Zhang, K., Wang, J., Wang, Y., Chen, J., Huang, N., 2014. Immobilization of heparin/poly-(L)-lysine nanoparticles on dopamine-coated surface to create a heparin density gradient for selective direction of platelet and vascular cells behavior. Acta Biomater. 10, 1940–1954.

Loop, F.D., Lytle, B.W., Cosgrove, D.M., Stewart, R.W., Goormastic, M., Williams, G.W., Golding, L.A., Gill, C.C., Taylor, P.C., Sheldon, W.C., 1986. Influence of the internal mammary-artery graft on 10-year survival and other cardiac events. N. Engl. J. Med. 314, 1–6.

Loskot, P., Tonar, Z., Baxa, J., Valenta, J., 2016. The descending branch of the lateral circumflex femoral artery as an alternative conduit for coronary artery bypass grafting: experience from an anatomical, radiological and histological study. Clin. Anat. 29, 779–788.

Lossi, L., D'Angelo, L., De Girolamo, P., Merighi, A., 2016. Anatomical features for an adequate choice of experimental animal model in biomedicine: II. Small laboratory rodents, rabbit, and pig. Ann. Anat. 204, 11–28.

Lu, S., Zhang, P., Sun, X., Gong, F., Yang, S., Shen, L., Huang, Z., Wang, C., 2013. Synthetic ePTFE grafts coated with an anti-CD133 antibody-functionalized heparin/collagen multilayer with rapid in vivo endothelialization properties. ACS Appl. Mater. Interfaces 5, 7360–7369.

Malfait, F., 2018. Vascular aspects of the ehlers-danlos syndromes. Matrix Biol. 71–72, 380–395.

Martínez-González, B., Reyes-Hernández, C.G., Quiroga-Garza, A., RodríguezRodríguez, V.E., Esparza-Hernández, C.N., Elizondo-Omana, R.E., Guzmán-López, S., 2017. Conduit used in coronary artery bypass grafting: a review of morphological studies. Ann. Thorac. Cardiovasc. Surg. 23, 55–65.

McClure, M.J., Simpson, D.G., Bowlin, G.L., 2012. Tri-layered vascular grafts composed of polycaprolactone, elastin, collagen, and silk: optimization of graft properties. J. Mech. Behav. Biomed. Mater. 10, 48–61.

Menasche, P., Flaus, P., Huc, A., Piwnica, A., 1984. Collagen vascular grafts: a step towards improved compliance in small-calibre bypass surgery; preliminary report. Life Support Syst. 2, 233–237.

Mrowczynski, W., Mugnai, D., de Valence, S., Tille, J.C., Khabiri, E., Cikirikcioglu, M., Möller, M., Walpoth, B.H., 2014. Porcine carotid artery replacement with biodegradable electrospun poly-e-caprolactone vascular prosthesis. J. Vasc. Surg. 59, 210–219.

Naito, Y., Shinoka, T., Duncan, D., Hibino, N., Solomon, D., Cleary, M., Rathore, A., Fein, C., Church, S., Breuer, C., 2011. Vascular tissue engineering: towards the next generation vascular grafts. Adv. Drug Deliv. Rev. 30, 312–323.

Nedorost, L., Uemura, H., Furck, A., Saeed, I., Slavik, Z., Kobr, J., Tonar, Z., 2013. Vascular histopathologic reaction to pulmonary artery banding in an in vivo growing porcine model. Pediatr. Cardiol. 34, 1652–1660.

Negishi, J., Funamoto, S., Kimura, T., Nam, K., Higami, T., etal., 2011. Effect of treatment temperature on collagen structures of the decellularized carotid artery using high hydrostatic pressure. J. Artif. Organs 14, 223–231.

Nikoubashman, O., Heringer, S., Feher, K., Brockmann, M.-A., Sellhaus, B., Dreser, A., Kurtenbach, K., Pjontek, R., Jockenhövel, S., Weis, J., Kießling, F., Gries, T., Wiesmann, M., 2018. Development of a polymer-based biodegradable neurovascular stent prototype: a preliminary in vitro and in vivo study. Macromol. Biosci. 18, e1700292.

Ong, C.S., Zhou, X., Huang, C.Y., Fukunishi, T., Zhang, H., Hibino, N., 2017. Tissue engineered vascular grafts: current state of the field. Expert Rev. Med. Devices 14, 383–392.

Otsuka, F., Yahagi, K., Sakakura, K., Virmani, R., 2013. Why is the mammary artery so special and what protects it from atherosclerosis? Ann. Cardiothorac. Surg. 2, 519–526.

Ozolanta, I., Tetere, G., Purinya, B., Kasyanov, V., 1998. Changes in the mechanical properties, biochemical contents and wall structure of the human coronary arteries with age and sex. Med. Eng. Phys. 20, 523–533.

Pashneh-Tala, S., MacNeil, S., Claeyssens, F., 2016. The tissue-engineered vascular graft—past, present and future. Tissue Eng. B Rev. 22, 68–100.

Popesko, P., 1978. Atlas of Topographical Anatomy of the Domestic Animals, second edition. W.B. Saunders Co., Philadelphia.

Qiu, X., Lee, B.L., Ning, X., Murthy, N., Dong, N., Li, S., 2017. End-point immobilization of heparin on plasma-treated surface of electrospun polycarbonate-urethane vascular graft. Acta Biomater. 51, 138–147.

Quint, C., Kondo, Y., Manson, R.J., Lawson, J.H., Dardik, A., Niklason, L.E., 2011. Decellularized tissue-engineered blood vessel as an arterial conduit. Proc. Natl. Acad. Sci. U.S.A. 108, 9214–9219.

Rich, L., Whittaker, P., 2005. Collagen and Picrosirius Red staining: a polarized light assessment of fibrillar hue and spatial distribution. Braz. J. Morphol. Sci. 22, 97–104.

Rothuizen, T.C., Damanik, F.F.R., Lavrijsen, T., Visser, M.J.T., Hamming, J.F., Lalaj, R.A., Duijs, J.M.G.J., van Zonneveld, A.J., Hoefer, I.E., van Blitterswijk, C.A., Rabelink, T.J., Moroni, L., Rotmans, J.I., 2016. Development and evaluation of in vivo tissue engineered blood vessels in a porcine model. Biomaterials 75, 82–90.

Rotmans, J.I., Heyligers, J.M., Verhagen, H.J., Velema, E., Nagtegaal, M.M., de Kleijn, D.P., de Groot, F.G., Stroes, E.S., Pasterkamp, G., 2005. In vivo cell seeding with anti-CD34 antibodies successfully accelerates endothelialization but stimulates intimal hyperplasia in porcine arteriovenous expanded polytetrafluoroethylene grafts. Circulation 112, 12–18.

Rychter, M., Gaucher, C., Boudier, A., Leroy, P., Lulek, J., 2016. S-Nitrosothiols-NO donors regulating cardiovascular cell proliferation: insight into intracellular pathway alterations. Int. J. Biochem. Cell Biol. 78, 156–161.

Sarkar, S., Sales, K.M., Hamilton, G., Seifalian, A.M., 2007. Addressing thrombogenicity in vascular graft construction. J. Biomed. Mater. Res. B Appl. Biomater. 82, 100–108.

Schindelin, J., Arganda-Carreras, I., Frise, E., Kaynig, V., Longair, M., Pietzsch, T., Preibisch, S., Rueden, C., Saalfeld, S., Schmid, B., Tinevez, J.Y., White, D.J., Hartenstein, V., Eliceiri, K., Tomancak, P., Cardona, A., 2012. Fiji: an open-source platform for biological-image analysis. Nat. Methods 9, 676–682.

Shin, Y.M., Lee, Y.B., Kim, S.J., Kang, J.K., Park, J.C., Jang, W., Shin, H., 2012. Mussel-inspired immobilization of vascular endothelial growth factor (VEGF) for enhanced endothelialization of vascular grafts. Biomacromolecules 13, 2020–2028.

Shrout, P.E., Fleiss, J.L., 1979. Intraclass correlations: uses in assessing rater reliability. Psychol. Bull. 86, 420–428.

Sisto, T., Isola, J., 1989. Incidence of atherosclerosis in the internal mammary artery. Ann. Thorac. Surg. 47, 884–886.

Sokolis, D.P., 2007. Passive mechanical properties and structure of the aorta: segmental analysis. Acta Physiol. (Oxf.) 190, 277–289.

Sokolis, D.P., Boudoulas, H., Karayannacos, P.E., 2008. Segmental differences of aortic function and composition: clinical implications. Hellenic J. Cardiol. 49, 145–154.

Sokolis, D.P., Sassani, S., Kritharis, E.P., Tsangaris, S., 2011. Differential histomechanical response of carotid artery in relation to species and region: mathematical description accounting for elastin and collagen anisotropy. Med. Biol. Eng. Comput. 49, 867–879.

Stary, H.C., 2000. Natural history and histological classification of atherosclerotic lesions: an update. Arter. Thromb. Vasc. Biol. 20, 1177–1178.

Stary, H.C., Chandler, A.B., Glagov, S., Guyton, J.R., Insull Jr., W., Rosenfeld, M.E., Schaffer, S.A., Schwartz, C.J., Wagner, W.D., Wissler, R.W., 1994. A definition of initial, fatty streak, and intermediate lesions of atherosclerosis. A report from the Committee on Vascular Lesions of the Council on Arteriosclerosis, American Heart Association. Circulation 89, 2462–2468.

Stevens, R.L., Colombo, M., Gonzales, J.J., Hollander, W., Schmid, K., 1976. The glycosaminoglycans of the human artery and their changes in atherosclerosis. J. Clin. Invest. 58, 470–481.

Stewart, J.K., Perkins, S.S., Kim, C.Y., 2017. Creation of an extraluminal arterial bypass graft using a commercially available self-expanding stent graft: feasibility study in a porcine model. Cardiovasc. Intervent. Radiol. 40, 1447–1453.

Sun, J., Sun, K., Bai, K., Chen, S., Wang, F., Zhao, F., Hong, N., Hu, H., 2019. A novel braided biodegradable stent for use in congenital heart disease: short-term results in porcine iliac artery. J. Biomed. Mater. Res. A 107, 1667–1677.

Szafron, J.M., Ramachandra, A.B., Breuer, C.K., Marsden, A.L., Humphrey, J.D., 2019. Optimization of tissue-engineered vascular graft design using computational modeling. Tissue Eng. C Methods 25, 561–570.

Tang, X.F., Liu, J.J., Wu, Y.J., Chen, K.M., Jin, Y., Gao, P.J., Zhu, D.L., Shen, G.X., 2010. Effect of hirulog-like peptide on balloon catheter injury-induced neointimal formation in femoral arteries of minipigs and relationship with inflammatory mediators. J. Vasc. Res. 47, 262–269.

Tara, S., Kurobe, H., Rocco, K.A., Maxfield, M.W., Best, C.A., Naito, Y., Breuer, C.K., Shinoka, T., 2014. Well-organized neointima of large-pore poly(L-lactic acid) vascular graft coated with poly (L-lactic-co--caprolactone) prevents calcific deposition compared to small-pore electrospun poly(L-lactic acid) graft in a mouse aortic implantation model. Atherosclerosis 237, 684–691.

Teebken, O.E., Pichlmaier, A.M., Haverich, A., 2001. Cell seeded decellularised allogeneic matrix grafts and biodegradable polydioxanone-prostheses compared with arterial autografts in a porcine model. Eur. J. Vasc. Endovasc. Surg. 22, 139–145.

Tonar, Z., Kubíková, T., Prior, C., Demjén, E., Liska, ˘ V., Králícková, ˘ M., Witter, K., 2015. Segmental and age differences in the elastin network, collagen, and smooth muscle phenotype in the tunica media of the porcine aorta. Ann. Anat. 201, 79–90.

Tonar, Z., Kural Jr., T., Kochova, P., Nedorost, L., Witter, K., 2012. Vasa vasorum quantification in human varicose great and small saphenous veins. Ann. Anat. 194, 473–481.

Tonar, Z., Tomásek, ˘ P., Loskot, P., Janácek, ˘ J., Králícková, ˘ M., Witter, K., 2016. Vasa vasorum in the tunica media and tunica adventitia of the porcine aorta. Ann. Anat. 205, 22–36.

Tschanz, S., Schneider, J.P., Knudsen, L., 2014. Design-based stereology: planning, volumetry and sampling are crucial steps for a successful study. Ann. Anat. 196, 3–11.

Tzchori, I., Falah, M., Shteynberg, D., Levin Ashkenazi, D., Loberman, Z., Perry, L., Flugelman, M.Y., 2018. Improved patency of ePTFE grafts as a hemodialysis access site by seeding autologous endothelial cells expressing Fibulin-5 and VEGF. Mol. Ther. 26, 1660–1668.

Ueberrueck, T., Meyer, L., Zippel, R., Nestler, G., Wahlers, T., Gastinger, I., 2005. Healing characteristics of a new silver-coated, gelatine impregnated vascular prosthesis in the porcine model. Zentralbl. Chir. 130, 71–76.

Vrtkova, I., 2015. Genetic admixture analysis in Prestice Black-Pied pigs. Arch. Anim. Breed 58, 115–121.

Wang, K., Zhang, Q., Zhao, L., Pan, Y., Wang, T., Zhi, D., Ma, S., Zhang, P., Zhao, T., Zhang, S., Li, W., Zhu, Y., Zhang, J., Qiao, M., Kong, D., 2017. Functional modification of electrospun poly(-caprolactone) vascular grafts with the fusion of protein VEGF-HGFI enhanced vascular regeneration. ACS Appl. Mater. Interfaces 9, 11415–11427.

Wang, S.D., Zhang, Y.Z., Yin, G.B., Wang, H.W., Dong, Z.H., 2010. Fabrication of a composite vascular scaffold using electrospinning technology. Mater. Sci. Eng. C Mater. Biol. Appl. 30, 670–676.

Weizsäcker, H.W., Zierler, E., Juch, H., 2014. A simple method for vital staining of elastin in arterial tissue. Biomed. Tech. (Berl.) 59, 367–373.

Wharton,S.B.,Cary,N.R.B.,Gresham,G.A.,1994.Observationsondetailedhistologyoftheinternal thoracicarteryandtheirrelevancetoitscomparativelylow incidenceofatheroma.Clin.Anat.7, 215–218.

Wise,S.G.,Byrom,M.J.,Waterhouse,A.,Bannon,P.G.,Weiss,A.S.,2011.Amultilayeredsynthetic human elastin/polycaprolactone hybrid vascular grafts with tailored mechanical properties. ActaBiomater.7,295–303.

Witter,K.,Tonar,Z.,Matejka,V.M.,Martinca,T.,Jonak,M.,Rokosny,S.,Pirk,J.,2010. Tissuereaction tothreedifferenttypesoftissuegluesinanexperimentalaorta dissectionmodel:aquantitative approach.Histochem.CellBiol.133,241–259.

Witter,K.,Tonar,Z.,Schöpper,H.,2017.Howmanylayershastheadventitia?Structureofthearterial Tunica externa revisited. Anat. Histol. Embryol. 46, 110–120. Wu, T., Zhang, J., Wang, Y., Li, D., Sun,B.,El-Hamshary,H.,Yin,M.,Mo,X.,2018. Fabricationandpreliminarystudyofabiomimietic tri-layeredgraf˙ tbasedon fibersandfiberyarnsforvasculartissueengineering.Mater.Sci.Eng.C Mater. Biol.Appl.82,121–129.

Wyatt, H.L., Richards, R., Pullin, R., Yang, T.J., Blain, E.J., Evans, S.L., 2016. Variation in electrosurgicalvesselsealqualityalongthelengthofaporcinecarotidartery. Proc.Inst.Mech. Eng.230,169–174.

Yazdani,K.S.,Otsuka,F.,Nakano,M.,Ladich,E.,Virmani,R.,2013.Pathologyofsaphenousveingrafts. Interv.Cardiol.Clin.2,241–249.

Zhou,Z.-H.,Peng,J.,Meng,Z.-Y.,Chen,L.,Huang,J.-L.,Huang,H.-Q.,Li,L.,Zeng, W.,Wei,Y., Zhu,C.-H.,Chen,K.-N.,2016.NovelA20-gene-elutingstentinhibits carotidarteryrestenosis inaporcinemodel.DrugDes.Dev.Ther.10,2341–2351.

Zilla,P.,Bezuidenhout,D.,Human,P.,2007.Prostheticvasculargrafts:wrongmodels, wrongquestions andnohealing.Biomaterials28,5009–5027.